WASHINGTON UNIVERSITY
SEVER INSTITUTE OF TECHNOLOGY

DEPARTMENT OF CHEMICAL ENGINEERING

EXPERIMENTAL INVESTIGATION OF BUBBLE COLUMN HYDRODYNAMICS
- EFFECT OF ELEVATED PRESSURE AND SUPERFICIAL GAS VELOCITY -

by
Booncheng Ong
Prepared under the direction of Prof. M. P. Dudukovic' and Prof. M. H. Al-Dahhan

---

A dissertation presented to the Sever Institute of
Washington University in partial fulfillment
of the requirements for the degree of

DOCTOR OF SCIENCE

May, 2003
Saint Louis, Missouri, USA

WASHINGTON UNIVERSITY
SEVER INSTITUTE OF TECHNOLOGY

DEPARTMENT OF CHEMICAL ENGINEERING

ABSTRACT

EXPERIMENTAL INVESTIGATION OF BUBBLE COLUMN HYDRODYNAMICS - EFFECT OF ELEVATED PRESSURE AND SUPERFICIAL GAS VELOCITY -

by Booncheng Ong

ADVISORS: Prof. M. P. Dudukovic' and Prof. M. H. Al-Dahhan

May, 2003
Saint Louis, Missouri, USA

Bubble column reactors are widely used in the chemical and biochemical industries. They were reactors of choice in syngas conversion to clean fuels and chemicals. Most of the current applications of bubble column reactors in the chemical process industry require operation at high-pressure conditions. Further, to enhance the volumetric productivity, high gas flow rates are employed. The fundamental description of bubble column hydrodynamics under these conditions is very complex and complete understanding has not yet been established in spite of concerted research efforts. In order to improve our ability to quantify phenomena in bubble columns, it is essential that

precise and quality experimental information is available to advance the state of the art in bubble column design and operation. In this study, measurements of gas holdup, from Computed Tomography, and of time-averaged liquid velocity and turbulence, from Computer Automated Radioactive Particle Tracking, are obtained in a 6.4” diameter stainless steel bubble column at elevated pressure and at high superficial gas velocity with different gas spargers.

It is shown quantitatively that deep in the churn-turbulent regime, gas holdup and liquid recirculation increase with pressure and superficial gas velocity while sparger effects are predominantly confined to the distributor zone. Additionally, an increase in pressure results in the reduction of turbulent normal stresses and eddy diffusivities most likely due to a reduction in bubble size. Based on the experimental data obtained from this study, a correction factor to the correlation of Zehner (1986) for predicting the centerline liquid velocity is developed to account for pressure effect on liquid recirculation. The correction factor indicates an one-eighth power dependency on gas density. Comparison of the experimentally estimated eddy viscosity with the model of Ohnuki and Akimoto (2001) suggests that the contribution of bubble-induced turbulence to the effective eddy viscosity is small as compared to that from the shear-induced turbulence. Though further studies are required to comprehend the pressure effects on larger diameter column, this study provides the first detail hydrodynamic data set at high pressure and very high superficial gas velocity.

to my parents, siblings and soul-mate

Contents

Tables

Figures

Nomenclature

AF	acceleration factor for large bubble rise velocity
A_o	area of distributor plate per orifice, m^2/orifice
C_D	drag coefficient
C_0, C_1	constants obtained from fitting the drift flux model
c	parameter in the hold-up profile to allow non-zero hold-up at the wall
D_C, D_T, D	column diameter, cm
DF	density factor for large bubble rise velocity
D_{rr}	radial turbulent diffusivity, cm^2/s
D_{zz}	axial turbulent diffusivity, cm^2/s
$D_{\theta\theta}$	azimuthal turbulent diffusivity, cm^2/s
d_b, d_{be}	mean (effective) bubble diameter, cm
d_{blarge}	bubble diameter of large bubbles, cm
d, d_n	sparger orifice diameter, mm
F	steepness of radial gas holdup profile
g	acceleration due to gravity, cm^2/s
H	column height, cm
H_D	expanded height of gas-liquid mixture in column, cm
H_i	static height of liquid in column, cm
h*	height above the sparger at which bubbles attain their equilibrium size, m
j_{GL}	drift flux, cm/s
k	turbulent kinetic energy, cm^2/s
L_j	penetration length, cm
l_r	characteristic radial turbulent length, cm
l_z	characteristic axial turbulent length, cm

l	mixing length, cm
m	power law exponent in the radial gas hold-up profile
N_r	number of radial positions for column discretization
$N_{\theta,max}$	maximum number of azimuthal positions for column discretization
N_z	number of axial positions for column discretization
n	Richardson-Zaki coefficient
n_v	number of bubbles per unit volume
P	operating pressure, MPa
p_H	hydrostatic pressure at the orifice plate
Q	flow rate, cm^3/s
R	column radius, cm
R_{ij}	Lagrangian autocorrelation coefficient
r	radial position in the column, cm
SF	shape factor for large bubble rise velocity
T	operating temperature, K
t	time, sec
U	phase superficial velocity, cm/s
U_b	bubble terminal rise velocity, cm/s
U_{gtrans}	transition superficial gas velocity, cm/s
U_s	slip velocity, cm/s
$\overline{u_i' u_j'}$	transport of momentum due to turbulent velocity fluctuations along ith direction due to instantaneous flow in jth direction, cm^2/s
u	local phase velocity, cm/s
$u_{b\infty}$	terminal single bubble rise velocity, m/s
u_0	centerline interstitial liquid velocity, cm/s
$\bar{u}$	radially averaged mean velocity, cm/s
$V^0_{b,small}$	unhindered rise velocity of a small bubble, cm/s
$V_{b,small}$	rise velocity of dense bubble phase, cm/s
$V_{b,large}$	rise velocity of large bubble phase, cm/s

V_{ch}	chamber volume, m^3/s
W	width of rectangular bubble column, m
z	axial position in the column, cm

Greek Symbols

δ	thickness of wall boundary layer
ε	phase hold-up
ε_c	gas hold-up at column center
$\bar{\varepsilon}$	cross-sectional averaged phase hold-up
$\tilde{\varepsilon}$	chordal averaged phase hold-up
ϕ	shape factor
κ	first von Karman parameter
λ	point of flow inversion
μ	viscosity, g/cm.s
ν	kinematic viscosity, cm^2/s
ρ	density, g/cm^3
σ	surface tension, mN/m
τ_L	integral time scale, s
ξ	dimensionless radius

Dimensionless groups

Bo	Bond Number $\left(g\rho_l d_o^2/\sigma\right)$
Eo	Eotvos Number $\left(g\left(\rho_l-\rho_g\right)d_b^2/\sigma_l\right)$
Fr	Froude Number $\left(U_g^2/gD_c\right)$
Fr_o	Orifice Froude Number $\left(u_o^2/gd_o\right)$
Mo_L	Morton Number $\left(g\mu_l^4/\left(\rho_l-\rho_g\right)\sigma^3\right)$

Nc	Capacitance Number $\left(4V_{ch} g\rho_l / \pi d_o^2 p_h\right)$
Nw	Gas Flow Number $\left(BoFr_o^{0.5}\right)$
Re_G	Reynolds Number $\left(U_g\left(\rho_l - \rho_g\right)D_c / \mu_l\right)$
Re_o	Orifice Reynolds Number based on gas properties $\left(u_o \rho_g d_o / \mu_g\right)$
We	Weber Number $\left(g\rho_l d_o^2 / \sigma\right)$

Subscripts

b	bubble
g, G	gas
l, L	liquid
m	molecular
t	turbulent

Acknowledgements

I would like to make use of this opportunity to thank my advisor, Professor M. P. Dudukovic for his supervision and advice, which make this work possible. I would also like to thank my co-advisor Prof. M. H. Al-Dahhan, whose outlook in various issues made it possible for me to finish this project. Additionally, I would like to acknowledge the members of my committee, namely, Prof. P. A. Ramachandran, Prof. Brian Wrenn (Department of Environmental Engineering), Prof. R. A. Gardner (Department of Mechanical Engineering) for taking interest in my work, and examining my thesis.

I also wish to gratefully acknowledge the financial support of the Department of Energy and the industrial participants of the CREL consortium, which made this research work possible.

In addition, I would like to express my gratitude to several people at CREL and in the Department of Chemical Engineering, who made significant contributions in making my work and life at Washington University an enjoyable experience. In particular, I would like to express my gratitude to Dr. Puneet Gupta for his persistent encouragement and assistance during the difficult phases of my doctoral program. I also thank Mr. Satish Bhusarapu, Mr. Ashfaq Sheikh, Mr. Huping Luo, Mr. Junli Xue, Mr. Rados Novica, Dr. Sujatha Degaleesan, Dr. Yuanxin Wu and Dr. Kemoun Abdenour for their assistance in my experimental work as well as clearing my doubts in my area of research. I would like to thank Mr. Aravind Rammohan and Mrs. Arpita Mitra for their support. My sincere appreciation also goes to Steve Picker, Pat Harkins and John Krietler for their assistance during the high-pressure bubble column construction; and Dr. Y. Yamashita for his help in resolving numerous network-related issues. My sincere thanks also go to Dr. Milind Kulkarni and Mrs. Sushma Patil whose encouragement was invaluable during my stay in Saint Louis. I also wish to thank the entire Chemical Engineering Department,

particularly the secretaries for their help with numerous formalities. Finally, thanks to my roommates and friends whose company made my stay in Saint Louis a pleasant and memorable one.

Last, but not the least, my heartfelt gratitude goes to my parents and my siblings for their patience and support in these years of my doctoral program.

Booncheng Ong
Washington University, St. Louis
May 2003

Chapter 1. Introduction

Bubble columns, operated as reactors or absorbers, are vertical cylindrical vessels, in which a gas, made up of one or several soluble reactive components, is contacted with a liquid or slurry. Figure 1-1 shows a simple bubble column, where both the liquid and the gas are introduced at the bottom of the column. This is the co-current mode of operation. However, bubble columns can also be operated with the liquid as either batch or flowing counter-currently to the gas, the latter being necessary in absorbers and reactors where gas-liquid mass transfer is limiting the overall process rate. In all these systems, gas is usually dispersed through a sparger and bubbles through the liquid. Reactive or catalytic particles may also be suspended in the liquid phase (slurry/three phase bubble column).

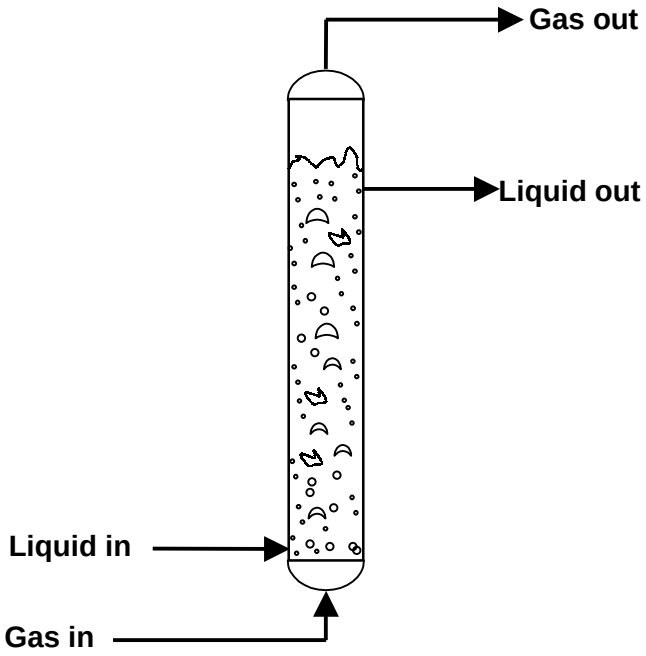

Figure 1-1. Schematic diagram of a simple bubble column.

Bubble column reactors have gained considerable attention over the past few decades due to the various advantages they offer. They are simple to construct and do not involve any mechanically moving parts. Therefore, they are very suitable for high pressure operating conditions where one is concerned with leakage around rotating shafts in stored vessels. In addition, they exhibit excellent heat and mass transfer characteristics, which help in operating the reactor at close to isothermal conditions. All of these characteristics make bubble columns reactors of choice for numerous applications. However, the excessive backmixing of the liquid phase resulting from the buoyancy driven recirculation in bubble columns, is sometimes a serious disadvantage. To overcome this limitation, modifications to the design of the bubble columns have been considered in order to reduce the backmixing. This includes addition of internals, baffles, etc. (Deckwer, 1991). In spite of the myriad of published literature spanning several decades, bubble column design and scale-up is limited by the incomplete understanding of the excessively complex hydrodynamics.

Table 1-1 shows several of the various industrial applications of bubble column reactors along with typical operating conditions. These are only some of the many applications where bubble columns are used in processing of chemicals. In addition, bubble columns are also used in biotechnology (Schügerl *et al*., 1977; Blenke, 1979) such as antibiotic fermentation (Fregapane *et al*., 1999), single cell protein production and animal cell culture (Chisti, 1989). Other applications include wastewater treatment (Beltran *et a*l., 1995; Boyes *et al*., 1995), and dehydration of ortho-boric acid (Kang *et al*., 1995).

Table 1-1. Industrial applications of bubble column reactors.

	Temperature, °C	Pressure, atm (MPa)	References
Partial oxidation of ethylene to acetaldehyde	130	3 (0.3)	Deckwer, 1991
Wet-air oxidation of sewage sludge	200 – 300	40 – 120 (4 – 12)	Deckwer, 1991
Oxidation of cumene to phenol	80 – 125	5 – 8 (0.5 – 0.8)	Deckwer, 1991
Hydroxilamine formation by hydrogenation	50 – 60	25 – 30 (2.5 – 3)	Deckwer, 1991
Conversion of natural gas to liquid fuels via syngas	900	15 – 30 (150 – 300)	Wender, 1996
Methanol synthesis	(1) 350 – 400	(1) 250–350 (25–35)	Wender, 1996
(1) BASF	(2) 220 – 250	(2) 50 – 100 (5 – 10)	
(2) Eastman Chemicals, Air-Product, DOE			
Fischer-Tropsch synthesis	220 – 260	136 – 204 (13.6 – 20.4)	Wender, 1996
Hydroformylation (Oxo) processes	160 – 200	50 – 100 (5 – 10)	Wender, 1996

Among the chemical processes listed in Table 1-1, the conversion of natural gas to syngas (synthesis gas - a mixture of carbon monoxide and hydrogen gases) has recently gained significant importance. Figure 1-2 shows the relative mix of different sources of energy based upon recent United States Department of Energy (DOE) data. As evident from Figure 1-2, the most consumed energy source is oil, followed by coal and natural gas. Usage of oil and other natural sources of fuels have been increasing due to increased demands for electricity and gasoline for aircraft and automobiles as a result of increasing world population. Thus, oil reserves are continuously being depleted and alternative energy sources have to be sought. One alternative is the usage of syngas, obtained either from coal or natural gas, to produce hydrocarbons as alternate sources of fuel. Figure 1-3 shows the major commercial, near commercial and potentially commercial chemical uses of syngas (Wender, 1996). The four main commercial uses are the manufacture of hydrogen for ammonia synthesis, the manufacture of methanol to obtain methyl t-butyl ether (MTBE), the synthesis of fuels and chemicals from coal based syngas (Fischer-Tropsch synthesis), and the hydroformylation of olefins to aldehydes and alcohols. Further details of various reactions that utilize syngas can be found in Wender (1996). The operating conditions for the above mentioned commercial uses of syngas are shown in Table 1-1.

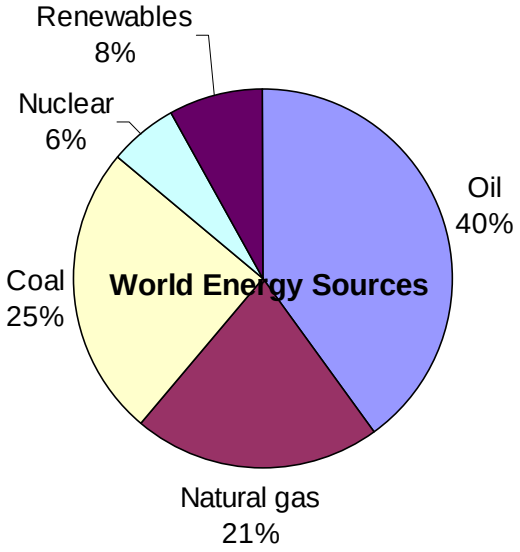

Figure 1-2. Relative mix of different sources of energy.

(Source: U.S. Department of Energy, International Energy Outlook, 1998)

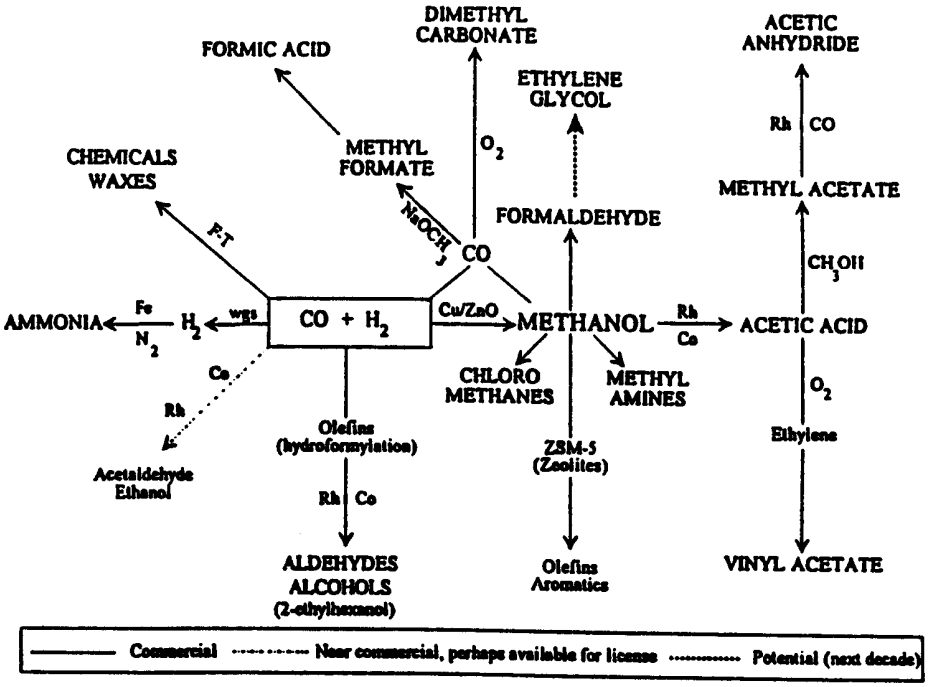

Figure 1-3. Major commercial, near commercial and potentially commercial chemical uses of syngas (Wender, 1996).

1.1. Motivation

As mentioned previously, in spite of the simplicity of the mechanical design of bubble columns without internals other than heat transfer tubes, their hydrodynamics is complicated and the understanding required for design and scale-up is still incomplete. Ideally, given the physicochemical parameters of the system of interest, catalyst type and properties and some measures of kinetics, one would like to be able to design a bubble column of high volumetric productivity that will operate stably. However, high volumetric productivity requires that a bubble column reactor operates at high pressure and high superficial gas velocities. And this is where the real challenge for designing these reactors lies as there are numerous parameters that affect the bubble column performance, namely, operating conditions (pressure, temperature, superficial gas velocity, etc.), design variables (sparger design and configuration, reactor geometry, reactor internals, heat transfer duty, etc.), physical and thermodynamic properties, and

chemical kinetics. All of these parameters influence the flow pattern, breakup and coalescence of bubbles, gas holdup, the intensity of liquid turbulence, etc. A simple flow chart that represents the factors influencing bubble column performance is shown in Figure 1-4.

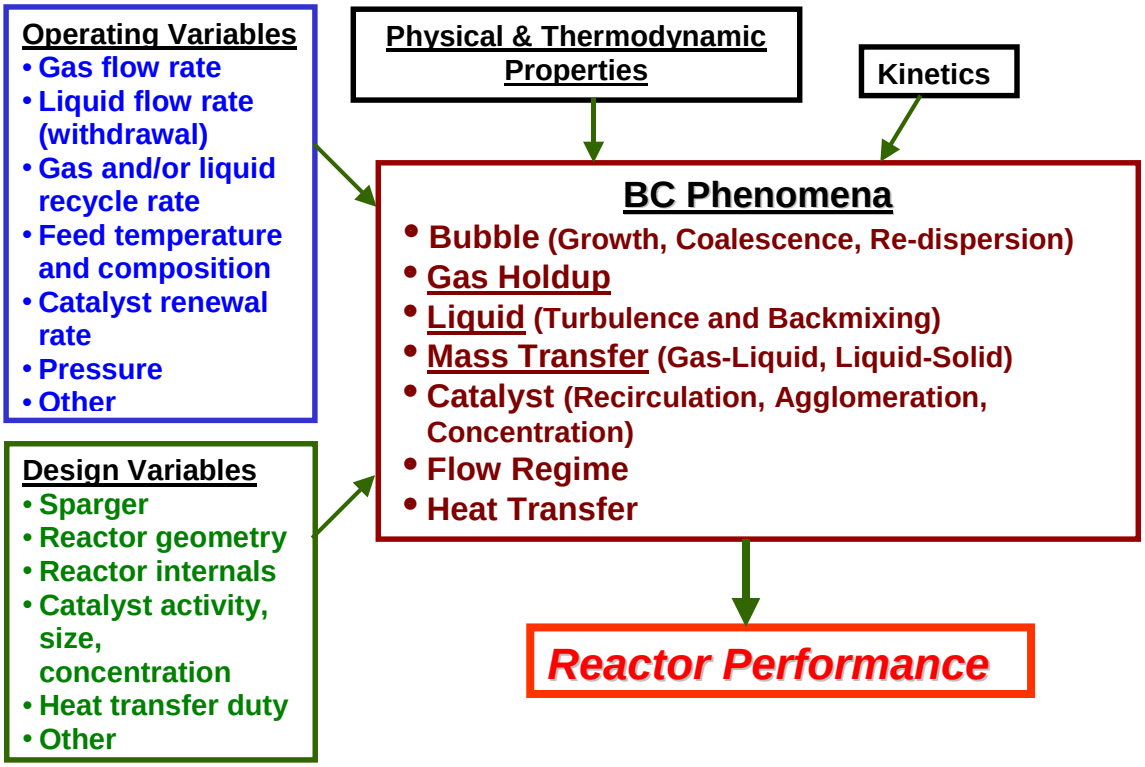

Figure 1-4. Factors influencing bubble column performance.

Several studies have been reported in the literature on detailed bubble column hydrodynamics (Devanathan, 1991; Yao *et al.*, 1991; Kumar, 1994; Sannaes, 1997; Degaleesan, 1997). However, all the studies mentioned above, and numerous other studies reported in the literature, are restricted to the analysis of hydrodynamics at atmospheric pressure, with gas superficial velocity up to a maximum of 12-15 cm/s. In spite of the wealth of information that these studies provide at atmospheric pressure, very little information is available that is of relevance at high-pressure conditions. The exceptions are the theses and related papers by Wilkinson (1991), de Swart (1996) and Letzel (1997). However, the hydrodynamic parameters that have been investigated by

them are limited to overall gas holdup, overall mass transfer and analysis of regime transitions. Therefore, very little is known about detailed hydrodynamics and structure of turbulence in such vessels at high pressure and at high superficial gas velocity conditions, which are of the greatest importance and relevance to industrial operation of bubble and slurry bubble column reactors (specifically with respect to Fischer-Tropsch chemistries). Furthermore, with the exception of the work from Sandia National Laboratory on gas holdup distribution (George *et al.*, 2000[a,b]), the author is not aware of any other published work that investigates the details of the three-dimensional phase distributions, liquid recirculation and associated turbulent quantities at high pressures. Few studies have been performed that investigate the bubble hydrodynamics at very high gas flow rates at elevated pressures, which are of industrial interest as means to increasing reactor productivity. At such conditions, frequently referred to as the churn-turbulent flow conditions, coalescence and breakup of bubbles are enhanced leading to an increase in renewal rate of the bubble surface (De Swart, 1996). Hence, the gas-liquid interface and its rate of renewal is increased and this increases the volumetric mass transfer coefficients. Additionally, increased heat transfer rate from turbulence and liquid recirculation helps in maintaining the uniform temperature in the system, which is favorable for processes involving highly exothermic reactions. Thus, the lack of detailed hydrodynamic characterization of bubble column flows at the industrially relevant churn-turbulent flow conditions and an opportunity to extend the use of the powerful non-invasive flow diagnostic tools (CT and CARPT) to truly churn-turbulent flows form the motivation for this study.

1.2. Objectives

As mentioned above, there is a need to understand the physics behind the phenomena involved in the complex hydrodynamics presented by a bubble column flow, especially at high pressure and at high superficial gas velocity (as shown in Table 1-1). The overall objective of this work is to obtain data at ***high-pressure*** and at ***high superficial gas velocity*** that is needed to advance the understanding and knowledge of

bubble columns operated at such conditions. The experimental data from this study will not only be the first of its kind but also serve as inputs to mechanistic models and benchmarks for validation of CFD simulations of bubble columns, which are increasingly becoming popular for design and scale up purposes. The specific goals of this work are:

- Non-invasive measurements of gas holdup distribution and liquid recirculation in the fully developed flow regions of the column at high pressure and at high U_g conditions. This includes:
  - Determination of radial gas holdup distribution, via Computed Tomography (CT), and of overall gas holdup. Development of a compact, user-friendly software for data processing.
  - Determination of liquid recirculation velocity profiles and turbulent parameters (Reynolds stresses, turbulent kinetic energy, turbulent eddy diffusivities, etc.), via Computer Automated Radioactive Particle Tracking (CARPT).
  - Evaluation of the effect of sparger design on the above-mentioned parameters at high superficial gas velocity.

1.3. Thesis Organization

A brief general review of the literature on gas holdup and liquid recirculation in bubble column reactors is provided in Chapter 2 while Chapter 3 presents the details of the experiments conducted to generate the desired sets of experimental data. In addition, each subsequent individual chapter is accompanied by specific topical reviews. Chapter 4 covers the developments related to gas holdup measurements using Computed Tomography (CT) in a bubble column with batch liquid. Chapter 5 presents the liquid recirculation and turbulence parameters measurements using Computed Automated Radioactive Particle Tracking (CARPT) technique. Lastly, Chapter 6 provides the conclusions with recommendations and outlines the possibilities for future efforts.

Chapter 2. Literature Review

As mentioned in Chapter 1, there are numerous parameters that affect bubble column hydrodynamics (refer to Figure 1-4). Extensive studies of the bubble column performance have been investigated and reviewed (Deckwer, 1991; Joshi *et al*., 1998). Due to the vast literature on bubble columns and the different phenomena that affect their performance, only studies that discussed gas holdup and its distribution, bubble size distribution, and liquid recirculation are reviewed here. A summary of these studies and their findings is presented in Table 2-1. As shown in Table 2-1, different techniques have been used to measure gas holdup, bubble size distribution and liquid recirculation in different column diameters using different gas-liquid and gas-liquid-solid systems. Some of these studies resulted in correlations for some quantities of interest while others merely describe their observations. In this section, several studies from Table 2-1 are reviewed.

2.1. Gas Holdup

Gas holdup has been identified as one of the most important parameters that govern the liquid recirculation in bubble column operation and is defined as the fraction of the gas-liquid volume occupied by gas. Gas holdup can be referred to either at a point in the reactor (local holdup) or to the average value over the entire reactor (overall holdup). There are a number of factors that influence the gas holdup and its distribution in a bubble column operation and these include both geometric as well as operating variables as discussed subsequently.

Table 2-1. A summary of studies of gas holdup, bubble size distribution and liquid recirculation in bubble columns.

References	System	Apparatus	Conditions	Methods employed			Key Findings
				Gas Holdup	Bubble size distribution	Liquid Recirculation/ Mixing	
Braulick *et al.* (1965)	Air-H_2O/Electrolyte solutions	D = 0.076, 0.102, 0.152 m 4-arm spargers	P = 0.1 MPa U_g = up to 36 cm/s	Manometer	-	-	Large no. of smaller bubbles observed in electrolyte solutions (higher ε_g than air-H_2O)
Yoshida & Akita (1965)	Air-H_2O/sodium sulfite/sodium sulfate solution	D = 0.077, 0.152, 0.301, 0.6 m Single nozzle spargers (nozzle diameter depending on column diameter)	P = 0.1 MPa U_g = up to 28 cm/s	Bed expansion	-	-	Insignificant effect of d_o on overall gas holdup Irregular behavior of gas holdup using different liquid viscosities
Akita & Yoshida (1973)	He/CO_2/O_2/air-H_2O/ Glycol/Methanol/ CCl_4/Na_2SO_3/NaCl	D = 0.152, 0.301, 0.6 m Single hole sparger (5.0 mm)	P = 0.1 MPa T = 283 - 313 K U_g = 0.5 - 40 cm/s	Bed expansion	-	-	Gas holdup correlation was proposed
Hills (1974)	Compressed air - ordinary Cambridge tapwater	D = 0.138 m H = 1.37 m Sieve plates (32 holes of 0.4 mm, 61 holes of 0.4 mm, 7 holes of 1.6 mm)	P = 0.1 MPa U_g = up to 16.9 cm/s	*Conductivity Probe	-	Modified Pitot Tube (Pavlov tube)	Radial variation of gas holdup and liquid recirculation velocity profiles
Deckwer *et al.* (1974)	Air-tap H_2O/sodium sulfate/sodium chloride molasses	D = 0.15, 0.2 m H = 4.4, 7.23 m Cross sparger (56 holes of 1 mm) Glass sintered porous plate (mean pore diameter of 150 μm)	P = 0.1 MPa T = 289 °C U_g = up to 9 cm/s U_l = 0.707 cm/s	Not specified	-	Stationary tracer (Electrolyte, dye and heat) Transient tracer	Significant effect of trace contaminants on overall gas holdup

Table 2-1. A summary of studies of gas holdup, bubble size distribution and liquid recirculation in bubble columns - Cont'd.

References	System	Apparatus	Conditions	Methods employed			Key Findings
				Gas Holdup	Bubble size distribution	Liquid Recirculation/ Mixing	
Hikita and Kikukawa (1974)	Air-H_2O/ methanol solution/cane sugar solution	D = 0.1, 0.19 m H = 1.5, 2.4 m Single nozzles (13 mm for 0.1 m column; 13.1, 20.6 and 36.2 mm for 0.19 m column)	P = 0.1 MPa U_g = 4.3 to 33.8 cm/s	Manometric method	-	Transient tracer (Aq. KCl solution)	Gas holdup correlation was proposed
Hills (1976)	Air-H_2O	D = 0.15 m H = 10.5 m Sparger cap (60 holes of 1/8")	P = 0.1 MPa U_g = 7 - 350 cm/s U_l = 0 - 270 cm/s	Static pressure variation with height	-	-	Gas holdup correlation as a function of U_g and U_l was proposed Correlation corrected for liquid inertia and wall friction
Botton *et al.* (1978)	Air-H2O/H2O+ tensioactive+ trisodium phosphate/glycol	D = 0.02, 0.075, 0.25, 0.48 m H = 0.32, 4.3, 2.2, 2 m 3 capillary tubes of 0.5 mm Perforated plates (4 mm, 3.2 %OA; 5mm, 5 %OA; 7 mm, 9.6% OA) 6 branches (54 holes of 1 mm) 6 branches (54 holes of 1.5 mm) 3 concentric toris (88 holes or 3 mm)	P = 0.1 MPa U_g = 0.47 - 1400 cm/s U_l = 0 - 5 cm/s	Bed expansion Manometric	-	-	Overall gas holdup dependent on column diameter for bubble flow regime (U_g < 0.2 m/s, D_c < 0.15-0.2 m) Operation diagram of bubble column at high U_g was given
Deckwer *et al.* (1978)	CO_2/O_2-tap water/ aq. sodium sulfate/ sodium chloride	D = 0.15, 0.2 m H = 4.4, 7.2 m Cross nozzles (56 holes of 1 mm) Glass sintered plate (150 μm)	P = 0.1 MPa U_g = 0.65 - 7.7 cm/s U_l = 0 - 5 cm/s	Manometric	Photographic & Particle size analyzer	-	In short columns, gas holdup does not vary axially if both entrance and end effects are neglected Gas holdup increases with column length for tall columns due to volume expansion caused by hydrostatic pressure

Table 2-1. A summary of studies of gas holdup, bubble size distribution and liquid recirculation in bubble columns - Cont'd.

References	System	Apparatus	Conditions	Methods employed			Key Findings
				Gas Holdup	Bubble size distribution	Liquid Recirculation/ Mixing	
Nakanoh and Yoshida (1980)	Air-H_2O+aq. sucrose/ sodium carboxylmethyl cellulose (CMC)/ sodium polyacrylate (PA)	D = 0.1455 m H = 0.19 m Single orifice (0.4 cm diameter)	P = 0.1 MPa T = 303 K U_g = up to 10 cm/s	Bed expansion	Photographic	-	Bubbles smaller than a few mm are observed in air-water, whereas large bubbles mingled with many very fine bubbles (< 1 mm) in viscous solutions, thus affecting holdup
Hikita *et al.* (1980)	$H_2/CO_2/CH_4/C_3H_8/$ H_2+N_2/ air-H_2O/Sucrose/ Methanol/n-Butanol/ Aniline/ i-Butanol/NaCl/ $Na_2SO_4/CaCl_2$/ $MgCl_2$/ $AlCl_3$/ KCl/ K_2SO_4/ K_3PO_4/ KNO_3	D = 0.10 m Nozzle (1.1 cm)	P = 0.1 MPa H_D/D = 15 U_g = 4.2 - 38 cm/s	Static pressure measurement	-	-	Gas holdup depends on the nature of the gas Gas holdup correlation obtained using dimensionless analysis and least-square method
Hammar *et al.* (1984)	N_2/He/Ar/CO_2/Air-H_2O/Organic liquids-glas ballotini	D = 0.106, 0.2 m Annuli or stars spargers (17 to 40 holes of 0.5, 1 or 2 mm ID)	P = 0.1 MPa T = 293 - 363 K U_g = 0.5 - 13 cm/s	Not specified	Photographic & laser impuls holography	-	Gas holdup correlation was proposed
Idogawa *et al.* (1985)	Air-H_2O	D = 0.05 m Porous plate (2, 100 μm) Capillary tubes (1, 3, 5 mm) Perforated plate (19 holes of 1 mm)	P = 0.1 - 15 MPa T = 288 - 293 K, H_D/D = 16.6 U_g = 0.5 - 5 cm/s	Electrical resistivity probe	Electrical resistivity probe	-	Gas holdup correlation was proposed

Table 2-1. A summary of studies of gas holdup, bubble size distribution and liquid recirculation in bubble columns - Cont'd.

References	System	Apparatus	Conditions	Methods employed			Key Findings
				Gas Holdup	Bubble size distribution	Liquid Recirculation/ Mixing	
Idogawa *et al.* (1986)	Air-H_2O	D = 0.05 m H = 0.83 m Single orifice (1, 3, 5 mm) Perforated plate (19 holes of 1 mm) Porous plate (0.002, 0.1 mm)	P = up to 15 MPa T = 288 - 293 K H_o = 0.7 m U_g = 0.5 - 5 cm/s	Electrical resistivity probe	Electrical resistivity probe	-	Narrower bubble size distribution observed at high P. No axial variation of d_b at 0.163 m from distributor
Reilly *et al.* (1986)	He/Ar/air-H_2O/solvent/ trichloroethylene-glass beads	D = 0.3 m Perforated plate (293 holes,1.5 mm) Single sparger Multiorifice sparger (13.4 mm)	P = 0.1 MPa T = 283 - 323 K U_g = 0.4 - 40 cm/s	Manometric	-	-	Gas holdup correlation proposed using statistical approach
Yang *et al.* (1986)	Air- H_2O/Aq. Methanol	D = 0.15 m H = 0.6 m Perforated plate (81 holes of 0.5 mm)	P = 0.1 MPa U_g = 2.4-7.2 cm/s U_l = 1.0 cm/s	-	*5-point electrical conductor microprobes	Tracer experiments (3-5% sodium chloride)	Determination of inversion of liquid flow using tracer experiments Development of a semi-theoretical equation to predict mean gas holdup
Idogawa *et al.* (1987[a])	H_2/He/Air-H_2O/Methanol/ Ethanol/Acetone/ Aqueous alcohol solution	D = 0.05 m Perforated plate (19 holes of 1 mm)	P = 0.1 - 5 MPa T = 284 - 293 K H_D/D = 16.6 U_g = 0.5 - 5 cm/s	Electrical resistivity probe	Electrical resistivity probe	-	Bubble characteristics independent of liquid viscosity (< 3 MPa.s), but affected by surface tension at P < 5 MPa Proposed gas holdup correlation
Menzel *et al.* (1989)	Air-H_2O/Aq. Glycerol/0.22wt% Aq. Propanol	D_1 = 0.15 m; D_2 = 0.6 m H_1= 2.58 m; H_2 = 3.46, 5.44 m	P = 0.1 MPa U_g = 1.2-9.6 cm/s	*One-point Electro-conductivity microprobe	-	*Hot film anemometry with triple split probes	Measurement of Reynolds shear stress and development of an empirical correlation to predict turbulence intensities

Table 2.1. A summary of studies of gas holdup, bubble size distribution and liquid recirculation in bubble columns - Cont'd.

References	System	Apparatus	Conditions	Methods employed			Key Findings
				Gas Holdup	Bubble size distribution	Liquid Recirculation/ Mixing	
Oyevaar *et al.* (1989)	CO_2/N_2-distilled H_2O/aq. DEA solution	D = 0.0855 m H = 0.63 m Cross shaped (16 holes of 0.5 mm)	P = 0.15 - 1.85 MPa H_D/D = 6.1 U_g = 1 - 9.0 cm/s	Bed expansion	-	-	Transition from the bubbly flow to the churn-turbulent regime is delayed
Wilkinson & Dierendonck (1990)	$He/N_2/Ar/CO_2$/ sulphur hexafluoride	D = 0.16 m H = 1.5, 2.0 m Sparger rings (37 holes of 2 mm; 19 holes of 10 mm)	P = up to 2.0 MPa U_g = 3 - 12 cm/s	Overflow technique	-	-	Influence of pressure and gas molecular weight on gas holdup have the same cause
Devanathan (1991)	Air-H_2O	D = 0.114, 0.19, 0.292 m Porous tetraglass sheets (40 μm) Porous stainless steel (25 μm)	P = 0.1 MPa H_o = 0.572- 0.581 m U_g = 2 - 18.4 cm/s	Bed expansion	-	Computer Automated Radioactive Particle Tracking (CARPT)	Developed CARPT (non-intrusive) Concluded that the entry region was ~1-1.5 D_c Strong axial eddy dispersion coefficient
Kojima *et al.* (1991)	Compressed air- tap H_2O-glass beads (0.105 - 0.125 mm)/fine glass beads (17 μm)/ $CaCO_3$ (16 μm)	D = 0.045 m Single nozzle (1.0, 2.0, 3.0 mm)	P = 0.1 - 1.1 MPa H_o = 0.83 - 1.4 m U_g = 1.5 - 10 cm/s C_s = 0 - 30 wt. %	Bed expansion	-	-	Effect of pressure on gas holdup more pronounced with increase in Ug and decrease in do
*Yao *et al.* (1991)	Air-deionized H_2O	D = 0.29 m H = 4.5 m	P = 0.1 MPa H_o = 0.75 - 3.5 m U_g = up to 10 cm/s U_l = 1 - 2.5 cm/s	Electrical conductivity microprobe (ECM)	ECM Ultrasonic Doppler (UDT)	Hot film anemometer (HFA)	Radial profiles of d_b, bubble rise velocity, gas and liquid phases velocities, and gas holdup were measured

Table 2-1. A summary of studies of gas holdup, bubble size distribution and liquid recirculation in bubble columns - Cont'd.

References	System	Apparatus	Conditions	Methods employed			Key Findings
				Gas Holdup	Bubble size distribution	Liquid Recirculation/ Mixing	
Wilkinson *et al.* (1992)	N_2-H_2O/n-Heptane/Mono-ethylene glycol	D = 0.158, 0.23 m Sparger ring (4 holes of 7 mm)	P = 0.1 - 2.0 MPa H_o = 1.2 m U_g = 0 - 60 cm/s	Overflow technique	-	-	Insignificant effect on gas holdup for all pressures provided: D_c > 0.15m H/D > 5 d_o > 1-2 mm
Kumar (1994)	Air-H_2O/deionized H_2O/ 50 % isopropanol-water/	D = 0.102, 0.14, 0.19 0.26, 0.3m Perforated plate (95 holes, 0.23 %OA; 61 holes of 0.4 mm; 156 holes of 0.1 %OA; 193 holes of 0.05 %OA; 181 holes of 0.1 %OA) Bubble cap Cone distributor	P = 0.1 MPa U_g = 2 - 12 cm/s	Bed expansion Computed Tomography (CT)	-	CARPT	Effect of D_c on gas holdup and its distribution more pronounced for smaller columns, diminishes after a critical D_c (~0.19 m) Increase U_g increase holdup Holdup larger using perforated plate compared with a cone or bubble cap distributor Decrease in surface tension results in smaller bubbles, thus higher holdup
Ityokumbul *et al.* (1994)	Air-water	D = 0.06 m H = 1.06 m Porous stainless steel plate (134 μm)	P = 0.1 MPa U_g = 0-2.5 cm/s U_l = 0-0.8 cm/s	Static Pressure Measurements	-	-	Insignificant effect of liquid velocity on gas holdup and liquid dispersion coefficient Liquid dispersion coefficient in bubbly flow regime shows no dependence with gas velocity

Table 2-1. A summary of studies of gas holdup, bubble size distribution and liquid recirculation in bubble columns - Cont'd.

References	System	Apparatus	Conditions	Methods employed			Key Findings
				Gas Holdup	Bubble size distribution	Liquid Recirculation/ Mixing	
Pannek *et al.* (1994)	Air-water	D = 0.15, 0.6 m	P = 0.1 MPa U_g = 2.4 cm/s	-	-	*Electrodiffusion method	New technique with oxygen as depolarizer shows good agreement with those obtained using hot film anemometry
Sotelo *et al.* (1994)	Air/CO_2-H_2O/ ethanol/ saccharose/glycerin	D = 0.04, 0.08 m Porous gas diffusers (30,65,150μm)	P = 0.1 MPa H_o = 1.5-2.0 m U_g = 0 - 20 cm/s	Bed expansion	-	-	Gas holdup correlation proposed includes the ratio of sparger pore diameter to the column diameter
Stegeman (1994)	N_2+CO_2-demineralised H_2O/DEA+ ETC+ demineralised H_2O	D = 0.156 m Perforated plate (284 holes of 0.4 mm)	P = 0.1 - 5.6 MPa H_D = 0.64 m U_g = up to 6 cm/s	Bed expansion	-	-	Transition regime shifted to higher U_g as P increases or with a decrease in liquid viscosity
Shollenberger *et al.* (1995)	Air-H_2O	D = 0.19 m H = 1.8 m Bubble cap sparger	P = 0.1 MPa U_g = 0 - 12 cm/s	Bed expansion Gamma-densitometry tomography (GDT)	-	-	Chordal average gas holdup obtained.
Jiang *et al.* (1995)	N_2-Paratherm NF	D = 0.0508 m H = 0.8 m Multi-orifice sparger (3 mm ID)	P = up to 21 MPa T = 303 K Ug = up to 8 cm/s U_l = 0 - 2.6 cm/s	Bed expansion	PIV		An increase in pressure leads to a decrease in bubble size and a narrower bubble size distribution

Table 2-1. A summary of studies of gas holdup, bubble size distribution and liquid recirculation in bubble columns - Cont'd.

References	System	Apparatus	Conditions	Methods employed			Key Findings
				Gas Holdup	Bubble size distribution	Liquid Recirculation/ Mixing	
Krishna & Ellenberger (1996)	Air/He/Ar/SF_6-H_2O/ paraffin oil/ Separan/ tetradecane	D = 0.1,0.174,0.19,0.38,and 0.63m Spider sparger Sintered glass plate (mean pore size of 150-200 μm) Polyacrylate sieve plate (2.5mm ID) Sintered bronze plate (mean pore size of 50 μm)	P = 0.1 MPa U_g = 0.1 - 85 cm/s	Dynamic gas disengagement	-	-	For U_g > 0.1 m/s, insignificant effect on gas distribution Gas holdup correlation was proposed
Adkins *et al.* (1996)	Air-H_2O	D = 0.48 m H = 3 m Sparger ring (12 holes of 3.18 mm)	P = up to 0.4 MPa U_g = up to 16 cm/s	Differential pressure transducers GDT	-	-	Increasing headspace pressure increases gas holdup Increasing U_g at a fixed P causes gas holdup to increase more in the center than near the side wall
Degaleesan (1997)	Air-H_2O	D = 0.1, 0.14, 0.19, 0.44 m Perforated plate (61 holes of 0.4 mm; 121 holes of 1.0 mm; 166 holes of 0.33 mm; 301 holes of 0.7 mm) Bubble cap Cone distributor	P = 0.1 MPa H_o = 0.955 - 1.79 m U_g = 2 - 12 cm/s	Bed expansion	-	CARPT	Measured liquid velocity profile for D_c = 0.19m using perforated plate is higher than that using cone or bubble cap distributor
Deshpande & Joshi (1997)	Air-H_2O	Rectangular bubble column: HxWxD = 0.15 x 0.012 x 0.7 m^3 Sparger: 23 hypodermic needles	P = 0.1 MPa U_g = 1.57-3.42 cm/s	Bed expansion	-	Laser Doppler Velocimeter	Development of a technique for simultaneous measurement of gas and liquid velocities along with gas holdup

Table 2-1. A summary of studies of gas holdup, bubble size distribution and liquid recirculation in bubble columns - Cont'd.

References	System	Apparatus	Conditions	Methods employed			Key Findings
				Gas Holdup	Bubble size distribution	Liquid Recirculation/ Mixing	
Shollenberger *et al.* (1997)	Air-H_2O	D = 0.19, 0.48 m H = 1.8 m, 3.0 m Bubble cap (6 holes of 0.32 cm) Ring-type (12 holes of 0.32 cm)	P = 0.1 MPa U_g = 0 - 11.76 cm/s	Differential pressure transducers GDT	-	-	Chordal average gas holdup is in good agreement with that obtained from level and differential pressure measurements
Kojima *et al.* (1997)	Air-H_2O/Aqueous buffered solution/Aqueous enzyme solution	D = 0.045 m Nozzle (1.38, 2.1, 2.9, 4.03 mm)	P = 0.1 - 1.1 MPa T = 290 - 300 K, H_D/D = 20 - 26.7 U_g = 0.005 - 0.15 cm/s	Bed expansion	-	-	Gas holdup increases with P and trend becomes more significant with decrease of d_o Correlation for gas holdup was proposed
Letzel (1997)	N_2-demineralized water	D = 0.15 m Perforated plate (200 evenly distributed orifices of 0.5 mm ID)	P = 0.1 - 1.3 MPa U_g = up to 40 cm/s	Overflow technique & Pressure transducer	-	-	Use of chaos theory to obtain regime transition point Developed gas holdup correlation including high pressure data
Mudde *et al.* (1997[a])	Air-H_2O	D = 0.152, 0.234, 0.384 m Sintered polyethylene porous plate (40 μm)	P = 0.1 MPa H_D/D = 8 - 10 U_g = up to 6.7 cm/s	-	-	*Laser Doppler Anemometry (LDA)	Observed the gross circulation and the axial velocity changes sign at r/R ≈ 0.7 Larger axial normal Reynolds stresses compared to the tangential normal ones -- anisotropic turbulence

Table 2-1. A summary of studies of gas holdup, bubble size distribution and liquid recirculation in bubble columns - Cont'd.

References	System	Apparatus	Conditions	Methods employed			Key Findings
				Gas Holdup	Bubble size distribution	Liquid Recirculation/ Mixing	
Lin *et al.* (1998)	N_2-Paratherm NF	D = 0.0508, 0.1016 m H = 0.8, 1.58 m Multi-orifice sparger (3 mm)	P = up to 20 MPa T = 27 - 78 °C U_g = up to 30 cm/s	Differential pressure transducer	Photographic	-	Increasing pressure increases gas holdup due to an increase in gas momentum and a decrease in surface tension As pressure increases, the dominant bubble size decreases
Lain *et al.* (1999)	Air-0.004 vol% propanol+tap H_2O	D = 0.14 m Porous membrane with pore size of 0.7 μm	P = 0.1 MPa U_g = 0.14-0.58 cm/s H_o = 0.65 m	-	Phase Doppler Anemometer	Phase Doppler Anemometer	Bubble rise velocity considerably larger than the terminal velocity of single bubbles for gas holdup in the range of 0.5-3 %
Luo *et al.* (1999)	N_2-Paratherm NF-alumina particles	D = 0.102 m Perforated plate (120 squared-pitched holes of 1.5 mm ID)	P = 0.1 - 5.6 MPa T = 298 - 351 K U_g = up to 45 cm/s	Dynamic gas disengagement	Fiber Optic Probe	-	Gas holdup correlation proposed includes the presence of slurry/particles
Zhang *et al.* (1999)	Air-H_2O	D = 0.207 m H = 2 m	P = 0.1 MPa U_g = 2-3 cm/s U_l = 0-1.429 cm/s	-	-	*Laser Doppler Anemometer	Increase in gas and liquid velocities increase liquid turbulent intensity Proposed an empirical relationship between turbulent intensity and liquid turbulent viscosity

Table 2-1. A summary of studies of gas holdup, bubble size distribution and liquid recirculation in bubble columns - Cont'd.

References	System	Apparatus	Conditions	Methods employed			Key Findings
				Gas Holdup	Bubble size distribution	Liquid Recirculation/ Mixing	
Chen *et al.* (2001)	Air-H_2O	D = 0.2, 0.4, 0.8 mm H = 3 m Perforated plates of 0.5 mm	P = 0.1 MPa U_g = 2-9 cm/s H_o = 2.0 m	*Hot-wire probe	-	-	Kolmogorov entropy decreases with an increase in column diameter and exhibits a flat radial distribution in the large-scale column Large scale column shows almost uniform radial holdup distributions as compared to the other columns
Kemoun *et al.* (2001)	Air-H_2O	D = 0.162 m H = 2.5 m Perforated plate (61 holes of 0.4 mm)	P = 0.1 - 0.7 MPa U_g = up to 18 cm/s	CT	-	-	Comparison of gas holdup with existing correlations for all pressures results shows a wide spread
Kulkarni *et al.* (2001[d])	Air-0.2% v/v aqueous n-butanol	D = 0.1 m H = 0.8 m Sintered plate (40 μm) Single hole of 1.8 mm	P = 0.1 MPa U_g = 0.086, 1.32 and 3.65 cm/s	-	-	Laser Doppler Velocimeter	Identification of principal time scales and estimation of bubble chord length distribution
Seeger *et al.* (2001)	Air-H_2O (rectangular column) Air-Glycerin (3-D column)	Rectangular column: HxWxD = 0.45 x 0.2 x 0.04 m^3 3-D column: D = 0.104 m H = 0.1 m Distributor: 91 injection needles of 0.34 mm	P = 0.1 MPa U_g = 0.1-0.3 cm/s	-	-	X-ray based Particle Tracking Velocimetry	Development of a multi-point technique to measure liquid velocity for any large void fraction

Table 2-1. A summary of studies of gas holdup, bubble size distribution and liquid recirculation in bubble columns - Cont'd.

References	System	Apparatus	Conditions	Methods employed			Key Findings
				Gas Holdup	Bubble size distribution	Liquid Recirculation/ Mixing	
Vial *et al.* (2001[a])	Air-H_2O	D = 0.1 m H = 2 m Single nozzle (5 mm) Multiple-orifice nozzle (50 holes of 1.0 mm) Porous glass plate (15 μm)	P = 0.1 MPa U_g = 0.6-15 cm/s	-	-	*Laser Doppler Anemometer	Multi-orifice plate has the highest centerline liquid velocity as compared to the other plates Development of a simple analytical model to estimate Reynolds shear stress

* Radial profiles are available

The primary geometric variables governing gas holdup in bubble columns are the reactor diameter and height, and depending on the operating conditions, the sparger design and configuration. Likewise, the primary operating variables are the reactor operating conditions, *viz.*, the superficial gas velocity and reactor pressure and temperature. Lastly, the physical properties of the liquid medium also influence the resulting gas holdup distribution in a bubble column operation. These physical properties are modified due to the presence of electrolytes, contaminants, solids, etc., making their characterization an important part of reactor design. The effect of some of the above geometric and operating variables on gas holdup is discussed next.

2.1.1. Flow regimes

The structure of gas holdup distribution in bubble columns is predominantly dictated by the prevalent flow regime under the specified operating conditions. Specifically, depending on the superficial gas velocity and column operating pressure, two different types of flow regimes are generally encountered in bubble column operation, namely, homogeneous and heterogeneous (Ramachandran and Chaudhari, 1983; Kastanek *et al*., 1993). The homogeneous regime is characterized by small, uniform-sized bubbles that rise without many interactions and is represented by a narrow bubble size distribution. At atmospheric pressure, this usually happens at a superficial gas velocity less than 3 cm/s. As the superficial gas velocity is increased beyond a critical value (roughly 7 cm/s for air-water system at atmospheric conditions) a transition to the heterogeneous (churn-turbulent) regime takes place (Kastanek *et al*., 1993; Joshi *et al.*, 1998). The bubble size distribution in the heterogeneous regime is broader as compared to that in the homogeneous regime (Yu and Kim, 1991; Kang *et al*., 2000). It has also been frequently reported that this bubble size distribution exhibits a bi-modality (Tassin and Nikitopoulos, 1995; deSwart, 1996; Krishna and Ellenberger, 1996; Krishna, 2000), which is characterized by a distinct presence of large and small bubbles leading not only to intense liquid turbulence, but also to enhanced bubble-bubble interactions (coalescence-redispersion phenomena). Figure 2-1 shows the pictorial images taken in a

rectangular bubble column at atmospheric pressure. The figure illustrates a change of uniform bubbles obtained at low superficial gas velocity to bubbles of varying sizes and shapes at a higher superficial gas velocity.

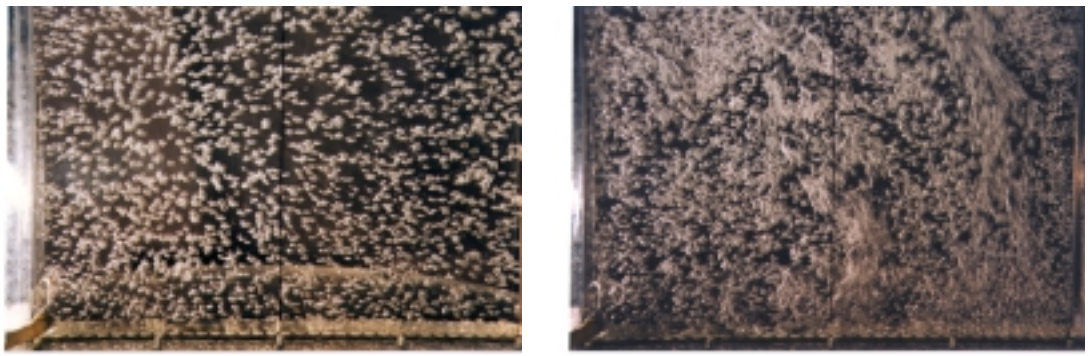

(a) (b)

Figure 2-1. Photographs from a 2-D rectangular bubble column (a) uniform bubbles (homogeneous regime); (b) bubbles of many sizes (churn-turbulent regime).

When one considers the distribution of gas holdup in a cross-sectional plane, one finds that in the homogeneous regime, the radial variation of gas holdup is minimal (Hills, 1974; Yao *et al*., 1991; Kumar, 1994). On the other hand, in the churn-turbulent regime, one observes significant variation of gas holdup in a cross-section, with greater gas holdup in the center than at the wall (Hills, 1974; Yao *et al*., 1991; Yu and Kim, 1991; Kumar, 1994; Chen *et al.*, 1998). It is known that the buoyancy forces resulting from the non-uniform cross-sectional gas holdup distribution are responsible for inducing the large-scale liquid recirculation in bubble columns. Since the difference in magnitude of these forces is small in the homogeneous regime (where the gas holdup is relatively uniform over the reactor cross-section), lower levels of liquid recirculation exist. However, in the churn-turbulent regime, due to the significantly higher gas holdup in the column center as compared to that near the wall, the difference in magnitude of these forces is significantly larger than in the homogeneous regime and one observes increased intensity of liquid recirculation and turbulence (Chen *et al.*, 1998; Chen *et al.*, 1999; Gupta, 2002). This gas holdup induced liquid recirculation indirectly influences the rates of mass and heat transfer, which in turn determine the performance of the reactor (Joshi

et al., 1998). It was also shown by de Swart (1996) that bubble columns operated in the churn-turbulent regime experience enhanced mass and heat transfer. Since gas holdup and liquid recirculation increase as one operates a bubble column reactor further in the churn-turbulent regime, it is reasonable to expect that on a macroscopic level, these two hydrodynamic phenomena have a significant role to play in enhancing the heat and mass transfer rates in bubble columns (Letzel, 1997).

Many studies have attempted to determine the transition between homogeneous and heterogeneous regimes in bubble columns. Traditionally, the variation of the overall gas holdup with superficial gas velocity, occasionally in conjunction with the drift-flux model, has been used to evaluate the regime transition (Reilly *et al*., 1994; Gavrilescu and Roman, 1996; Sarrafi *et al*., 1999; Ruzicka *et al.*, 2001). Recently, it is becoming increasingly prevalent to use time series analysis of fluctuation signals obtained using different experimental techniques to assess the regime transition in bubble columns (Bukur *et al*., 1996; Letzel *et al*., 1997[a]; Bennett *et al*., 1999; Lin *et al*., 2001; Vial *et al*., 2001[b]) and in two-phase flow in pipes (Mishima and Ishii, 1984; Barnea, 1987).

One of the early approaches to identify the flow regime transition is the drift flux model, which was introduced by Wallis (1969). The drift flux, j_{GL}, represents the volumetric flux of either phase relative to a surface moving at the volumetric average velocity (refer to Equation (2-1)).

$$j_{GL} = U_g\varepsilon_l \pm U_l\varepsilon_g = U_s\varepsilon_g\varepsilon_l \tag{2-1}$$

In the above equation, U_s is the slip velocity between the gas and liquid and the positive sign in front of U_l represents a counter-current flow of liquid relative to the gas phase, while a negative sign implies that liquid and gas phases flow co-currently. Figure 2-2 shows the typical plot of the drift flux versus gas holdup. As shown in Figure 2-2, a change in slope of the curve represents the transition from homogeneous to heterogeneous regime.

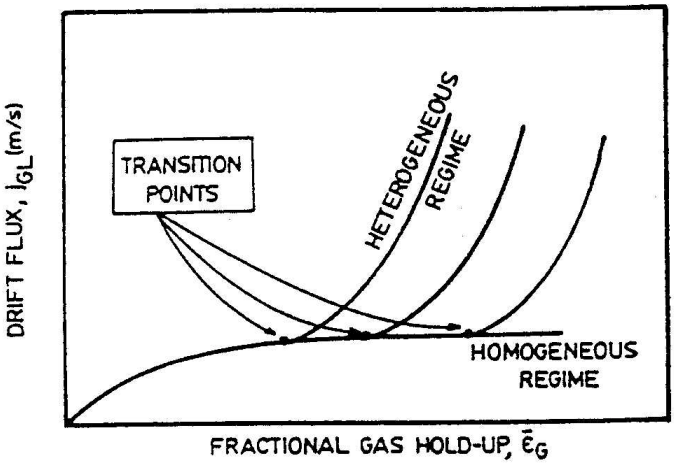

Figure 2-2. Plot of drift flux versus gas holdup (Degaleesan, 1997).

Zuber and Findlay (1965) explained the variation of gas holdup with superficial gas velocities by transforming the basic drift flux model equation (Equation (2-1)) to Equation (2-2) as shown below.

$$\frac{U_g}{\varepsilon_g} = C_o\left(U_g \pm U_l\right) + C_1 \tag{2-2}$$

In the above equation, C_0 and C_1 are constants obtained by fitting the drift flux model to experimental data with the signs in front of U_l indicating countercurrent and cocurrent flow, respectively as in Equation (2-1). In the above model, the value of C_0 indicates the extent of gas holdup profile non-uniformity while C_1 corresponds to slip velocity (Joshi *et al.*, 1998). In spite of the simplicity of the above model, there are no universal guidelines for prediction of the constants C_0 and C_1. Therefore, the utility of the above model is restricted to the particular gas-liquid systems and column configuration in which experiments were done to determine C_0 and C_1.

Recently, Sarrafi *et al.* (1999) introduced a criterion for obtaining the transition superficial gas velocity from the gas holdup versus superficial gas velocity data. They made use of the Lapidus-Elgin (1957) relationship, as shown in Equation (2-3), to account for the interaction among bubbles in the column.

$$U_s = U_b F(\varepsilon_g) \tag{2-3}$$

where U_s denotes the slip velocity; U_b denotes the bubble terminal rise velocity, and $F(\varepsilon_g)$ denotes the effect of the interaction of neighbouring bubbles within the column and is represented by Equation (2-4) (Deckwer, 1991).

$$F(\varepsilon_g) = (1-\varepsilon_g)^{n-1} \tag{2-4}$$

where n is 2.39 for particle (bubble) Reynolds numbers greater than 500 (Richardson and Zaki, 1954). Based on the gas holdup measurements, Sarrafi and coworkers proposed holdup correlations to predict gas holdup in the homogeneous and heterogeneous regimes using a form of Equation (2-4) (refer to Equation (2-5)). The data range for gas holdup considered include those in the literature, as well as the experimental results obtained from their study using both bed expansion and manometric methods at atmospheric pressure conditions.

Homogeneous regime: $$F(\varepsilon_g) = 0.71 - 9\varepsilon_g + 7.0\left(U_g / U_b\right)^{0.75} \tag{2-5a}$$

Heterogeneous regime: $$F(\varepsilon_g) = 0.045 - 7.5\varepsilon_g + 5.5\left(U_g / U_b\right)^{0.5} \tag{2-5b}$$

Combining Equations (2-4) and (2-5a) for the homogeneous regime and Equations (2-4) and (2-5b) for the heterogeneous regime, Sarrafi *et al.* (1999) were able to evaluate the gas holdup for different superficial gas velocities. Comparison of the predicted gas holdup with measurements reported in the literature, a good agreement was found with absolute mean average error between predicted and experimental results being approximately 6 %. In addition to gas holdup correlations, they also proposed a methodology to evaluate the transition superficial gas velocity by solving simultaneously Equation (2-4) and Equations (2-5a) and (2-5b). To obtain the transition superficial gas velocity, one first equates Equations (2-5a) and (2-5b), which gives a relationship between U_g and ε_g at transition. Making use of this relationship between U_g and ε_g at transition, and substituting Equation (2-4) for the left-hand side in Equation (2-5a), one

can solve for both these quantities by an iterative procedure. For the solution of the above equations, it is evident that one needs an estimation of the bubble rise velocity, U_b. Sarrafi *et al.* (1999) recommend using the correlation of Jamialahmadi *et al.* (1994) for this purpose (refer to Table 2-8). Since the estimation of U_b requires an estimation of bubble size, Sarrafi *et al.* (1999) propose using the theoretical model of Gaddis and Vogelpohl (1986) (refer to Table 2-7). Since their study was performed at atmospheric pressure conditions, the question remains regarding the validity of their correlations at high-pressure conditions.

Another empirical method that has been used for regime identification is the Dynamic Gas Disengagement (DGD) technique, which was first introduced by Sriram and Mann (1976). The underlying concept of the DGD technique is to monitor the drop in the liquid-gas interface at the top of the column upon shutdown of the gas supply and relate it to the gas holdup structure. Recently, Krishna and co-workers (Krishna and Ellenberger, 1995; Krishna *et al*., 1999; Krishna 2000; Krishna *et al*., 2001) have utilized this technique extensively in columns of several different sizes and in liquids of different physical properties to evaluate the holdup distribution of "**small**" and "**large**" bubble phases in a churn-turbulent bubble column. Upon investigation of the DGD time series data, it can be seen that there is an initial rapid drop in the gas-liquid interface following the shut-off of the gas supply. Krishna and coworkers attribute this initial drop to the escape of the large bubbles. Subsequently, the gas-liquid interface falls down slowly due to the relatively slower disengagement of the small bubbles. In spite of this conceptualization of the gas structure being composed of large and small bubbles from DGD data, no documented proof of direct visual observation of bimodality of the proposed bubble size distribution in large three-dimensional columns at sufficiently higher superficial gas velocity (>5 cm/s) seem to exist in the open literature. A brief description of the gas holdup model proposed by them, based on the data from this technique, is provided in the next sub-section.

In contrast to the use of the drift flux and the DGD technique discussed above for regime identification, recent trend has been towards utilization of the time-series analysis of signal fluctuations from a characteristic flow signature. Bukur *et al.* (1996) studied the

signals from a Nuclear Density Gauge (NDG) in two different columns of height 3 m and inner diameter of 0.05 m and 0.21 m, respectively. The distributor used for the former column was a single nozzle plate with orifice diameter of 2 mm, while for the latter column, a perforated plate with 19 orifices of 2 mm diameter was used. Nitrogen and Fischer-Tropsch derived waxes were used as gas and liquid phase, respectively, while the gas velocities ranged from 0.02 to 0.12 m/s. The time series analysis of the gamma-ray fluctuating signals from NDG measurements was used to evaluate the mean square deviation (MSD), probability density function (PDF) and the power spectral density (PSD). An increase in MSD indicated an increase in the variation of the gas holdup. A distinct change in the slope of the MSD curves between superficial gas velocities of 0.04 and 0.06 m/s was observed under all operating conditions and indicates transition from homogeneous bubbly regime to the churn-turbulent regime. The same conclusion was reached using PSD where the dominant frequency moved towards lower values with increasing velocity upon regime transition from bubbly to churn-turbulent flow.

On the other hand, pressure signals were used in other studies to characterize the regime transitions (Letzel *et al*., 1997[a]; Lin *et al*., 2001). In particular, Letzel *et al.* (1997[a]) used piezo-electric sensors to measure pressure fluctuations in two different columns of inner diameter of 0.1 and 0.19 m, respectively, with air as the gas phase and tap water as liquid phase. Superficial gas velocities up to 0.3 m/s were employed in the study. Using the low frequency part of the signals, the Kolmogorov entropy was calculated and plotted as a function of superficial gas velocity. The plot indicates a sharp transition from the homogeneous to heterogeneous regime. The transition velocity for the 0.1 m diameter column was identified as 0.07 m/s, which is within the transition range obtained from the ε_g-U_g plot (0.05-0.1 m/s). Letzel (1997) also used the Kolmogorov entropy technique to study the effect of pressure on regime transition. His conclusions were contrary to the common belief that with increasing system pressure, the transition from homogeneous to churn-turbulent regime shifts to higher superficial gas velocities. Letzel (1997) concluded that with increasing system pressure, only the gas holdup at transition increases whereas the transition superficial gas velocity remains unaffected. Upon closer examination of the graphical presentation of the results in his thesis (Letzel,

1997), it does appear that the transition superficial gas velocity is attained at almost the same value (5-6 cm/s) for a range of operating pressures. However, the minimum in the Kolmogorov entropy is sustained for U_g in the range of 8-10 cm/s at higher pressure (0.5, 0.7 and 0.9 MPa) while such is not case at atmospheric pressure conditions where the Kolmogorov entropy starts increasing rapidly from a U_g of 6 cm/s upwards.

Lin *et al.* (2001) measured pressure fluctuations at an operating pressure range of 0.1 MPa to 15 MPa, using a differential pressure transducer in a column of 0.0508 m in diameter and height of 0.8 m. Nitrogen and paratherm NF heat transfer fluid were used as the gas and liquid phase, respectively. The flow regime transition was determined from the sharp transition in the largest Lyapunov exponent, metric entropy or the correlation dimension as a function of superficial gas velocity. It was concluded that superficial gas velocity at regime transition increases with operating pressure (refer to Figure 2-3).

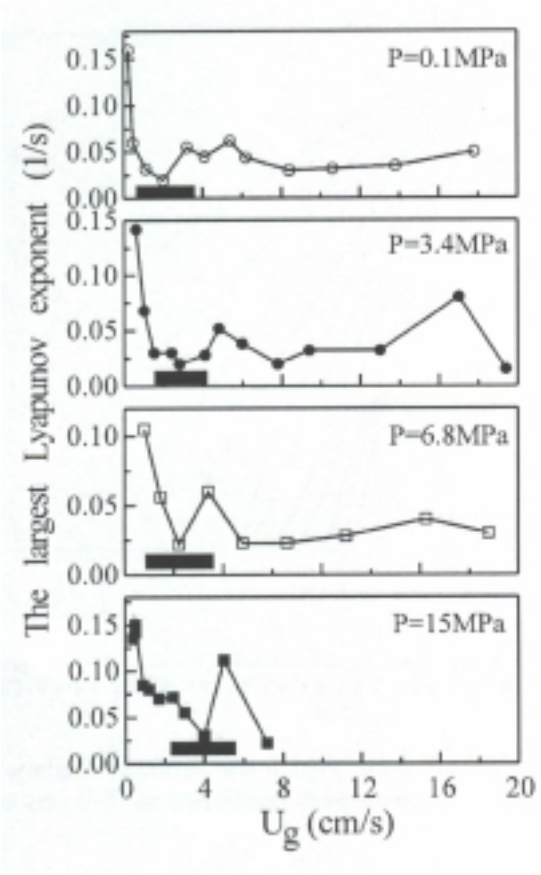

Figure 2-3. Largest Lyapunov exponent for different operating pressures (Lin *et al.*, 2001).

From the above review, it is clear that in general, the methods to determine regime transition have progressed from measurement of time-averaged overall hydrodynamic features like gas holdup as a function of superficial gas velocity to more quantitative analysis based on examination of temporal signatures from a representative hydrodynamic quantity. It, however, still remains a challenge to *a priori* predict the transition velocity for a new system without resorting to an extensive experimentation. Therefore, it appears that the utility of the time-series analysis techniques for regime identification is primarily restricted to assessment of existing reactor operations.

2.1.2. Pressure Effect on Gas Holdup

Gas holdup in the homogeneous regime has been the subject of extensive research via detailed experimental and numerical studies over the last two decades. Due to the relatively low volume fraction of the dispersed phase at low U_g and at atmospheric pressure, it has been possible to use experimental techniques like probes and photography to determine the gas holdup and its distribution (Hills, 1974; Sheng and Irons, 1991; Groen *et al.*, 1995). In addition, the tomography technique (including gamma ray and electrical impedance), which can be universally used in both regimes of operation, has been proven to be a very powerful non-invasive technique for holdup and holdup distribution measurements (Kumar *et al.*, 1997; Chaouki *et al.*, 1997; Shollenberger *et al.*, 1997; Chen *et al.*, 1998; George et al., 2000[a]; Schmitz and Mewes, 2000; Fransolet *et al.* 2001; Warsito and Fan, 2001). Nevertheless, in the churn-turbulent regime of operation, limited experimental information exists in the literature. This is primarily due to the inability of most experimental techniques, other than tomography, to reliably acquire data in opaque systems. The gamma ray tomography studies reported in the literature in the churn-turbulent regime are mainly the ones from the Chemical Reaction Engineering Laboratory at Washington University (Kumar *et al.*, 1997; Chen *et al.*, 1998; Kemoun *et al.*, 2001) and from Sandia National Laboratory (Adkins *et al.*, 1996; George *et al.*, 2000[b]; Shollenberger *et al.*, 2000; George *et al.*, 2001; Shollenberger *et al.*, 2001).

As mentioned earlier, most research on measurements of phase holdup distribution in bubble columns has been limited to operating conditions of atmospheric pressure, with only a few studies at high pressure (Adkins *et al*., 1996; Schmitz and Mewes, 2000; George *et al.,* 2000[b]; Shollenberger *et al.,* 2000; Kemoun *et al*., 2001). However, a vast amount of literature exists on overall gas holdup measurements in systems with varying fluid properties and over an entire spectrum of operating conditions. Some of the studies at atmospheric pressure are those from Akita and Yoshida (1973), Hikita *et al*. (1980), and Hammer *et al*. (1984) in which they developed correlations for the average gas holdup (refer to Table 2-2 for more gas holdup correlations). However, the literature that is pertinent to this work describes the findings in bubble columns operated at elevated pressures and a brief discussion of some of these studies is presented here.

At elevated pressure conditions there is generally an insignificant effect of pressure on gas holdup in the homogeneous regime (Kölbel *et al*., 1961; Deckwer *et al*., 1980). In addition, the transition to churn-turbulent flow is delayed (Lin *et al.,* 2001). From then onwards, gas holdup increases with pressure at higher gas throughputs (Jiang *et al*., 1995; Adkins *et al*., 1996; Lin *et al*., 1998; Fan *et al*., 1999; Kemoun *et al*., 2001). This behavior is primarily due to the smaller bubbles formed at high-pressure condition. Jiang *et al.* (1995) reported that a decrease in bubble size results from an increase in pressure, which leads to a narrower bubble size distribution. In homogeneous regime, the bubble size is also reduced with increasing pressure (Idogawa *et al.,* 1987; Lin *et al.,* 1998). This, due to reduced bubble rise velocity, implies that the gas holdup should increase, however, the increment in gas holdup is too small to be noticeable as compared to those obtained at a higher superficial gas velocity with increasing pressure (Lin *et al.,* 1998). Oyevaar and Westerterp (1989) reviewed critically the influence of pressure on mass transfer phenomena and hydrodynamics in bubble column. They reported that the initial bubble size at a single orifice decreases with increasing pressure. Overall, two different approaches have been suggested in interpreting the pressure effects on gas holdup. The first approach attributes the pressure effect to the increase in gas momentum (Wilkinson, 1991; Reilly *et al*., 1994), while the second concept attributes the pressure

effect to the decrease in the interfacial tension (Jiang *et al.*, 1995). An increase in gas momentum leads to a quicker overcoming of the liquid inertia above the orifice, which eventually results in shorter time intervals for bubble growth before bubble detachment from the orifice takes place, thereby leading to smaller bubble sizes (Wilkinson, 1991). Experimentally it is known that an increase in system pressure has a similar effect as an increase in the gas density, which is conceptualized by the first approach, whereas the latter implies that the decrease in bubble size is due to an inherent instability of bubble size. Further analysis of the effect of pressure on bubble size, and consequently gas holdup, will be presented in Chapter 4 along with the discussion of the data acquired from Computed Tomography measurements as part of this doctoral work.

Table 2-2 shows some of the correlations that are available in the literature for predicting the overall gas holdup. The correlations developed by Wilkinson *et al.* (1992), Krishna and Ellenberger (1996), Letzel (1997) and Sarrafi *et al.* (1999) take into account different flow regimes in predicting gas holdup. Some of the correlations are developed based on the overall gas holdup data measured at high-pressure conditions (those indicated as bold in Table 2-2). Recently, Krishna (2000) developed the following correlation to predict overall gas holdup.

$$\bar{\varepsilon}_g = \bar{\varepsilon}_{g,large} + \left(1 - \bar{\varepsilon}_{g,large}\right)\bar{\varepsilon}_{g,small} \tag{2-6}$$

where $\bar{\varepsilon}_{g,small}$ and $\bar{\varepsilon}_{g,large}$ are calculated by Equation (2-7).

$$\bar{\varepsilon}_{g,small} = \frac{U_g}{V_{b,small}} \qquad \text{for } U_g < U_{g,trans} \tag{2-7a}$$

$$\bar{\varepsilon}_{g,large} = \frac{U_g - U_{g,trans}}{V_{b,large}} \qquad \text{for } U_g > U_{g,trans} \tag{2-7b}$$

In Equation (2-7a), $V_{b,small}$ is the rise velocity of the small bubble phase and is evaluated based on Richardson-Zaki (1954) correlation (refer to Equation (2-8)).

$$V_{b,small} = V^0_{b,small}\left(1 - \bar{\varepsilon}_g\right)^{n-1} \qquad n = 2 \text{ for air-water system} \tag{2-8}$$

where $V^0_{b,small}$ is the unhindered rise velocity of a small bubble. The transition velocity, $U_{g,trans}$, is shown in Equation (2-9).

Table 2-2. Correlations for gas holdup.

References	Correlations
Akita & Yoshida (1973)	$\frac{\bar{\varepsilon}}{(1-\bar{\varepsilon})^4} = 0.2\left(\frac{gD^2\rho_l}{\gamma}\right)^{0.125}\left(\frac{gD^3}{\nu_l}\right)^{0.083}\frac{U_g}{(gD)^{0.5}}$
Hikita *et al*. (1980)	$\varepsilon = 0.672 f\left(\frac{U_g\mu_l}{\gamma}\right)^{0.578}\left(\frac{\mu_l^4 g}{\rho_l\gamma^3}\right)^{-0.131}\left(\frac{\rho_g}{\rho_l}\right)^{0.062}\left(\frac{\mu_g}{\mu_l}\right)^{0.107}$ where $f = \begin{cases} 1.0 & \text{for non-electrolyte solution} \\ 10^{0.0414I} & \text{for } 0<I<1.0 \text{ kg ion/m}^3 \\ 1.1 & \text{for } I>1.0 \text{ kg ion/m}^3 \end{cases}$
Hammar *et al*. (1984)	$\frac{\bar{\varepsilon}}{1-\bar{\varepsilon}} = 0.4\left(\frac{U_g\mu_l}{\gamma}\right)^{0.87}\left(\frac{\mu_l^4 g}{\rho_l\gamma^3}\right)^{-0.27}\left(\frac{\rho_g}{\rho_l}\right)^{0.17}$
Idogawa *et al*. (1985)	$\frac{\bar{\varepsilon}}{1-\bar{\varepsilon}} = 1.44 U_g^{0.58}\rho_g^{0.12}\sigma_l^{-0.16\exp(-P)}$
Reilly *et al*. (1986)	$\bar{\varepsilon} = 296 U_g^{0.44}\rho_l^{-0.98}\rho_g^{0.19}\gamma^{-0.16} + 0.009$
Idogawa *et al*. (1987[a])	$\frac{\bar{\varepsilon}}{1-\bar{\varepsilon}} = 0.059 U_g^{0.8}\rho_g^{0.17}\left(\frac{\sigma_l}{72}\right)^{-0.22\exp(-P)}$
Wilkinson *et al*. (1992)	$U_g < U_{trans} \quad \bar{\varepsilon} = \frac{U_g}{U_{s.b.}}$ $U_g > U_{trans} \quad \bar{\varepsilon} = \frac{U_{trans}}{U_{s.b.}} + \frac{U_g - U_{trans}}{U_{l.b.}}$ where $\frac{U_{trans}}{U_{s.b.}} = 0.5\exp(-193\rho_g^{-0.61}\mu_l^{0.5}\gamma^{0.11})$ $\frac{\mu_l U_{s.b.}}{\gamma} = 2.25\left(\frac{\gamma^3\rho_l}{g\mu_l^4}\right)^{-0.273}\left(\frac{\rho_l}{\rho_g}\right)^{0.03}$ $\frac{\mu_l U_{l.b.}}{\gamma} = \frac{\mu_l U_{s.b.}}{\gamma} + 2.4\left[\frac{\mu_l(U_g - U_{trans})}{\gamma}\right]^{0.757}\left(\frac{\gamma^3\rho_l}{g\mu_l^4}\right)^{-0.077}\left(\frac{\rho_l}{\rho_g}\right)^{0.077}$
Sotelo *et al*. (1994)	$\bar{\varepsilon} = \left\{129\left(\frac{U_g\mu_l}{\gamma}\right)^{0.99}\left(\frac{\mu_l^4 g}{\rho_l\gamma^3}\right)^{-0.123}\left(\frac{\rho_g}{\rho_l}\right)^{0.187}\left(\frac{\mu_g}{\mu_l}\right)^{0.343}\left(\frac{d_o}{D}\right)^{-0.089}\right\}$

Note: Correlations, which are indicated by bold, includes data at high pressure.

Table 2-2. Correlations for gas holdup - Cont'd.

References	Correlations
Krishna & Ellenberger (1996)	$U_g < U_{trans} \quad \bar{\varepsilon} \begin{cases} = 0.5 - \sqrt{0.25 - U_g / V_{small}} \\ \approx U_g / V_{small} \quad \text{after Taylor's expansion about } U_g = 0 \end{cases}$ $U_g > U_{trans} \quad \bar{\varepsilon} = \varepsilon_b + \varepsilon_{trans}(1-\varepsilon_b)$ Where $\varepsilon_b = 0.268 \dfrac{(U_g - U_{trans})^{0.58}}{D^{0.18}}$ $U_{trans} = V_{small}\varepsilon_{trans}(1-\varepsilon_{trans})$ $V_{small} = \dfrac{\gamma^{0.12}}{2.84\rho_g^{0.04}}; \qquad \varepsilon_{trans} = 0.59(3.85)^{1.5}\sqrt{\dfrac{\rho_g^{0.96}\gamma^{0.12}}{\rho_l}}$
Kojima *et al.* (1997)	$\bar{\varepsilon} = 1.18 U_g^{0.679}\left(\dfrac{\gamma}{\gamma_0}\right)^{-0.546} \exp\left[1.27\times10^{-4}\left(\dfrac{\rho_l Q^2}{d_o^3\gamma}\right)\left(\dfrac{P}{P_0}\right)\right]$
Letzel (1997)	$U_g < U_{trans} \quad \bar{\varepsilon} \begin{cases} = 0.5 - \sqrt{0.25 - U_g / V_{small}} \\ \approx U_g / V_{small} \quad \text{after Taylor's expansion about } U_g = 0 \end{cases}$ $U_g > U_{trans} \quad \bar{\varepsilon} = \varepsilon_b + \varepsilon_{trans}(1-\varepsilon_b)$ Where $\varepsilon_b = 0.268 \dfrac{(U_g - U_{trans})^{0.58}}{D^{0.18}}\left(\dfrac{\rho_g}{\rho_{g,atm}}\right)^{0.5}$ $U_{trans} = V_{small}\varepsilon_{trans}(1-\varepsilon_{trans})$ $V_{small} = \dfrac{\gamma^{0.12}}{2.84\rho_g^{0.04}}; \qquad \varepsilon_{trans} = 0.59(3.85)^{1.5}\sqrt{\dfrac{\rho_g^{0.96}\gamma^{0.12}}{\rho_l}}$
Luo *et al.* (1999)	$\dfrac{\bar{\varepsilon}}{1-\bar{\varepsilon}} = \dfrac{2.9\left(\dfrac{U_g^4\rho_g}{\gamma g}\right)^{\alpha}\left(\dfrac{\rho_g}{\rho_{sl}}\right)^{\beta}}{\left[\cosh\left(Mo_{sl}^{0.054}\right)\right]^{0.41}}$ where $Mo_{sl} = \dfrac{(\xi\mu_l)^4 g}{\rho_{sl}\gamma^3}$ $\alpha = 0.21 Mo_{sl}^{0.0079}; \beta = 0.096 Mo_{sl}^{-0.011}; \rho_{sl} = \rho_l; \xi = 1$
Sarrafi *et al.* (1999)	Homogeneous regime: $(1-\varepsilon_g)^{n-1} = 0.71 - 9\varepsilon_g + 7.0\left(U_g / U_b\right)^{0.75}$ Heterogeneous regime: $(1-\varepsilon_g)^{n-1} = 0.045 - 7.5\varepsilon_g + 5.5\left(U_g / U_b\right)^{0.5}$

Note: Correlations, which are indicated by bold, includes data at high pressure.

$$U_{g,trans} = \bar{\varepsilon}_{g,trans} V_{b,small}\Big|_{\bar{\varepsilon}_g = \bar{\varepsilon}_{g,trnas}} = V^0_{b,small}\ \bar{\varepsilon}_{g,trans}\left(1-\bar{\varepsilon}_{g,trans}\right) \tag{2-9}$$

where $\bar{\varepsilon}_{g,trans} = 4.46\sqrt{\dfrac{\rho_g^{0.96}\sigma_l^{0.12}}{\rho_l}}$; $V^0_{b,small} = \dfrac{\sigma_l^{0.12}}{2.84\rho_g^{0.04}}$ (Reilly *et al.*, 1994).

The bubble velocity of the large bubble phase, $V_{b,large}$, could be evaluated as follows.

$$V_{b_{large}} = V^0_{b_{large}}.SF.AF.DF; \qquad DF = \sqrt{\frac{1.29}{\rho_g}}$$

$$AF = \begin{cases} 2.73 + 4.505\left(U_g - U_{g_{trans}}\right) & Low\ \mu_l\ (like\ water, < 3\,cP) \\ 2.25 + 4.090\left(U_g - U_{g_{trans}}\right) & High\ \mu_l\ (like\ oil) \end{cases}$$

$$V^0_{b_{large}} = \begin{cases} 0.71\sqrt{g d_{b_{large}}} & Eo > 40 \\ \sqrt{\dfrac{2\sigma_l}{\rho_l d_{b_{large}}} + \dfrac{g d_{b_{large}}}{2}} & Eo < 40 \end{cases}$$

$$SF = \begin{cases} 1 & \dfrac{d_{b_{large}}}{D_T} \le 0.125\ , \quad Eo > 40 \\ 1.13\exp\left(-\dfrac{d_{b_{large}}}{D_T}\right) & 0.125 < \dfrac{d_{b_{large}}}{D_T} \le 0.6\ , \quad Eo > 40 \\ 0.496\sqrt{\dfrac{D_T}{d_{b_{large}}}} & \dfrac{d_{b_{large}}}{D_T} > 0.6\ , \quad Eo > 40 \\ \left\{1-\left(\dfrac{d_b}{D_T}\right)^2\right\}^{\frac{3}{2}} & Eo < 40 \end{cases} \tag{2-10}$$

where *Eo* is the Eotvos number $\left(Eo = \dfrac{g\left(\rho_l - \rho_g\right)d_b^2}{\sigma_l}\right)$.

It is not clear yet which correlation is the best in predicting gas holdup for all the operating conditions encountered in a typical bubble column operation. Therefore, further analysis of the gas holdup correlations and their ability to predict new experimental data will be tested in a later section in Chapter 4. It should, therefore, not be

surprising that in the absence of reliable information, the design and scale up of bubble column reactors at elevated pressures utilize either the guidelines from detailed experimental data collected at atmospheric conditions, or overall gas holdup data which has inherent measurement errors due to a fluctuating interface. This methodology of design and scale up thus suffers from an inherent limitation and its improvements are the primary motivation for this study. Moreover, it is clear from the review presented above and from Table 2-1 (studies not indicated by asterisks) that most of the research on gas holdup in high pressure bubble column has been restricted to the measurement of small gas holdup values in the homogeneous regime with little information on spatial distribution of gas holdup.

2.1.3. Effect of Sparger Design and Configuration on Gas Holdup

During bubble column design and operation a frequently asked question is whether spargers (gas distributors) affect column performance. Knowing the answer to this question is important since simpler sparger designs could represent significant cost savings in column construction. Additionally, an efficiently designed sparger can also minimize pressure drop across the sparger while maintaining a desired distribution of gas bubbles at the inlet. This in turn translates to significant savings in operating cost due to lower energy requirements (e.g. compression cost).

Numerous studies addressed bubble formation from a single orifice submerged in liquids at atmospheric pressure (e.g. Tsuge and Hibino, 1983; Snabre and Magnifotcham, 1998; Terasaka *et al.*, 1999; Hsu *et al.*, 2000) and at high pressure (LaNauze and Harris, 1974; Idogawa *et al.*, 1987[b]; Tsuge *et al.*, 1992; Yoo *et al.*, 1998). It is understood that the formation of bubbles at submerged orifices is influenced by many factors, such as the orifice diameter, superficial gas velocity through the orifice, liquid density, liquid viscosity, surface tension, orifice material and gravitational acceleration. As shown in Figure 2-4, each bubble is acted upon by buoyancy, convection currents in the fluid, and by the surface-tension force acting on that section of the bubble that is still in contact

with the orifice. Tadaki and Maeda (1963) proposed using dimensional analysis the following dimensionless numbersto characterize bubble formation.

$$\text{Dimensionless capacitance number} \quad N_c = \frac{4V_{ch} g\rho_l}{\pi d_o^2 p_h} \tag{2-11}$$

$$\text{Dimensionless gas flow rate} \quad N_w = BoFr_o^{0.5} \tag{2-12}$$

where V_{ch} is the chamber volume feeding the orifice; p_h is the hydrostatic pressure at the orifice plate; *Bo* is the Bond Number $\left(g\rho_l d_o^2/\sigma\right)$; Fr_o is the orifice Froude Number $\left(u_o^2/gd_o\right)$. To study the effect of operating pressure, it should be noted that p_h in Equation (2-11) is taken as the sum of hydrostatic pressure head resulting from the liquid column above the sparger and the operating pressure of the column.

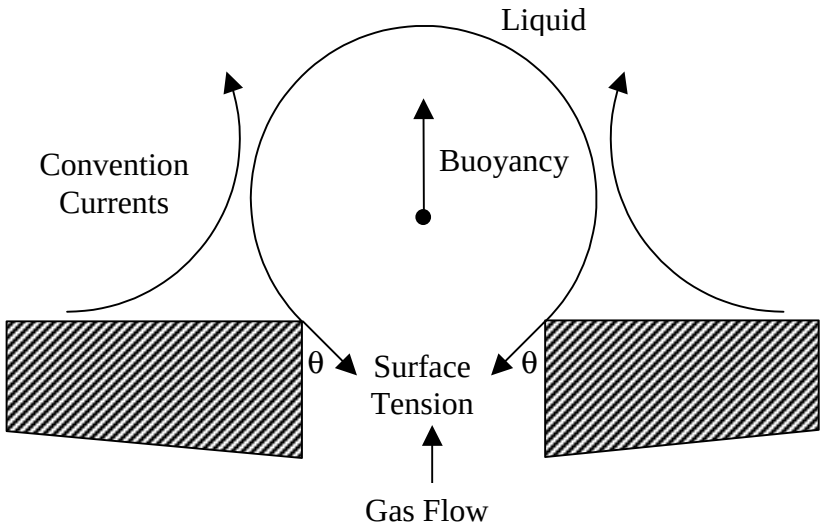

Figure 2-4. Forces acting on bubble at orifice (Azbel, 1981).

Bubble formation regimes are classified based on the values of N_c and N_w as shown in Tables 2-3 and 2-4. Constant pressure conditions occur when the size of the gas chamber volume is relatively large as would be encountered in most industrial gas distributors. Under such conditions (N_c > 9), the orifice gas flow rate is not constant and depends on the pressure fluctuations in the chamber and in the bubble. Usually, these phenomena are complex and difficulties exist in calculating the bubble volume by simple

explicit equations based on the bubble formation model (Tsuge, 1985). On the other hand, constant flow conditions, in which the gas flow rate through an orifice is constant throughout the bubble formation, exist at the orifice when the volume of the gas chamber is small ($N_c < 1$).

Table 2-3. Flow conditions at the orifice.

Range of N_c	Flow condition at the orifice
$N_c < 1$	Constant flow
$1 < N_c < 9$	Intermediate condition
$9 < N_c$	Constant pressure

Table 2-4. Formation of bubble at the orifice.

Range of N_w	
$N_w < 2.4\ (N_c - 1)$	Small, uniform bubbles are formed
$2.4\ (N_c - 1) < N_w < 16$	Bubble volume increases with N_w
$16 < N_w$	Bubbles break down after detachment at the orifice and distribution of bubble volumes is produced

In the study conducted by LaNauze and Harris (1974), it was shown that at constant gas flow rate of 10 cm^3/s and chamber volume of 375 cm^3, with increasing pressure, smaller and more frequent bubbles are formed at the orifice, which are attributed to the increased contribution of the gas momentum to the bubble formation process. Hence, greater interaction between bubbles is likely, due to higher bubble frequencies, at high pressure. Utilizing Equations (2-11) and (2-12) and for the ranges of static liquid height, system pressure and orifice diameters employed in the above study, the range of N_c is found to vary from 0.1 to 18 while the range of N_w varies from 0.8 to 41.5. In another study conducted by Idogawa *et al*. (1987[b]), where the employed system pressure was in the range of 0.1-15 MPa and superficial gas velocity was in the range 0.05-3.0 cm/s, it was found that a dispersed gas jet is formed at higher pressures whereas individual spherical gas bubbles are formed at atmospheric pressure. In their study, a stainless steel bubble column of diameter 0.05 m and height 0.83 m and orifices of

different diameter was used. Different gas-liquid systems were used (air-water; air-methanol; air-ethanol; hydrogen-water; helium-water) and constant flow conditions were maintained in their study. Based on the visual observation of bubble formation at the orifice, Idogawa *et al.* (1987[b]) identified three different regimes, *viz.*, bubbling, jetting and dispersed jetting. They also visually observed the orifice velocities at which the transition between the different regimes of bubble formation occurred. Based on this data, they developed correlations for determining the transitions for bubbling/jetting and jetting/dispersed jetting regimes (refer to Equation (2-13)) at elevated pressure conditions, which are given as:

Bubbling/jetting transition: $We_{B\text{-}J} = 1.4 \times 10^{36}\, Re_o^{-8}$ (2-13a)

Jetting/dispersed jetting transition: $We_{J\text{-}DJ} = 9.7 \times 10^{40}\, Re_o^{-8}$ (2-13b)

where Re_g is the orifice Reynolds number based on gas properties ($Re_o = \rho_g d_o u_o / \mu_g$); and We is the Weber number ($We = \rho_l d_o u_o^2 / \sigma$). Unfortunately, no expressions were developed to predict the bubble size at the sparger under different regimes of bubble formation. In the same study, Idogawa *et al.* (1987[b]) did report the bubble size distribution obtained at a superficial gas velocity of 3 cm/s for various operating pressures. They found that when the pressure increased from atmospheric pressure to 5 MPa, the regime of bubble formation changed from multiple bubbling (accompanied by coalescence) with the wider bubble size distribution to dispersed jetting with a narrower bubble size distribution. The applicability of this interesting observation regarding bubble size distributions at higher superficial gas velocity has unfortunately not been reported.

Tsuge *et al.* (1992) performed their experiments at system pressures of 0.1-8.1 MPa in a stainless steel bubble column of diameter 0.04 m and height of 0.33 m using distilled water and nitrogen as liquid and gas phases, respectively. The superficial gas velocity was varied from 0.004 to 0.8 cm/s while the gas chamber volume range was 13-365 cm^3 (N_c ranging from 0.005-30.7 while N_w ranged from 0.06-16). They also

concluded that with increasing pressure, bubble volume decreases. In addition, N_c decreases with an increase in pressure and bubble formation approaches the constant flow condition, where the bubble volume is independent of gas chamber volume. Also, at a pressure of 6.1 MPa, and using a gas chamber volume of 365 cm^3, they found that the bubble volume increases with increasing gas flow-rate. This also agrees with their earlier study (Tsuge and Hibino, 1983) where they concluded that the bubble volume increases with increasing N_c and Q_g, when N_c is smaller than 25, and becomes independent of gas flow rate when N_c is greater than 25. On the other hand, Yoo *et al.* (1998) concluded that surface tension is an important parameter to be considered in bubble formation modeling at high pressure conditions. In their study, a stainless steel bubble column of diameter 0.04 m and 0.33 m high was used. The gas chamber volume was 86.2 cm^3 and distilled water was used as liquid phase. The gases used were N_2 and CO_2. The range of pressures and gas flow rates studied were 0.1-8.0 MPa and 0.06-7 cm^3/s, respectively. They found that for distilled water-CO_2 system, bubble volume decreased with increasing system pressure and increasing gas flow-rate. However, for distilled water-N_2 system, bubble volume decreased significantly with increasing system pressure from 0.1 to 0.5 MPa, and remained constant when system pressure was passed beyond 0.5 MPa and gas flow-rate was below 1 cm^3/s.

As indicated in Table 2-4, a distribution of various bubble sizes is expected provided N_w is greater than 16. At a constant pressure of P_o (corresponding to N_{c1}, N_{w1}), small and uniform bubbles are formed only if N_{w1} falls below 2.4(N_{c1}-1). However, if one increases the system pressure sufficiently to P (corresponding to condition at N_{c2}, N_{w2}), N_{c2} becomes lower than N_{c1} while N_{w2} is still equal to N_{w1} since only the dimensionless capacitance number is dependent on pressure (refer to Equations (2-1) and (2-2)). Whether bubble formation at the orifice leads to small and uniform bubbles at pressure P depends on the value of N_w. If N_{w1} (=N_{w2}) is below 2.4(N_{c2}-1), small and uniform bubbles are formed even at a higher pressure P. However, if N_{w1} or N_{w2} lies between 2.4(N_{c2}-1) and 2.4(N_{c1}-1), bubble volume increases at pressure P even though formation of small and uniform bubbles are observed at P_o. Depending on the range of N_c and N_w, therefore, different bubble formation models (spherical and non-spherical) are proposed (Tsuge,

1985). More details on the bubble formation and detachment as well as the bubble rise velocity from the orifice have been described elsewhere (Azbel, 1981; Tsuge, 1985; Tsuge *et al*., 1992; Fan *et al*., 1999). All the studies mentioned above are solely based on bubble formation from a single orifice and bubble formation from multi-orifices or distributors of different designs is still not well understood.

Degaleesan (1997) reviewed different regimes of bubble formation at the orifice and also the correlations used to obtain the initial bubble diameter (refer to Table 2-5). Basically, there are three different regimes of bubble formation, namely, single bubble, intermediate bubble and jetting regimes. Bubble regime is characterized when discrete bubbles are produced one at a time. This occurs when orifice Reynolds number $\left(Re_o = \rho_g u_o d_o / \mu_g\right)$ is less than or equal to 200. When 200 < Re_o ≤ 2100, intermediate bubble regime prevails, that is, bubble formation frequency increases and the bubbles begin to grow in size. In this case, the bubble size becomes dependent on the viscous drag, inertial forces, buoyancy and surface tension. Jetting regime occurs when Re_o > 2100, turbulence occurs at the orifice and the gas stream approaches the appearance of a continuous jet. It should be noted that based on the equations for the initial bubble size presented in Table 2-5, it appears that the initial bubble size decreases slightly with pressure only in the jetting regime while an opposite trend is predicted for the other two regimes. The effect, however, is negligible for single bubble.

Table 2-5. Initial bubble size correlations.

Regimes	Bubble Size Equation	References
Single bubble	$d_b = \left[6\sigma d_o \Big/ \left(\rho_l - \rho_g\right)g\right]^{1/3}$	Azbel (1981)
Intermediate bubble	$d_b = 0.19\, d_o^{0.48}\, Re_o^{0.32}$ (d_b, d_o in inches)	Leibson *et al.* (1956)
Jetting criterion	$u_o > u_{o,crit}$	Azbel (1981)
	$\dfrac{u_{o,crit}\sqrt{\rho_g}}{\left[\sigma\left(\rho_l - \rho_g\right)\right]^{1/4}} = 1.3\left[\dfrac{g^2\sigma}{\left(\rho_l - \rho_g\right)d_o^2}\right]^{1/12}$	
Jetting	$d_b = 0.28\, Re_o^{-0.05}$ (d_b in inches)	Leibson *et al.* (1956)

Regarding bubble size, Ellenberger and Krishna (1994) advocate the extension of two-phase model for bubbling gas-solid fluidized beds to bubble column slurry reactors operating in the heterogeneous flow regime. They developed a correlation for initial bubble size, which matches closely that developed by Darton *et al.* (1977) and is given below:

$$d_b = \alpha_1 \left(U_g - U_{g,trans}\right)^{2/5} \left(h_o\right)^{4/5} g^{-1/5} \tag{2-14}$$

where $U_{g,trans}$ is the transition superficial gas velocity; g is the gravitational acceleration; h_o is the parameter determining the initial bubble size at the gas distributor. For air-water system:

$$\alpha_1 = 1;\ U_{g,trans} = 2.25\varepsilon_{trans}\left(\frac{\sigma}{\mu_l}\right)\left(\frac{\sigma^3\rho_l}{g\mu_l^4}\right)^{-0.273}\left(\frac{\rho_l}{\rho_g}\right)^{0.03};$$

$$\varepsilon_{trans} = exp\left(-193\rho_g^{-0.61}\mu_l^{0.5}\sigma^{0.11}\right);$$

$h_0 = 4\sqrt{A_o}$ and A_o is the area of distributor plate per orifice

Based on the above set of equations, it is clear that $U_{g,trans}$ increases with increase in pressure, thereby leading to a decrease in d_b.

It is also frequently reported that sparger design and its configuration have a significant effect on gas holdup only in the ***bubbly flow regime*** and that this effect diminishes as higher superficial gas velocities, characteristic of churn-turbulent flow, are employed (Kumar, 1994; Hebrard *et al*., 1996; Krishna and Ellenberger, 1996; Joshi *et al*., 1998). However, some other studies do not support this point of view. Freedman and Davidson (1969) studied the effect of non-uniform gas distribution in columns of a square cross-section of 22.9-cm and 61.0-cm (column height of 304.8 and 426.7-cm, respectively) for superficial gas velocities of up to 12 cm/s. They observed a significant variation in gas holdup depending on the percentage of the distributor cross-section occupied by the sparger holes. Ueyama *et al*. (1980) compared the effect of single and

multi-nozzle spargers on a pilot-scale unit using air-tap water system with the superficial gas velocities up to 33.1 cm/s. The column had a 60-cm internal diameter (D) and a total height (L) of 303-cm resulting in a column aspect ratio (L/D) of 5.1. Axial profiles of the cross-sectional mean holdup were estimated using pressure taps, while lateral distributions of holdup and bubble velocities were obtained using an electrical resistivity probe. They reported significant axial variations of gas holdup with sparger design for smaller dispersed height to diameter ratio ($L_s/D < 2.2$). However, for higher L_s/D (2.2-3) ratio, and at superficial gas velocity greater than 15.5 cm/s, insignificant axial variation in the average gas holdup was observed beyond a z/D value of 1. They also observed a significant effect of distributors on the radial gas holdup profiles even at a very high superficial gas velocity of 32.4 cm/s when the dispersed height to diameter ratio (L_s/D) was kept low at 0.58. This is to be expected since the measurements in such a short column would invariably reflect the behavior in the distributor region.

Mikkilineni and Knickle (1987) studied the effect of the porous plate distributor thickness (1.59-12.7 mm) and pore size (35-70 μm) on gas holdup and flow patterns in a 15.2-cm ID bubble column using the air-water system. They conducted the study for gas superficial velocities of up to 35 cm/s and concluded that there is insignificant variation in holdup with pore size and plate thickness in the churn-slug regime. Rivas *et al*. (1987) studied the effect on holdup using a perforated plate, mesh plate and cone distributor in a 30-cm ID column ($L/D = 10$ and 13.3) with two organic solvents as the liquid and air as the gas phase. They measured the mean gas holdup using pressure taps for gas superficial velocities up to 18 cm/s. No significant effect of the distributor on holdup was observed. This was attributed to distributor effects being confined to the bottom region of the column near the distributor.

Tsuchiya and Nakanishi (1992) studied various perforated plate configurations in a 14.8-cm ID bubble column (column height of 802-cm) using air as gas and water as liquid. The study was performed for superficial gas velocities of up to 54 cm/s and the overall gas holdup was obtained based on the bed expansion method. By keeping the size of the distributor holes fixed, they found that the overall gas holdup increased with the increased number of holes on the perforated plate. When the number of holes on the

perforated plate was fixed, the average gas holdup decreased with increasing orifice diameter provided that it was maintained between 1–2 mm. The above conclusions were based on the holdup obtained in both homogeneous and transition regimes. No significant effect of distributors was observed for gas superficial velocities greater than 14 cm/s when the flow appeared to be churn-turbulent.

2.1.4. Effect of Liquid Properties on Gas Holdup

Liquid properties play an important role on gas holdup and several researchers have studied their effect (Idogawa *et al.*, 1987[a]; Zahradnik *et al*., 1987; Jamialahmadi and Müller-Steinhagen, 1992; Joshi *et al.*, 1998; Camarasa *et al.*, 1999) as well as developed correlations to estimate the overall gas holdup (Akita and Yoshida, 1973; Hikita *et al*., 1980). Akita and Yoshida (1973) investigated the effect of liquid properties on gas holdup using the bed expansion method. The bubble columns used in their study had a range of inner diameters of 0.152-0.6 m. A single nozzle distributor of orifice diameter of 5.0 mm was used and the superficial gas velocity range was from 0.53-41.94 cm/s. Different systems were used in their study (refer to Table 2-1). Considering only the measured gas holdup data at atmospheric pressure, a correlation was developed (refer to Table 2-2).

There are two opposite effects of liquid viscosity on gas holdup (Joshi *et al.*, 1998). With increasing liquid viscosity, and for bubbles of the same size, gas holdup increases due to a decrease in bubble rise velocity. On the other hand, due to the decrease in rise velocity, the bubbles get a greater chance to interact with each other leading to their coalescence. Thus, gas holdup decreases with increasing liquid viscosity because of the increasing coalescing nature of the liquid phase leading to larger bubbles, which increases the bubble rise velocity. Combining these two effects, gas holdup is observed to increase with increasing liquid viscosity and at about a liquid viscosity of 3-4 cP, gas holdup starts to decrease (refer to Figure 2-5 for a figure shown in Joshi *et al.*, 1998).

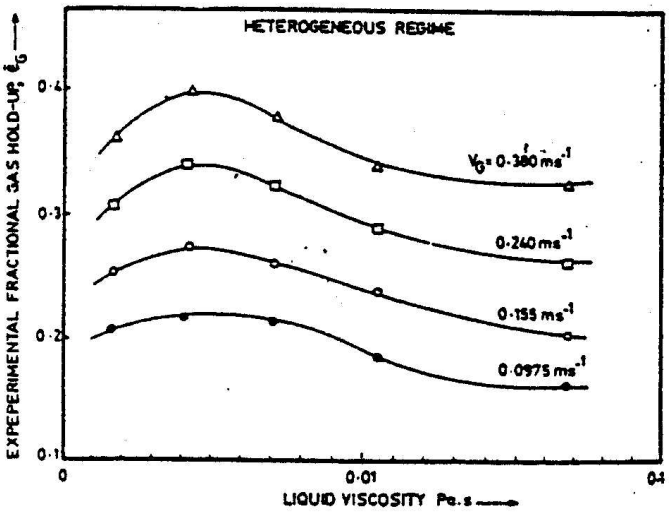

Figure 2-5. Effect of liquid viscosity on gas holdup (Joshi *et al.*, 1998).

On the other hand, Idogawa *et al.* (1987[a]) found that the effect of the viscosity of liquid methanol, ethanol and acetone on gas holdup is negligible in the range of 0.35-1.4 cP. Their studies were conducted in a stainless steel bubble column of 0.05 m in diameter and 0.83 m in height using a perforated plate distributor (19 orifices of 1 mm in diameter and with an equilateral triangular pitch of 10 mm) at U_g ranging from 0.5 to 5.0 cm/s.

Shollenberger *et al.* (2001) studied the effect of liquid viscosity on gas holdup using Drakeol 5 and 10 (viscosity of 11.9 and 31.0 cP, respectively). Bubble column of diameter 0.483 m and height 3.15 m was used with air as the gas phase. Throughout the study, a cross sparger composed of 96 orifices with 1.59 mm diameter was utilized. The pressure and superficial gas velocity were varied from 0.1 to 0.52 MPa and from 5 to 30 cm/s, respectively. They found that the average gas holdup decreases as liquid viscosity increases. In addition, they concluded that the entrance length increases with gas flow rate, column pressure, and liquid viscosity. Chen *et al.* (1998) found similar trends in gas holdup variation with liquid viscosity. Their study was conducted in a 44 cm diameter bubble column. However, the operating conditions were limited to atmospheric pressure and superficial gas velocity of 10 cm/s.

Other than liquid viscosity, surface tension also plays a role in bubble column performance. Figure 2-6 displays the effect of pressure on surface tension for gas-water

systems (Massoudi and King, 1974). As shown in Figure 2-6, for gases of relatively low solubility (He, H_2, Ar, N_2), the surface tension changes within only a 10 % for a pressure change between 0.1 and 6 MPa. However, the surface tension decreases by about 50 % in the same pressure range for highly soluble gases like carbon dioxide.

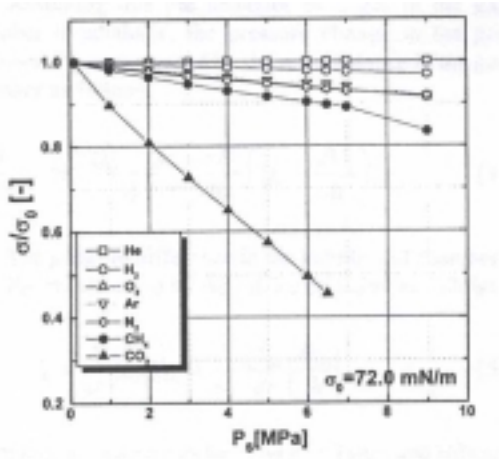

Figure 2-6. Effect of pressure on surface tension for gas-water systems (Massoudi and King, 1974).

It is well understood that with an increase in surface tension, bubble size increases, hence, gas holdup decreases. This was shown in the study conducted by Idogawa *et al.* (1987[a]) who concluded that gas holdup decreases with an increase in liquid surface tension at atmospheric pressure, and becomes independent of liquid surface tension at a higher pressure of 5 MPa. Several other researchers also studied the effect of surfactants and alcohol on gas holdup (Zahradnik *et al.*, 1987; Jamialahmadi and Müller-Steinhagen, 1992; Camarasa *et al.*, 1999). Additions of small quantities of aliphatic alcohol, electrolyte, surface-active impurities to pure liquids introduce a non-coalescing characteristic to the liquid mixture. This reduces the bubble size and consequently the bubble rise velocity due to a decrease in surface tension of the pure liquid (Camarasa *et al.*, 1999). Hence, gas holdup for air-aliphatic alcohol systems is higher than for an air-pure liquid system (Zahradnik *et al.*, 1987; Jamialahmadi and Müller-Steinhagen, 1992; Camarasa *et al.*, 1999). The studies of Zahradnik *et al.* (1987) as well as Jamialahmadi and Müller-Steinhagen (1992) were not limited to the bubbly

flow conditions (U_g as high as 20 cm/s was employed) and a noticeable effect of liquid surface tension on gas holdup was reported. This implies that even possibly in the churn-turbulent regime of operation, surface tension effects are significant and should be considered in any design or scale-up strategy.

2.2. Bubble Size Distribution

Bubble size seems to affect gas holdup in bubble columns at a given operating condition. Equation (2-15) shows the relationship between gas holdup and bubble size based on the assumption that all bubbles are spherical and uniform in size ($\Phi = 1$):

$$\varepsilon_g = \frac{V_g}{V_T} = \frac{\pi/6\, d_b^3 N \Phi}{V_T} = \frac{\pi}{6} d_b^3 n_v \Phi \qquad (2\text{-}15)$$

where Φ is the shape factor; and n_v is the number of bubbles per unit volume. Thus, Equation (2-15) relates gas holdup and bubble size and could provide an explanation for higher gas holdup at elevated pressure conditions. As was mentioned earlier (Equation (2-14)), bubble size decreases with increasing pressure. Hence, from Equation (2-15), gas holdup should theoretically decrease with increasing pressure if n_v is constant. However, gas holdup is known to increase with pressure due to a narrower bubble size distribution and an increase in the fraction of bubbles per unit volume (n_v) observed at elevated pressures. Idogawa *et al.* (1987[b]) attributed this increase in the frequency of bubbling due to an increase in gas momentum resulting from higher operating pressures. Therefore, with increasing pressure, the increase in n_v offsets the decrease in d_b and overall, one observes an increase in gas holdup. This could be seen from the study conducted by Lin *et al.* (1998) as illustrated in Figure 2-7, which shows that large bubbles disappear progressively with increasing pressure at both superficial gas velocities. In addition, the fraction of large bubbles is smaller at a superficial gas velocity of 2 cm/s as compared to that obtained at a superficial gas velocity of 8 cm/s, especially for the lower pressures

(Lin *et al.*, 1998). In the same study, it was reported that at low superficial gas velocities (bubbly flow), small and uniform-sized bubbles are found, whereas coalescence and breakup of bubbles are frequently observed as the gas superficial velocity is increased beyond a critical value (churn-turbulent flow). In addition, the bubble size distribution is broader in the churn-turbulent flow compared to that in the bubbly flow. Thus, it is important to know the bubble size distribution since bubble size is influenced by pressure and superficial gas velocity and ultimately controls the gas holdup and its distribution in a bubble column operation.

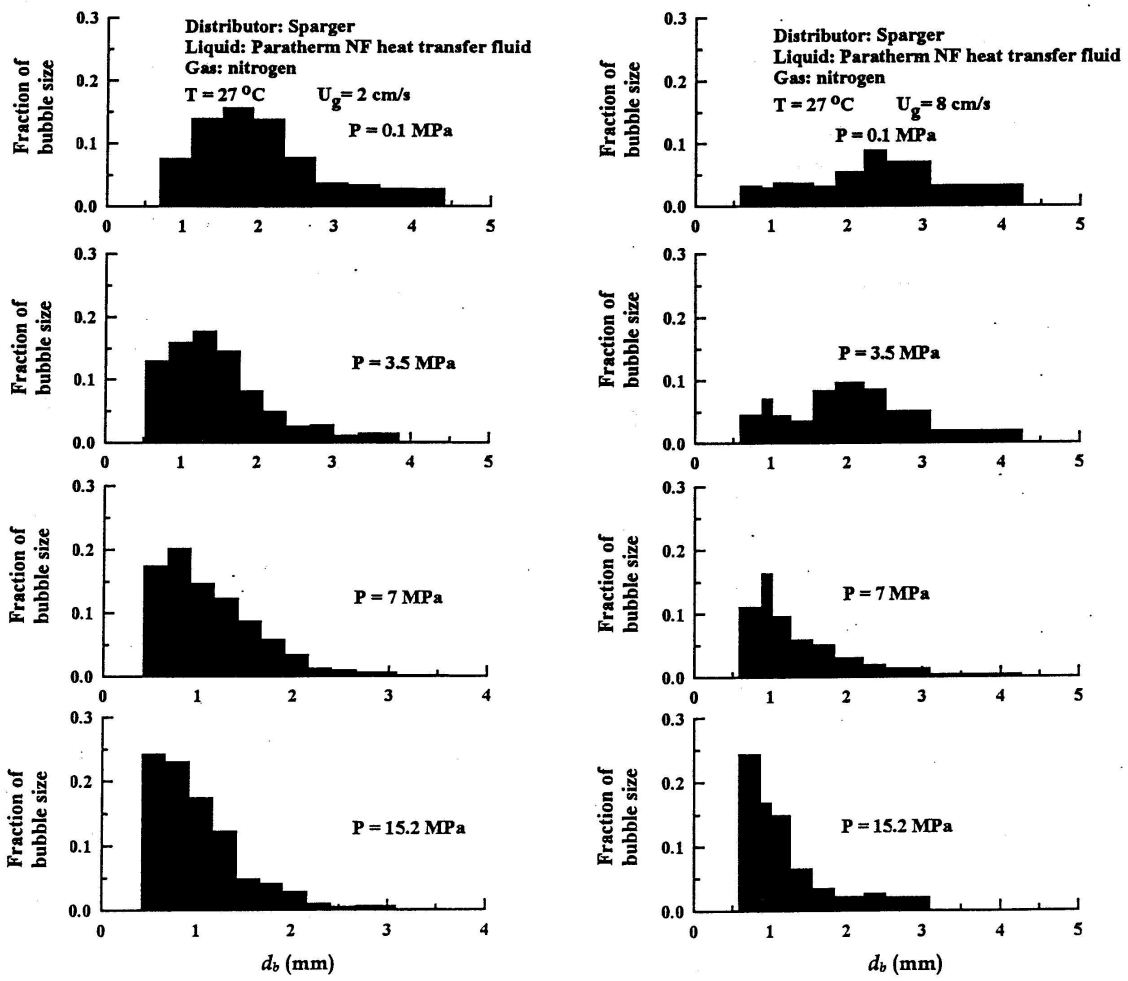

(a) (b)

Figure 2-7. Bubble size distributions obtained at a superficial gas velocity of (a) 2 cm/s; (b) 8 cm/s (Lin *et al.*, 1998).

The measurement of bubble sizes and rise velocities in two and three-phase systems has always been a challenging problem (Koide *et al*., 1979; Cartellier, 1990; Cartellier, 1992; Yao *et al*., 1991; Jiang *et al*., 1995; Luo *et al*., 1999; Camarasa *et al*., 1999). The problem is even much more complex when the system being considered is no longer in the bubbly flow regime, but rather in the churn-turbulent flow regime (which is the focus of this work). It has been reported in the literature that in this regime of flow (Vermeer and Krishna, 1981; deSwart, 1996), there exists a bi-modal bubble size distribution. There has been considerable debate as to whether the bubble size distribution is really bi-modal, or it is just that the distribution gets much broader as one goes from the bubbly to the churn-turbulent flow regime. The appeal of non-invasive techniques has led to attempts to capture the size distribution using photographic techniques (refer to Table 2-1). These have been restricted to very limited number of applications, specifically in 2-D transparent columns, where light can penetrate to provide a reasonable field-of-view. In real 3-D columns, these techniques provide little hope of capturing anything beyond the reactor wall. Also, these methods could not be used in a real system, where the column is operated under high temperature and pressure conditions, and could not be made of a transparent material. Thus, invasive techniques are still the state of the art when it comes to bubble size and rise velocity measurements. Although very high speed tomography (such as ECT - Electrical Capacitance Tomography, e.g., Dicken *et al*., 1993; O'Hern *et al*., 1995) is being tried for capturing the local holdup structure, the spatial resolution achieved by any such technique is still far from providing a reasonable bubble size distribution measurement. In addition, as the bubbles are three dimensional, one has to resort to a cone-beam type of configuration to capture the 3-D bubble structure. The tomographic techniques have been successfully used and well proven to work for medical imaging. But there the specimen (a human being) imaged is stationary for all practical purposes. When it comes to imaging industrial flows, the systems being imaged are in highly turbulent motion, and one cannot expect to get anything better than a time-averaged result. Also, the costs of setting up a tomographic facility are high. Of the several techniques reported in the literature (conductivity probes, optical probes, electrical resistivity probes, intrusive cameras,

UDT-Ultra-sound Doppler Technique), the various microprobes are of the greatest appeal as they seem to be the least offenders in altering the local flow field which would exist in the absence of the probe.

Of the microprobes, the optical fiber probe utilizes the difference in optical reflectivity of the gas and liquid phases while the conductivity probe makes use of the difference in their electrical conductivities to produce a sequence of voltage pulses when a bubble approaches the probe sensor assembly. Optical fiber probe of different designs have been used to measure the local fluid dynamic parameters such as the gas holdup, the bubble chord length, the bubble rise velocity and the bubble frequency in multiphase systems (Frijlink, 1987; Mudde *et al*., 1992; Chabot *et al*., 1992; Groen *et al*., 1996; Luo *et al*., 1999). The conductivity probe is extremely useful for studying liquid-liquid dispersions where the conductivity difference may be significant, whereas the refractive indices of the two liquids may be the same. Nevertheless, successful applications of the conductivity probe for gas-liquid systems have been reported in the literature (Steinemann and Buchholz, 1984; Luo, 1993). From the literature review above regarding various techniques of measuring bubble sizes and rise velocity, it is evident that the applicability of most of these techniques is limited to the bubbly flow regime with low gas volume fraction. Unfortunately, the reliability of the data acquired and its subsequent processing to estimate bubble properties in churn-turbulent flow is poor.

Table 2-6a lists some of the correlations for predicting the mean bubble size in a bubble column operation while Table 2-6b shows correlations for predicting the maximum stable bubble size. As can be seen from Table 2-6a, only the correlations of Kumar *et al.* (1976), Wilkinson (1991), Ellenberger and Krishna (1994) and Krishna (2000) capture the trend of decrease in bubble size with increase in pressure. For the effect of superficial gas velocity on bubble size, other than the correlations of Gaddis and Vogelpohl (1986), Ellenberger and Krishna (1994) and Krishna (2000), all other correlations indicate that the mean bubble size decreases with U_g. In Table 2-6b, all the correlations predict a decrease in maximum stable bubble size with increasing U_g, while only the correlation of Lin *et al.* (1998) captures the effect of pressure on the reduction of the maximum stable bubble size.

Table 2-6a. Bubble size correlations.

References	Correlations	Units
Lee and Meyrick (1970)	$d_b = \frac{4.15\sigma^{0.6}}{(\rho_l g U_g)^{0.4}\rho_l^{0.2}}\varepsilon_g^{0.5} + 9\times10^{-4}$	m
Akita and Yoshida (1973)	$\frac{d_b}{D_c} = 26\left(\frac{D_c^2 g\rho_l}{\sigma}\right)^{-0.5}\left(\frac{gD_c^3}{\nu_l^2}\right)^{-0.12}\left(\frac{U_g}{\sqrt{gD_c}}\right)^{-0.12}$	m
Kumar *et al.* (1976)	$d_b = \begin{cases} 1.56\,Re_o^{0.058}\left(\frac{d_o^2\sigma}{(\rho_l-\rho_g)g}\right)^{0.25} & for\ \ 0 < Re_o < 10 \\ 0.32\,Re_o^{0.425}\left(\frac{d_o^2\sigma}{(\rho_l-\rho_g)g}\right)^{0.25} & for\ \ 10 < Re_o < 2100 \\ 100\,Re_o^{-0.4}\left(\frac{d_o^2\sigma}{(\rho_l-\rho_g)g}\right)^{0.25} & for\ \ 4000 < Re_o < 70000 \end{cases}$	cm
Gaddis and Vogelpohl (1986)	$d_b = \left[\left(\frac{6d_o\sigma}{\rho_l g}\right)^{4/3} + \left(\frac{81\upsilon_l Q_g}{\pi g}\right) + \left(\frac{135Q_g^2}{4\pi^2 g}\right)^{4/3}\right]^{1/4}$	cm
Wilkinson (1991)	$d_B = 3g^{-0.44}\sigma^{0.34}\mu_l^{0.22}\rho_l^{-0.45}\rho_g^{-0.11}U_g^{-0.02}$	m
Ellenberger and Krishna (1994)	$d_b = \alpha_1(U_g - U_{g,trans})^{2/5}(h^* + h_o)^{4/5}g^{-1/5}$ where for air-water system, $\alpha_1 = 1$; $h^* = 0.018 + 1.05\,(U_g - U_{g,trans})$; $U_{g,trans} = 2.25\varepsilon_{trans}\left(\frac{\sigma}{\mu_l}\right)\left(\frac{\sigma^3\rho_l}{g\mu_l^4}\right)^{-0.273}\left(\frac{\rho_l}{\rho_g}\right)^{0.03}$; $\varepsilon_{trans} = exp\left(-193\rho_g^{-0.61}\mu_l^{0.5}\sigma^{0.11}\right)$; $h_0 = 4\sqrt{A_o}$; A_o is the area of distributor plate per orifice	m
Krishna (2000)	$d_{b,large} = 0.069(U - U_{trans})^{0.376}$ where U_{trans} is obtained from Reilly *et al.* (1994): $U_{trans} = V_{b,small}^0\varepsilon_{trans}(1-\varepsilon_{trans})$; $\varepsilon_{trans} = 4.46\sqrt{\frac{\rho_g^{0.96}}{\rho_l}\sigma^{0.12}}$; $V_{b,small}^0 = \frac{1}{2.84}\frac{1}{\rho_g^{0.04}}\sigma^{0.12}$	m

Table 2-6b. Maximum stable bubble size correlations.

References	Correlations	Units
Hinze as reported in Wallis (1969)	$d_b = 0.725\left(\frac{\sigma}{\rho_l}\right)^{3/5}\left(\frac{P}{M}\right)^{-2/5}$ where $\frac{P}{M} = gU_g$ represents the mechanical power dissipated per unit mass	cm
Walter and Blanch (1986)	$d_b = 1.12\frac{\sigma^{0.6}}{\rho_l^{0.2}(P/V)^{0.4}}\left(\frac{\mu_l}{3\mu_g}\right)^{0.1}$ where $P/V = \rho_l g U_g$ (W/m^3), all other variables in CGS units	cm
Lin *et al.* (1998)	$d_b = We_c^{0.6}\frac{\sigma^{0.6}}{\rho_g^{0.2}(P/V)^{0.4}}\left(\frac{\mu_l}{\mu_g}\right)^{0.1}$ where We_c = 0.7 for 78°C and 1.36 for 27°C, respectively for N_2-Paratherm NF system	m

Table 2-7 shows several correlations that are used to predict the single bubble rise velocity. Lin *et al.* (1998) compared their single bubble rise velocity measurements with those predicted in Table 2-7. They concluded that there is limited agreement between the measured and calculated results when using the correlation developed by Mendelson (1967) since their correlation is only valid under inviscid conditions. However, the remaining correlations demonstrate good overall predictive capability. In the table, d_e is the diameter of the sphere having the same volume as the bubble; *Mo* is the Morton number $\left(g\Delta\rho\mu_l^4/\rho_l^2\sigma^3\right)$; *Re* is the Reynolds number $\left(d_e U_b \rho_l/\mu_l\right)$; and *Eo* is the Eotvos number $\left(g\Delta\rho d_e^2/\sigma\right)$.

Table 2-7. Single bubble rise velocity correlations.

References	Single Bubble Rise Velocity
Mendelson (1967)	$U_b = \left[\frac{2c\sigma}{\rho_l d_e} + \left(\frac{\Delta\rho}{\rho_l}\right)\frac{g d_e}{2}\right]^{1/2}$
Fan and Tsuchiya (1990)	$U_b^{'} = U_b\left(\frac{\rho_l}{\sigma g}\right)^{1/4}$ $= \left\{\left[\frac{Mo^{-1/4}}{K_b}\left(\frac{\Delta\rho}{\rho_l}\right)^{5/4} d_e^{'2}\right]^{-n} + \left[\frac{2c}{d_e^{'}} + \left(\frac{\Delta\rho}{\rho_l}\right)\frac{d_e^{'}}{2}\right]^{-n/2}\right\}^{-1/n}$ where $d_e' = d_e\,(\rho_l g/\sigma)^{1/2}$; $n = \begin{cases} 0.8 & \text{for contaminated liquids} \\ 1.6 & \text{for purified liquids} \end{cases}$; $c = \begin{cases} 1.2 & \text{for monocomponent liquids} \\ 1.4 & \text{for multicomponent liquids} \end{cases}$; $K_b = max(K_{bo}\, Mo^{-0.038}, 12)$ $K_{b0} = \begin{cases} 14.7 & \text{for aqueous solutions} \\ 10.2 & \text{for organic solvents / mixtures} \end{cases}$
Jamialahmadi *et al.* (1994)	$U_b = \frac{U_b^{sp} U_b^{w}}{\sqrt{\left(U_b^{sp}\right)^2 + \left(U_b^{w}\right)^2}}$ where $U_b^{w} = \sqrt{\frac{2\sigma}{d_b\left(\rho_l + \rho_g\right)} + \frac{g d_b}{2}}$; $U_b^{sp} = \frac{\left(\rho_l - \rho_g\right)}{18\mu_l} g d_b^2 \left(\frac{3\mu_l + 3\mu_g}{2\mu_l + 3\mu_g}\right)$
Ellenberger and Krishna (1994)	$U_b = \phi\sqrt{g d_b}$ where for air-water system, $\phi = 1.95 D_c^{1/6}$
Tomiyama *et al.* (1995)	$C_D = \frac{4 g \Delta\rho d_e}{3\rho_l U_b^2}$ where for purified systems: $C_D = max\left\{min\left[\frac{16}{Re}\left(1 + 0.15\,Re^{0.687}\right), \frac{48}{Re}\right], \frac{8}{3}\frac{Eo}{Eo+4}\right\}$ Partially contaminated systems: $C_D = max\left\{min\left[\frac{24}{Re}\left(1 + 0.15\,Re^{0.687}\right), \frac{72}{Re}\right], \frac{8}{3}\frac{Eo}{Eo+4}\right\}$ Sufficiently contaminated systems: $C_D = max\left[\frac{24}{Re}\left(1 + 0.15\,Re^{0.687}\right), \frac{8}{3}\frac{Eo}{Eo+4}\right]$

2.3. Liquid Recirculation Velocity

As mentioned earlier in this chapter, gas holdup and its radial distribution are among the main factors that govern the levels of turbulent liquid circulation in a bubble column. Table 2-8 displays the various techniques, along with their limitations, that are used to quantify the liquid hydrodynamics in bubble column. Additional details of the measurement techniques are described elsewhere (Degaleesan, 1997) and are not discussed here. As shown in Table 2-8, most of the techniques fail to quantify liquid hydrodynamics at high superficial gas velocity, where bubbles of various sizes exist along with a high volume fraction of the dispersed phase. Optical methods like Laser Doppler Velocimetry and Particle Tracking Velocimetry face the problems of limited applicability in churn-turbulent flows due to the reflection and dispersion at phase boundaries. Other techniques, like hot film velocimetry and electrodiffusion methods, have the capability for measurements in churn-turbulent flow. However, these methods are usually intrusive and could alter the very flow structure of liquid that they are supposed to measure. Computer Automated Radioactive Particle Tracking (CARPT) technique is a non-intrusive method that can capture the liquid flow field in both heterogeneous regime and at high-pressure conditions (Devanathan *et al.*, 1990; Larachi *et al.*, 1994; Degaleesan, 1997; Chen *et al.*, 1999; Gupta, 2002).

Numerous measurements of liquid phase dynamics confirm that a recirculation cell with liquid flowing up in the center and down at the wall (Hills, 1974; Menzel *et al.* 1990; Yao *et al*., 1991; Mudde *et al.*, 1997[a,b]; Degaleesan, 1997; Vial *et al*., 2001[a]; Lee *et al.*, 2001) exists in the fully developed flow section of the column. Hills (1974) measured liquid velocities using a modified Pitot tube in a bubble column with internal diameter of 0.14 m and a height of 1.37 m using three different sieve plate distributors (A: 32 orifices of 0.4 mm; B: 61 orifices of 0.4 mm; C: 7 orifices of 1.6 mm) at superficial gas velocities varying from 1.9 to 16.9 cm/s. It was found that the liquid flow exhibits a gulf stream pattern, where liquid flows upwards at the center and downwards near the column wall. He also found that at the high superficial gas velocity of 16.9 cm/s, distributors B and C generate almost similar liquid velocity profiles.

Table 2-8. Various measurement techniques used to understand liquid hydrodynamics.

References	Measurement Techniques	Measurement Parameters	Limitations/Challengers
Hills (1974)	Modified Pitot Tube (Pavlov tube)	Volume averaged liquid velocity profile	Assume pseudo- homogeneous flow of gas and liquid, questionable in churn-turbulent flow Difficulty in measuring two phase differential pressure
Nottenkamper *et al.* (1983)	Flywheel anemometry	Volume averaged liquid velocity profile	Questionable at high superficial gas velocities due to large gas holdup and at high pressure due to increased gas density
Delhaye (1969); Serizawa *et al.* (1975); Herringe and Davis (1974); Yao *et al.* (1991)	Hot film anemometry	Averaged liquid velocity Turbulent normal stresses	Difficulties arise in churn-turbulent flows due to incomplete piercing or sliding of bubbles on the probe
Menzel *et al.* (1989), Menzel *et al.* (1990)	Hot film anemometry with triple split probes	Reynolds shear stress	Same as above
Pannek *et al.* (1994)	Electrodiffusion method	Local and axial liquid velocities	Intrusive technique
Reese and Fan (1994)	Particle Image Velocimetry	Full field flow information of both gas and liquid phase	Restricted to bubbly flow since it is an optically based technique
Devanathan (1991); Degaleesan (1997); Chen *et al.* (1999)	Computer Automated Radioactive Particle Tracking (CARPT)	Time-averaged liquid velocities, turbulent stresses and kinetic energy	Instantaneous spatial distribution of velocity cannot be captured
Gross and Kuhlman (1990); Deshpande and Joshi (1997); Kulkarni *et al.* (2001[d])	Laser Doppler Velocimetry (LDV)	Gas and liquid velocities along with gas holdup	Difficulty in distinguishing signals caused by dispersed phase from those caused by continuous phase
Mudde *et al.* (1997[a]); Mudde *et al.* (1998); Zhang *et al.* (1999); Vial *et al.* (2001[a])	Laser Doppler Anemometry (LDA)	Local time averaged holdups Local phasic averaged liquid velocities	Restricted to bubbly flow due to scattering caused by bubbles in the flow Limitation to outer region of the bubble column
Broder and Sommerfeld (1998)	Phase Doppler Anemometer	Bubble size and velocities, continuous phase velocities	Restricted to bubbly flow
Seeger *et al.* (2001)	X-ray based Particle Tracking Velocimetry	Three dimensional velocity of the liquid phase	Low image frequency Large particles used

Menzel *et al.* (1990) made use of hot film anemometry with triple split probes to measure Reynolds shear stress in bubble columns of different diameters and heights (A: D = 0.15 m; H = 2.575 m; B: D = 0.6 m, H = 3.455 m; C: D = 0.6 m, H = 5.44 m) at superficial gas velocity up to 9.6 cm/s as shown in Figure 2-8.

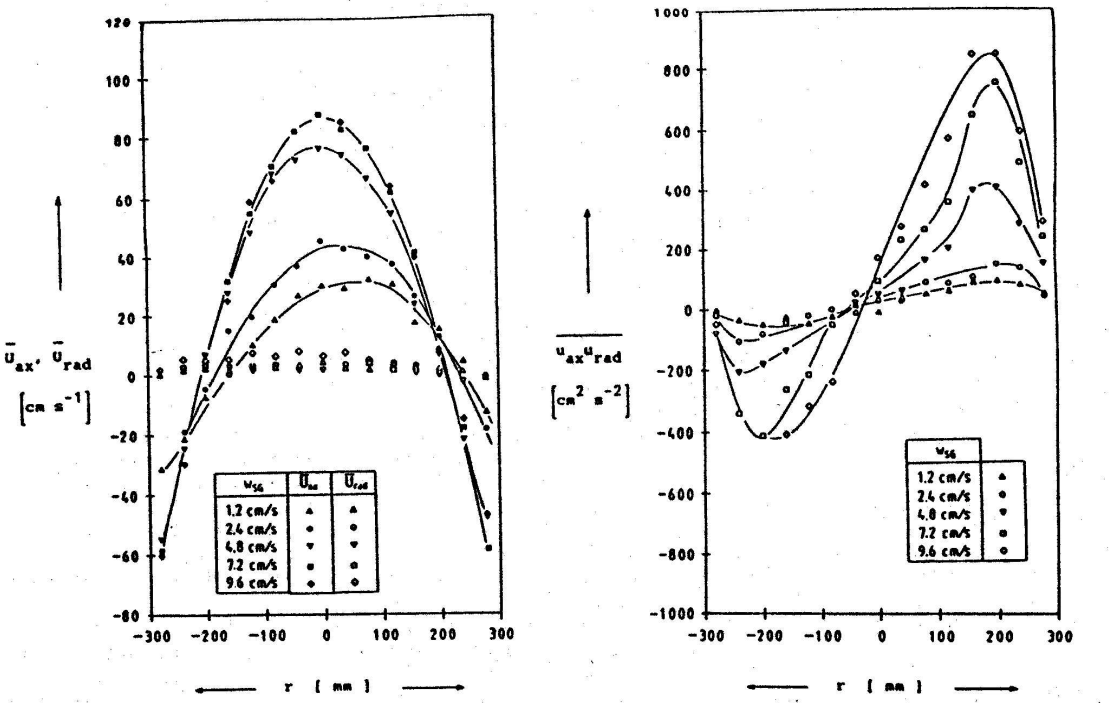

Figure 2-8. Radial profiles of $\overline{u_{ax}}$, $\overline{u_{rad}}$, $\overline{u_{ax}u_{rad}}$ obtained in a bubble column of diameter 0.6 m in air-water system (Menzel *et al.*, 1990).

In the above study, air was used as the gas phase and liquids of varying molecular viscosity (water and glycerol/water) and coalescence behavior (water; 0.22 wt % propanol/water) were used. It was found that other than in homogeneous regime, the liquid velocity profiles become flatter with increasing liquid molecular viscosity and also when using noncoalescing liquid. It is rather interesting to note from Figure 2-8 that in spite of a reasonably well pronounced symmetry in the reported profiles of the mean liquid velocity components along the central chord, the same cannot be said of the profile of the mean cross-correlation between the axial and radial components of the liquid

velocity. One possible explanation for this observation is the length of the probe that would have to extend into the column to measure velocity at a desired location along the central chord. The farther the probe extends into the column, greater would be the vibrations that it will pick up due to the flow structure and greater would be the artifacts in the measured velocity components.

Reese and Fan (1994) determined the entrance length required for the flow to become fully developed using particle image velocimetry (PIV) in a bubble column with inside diameter of 0.102 m and a height of 2.2 m in a range of superficial gas velocities varying from 0.1 to 5.2 cm/s. Air and water were used as gas and liquid phases, respectively. Two different distributors were used for this investigation: porous plate (mean pore diameter of 1 mm) and perforated plate (14 tubes of 1 cm diameter). Using PIV, they demonstrated that the liquid flow behavior in the entrance region is more turbulent than the flow occurring in the fully developed region. They also concluded that the flow phenomenon in the entrance region is independent of the distributor if the gas inlet to the column is uniform and the inlet bubble sizes are similar. Figure 2-9 displays the effect of gas velocity on entrance length and indicates that the entrance length decreases with increasing gas velocity. As gas velocity increases, the flow structure develops more rapidly and the entrance and bulk regions exhibit similar phenomena. Also, the entrance length becomes very small when the gas velocity exceeds 3.0 cm/s. No physical model was used to explain the experimental observations and therefore it is not clear whether similar conclusions would be reached at elevated pressure conditions.

Mudde *et al.* (1997[a]) made use of laser Doppler anemometry to measure liquid velocity and Reynolds stresses in bubble columns 0.152, 0.234 and 0.384 m in diameter at superficial gas velocities ranging up to 6.7 cm/s. The system was air-tap water and the distributor used for this study was a sintered polyethylene porous plate (mean pore diameter of 40 μm, porosity 40%). They found that the averaged liquid flow is symmetric and that there is no net liquid flow through a horizontal cross section of the column. They also concluded that turbulence in bubble column is anisotropic based on the fact that the axial normal stress is higher than the tangential stress. In addition, the axial normal stress shows a minimum at a dimensionless radial position of 0.8 and this

minimum becomes more pronounced with increasing gas fraction. The axial-tangential Reynolds shear stress is essentially zero.

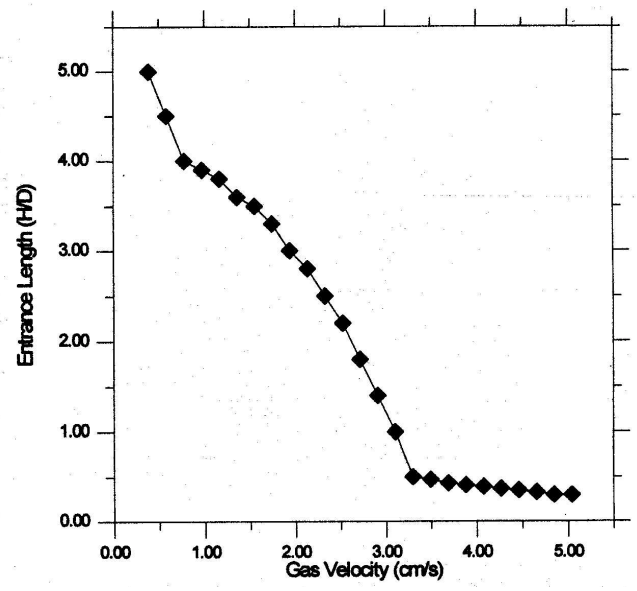

Figure 2-9. Effect of gas velocity on entrance length (Reese and Fan, 1994).

Vial *et al.* (2001[a]) studied the effect of distributors on liquid velocity using laser Doppler anemometry in a bubble column with inside diameter of 0.1 m and a height of 2-m for superficial gas velocity up to 15 cm/s for air-water system. They also estimated the Reynolds shear stress using a simple model based on bubble-induced turbulence. The distributors used in this study are a single orifice nozzle (5 mm in diameter), a multiple-orifice nozzle (50 orifices of 1 mm) and a porous glass plate (mean pore diameter of 15 μm). It was reported in their earlier study (Vial *et al.*, 2000) that the single orifice nozzle always operates in the heterogeneous regime in the range of superficial gas velocities investigated. Multiple-orifice nozzle exhibits heterogeneous regime when U_g is greater than 11-12 cm/s and the transition for porous plate is strongly dependent on the start-up procedure. They reached similar conclusions as previous investigators that liquid flows upwards in the center and downwards near the wall of the column for all operating conditions and for all different distributors. The liquid velocity profiles measured for a

single gas nozzle were flatter and had lower axial mean velocity values as compared to the other two distributors.

Several researchers also analyzed the time series velocity data using chaos and multiresolution analysis in order to understand further the hydrodynamics of the bubble column (Kulkani *et al*., 2001[a,b]; Cassanello *et al.*, 2001). Kulkani *et al*. (2001[b]) developed a new strategy using wavelet transforms for multiresolution analysis of bubble column hydrodynamics from laser Doppler anemometer measurements of the axial velocity to detect singularities with respect to bubble passage in the column. They estimated fractional gas holdup based on the criteria employed for Local Intermittency Measure (LIM) thresholding and concluded that it may be possible to infer properties about the local hydrodynamics using a simple LDA assembly with single axial velocity rather than 2-D velocity measurements.

As shown in this section, most of the study on liquid recirculation that have been conducted so far were performed at atmospheric pressure conditions at a maximum gas velocity of 16.9 cm/s. Lee *et al.* (2001) investigated the effect of pressure on liquid hydrodynamics using both nitrogen-water and nitrogen-Paratherm NF heat transfer fluid in bubble columns of diameter 5.1 and 10.2 cm using Laser Doppler Velocimetry (LDV). The pressures investigated range from 0.1 to 7 MPa. They found that both the liquid velocities and the turbulent stresses decrease with increasing pressure. This is caused by a decrease in the fluctuations of the liquid phase caused by bubbles because of a narrower bubble size distribution with a smaller mean bubble size at elevated pressure. However in their study, the maximum superficial gas velocity investigated was 5 cm/s, which is usually considered to be in bubbly regime especially at elevated pressure. Hence, little is known about the hydrodynamics at high pressure and deep in churn-turbulent flow conditions.

2.3.1. One-Dimensional Time-Averaged Liquid Velocity Model

Generally, there are three types of models that are used to describe the gas and liquid flow in bubble column reactors. The first type of model is based on ideal flow

pattern assumption. A typical example is the one where the gas and liquid phases are treated as plug and mixed flow, respectively. This type of model does not account for the hydrodynamics of bubble column reactors, and it usually results in the over-design of the reactor. At the other extreme (third type) is the model that is based on solution of properly averaged Navier Stokes equations (Computational Fluid Dynamics). However, in this kind of formulation, since direct numerical simulation of large columns is not possible, closure schemes are needed in the framework of the multi-fluid model which need to be verified and the solution of the model requires extensive computational effort. Lying between these two extremes is phenomenological modeling (second type). This type of model is based on the experimentally observed flow pattern and rationalized based on physical arguments. Hence, it reflects the bubble column phenomena as compared to the first type of model although a database for evaluation of several parameters is needed.

There exist numerous models in the literature -- mechanistic and CFD that are used to model the bubble column hydrodynamics. All these models need closures for eddy viscosity/mixing length, drag coefficient, virtual mass coefficient, etc. While it is a task of the fluid dynamic model to predict liquid velocities and their variation, for design and scale-up it is of interest to predict the liquid recirculation profile based on simple hydrodynamic models. One of the frequently used models, a simplified one-dimensional two-fluid model, has been widely used by various researchers (Miyauchi and Shyu, 1970; Ueyama and Miyauchi, 1979; Kojima *et al*., 1980; Riquarts, 1981; Sekizawa *et al*., 1983; Clark *et al*., 1987; Kawase and Moo-Young, 1989; Devanathan, 1991; Kawase and Tokunaga, 1991; Geary and Rice, 1992; Kumar *et al*., 1994; Kumar, 1994; Liu *et al*., 1998; Gupta *et al.*, 2001[a,b]; Gupta, 2002) to obtain the liquid recirculation velocity profile. The differences among the models arise from the different types of constitutive equations that are used for closing the liquid phase turbulence which can either be accomplished via eddy viscosity (refer to Table 2-9) or Prandtl's mixing length (refer to Table 2-10). For a discussion on the derivation of the basic governing equations of the simplified one-dimensional model, the reader is referred to Appendix A. To assess the effect of model input parameters on the predicted turbulent shear stress and liquid

recirculation, one can referred to Equations (A-20) to (A-23), (A-28) and (A-29) in Appendix A. Even though it may not be obvious at first sight, the following can be deduced from these above equations:

- Both the turbulent shear stress as well as the magnitude of liquid recirculation increases with an increase in the cross-sectional average gas holdup.
- In addition, for a given gas holdup profile, liquid recirculation will also increase with decreasing turbulent eddy viscosity.

Since it is known that gas holdup increases with an increase in operating pressure, it is clear that the turbulent shear stress will increase with pressure. Whether the magnitude of the liquid recirculation also increases with pressure will depend on the magnitude of the turbulent eddy viscosity. It is the intent of the CARPT experiments conducted as part of this doctoral work to explore the effect of pressure on liquid recirculation.

Table 2-9. Existing eddy / kinematic viscosity closures

Researchers	Eddy kinematic viscosity	Units
Miyauchi and Shyu, 1970	$\mu_t = 0.05D^{1.8}$	g/cm.s
Kojima *et al*., 1980	$\mu_t = 0.053D^{1.77}$	g/cm.s
Miyauchi *et al*., 1981	$\nu_t = 0.160D^{1.5}U_g^{1/6}$	cm^2/s
Riquarts, 1981	$Re_t = 90.9\,Re_l^{-1/8}\,Fr^{3/8}$ or $\nu_t = 0.011D^{1.5}U_g^{3/8}\nu_l^{-1/8}g^{3/8}$	cm^2/s
Sekizawa *et al*., 1983	$\nu_t = 0.265D^{1.5}$	cm^2/s
Kawase & Moo-Young, 1989	$Re_t = 33.9Fr^{1/3}$ or $\nu_t = 0.0295D^{4/3}U_g^{1/3}g^{1/3}$	m^2/s
Devanathan, 1991	$\nu_t = \begin{cases} 0.85U_g & U_g \le 6\ cm/s \\ 8.42 / (1-0.05U_g) & U_g \ge 6\ cm/s \end{cases}$	cm^2/s

Table 2-10. Existing mixing length closures

Researchers	Mixing length	Units
Nikuradse (Boussinesq, 1896)	$l(\xi) = R(0.14 - 0.08\,\xi^2 - 0.06\,\xi^4)$	cm
Joshi (1980)	$\bar{l} = 0.08D$	cm
Kawase and Tokunaga, 1991	$\bar{l} = 0.2589U_g^{-0.38}D$	cm
Geary and Rice, 1992	$l = \max(l_B, l^*) \qquad 0 \le \xi \le \lambda$ $l^* = R(0.14 - 0.08\,\xi^2 - 0.06\,\xi^4)$ $l_b = \frac{d_b}{\alpha^{1/3}}\frac{\varepsilon_g(\xi)}{\bar{\varepsilon}}$	cm
Kumar (1994)	$l(\xi) = \frac{a(1-\xi)}{(\xi+b)^c} + d(1-\xi)^e$ where a, b, c, d and e are defined based on U_g.	cm

	a	b	c	d	e
$0 < U_g \le 5.0$	10.42	1.94	0.57	-6.53	1.14
$5 < U_g \le 8.0$	6.29	1.22	2.17	-3.40	2.25
$8 < U_g$	7.85	1.20	3.08	-3.81	2.86

Some of the correlations in Tables 2-9 and 2-10 incorporate the physical properties of the liquid phase. For example, the correlations of Riquarts (1981) and Kawase & Moo-Young (1989) involve dimensionless groups such as *Re*, *Fr*, and *Mo* which are defined as

$$Re = \frac{U_{sg}\rho_l D_c}{\mu_l};\ Fr = \frac{U_{sg}^2}{gD_c};\ Mo = \frac{g\mu_l^4}{\rho_l\sigma_l^3}$$

The expressions for these dimensionless groups, once substituted in the correlations proposed by the above researchers, result in the expressions for eddy viscosity reported in Table 2-9. It is to be noted that most of these correlations have been developed based on experimental data acquired at atmospheric conditions and at superficial gas velocities of up to 20 cm/s. In the previous study by Kumar (1994), it was shown that none of the existing correlations fit well the data obtained by Hills (1974) and Yao *et al.* (1991) at superficial gas velocity up to 16.9 cm/s. The question then arises whether the existing correlations can be used for conditions involving high pressure and very high superficial

gas velocities. Hence, it is appropriate to review the basic assumptions incorporated in the various liquid recirculation models.

Miyauchi and Shyu (1970) assumed that there exists a laminar sublayer near the wall, and that the turbulent viscosity is constant over the entire cross section outside this sublayer. They also developed a correlation for this eddy viscosity. Ueyema and Miyauchi (1979), who solved the simplified one-dimensional model of the recirculation flow using similar assumptions as Miyauchi and Shyu (1970), applied the universal velocity profile (Schlichting, 1979) to obtain a simplified boundary condition near the wall of the column. In their model, they approximated the radial gas holdup profile using Equation (2-16).

$$\varepsilon_g(\xi) = \bar{\varepsilon}_g \left(\frac{m+2}{m} \right) \left(1 - \xi^m\right) \tag{2-16}$$

where $\bar{\varepsilon}_g$ is the cross-sectional average gas holdup; ξ is the dimensionless radial position, and *m* is the exponent. Ueyama and Miyauchi (1979) also developed an expression for eddy kinematic viscosity as a function of column diameter, mean gas holdup, gravitational acceleration, centerline velocity and the velocity at the wall. Using the necessary information, they calculated the eddy kinematic viscosity for different column diameters and found that it increases rapidly with increasing column diameter and is proportional to $D_c^{1.8}$ for small diameter columns. But, it appears to increase less strongly for larger column diameters.

Instead of solving the equations of motion to obtain the liquid recirculation velocity profile, Clark *et al*. (1987) made use of the force balance developed by Levy (1960) and the mixing length theory (Schlichting, 1979). In their model, they assumed the mixing length profile to be the one from Nikuradse's theory for single-phase pipe flow (Schlichting, 1979), which is represented by Equation (2-17).

$$l(\xi) = R\,[0.14 - 0.08\,\xi^2 - 0.06\,\xi^4] \tag{2-17}$$

In addition, the radial gas holdup was fitted by a radial power law equation

$$\varepsilon_g(\xi) = \varepsilon_c \left(1-\xi\right)^{1/p} \tag{2-18}$$

where ε_c is the void fraction at the column center and p is a value (typically 7) used to describe the power law curve. On the other hand, Anderson and Rice (1989) assumed three basic zones in the bubble column: core, buffer and clear laminar wall layer. The voidage distribution in this case is distributed into two zones with ε_g in the core and ε_g* in the buffer, such that ε_g* < ε_g. Near the wall layer, the voidage is assumed to be zero. Equation (2-19) represents the voidage distribution in these three zones.

$$\varepsilon_g(\xi) = \begin{cases} \varepsilon_g & for\ \ 0 \le \xi \le \delta \\ \varepsilon_g^* & for\ \ \delta \le \xi \le \lambda \\ 0 & for\ \ \lambda \le \xi \le 1 \end{cases} \tag{2-19}$$

where δ is the velocity inversion point of the axial liquid velocity. The Reynolds stresses for these three zones are treated differently and are shown in Equation (2-20). For the core layer, the Reynolds stress obtained from the simplified one-dimensional model was closed using von Karman's model while Prandtl's mixing length theory was chosen to represent the Reynolds stress in the buffer zone.

$$\tau_{l,rz} = \begin{cases} \rho_l \kappa^2 \left(-\dfrac{du_l}{d\xi}\right)^4 \Big/ \left(\dfrac{d^2u_l}{d\xi^2} - \dfrac{1}{\xi}\dfrac{du_l}{d\xi}\right)^2 & for\ 0 \le \xi \le \delta \\ \rho_l \left[\dfrac{\nu_m}{R}\left(-\dfrac{du_l}{d\xi}\right) + \dfrac{l^2(\xi)}{R^2}\left(-\dfrac{du_l}{d\xi}\right)^2\right] & for\ \delta \le \xi \le \lambda \\ \rho_l \dfrac{\nu_m}{R}\left(-\dfrac{du_l}{d\xi}\right) & for\ \lambda \le \xi \le 1 \end{cases} \tag{2-20}$$

where κ is the first von Karman parameter and is assumed to be approximately 0.4. In order to solve these equations, the macroscopic mass and energy balances together with gas flow rate and bulk voidage, ε' (refer to Equation (2-21)) are utilized.

$$\varepsilon' = \varepsilon\, \delta^2 + \varepsilon^* (\lambda^2 - \delta^2) \tag{2-21}$$

Kawase and Moo-Young (1989) developed a correlation for turbulent kinematic viscosity based on Prandtl's mixing length theory. To make use of this theory, they assumed a simple description for the liquid velocity profile shown below.

$$\frac{u}{u_0} = -2\left(\frac{r}{R}\right)^2 + 1 \tag{2-22}$$

where the centerline velocity, u_o (m/s) is obtained using Zehner's (1986) correlation as shown by Equation (2-23).

$$u_o = 0.737 g^{1/3} D_c^{1/3} U_g^{1/3} \tag{2-23}$$

where g is the gravitation acceleration (m/s^2); D_c is the column diameter (m); and U_g is the superficial gas velocity (m/s).

Rice and Geary (1990) indicated that there exists a thin down-flowing liquid layer (1-2 mm) near the wall, which is entirely bubble-free. Hence, they proposed two principal zones with voidage distributions as follows:

$$\varepsilon_g(\xi) = \begin{cases} \bar{\varepsilon}_g \dfrac{m+2}{m} \dfrac{1}{\lambda^2}\left[1 - \left(\dfrac{\xi}{\lambda}\right)^m\right] & for\ \xi \le \lambda \\ 0 & for\ \xi \ge \lambda \end{cases} \tag{2-24}$$

where λ is the position of the maximum down-flowing velocity. The closure of Reynolds stress in their work was accomplished using the Prandtl's mixing length model. The locally varying mixing length was taken to be proportional to bubble size and local gas holdup (refer to Equation (2-25)).

$$l_B(\xi) = \frac{d_b \varepsilon_g(\xi)}{\bar{\varepsilon}_g} \tag{2-25}$$

In the later work (Geary and Rice, 1992) the model was extended to include the turbulence originating at the wall. The mixing length used was as follows.

$$l = Max(l_B, l^*) \qquad 0 < \xi \leq \lambda \tag{2-26}$$

where l^* is obtained using Nikuradse's theory for single phase pipe flow and l_B is obtained using Equation (2-25). The authors made use of the local energy minimization approach to allow both the liquid circulation and eddy viscosity to be estimated.

Kawase and Tokunaga (1991) suggested that a single characteristic mixing length should be used, instead of its local value, since flow in a bubble column is highly chaotic and local properties in two-phase flows are difficult to measure. They developed a correlation for the characteristic mixing length as a function of column diameter and superficial gas velocity. Luo and Svendsen (1991) made use of the eddy viscosity expression derived by Reichardt (1951) for single-phase flow (which is given by Equation (2-27)).

$$\frac{\nu_t}{\nu_l} = kR^+\left(1+2\xi^2\right)\left(1-\xi^2\right) \tag{2-27}$$

where k represents the Reichardt's constant; and R^+ is the dimensionless radius $\left(\frac{R\left(\sqrt{|\tau_w|/\rho_l}\right)}{\nu_l}\right)$. They concluded that a Reichardt's constant of 0.07 could be used to evaluate the liquid velocity profiles in most bubble columns.

Using the data from Hills (1974), and Yao *et al.* (1991), Kumar *et al*. (1994) showed that none of the existing correlations for prescribing the turbulence parameters are of universal significance. They developed an empirical correlation for the mixing length profile based on the data collected from Hills (1974), Yu and Kim (1991), Yao *et al.* (1991), Nottenkaemper *et al.* (1983), and Menzel *et al.* (1990) (refer to Equation (2-28)). The first three studies were performed using air-water system, while Menzel *et al.* (1990) studied the effect of liquid viscosity on liquid turbulence. Except for Hills (1974), who conducted experiments in a batch system, the rest performed their experiments in the co-current flow mode of operation. However, the correlation proposed by Kumar *et al.* (1994) does not rest on any physically based model, and is given by

$$l(\xi) = \frac{a(1-\xi)}{(\xi+b)^c} + d(1-\xi)^e \tag{2-28}$$

and the values of the constants *a*, *b*, *c*, *d* and *e*, shown in Table 2-9, are empirically obtained by fitting the data.

In addition to the 1-D momentum balance, other attempts have been made to predict the average liquid recirculation velocity (Joshi and Shah, 1981) and the centerline velocity (Riquarts, 1981; Zehner, 1986) in bubble columns. The prediction of the average liquid recirculation velocity requires the information on the terminal rise velocity of a single bubble. On the other hand, Riquarts (1981) and Zehner (1986) developed correlations to predict the centerline velocity as shown in Equations (2-29) and (2-30), respectively. Wu and Al-Dahhan (2001) made use of the data available in the literature, as well as the existing CARPT database, to develop the correlation to predict the axial liquid velocity profile by Equation (2-33) based on the radial gas holdup profile of Equation (2-16).

Riquarts (1981):
$$u_{o,Riquarts} = 0.21(gD_c)^{1/2}\left(\frac{U_g^3\rho_l}{g\mu_l}\right)^{1/8} \tag{2-29}$$

Zehner (1986):
$$u_{o,Zehner} = 0.737 g^{1/3} D_c^{1/3} U_g^{1/3} \tag{2-30}$$

Wu and Al-Dahhan (2001):
$$\frac{u_L(\xi)}{u_{L0}} = 1 - 2.65m^{0.44}c\xi^{2.65m^{0.44}c} \tag{2-31}$$

where g is the gravitational acceleration (m/s^2); D_c is the column diameter (m); U_g is the superficial gas velocity (m/s); μ_l and ρ_l are the liquid viscosity and density, respectively; m and c are the radial gas holdup profile parameters predicted by Wu *et al.* (2001) represented as follows.

$$m = 2.188\times10^{3}\ Re_g^{-0.598}\ Fr_g^{0.146}\ Mo_L^{-0.004}$$
$$c = 4.32\times10^{-2}\ Re_g^{0.2492}$$

where $Re_g = D_c U_g(\rho_l - \rho_g)/\mu_l$; $Fr_g = U_g^2/gD_c$; $Mo_L = g\mu_l^4/(\rho_l - \rho_g)\sigma_l^3$.

The one-dimensional model is a very simplified representation of the long-time averaged liquid recirculation in bubble column reactors. As can be seen from the above review, the eddy viscosity approach has been widely used to close the liquid phase recirculation. While the use of these correlations is promising in predicting liquid recirculation at atmospheric conditions and at relatively low superficial gas velocity, their applicability has not been explored for bubble column operations at high superficial gas velocity and at high pressure. The primary reason for this situation is that to date, there is no experimental data available on liquid recirculation in bubble columns beyond a superficial gas velocity of 20 cm/s (refer to Table 2-1). Moreover, most of the measurements reported in the literature on liquid recirculation are limited to atmospheric pressure condition. Therefore, there have been no experimental data to test the validity of eddy viscosity correlations under conditions typically encountered in industrial-scale bubble columns, *viz.*, high pressure and high superficial gas velocity. It is one of the objectives of this study to remedy this situation by detailed measurements of phase distribution, liquid recirculation and liquid phase turbulence at high pressure and at high superficial gas velocity conditions.

Chapter 3. Experiments

In this chapter, a brief description of the experimental setup is provided. In addition, the techniques for measuring gas holdup (Computed Tomography) and liquid recirculation velocity (Computed Automated Radioactive Particle Tracking) are briefly described. Finally, the choice of operating conditions for CARPT experiments is outlined.

3.1. Experimental Setup

Figure 3-1 shows the schematic of the bubble column apparatus used in this study which has been designed to deliver high flow rate of air up to 5000 SCFH (142 SCM/hr) at a pressure of up to 150 psig. However, all the equipment used in this study could potentially support operation at a maximum pressure of 200 psig. The bubble column used for acquiring tomographic scans is a stainless steel tube with an inner diameter of 16.2-cm (6.4”) and a total column height of 250-cm (8.2-ft). As shown in Figure 3-1, a transparent glass window is situated at the top of the column and is named “blue eye”. This window allows viewing the system before starting the CT scan. Compressed air was used as the gas phase after appropriate filtering and the liquid was tap water. The experiments were conducted batchwise with respect to the liquid but with a continuous flow of gas at ambient temperature conditions. The gas flow rate was controlled using four rotameters to cover the entire range of desirable flow rates.

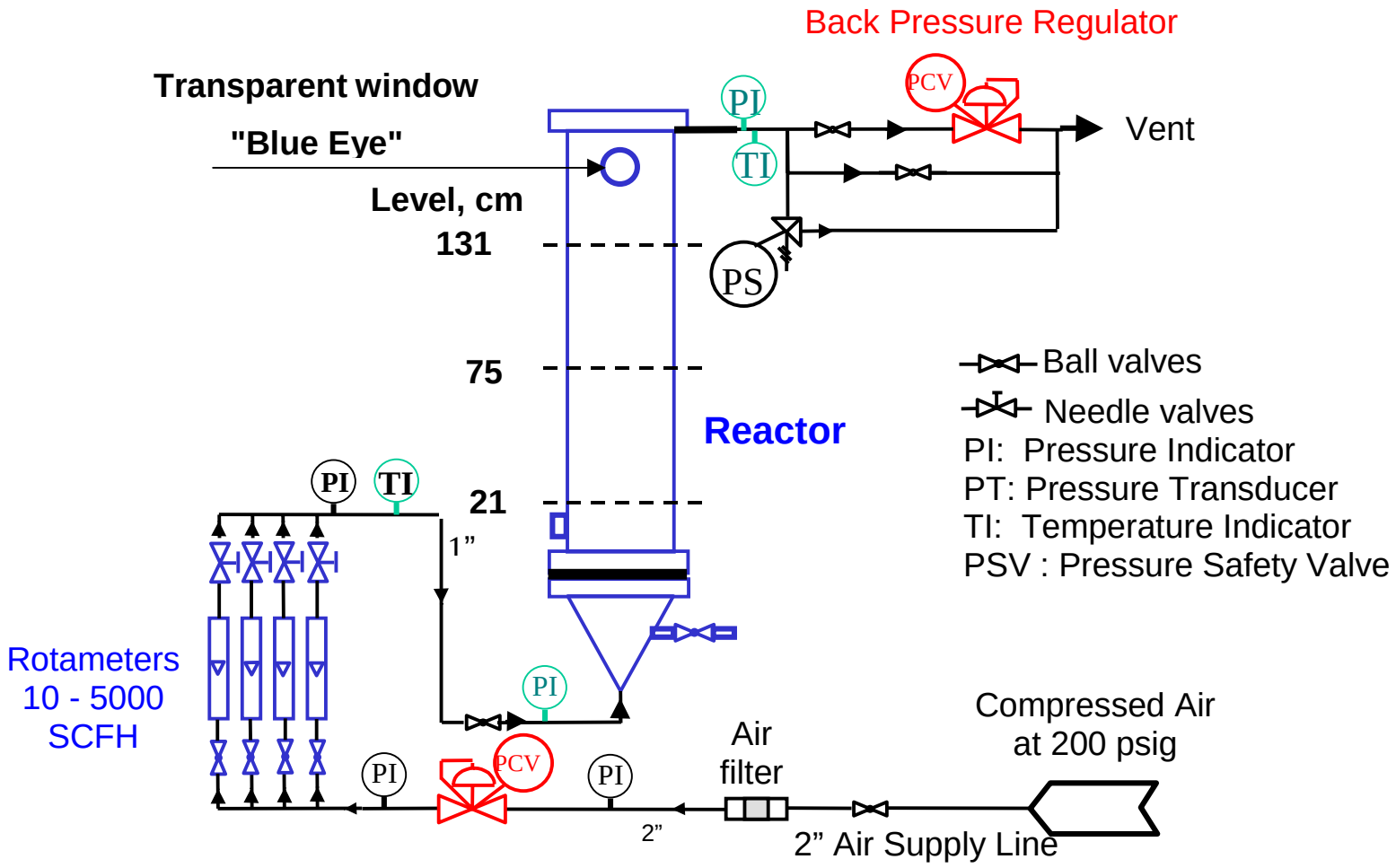

Figure 3-1. Schematic diagram of the experimental setup.

After exiting the bubble column, the gas passes through a backpressure regulator, which is used to control the pressure in the column. It is then discharged into the atmosphere through the vent. Two pressure safety valves were mounted both at the top and bottom of the column to prevent accidental over-pressurization. Throughout all the experiments, the height of the dispersed phase was maintained between 180-200 cm.

Figure 3-2 shows the schematic of the various distributors used in this study to investigate the sparger effect on gas holdup. The design specification and configuration of these spargers are summarized in Table 3-1.

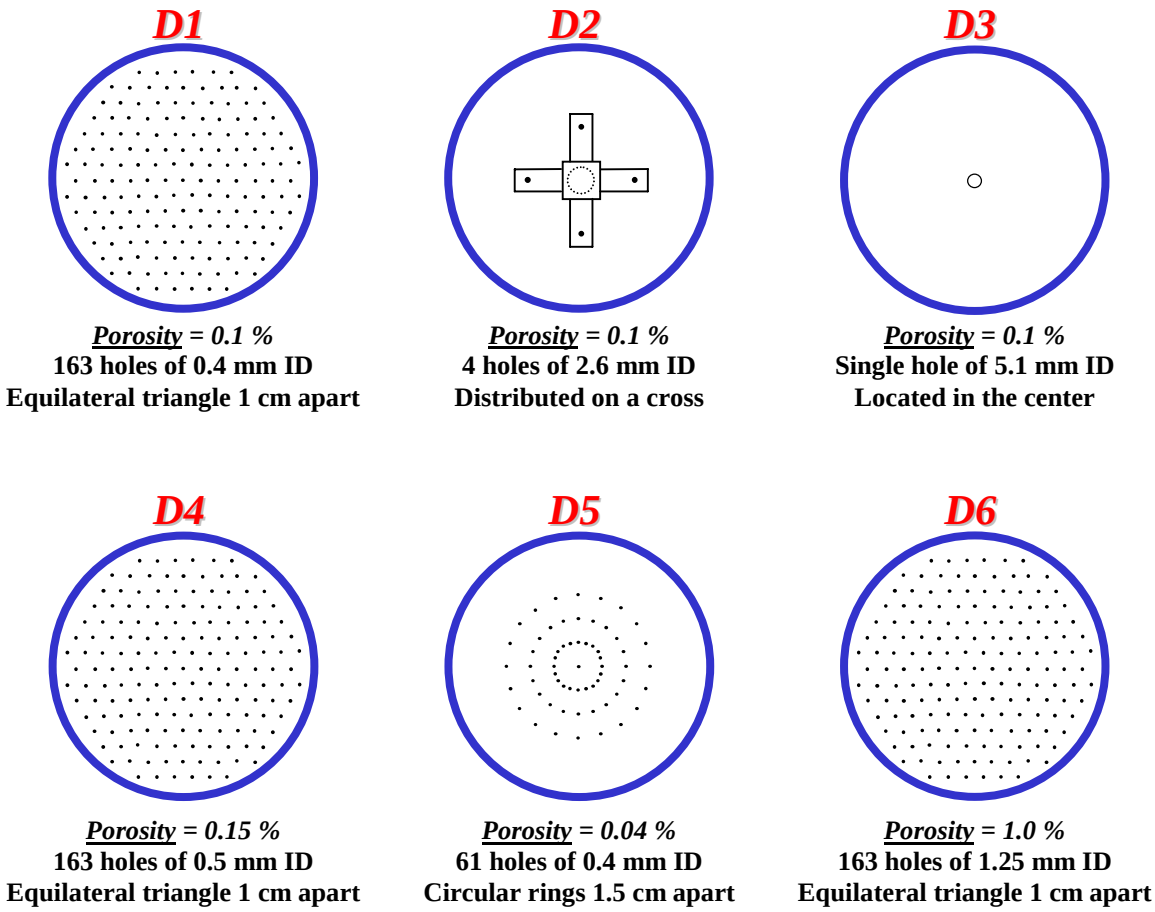

Figure 3-2. Sparger design and configuration.

Table 3-1. Description of the spargers used in this study.

Name	Type and description
D1	Perforated plate, 163 holes of 0.4 mm ID, 0.1 % open area, equilateral triangle of 1 cm apart
D2	Cross sparger, 4 holes of 2.6 mm ID, 0.1 % open area
D3	Single nozzle, 5.1 mm ID, 0.1 % open area
D4	Perforated plate, 163 holes of 0.5 mm ID, 0.15 % open area, equilateral triangle of 1 cm apart
D5	Perforated plate, 61 holes of 0.4 mm ID, 0.04 % open area, 3 circular rings of 1.5 cm apart
D6	Perforated plate, 163 holes of 1.25 mm ID, 1.0 % open area, equilateral triangle of 1 cm apart

3.2. Computed Tomography

The cross-sectional gas holdup distribution was measured using the gamma ray scanner and associated tomography reconstruction algorithms developed in CREL, which was discussed in detail by Kumar (1994) and reported by Kumar *et al.* (1995). The CREL scanner (shown in Figure 3-3) is a versatile instrument that enables the quantification of the time-averaged holdup distribution for two-phase flows under a wide range of operating conditions (Kumar *et al.*, 1997; Chen *et al.*, 1998; Kemoun *et al*., 2001). The fan beam configuration of the scanner consists of an array of NaI detectors of 5 cm in diameter (5 detectors were used in this study), and an encapsulated 100 mCi Cs^{137} source located opposite to the center of the array of detectors. The measurements can be made at different axial locations. This allows the full quantification of the effects of operating conditions on the gas holdup distribution at various column elevations. The spatial resolution of the Computed Tomography scanner is about 4 mm and the density resolution is better than 0.05 g/cm^3.

Table 3-2 lists the operating conditions at which tomographic scans were acquired at z/D = 2.1, 5.5 and 9.0, respectively. At the same time, overall gas holdup was measured using the bed expansion method. Both initial and dynamic liquid heights were measured and the overall gas holdup was calculated using Equation 3-1.

$$\varepsilon_g = \frac{H_D - H_i}{H_D} \tag{3-1}$$

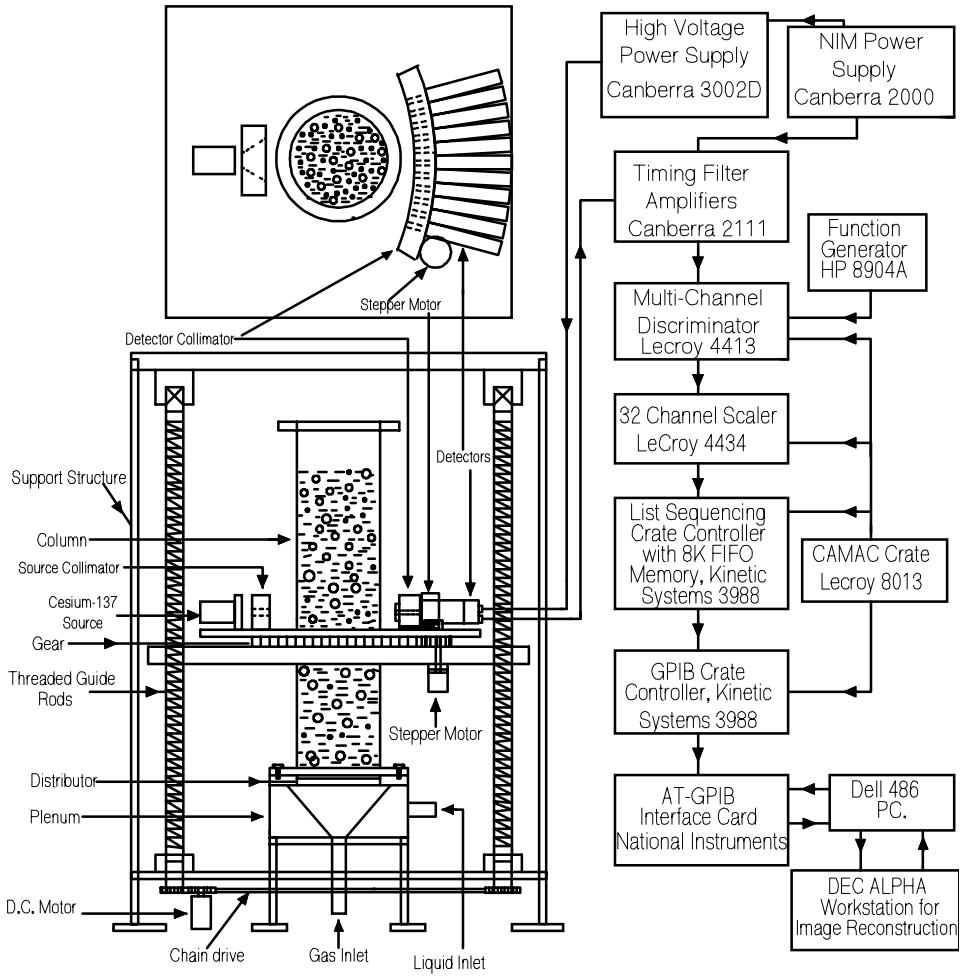

Figure 3-3. Schematic diagram of the Computed Tomography scanner (Kumar, 1994).

Table 3-2a. Column dimensions and selected operating conditions.

Column ID, cm (in.)	16.2 (6.4)
U_g (Air), cm/s	
P = 1 atm (0.1 MPa)	2, 8, 14, 30, 45, 60
P = 4 atm (0.4 MPa)	2, 8, 14, 30, 45
P = 10 atm (1.0 MPa)	2, 8, 14
Liquid (Water: ρ_l = 998.2 kg/m^3; μ_l = 0.993 mPa.s; σ = 0.072 N/m)	Batch
Temperature, °C	20
Dynamic liquid height, cm (in.)	180 (70.9)
CT scan levels from the distributor, z, cm (in.)	34 (13.4), 89 (35.0), 145 (57.1)
z/D	2.1, 5.5, 9.0

Table 3-2b. Detailed experimental conditions for each distributor.

Sparger	P, atm	U_g, cm/s
D1: Perforated plate (0.1%)	1	14, 30, 45
	4	30
D2: Cross sparger (0.1%)	1	14, 30
	4	30
D3: Single nozzle (0.1%)	1	14, 30
	4	30
D4: Perforated plate (0.15%)	1	2, 8, 14, 30, 45, 60
	4	2, 8, 14, 30, 45
	10	2, 8, 14
D5: Perforated plate (0.04%)	1	14
D6: Perforated plate (1.0%)	1	30
	4	30
	10	30

3.3. CARPT Facility

To study the effect of pressure, superficial gas velocity and distributor on liquid velocity and turbulence parameters, Computed Automated Radioactive Particle Tracking (CARPT) was employed. This technique was introduced in CREL by Devanathan (1991) and further developed by Degaleesan (1997), Gupta (2002) and others. A brief description of the facility is provided in the next section. Information on the distributor design and configuration used in this study have already been discussed earlier in Figure 3-2 and Table 3-1.

3.3.1. Overview of CARPT

The CARPT technique involves tracking the temporal Lagrangian trajectories of a radiotracer (Sc^{46} for applications in CREL) particle with the aid of a strategically located array of scintillation detectors (2” NaI crystals for applications in CREL). A calibration

map of detector counts versus particle distance has to be obtained first in order to evaluate the instantaneous tracer locations and subsequently the liquid recirculation velocity and turbulence parameters. For the experiments in this work, this was done by placing a neutrally buoyant radioactive particle of diameter 1.0 mm at several known locations (approximately 2000-3000 locations in a 6.4" diameter and 8-2 ft tall bubble column) in the system of interest operated at a specified condition. The particle was chosen such that it exhibits a similar density as that of the liquid so as to track the liquid flow using an array of strategically located scintillation detectors as mentioned previously. At all operating conditions a total of 30 scintillation detectors were positioned between z/D = 1.9 and 8.7. There were 2 detectors on each level situated 180° away from each other (refer to Figure 3-4). Hence, a calibration map (counts versus distance) is obtained. Next, the particle is introduced into the column and the experiment is conducted for 24 hours with data acquired at a frequency of 50 Hz. Throughout the experiment, the particle counts were tracked via the detectors. With this data set and the calibration map information, the instantaneous positions of the particle were obtained using the Monte Carlo reconstruction algorithm (Gupta, 2002). With the instantaneous particle position data, the liquid velocity and turbulence parameters were calculated after filtering the data using the wavelet-filtering methodology (Degaleesan *et al.*, 2002). Processing of the CARPT data using Monte Carlo method is discussed in Chapter 5. More details on CARPT facility can be found elsewhere (Devanathan, 1991; Degalessan, 1997).

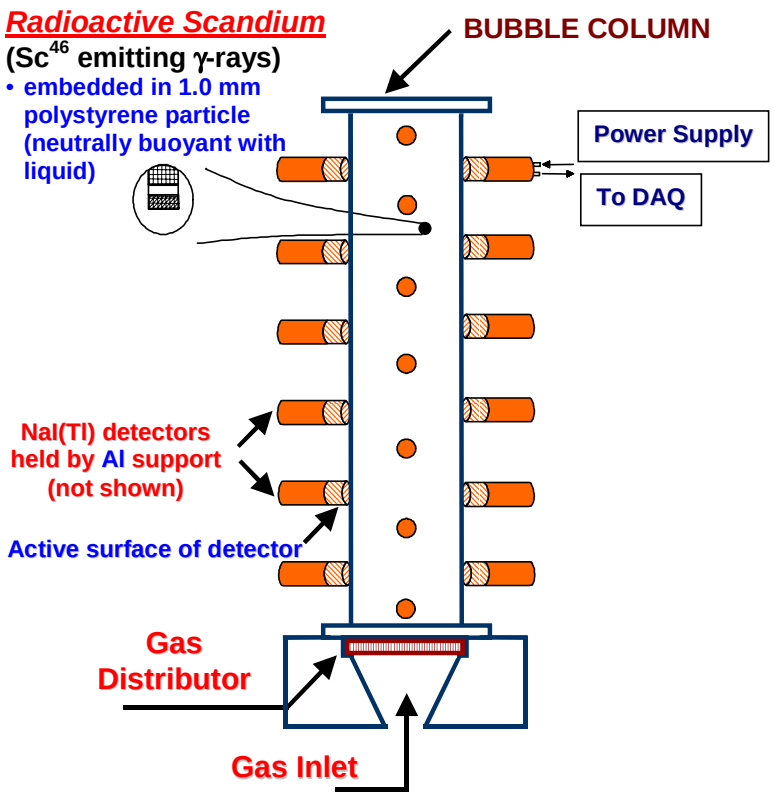

Figure 3-4. Typical CARPT setup for a bubble column (Gupta, 2002).

3.3.2. Radioactive Particle

Generally, it is desirable to have a small tracer particle so as to minimize the drag and other forces experienced by it. Previously, a composite spherical particle of 2.3 mm in diameter made up of Scandium-46, polyproylene and air was used (Devanathan, 1991; Degaleesan, 1997; Chen *et al.*, 1999). The reason for encapsulating Scandium-46 and air in polypropylene is to obtain a similar density of the composite particle as that of liquid so as to maintain neutral buoyancy. This type of particle for studies in water has a diameter of 2.3 mm. This poses difficulty in this study, as the relatively large particle cannot track liquid effectively at extreme conditions of high gas holdup. The composite particle has to be kept as small as possible in order to enable the particle to follow the liquid. Therefore, for this study, Scandium-46 particle was activated to 500 μCi and then encapsulated in a polystyrene hollow spherical particle (of density 1.05 g/cm^3) with outer

diameter 1.0 mm and inner diameter 0.3 mm. The reason for using a hollow and spherical polystyrene particle instead of polypropylene particle is due to the smaller Scandium-46 particle used in this study. A smaller Sc^{46} particle that needed to be activated to strength of 500 μCi required that a higher neutron flux be used in the nuclear reactor during activation. Unfortunately, under these high flux conditions, polypropylene gets thermally degraded and therefore a need arose to chose a material with a higher melting point. Given the density restrictions so as to have the final composite tracer particle have a density almost same as that of water, polystyrene was identified as the most suitable alternative. Thus, with this combination of Sc^{46} particle inside a hollow and spherical polystyrene particle, it was possible to achieve desired levels of radioactive strength as well as reduce the size of the tracer particle to 1 mm from 2.3 mm. Figure 3-5 shows the schematic diagram of the Scandium-46 particle and its encapsulation. The particle, once activate, is then sprayed with black paint to ensure that the particle is wetted during the operation. The approximate density of the composite particle is between 0.999-1.001 g/cm^3 and its rise velocity is about 0.02 to 0.1 cm/s (slight swelling of the polystyrene changes the settling velocity as a function of time of exposure to water).

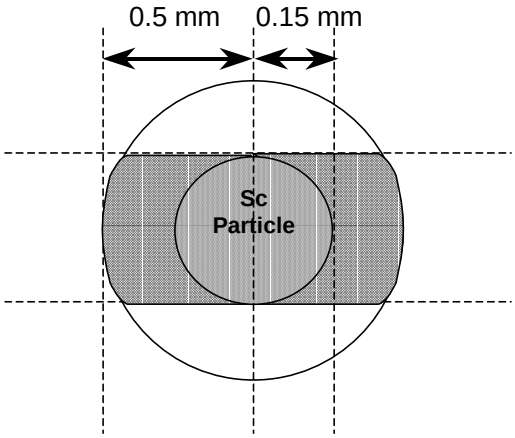

Figure 3-5. Schematic diagram of the encapsulated Scandium particle (Not drawn to scale).

3.3.3. Detector Locations and Configuration

As displayed in Figure 3-4, the detectors are strategically positioned around the column. The total number of detectors used in this study is 30, and each detector is a cylinder with a diameter of 2.125” and a length of 10.25”. Residing inside each detector is an active cylindrical NaI scintillation crystal of diameter and length of 2”. The detectors are held by aluminium support structures which are in turn supported on 4 vertical unistrut bars positioned at 90° intervals around the column. More details on the construction of the supports can be found elsewhere (Devanathan, 1991). One has to take note that it is very crucial to obtain exact locations of the detectors as misalignment leads to error in particle locations. However, this is diffcult to achieve in practice. In this study, a laser pointer is used to align the detectors with the center of the column.

Figure 3-6 shows the cross-sectional view of the detectors’ positions and configuration. At each level, two detectors are positioned 180° from each other and form a pair. The angular position of the next pair of detectors is incremented by 45° from those at the lower level. This ensures equal spacing between all the detectors in all directions and enables the particle to be in the proximity of a pair of detectors in the column during the experiment except close to the distributor and at the gas-liquid interface at the top of the column. As shown in Figure 3-4, the lowest and highest detector position in the *z* direction is 30 cm and 149 cm from the distributor, respectively.

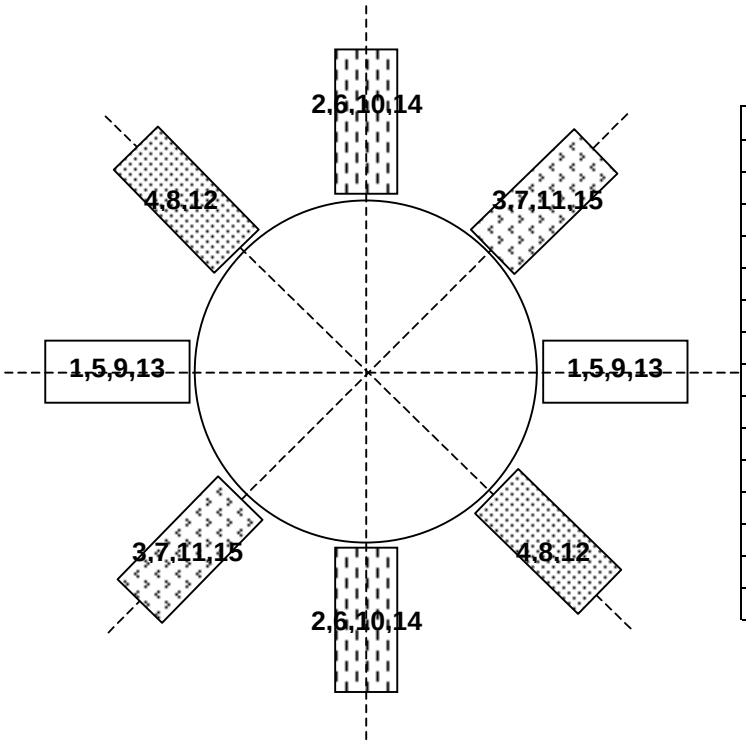

L	r (cm)	z (cm)	θ (°)
1	13.2, 14.2	30	0, 180
2	13.2, 14.2	38.5	90, 270
3	13.2, 14.2	47	45, 225
4	13.2, 14.2	55.5	135, 315
5	13.2, 14.2	64	0, 180
6	13.2, 14.2	72.5	90, 270
7	13.2, 14.2	81	45, 225
8	13.2, 14.2	89.5	135, 315
9	13.2, 14.2	98	0, 180
10	13.2, 14.2	106.5	90, 270
11	13.2, 14.2	115	45, 225
12	13.2, 14.2	123.5	135, 315
13	13.2, 14.2	132	0, 180
14	13.2, 14.2	140.5	90, 270
15	13.2, 14.2	149	45, 225

Figure 3-6. Cross-sectional view of the configuration of detectors in CARPT experiments.

3.4. Selection of Conditions for CARPT Experiments

A typical CARPT experiment usually takes at least 2-3 days to execute. For that reason, it was not feasible to do CARPT experiments at all 28 operating conditions at which CT runs were obtained. Hence, it was decided to choose the operating conditions in such a way as to get the overall picture of the flow dynamics in the column as a function of the operating and geometrical variables as well as to reduce the matrix of operating conditions. There are three input variables of primary interest, namely, pressure, gas superficial velocity and distributor type. The following sub-sections discuss the operating conditions selected for the CARPT experiments in order to determine the effect of each of the above three key input variables. Table 3-3 displays the summary of operating conditions for the CARPT experiments.

Table 3-3. Operating conditions used for CARPT experiments.

Distributor	P, bar	U_g, cm/s
D2: Cross sparger (0.1%)	1	30
D3: Single nozzle (0.1%)	4	30
D4: Perforated plate (0.15%)	1	30, 45
	4	30, 45
D6: Perforated plate (1.0%)	1	30
	4	30
	10	30

3.4.1. Effect of Distributors on Liquid Velocity and Turbulence

In order to investigate the effect of distributors on liquid velocity and turbulence, both pressure and gas superficial velocity has to be kept constant. Figure 3-7 shows the radial gas holdup profiles measured using Computed Tomography at z/D = 5.5 and superficial gas velocity of 30 cm/s at atmospheric pressure. Similar results for P = 4 atm are shown in Figure 3-8. One observation from Figure 3-7 is that the radial gas holdup profiles of the perforated plate with 0.1% open area, D1 and cross sparger, D2, of same percent open area are almost identical. In addition, perforated plate (1.0% open area), D6, produces the highest gas holdup. Since most CT experiments were performed using perforated plate, D4, with 0.15% open area and the cross sparger, D2 is the distributor of most industrial interest, while D6 has the highest porosity, the following operating conditions at P = 1 atm were selected:

P = 1 atm; U_g = 30 cm/s ***Distributors: Cross sparger D2 (0.1%), Perforated plate D4 (0.15%), Perforated plate D6 (1.0%)***

Using similar arguments, the following operating conditions at P = 4 atm were selected:

P = 4 atm; U_g = 30 cm/s ***Distributors: Single nozzle D3 (0.1%), Perforated plate D4 (0.15%), Perforated plate D6 (1.0%)***

At P = 4 atm, it was important to perform CARPT experiments for the single nozzle, D3, since it yields a higher gas holdup as compared to other distributors (refer to Figure 3-8). However, this causes concern while performing CARPT experiments since the orifice diameter of D3 is about five to six times larger than the size of radioactive particle (1 mm). Hence, care was taken to avoid the possibility of the radioactive particle getting drained out of the system.

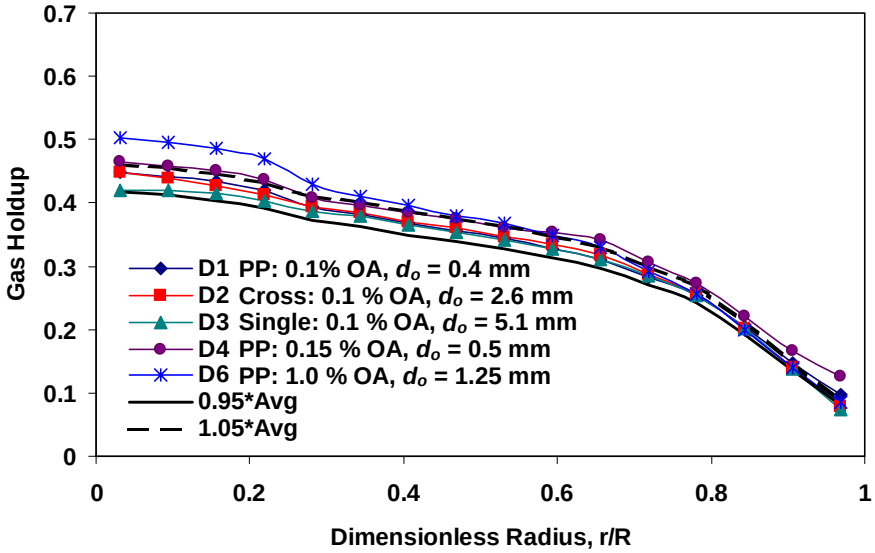

Figure 3-7. Effect of spargers at U_g = 30 cm/s at scan level z/D = 5.5 (P = 1 atm).

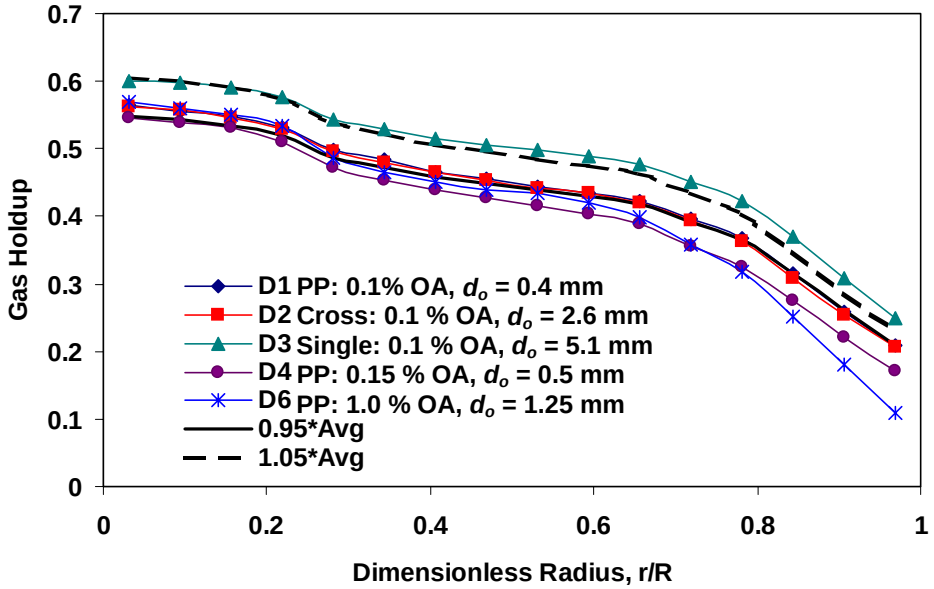

Figure 3-8. Effect of spargers at U_g = 30 cm/s at scan level z/D = 5.5 (P = 4 atm).

3.4.2. Effect of Pressure on Liquid Velocity and Turbulence

It was found that the maximum superficial velocity that can be reached using perforated plate distributor, D4 with 0.15% open area at P = 10 atm is less than 30 cm/s. In order to study the effect of pressure at very high superficial gas velocity on liquid velocity and its turbulence, the perforated plate of 1 % open area, D6, had to be used. The following operating conditions were selected:

Distributor = Perforated plate D6 (1.0%); U_g = 30 cm/s P = 1, 4, 10 atm
Distributor = Perforated plate D4 (0.15%); U_g = 45 cm/s P = 1, 4 atm

3.4.3. Effect of Superficial Gas Velocity on Liquid Velocity and Turbulence

The above selected experiments also enable one to study the effect of superficial gas velocity on the levels of liquid velocity and turbulence. The conditions at P = 1 atm and at lower superficial gas velocity (U_g < 30 cm/s) are not considered here since many CARPT experiments were performed at lower superficial gas velocity in earlier studies (Devanathan, 1991; Degaleesan, 1997; Chen *et al*., 1999). The following summarizes the conditions selected to study the effect of superficial gas velocity on liquid velocity and turbulence.

Distributor = Perforated plate D4 (0.15%); P = 1 atm U_g = 30, 45 cm/s
Distributor = Perforated plate D4 (0.15%); P = 4 atm U_g = 30, 45 cm/s

3.4.4. Final Remarks

Based on the above reasoning, the operating conditions chosen for the CARPT experiments reduce to the following set in order to study the effects of the aforementioned variables on liquid velocity and turbulence (as shown in Table 3-3).

P = 1 atm; U_g = 30 cm/s	***Distributors: D2, D4, D6***
P = 4 atm; U_g = 30 cm/s	***Distributors: D3, D4, D6***
P = 10 atm; U_g = 30 cm/s	***Distributor: D6***
P = 1 atm; U_g = 45 cm/s	***Distributor: D4***
P = 4 atm; U_g = 45 cm/s	***Distributor: D4***

The total number of experiments was therefore reduced from 28, performed using CT, to 9 for CARPT runs.

Chapter 4. Computer Tomographic Study of Gas Holdup Distribution in Churn-Turbulent Bubble Columns

One of the primary objectives of this study is to evaluate the effect of superficial gas velocity, pressure and gas distributor on the gas holdup and its distribution in a bubble column operation. As mentioned previously, many studies have been reported in the literature (refer to Chapter 2) where the overall gas holdup has been measured using either the Dynamic Gas Disengagement (DGD) technique or with the help of intrusive probes. The shortcomings of the above techniques are the measurement inaccuracies associated with measuring high gas volume fractions and transient accelerating/ decelerating flows. Therefore, although some studies have been conducted to measure the overall gas holdup at high pressures and relatively high U_g (10-25 cm/s); little has been done to quantify the effect of these operating variables by reliable and non-intrusive diagnostics. It is the intent of this study therefore, to provide the scientific community with reliable experimental data on gas holdup and its distribution in a high-pressure bubble column vessel operated at high gas velocity. Additionally, it is expected that this data set would be able to provide some improved insight into the physics of the complex hydrodynamics prevalent at these operating conditions.

Given the objectives specified above, one of the primary tasks in this study was the non-invasive measurement of the cross-sectional gas holdup distribution at three different axial locations (refer to Chapter 3). For this purpose, computer tomographic measurements of cross-sectional gas holdup distribution were performed using six

different distributors described in Figure 3-2 in a 16.2-cm (6.4”) diameter column operated at gas superficial velocity in the range from 2 cm/s to 60 cm/s and at operating pressure from 1 to 10 atm. The liquid was tap water, used in the batch mode, and the dynamic liquid height was maintained at 180 cm above the distributor.

The rest of the chapter is organized as follows. First, the values of the dimensionless capacitance and gas flow rate numbers are provided (see Chapter 2) for all the operating conditions and distributors used. Next, the effect of different distributors, superficial gas velocity and pressure on measured gas holdup profiles is described. Finally, a comparison of the average gas holdup with predictions of various existing correlations is presented.

4.1. Bubble Formation at the Spargers – Analysis based on N_c and N_w

As discussed earlier in Chapter 2, the expressions for the dimensionless capacitance, N_c, and gas flow rate numbers, N_w, (refer to Equations 2-1 and 2-2) are based on a single orifice submerged in liquid. In this study, however, all spargers (except D3) have multiple orifices. Therefore, the calculation of both of these dimensionless numbers for all the six spargers at the various operating conditions required certain assumptions, which are discussed subsequently at appropriate places in this section. As can be seen from Equation (2-1), the dimensionless capacitance number requires the gas chamber volume as input. In this study, the chamber volume per unit orifice is evaluated as V_{ch}/N_o (N_o represents the number of orifices on a sparger) and is subsequently used to calculate N_c instead of the total chamber volume. The total chamber volume, V_{ch}, is 1460 cm^3. Table 4-1 displays N_c and N_w as a function of pressure and U_g for the six distributors used in this study.

Table 4-1. N_c and N_w values as a function of P for all the distributors studied.

	P, atm	U_g, m/s	u_o, m/s	H_s, m	N_c	N_w	Bubble Formation Criterion	
							Based on N_c	Based on N_w †
D1 (0.1%, 163 orifices of 0.4 mm)	1	0.14	140	1.49	6.89	48.7	Intermediate	3
	1	0.3	301	1.43	6.89	104	Intermediate	3
	1	0.45	332*	1.35	6.89	115	Intermediate	3
	4	0.3	300	1.32	1.72	104	Intermediate	3
D2 (0.1%, 4 orifices of 2.6 mm)	1	0.14	135	1.53	6.64	779	Intermediate	3
	1	0.3	289	1.43	6.64	1670	Intermediate	3
	4	0.3	289	1.32	1.66	1670	Intermediate	3
D3 (0.1%, 1 orifices of 5.1 mm)	1	0.14	140	1.52	6.91	2230	Intermediate	3
	1	0.3	301	1.43	6.91	4770	Intermediate	3
	4	0.3	301	1.27	1.73	4770	Intermediate	3
D4 (0.15%, 163 orifices of 0.5 mm)	1	0.02	12.8	1.64	4.41	6.23	Intermediate	**1**
	1	0.08	51.2	1.38	4.41	24.9	Intermediate	3
	1	0.14	89.6	1.42	4.41	43.6	Intermediate	3
	1	0.3	192	1.40	4.41	93.4	Intermediate	3
	1	0.45	288	1.33	4.41	140	Intermediate	3
	1	0.6	332*	1.28	4.41	161	Intermediate	3
	4	0.02	12.8	1.65	1.10	6.23	Intermediate	**2**
	4	0.08	51.2	1.37	1.10	24.9	Intermediate	3
	4	0.14	89.6	1.45	1.10	43.6	Intermediate	3
	4	0.3	192	1.35	1.10	93.4	Intermediate	3
	4	0.45	288	1.28	1.10	140	Intermediate	3
	10	0.02	12.8	1.64	0.44	6.23	Constant Flow	**2**
	10	0.08	51.2	1.39	0.44	24.9	Constant Flow	3
	10	0.14	89.6	1.32	0.44	43.6	Constant Flow	3
D5 (0.04%, 61 orifices of 0.4 mm)	1	0.14	332*	1.49	18.4	116	Constant Pressure	3
D6 (1.25%, 163 orifices of 1.25 mm)	1	0.3	30.7	1.41	0.705	59.1	Constant Flow	3
	4	0.3	30.7	1.36	0.176	59.1	Constant Flow	3
	10	0.3	30.7	1.27	0.071	59.1	Constant Flow	3

†1. Single, uniform bubbles are formed
2. Bubble volume increases with N_w
3. Bubbles break down after detachment at the orifice and a distribution of bubble volumes is produced.

* Sonic velocity at 70 °F (298 K) = 332 m/s. Choked flow occurs when sonic velocity has reached.

As can be seen from column 6 of Table 4-1, constant flow conditions prevail at the orifice (N_c < 1) if the orifice diameter is close to or above 1.25 mm and for $P \geq 10$ atm. In other words, at these conditions, the flow through the orifice can be assumed to be constant. The other noteworthy observation from Table 4-1 based on N_c values is that, except for distributor D5 operated at atmospheric conditions, no distributor operates at N_c > 9. This implies that bubble volume at the sparger is dependent on the chamber volume. Only for distributor D5, bubbles are formed under constant pressure conditions. The other factor controlling the formation of bubbles at the orifice is the dimensionless gas flow rate, N_w. As presented in Chapter 2, when N_w is greater than 16, the bubbles formed at the sparger break down after detachment at the orifice resulting in a distribution of bubble sizes. It is therefore of interest to determine the superficial gas velocity at which N_w exceeds 16 for the six distributors used in the study. This can be readily inferred from Figure 4-1 where the variation of N_w with U_g is presented graphically.

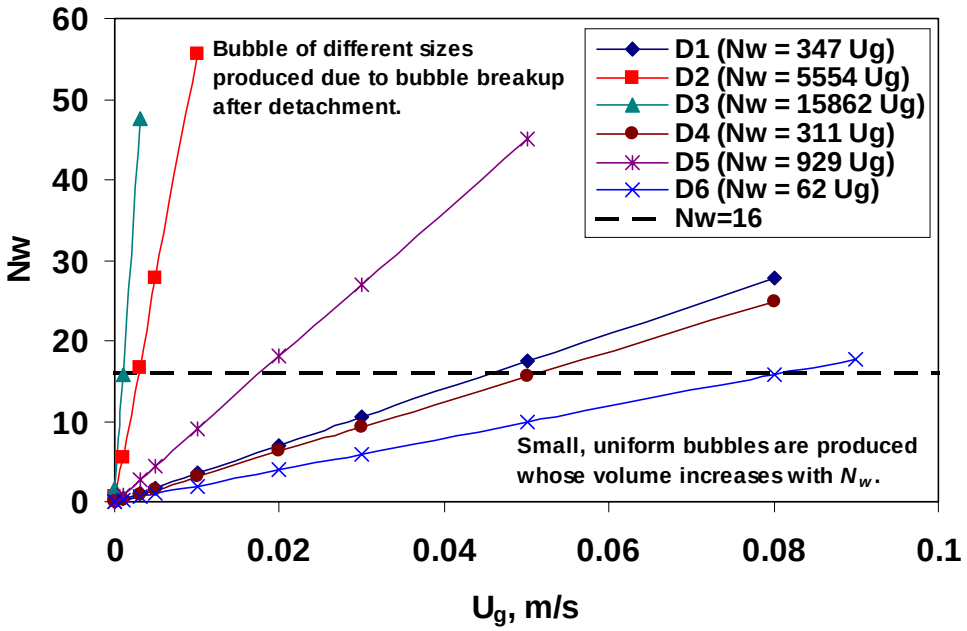

Figure 4-1. Dimensionless gas flow rate versus superficial gas velocity for all the distributors studied $\left(N_w = BoFr_o^{0.5}\right)$.

From Figure 4-1, it can be seen that the superficial gas velocity at which N_w becomes equal to 16 is the smallest for single nozzle distributor (D3), followed by the cross sparger (D2) and then the perforated plates in increasing order of the percent open area (D5, D1, D4, D6). It is also noteworthy that for the same number of orifices (D1, D4 and D6), increasing the size of the orifice increases the transition superficial gas velocity, implying that for the same U_g and same number of orifices, an increase in orifice diameter leads to more stabilized bubble detachment with lower subsequent bubble break-up. It should be noted that the gas density does not appear anywhere in the expression for N_w implying that it is independent of operating pressure. Additionally, irrespective of the type of distributor, the superficial gas velocity at which N_w exceeds 16 is less than 10 cm/s. Therefore, based on this criterion, the bubble formation at the sparger for the majority of the experiments performed in this study, results in a distribution of bubble sizes. This can also be seen from Table 4-1 where the values of N_w for most spargers and operating conditions are greater than 16, implying that a broad spectrum of bubble sizes are formed at the sparger. The above analysis indicates that a single estimate of the mean bubble size at the sparger, presented in subsequent sections based on theories available in the open literature, should be accepted with caution. The conclusions from the above analysis, however, still do not indicate whether the flow is in the bubbling, jetting or dispersed jetting regimes. To establish this, Figure 4-2 displays the plot of the Weber number $\left(We = \rho_l u_o^2 d_o / \sigma\right)$ versus the Reynolds number $\left(Re_o = \rho_g u_o d_o / \mu_g\right)$ for different distributors at different operating conditions where the boundaries between the bubbling/jetting and jetting/dispersed jetting regime are given by Equations (2-13a) and (2-13b).

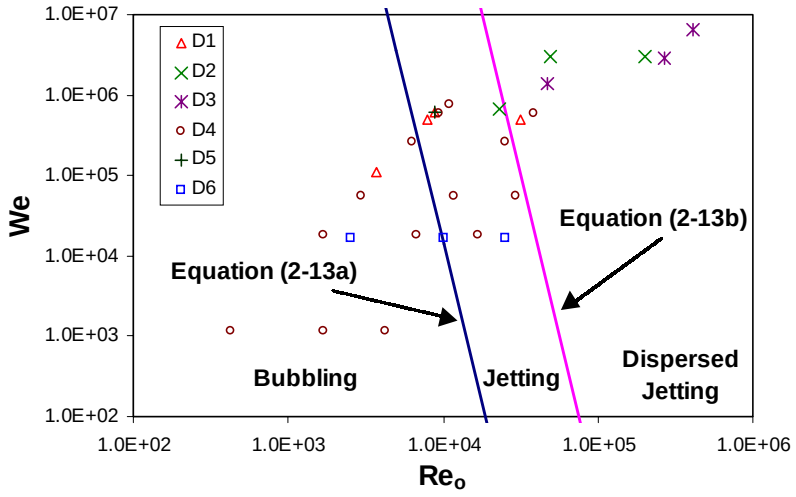

Figure 4-2. Plot of *We* number $\left(We = \rho_l u_o^2 d_o / \sigma\right)$ versus *Re* number $\left(Re_o = \rho_g u_o d_o / \mu_g\right)$ for different distributors at different operating conditions.

Table 4-2 lists the various operating conditions corresponding to different flow regimes shown in Figure 4-2. As shown in Table 4-2, beyond a superficial gas velocity of 14 cm/s, the flow is either in the jetting or dispersed jetting regime for most operating conditions. The only exceptions occur when using the perforated plate distributors D4 (0.15% open area) and D6 (1.0% open area) operating at a pressure of 1 atm and superficial gas velocity of 30 cm/s (refer to Table 4-2). These two distributors have a larger percent open area as compared to perforated plate distributor D1 (0.1%). Hence, the orifice velocity using the perforated plate distributor D1 is higher as compared to the other two distributors. In fact, the perforated plate distributor D1 was designed in such a way that the orifice velocity approaches the sonic velocity. Another important observation to make from Table 4-2 is that for distributor D4 the onset of jetting is expedited with pressure, *i.e.*, the jetting regime is attained at a lower superficial gas velocity with increasing pressure. Hence, it can be hypothesized that bubbling regime is in general favored by flow through perforated plate distributors of sufficient open area and at lower operating pressures.

Table 4-2. Bubble formation regimes at various operating conditions.

	P, atm	U_g, m/s	u_o, m/s	Re_o	We	Bubble Formation Regime	
						Idogawa *et al.* (1987[b])	Leibson *et al.* (1956)
D1 (0.1%, 163 orifices of 0.4 mm)	1	0.14	140	3710	109000	Bubbling	Jetting
	1	0.3	301	7940	499000	Jetting	Jetting
	1	0.45	332*	8790	611000	Jetting	Jetting
	4	0.3	301	31800	499000	Dispersed Jetting	Jetting
D2 (0.1%, 4 orifices of 2.6 mm)	1	0.14	135	23200	658000	Jetting	Jetting
	1	0.3	289	49800	3020000	Dispersed Jetting	Jetting
	4	0.3	289	199000	3020000	Dispersed Jetting	Jetting
D3 (0.1%, 1 orifices of 5.1 mm)	1	0.14	140	47400	1390000	Dispersed Jetting	Jetting
	1	0.3	301	102000	6400000	Dispersed Jetting	Jetting
	4	0.3	301	406000	6400000	Dispersed Jetting	Jetting
D4 (0.15%, 163 orifices of 0.5 mm)	1	0.02	12.8	424	1140	Bubbling	Intermediate
	1	0.08	51.2	1700	18200	Bubbling	Intermediate
	1	0.14	89.6	2970	55700	Bubbling	Jetting
	1	0.3	192	6350	256000	Bubbling	Jetting
	1	0.45	288	9530	575000	Jetting	Jetting
	1	0.6	332*	11000	764000	Jetting	Jetting
	4	0.02	12.8	1700	1140	Bubbling	Intermediate
	4	0.08	51.2	6780	18200	Bubbling	Jetting
	4	0.14	89.6	11800	55700	Jetting	Jetting
	4	0.3	192	25400	256000	Jetting	Jetting
	4	0.45	288	38100	575000	Dispersed Jetting	Jetting
	10	0.02	12.8	4240	1140	Bubbling	Jetting
	10	0.08	51.2	16900	18200	Jetting	Jetting
	10	0.14	89.6	29700	55700	Jetting	Jetting
D5 (0.04%, 61 orifices of 0.4 mm)	1	0.14	332*	8790	611000	Jetting	Jetting
D6 (1.25%, 163 orifices of 1.25 mm)	1	0.3	30.7	2540	16400	Bubbling	Jetting
	4	0.3	30.7	10200	16400	Jetting	Jetting
	10	0.3	30.7	25400	16400	Jetting	Jetting

4.2. Cross-sectional Distribution of Gas Holdup

Before going into a detailed analysis of the effect of the various factors on the gas holdup measured by Computed Tomography, it is of interest to qualitatively analyze the data from typical CT scans. Figure 4-3 shows the cross-sectional time-average gas holdup distribution in the bubble column at selected pressures and at different superficial gas velocities with the perforated plate distributor D4. Gradual variation in the color shades for the gas holdup from the column center to the wall indicates a change in gas holdup values (red color shade indicates higher gas holdup as indicated in Figure 4-3). These plots confirm that gas holdup always increases with superficial gas velocity and also increases with pressure, but only in churn turbulent flow at higher superficial gas velocities. Visual observations of the column in the vicinity of the wall via the “blue eye” revealed much smaller bubbles when pressure was increased. Thus, gas holdup is seen to increase with pressure at high U_g of 14 cm/s, which is generally understood to be in the churn-turbulent regime. It can also be observed from Figure 4-3 that gas holdup distribution is almost uniform at lower superficial gas velocities of 2 and 8 cm/s. This is in agreement with the observations made in bubbly flow by several researchers (Kölbel *et al.*, 1961; Deckwer *et al.*, 1980; Letzel, 1997; Letzel *et al.*, 1997b).

The most important observation to be made from Figure 4-3 is the apparent symmetry of the gas volume fraction distribution. In previous studies at lower U_g and atmospheric pressure, gas holdup distribution was found to be approximately axisymmetric (Kumar *et al.*, 1997; Chen *et al.*, 1998). It is evident from Figure 4-3 that the assumption of axisymmetry is also valid at higher pressures. This axisymmetry was observed for all spargers and all operating conditions and further analysis of gas holdup distribution in this chapter is presented in terms of azimuthally averaged radial gas holdup profiles.

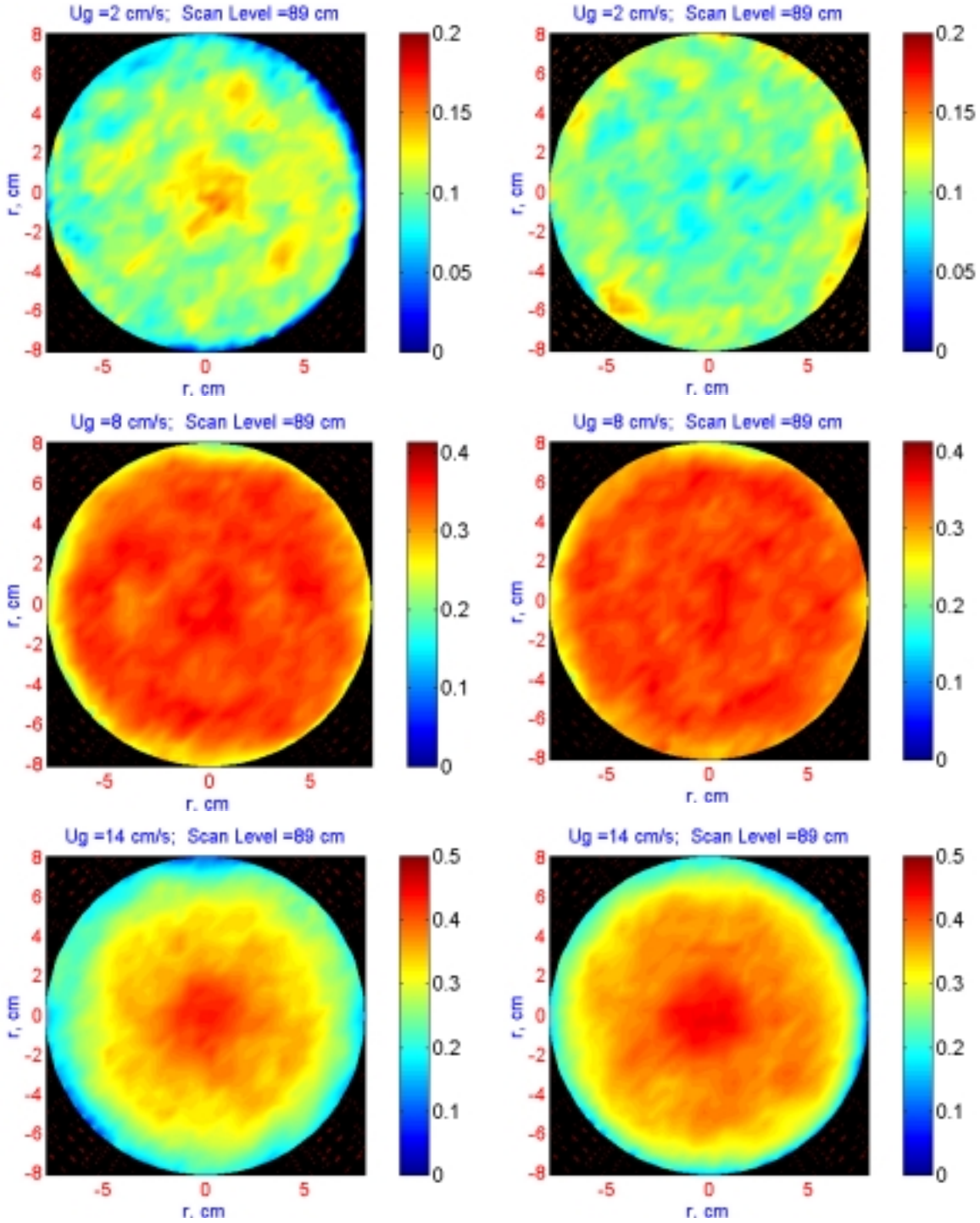

(a) P = 1 atm (b) P = 4 atm

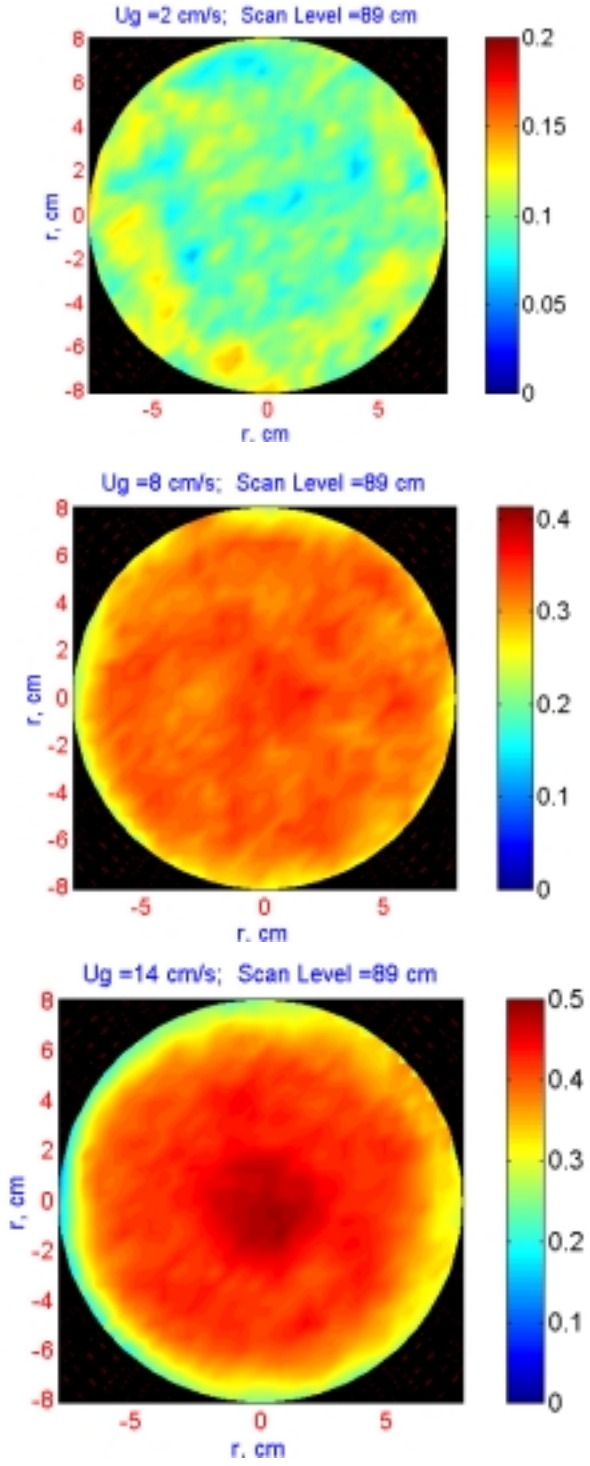

(c) P = 10 atm

Figure 4-3. Cross-sectional average gas holdup distribution for perforated plate distributor D4 (0.15 % open area; d_o = 0.5 mm), for different operating conditions.

To further examine the symmetry of the long time-averaged cross-sectional gas holdup distribution discussed in the above figure, radial variation of gas holdup in the four quadrants of the cross-sectional gas holdup image were computed and are shown in Figure 4-4 at the three axial locations where the scans were conducted for cross sparger, D2. Clearly, except for the near-wall region, the variation of gas holdup in the four quadrants is within 5% of the azimuthal mean of the four quadrants taken together. Hence, it is reasonable to assume that gas holdup distribution is axisymmetric along the length of the column.

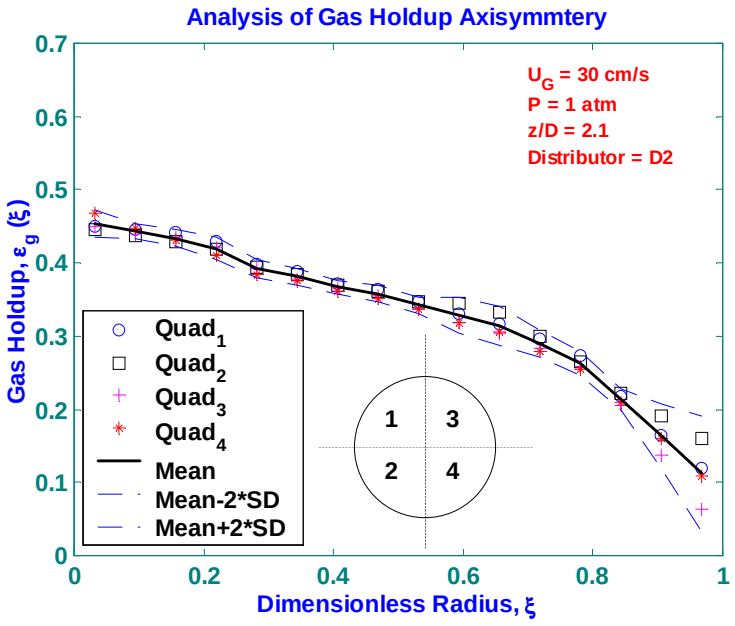

(a)

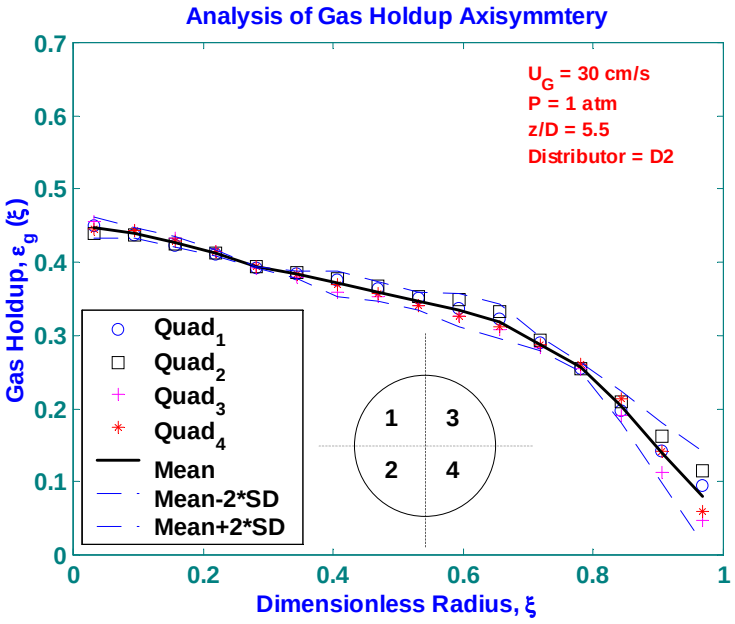

(b)

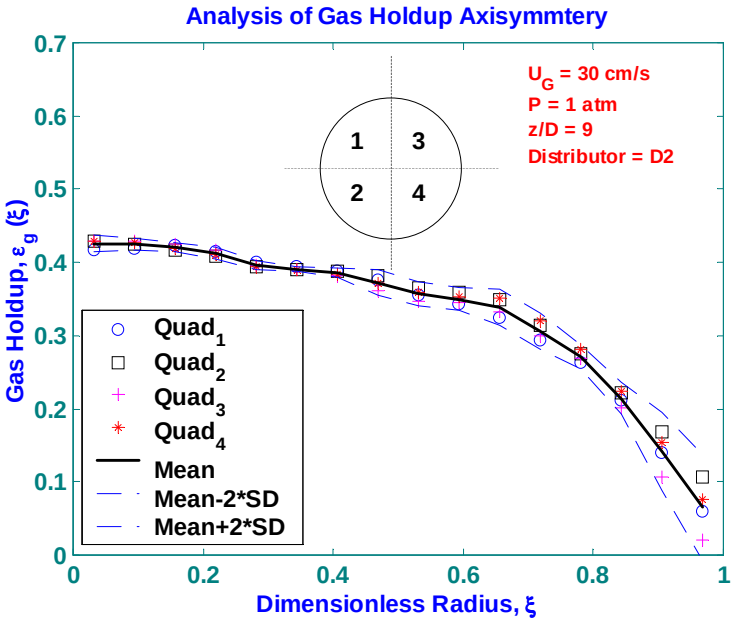

(c)

Figure 4-4. Radial gas holdup profiles in the four different quadrants of the cross-sectional gas holdup distribution: a) *z/D* = 2.1; b) *z/D* = 5.5; c) *z/D* = 9.0.

To assess the symmetry across the range of operating conditions used in this study, Figure 4-5 shows the radial variation of gas holdup in the four quadrants at three different pressures for perforated plate distributors (D4 and D6) and single nozzle sparger (D3). As with the axial variation presented in Figure 4-4, one can see that except for the near-wall regions, the differences in the radial gas holdup profiles in the four quadrants are within 5% of the overall azimuthally averaged radial gas holdup profiles.

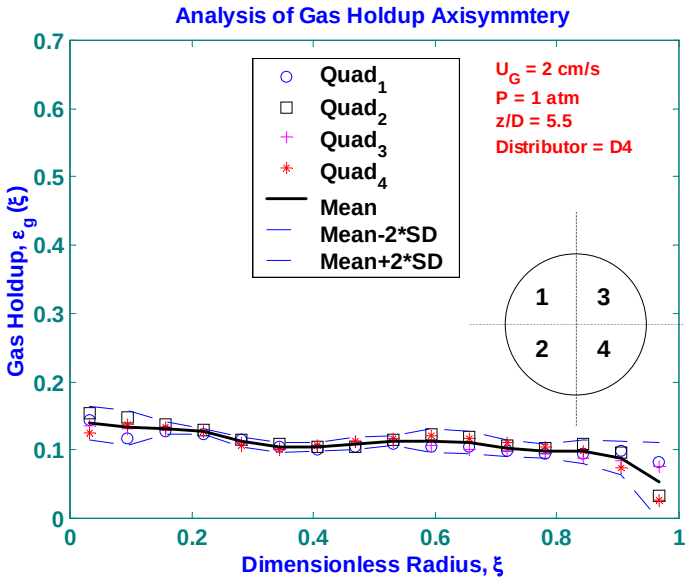

(a)

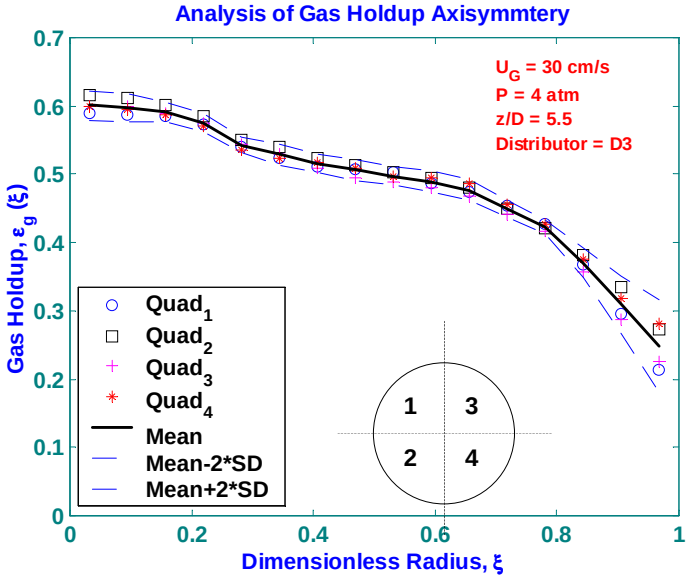

(b)

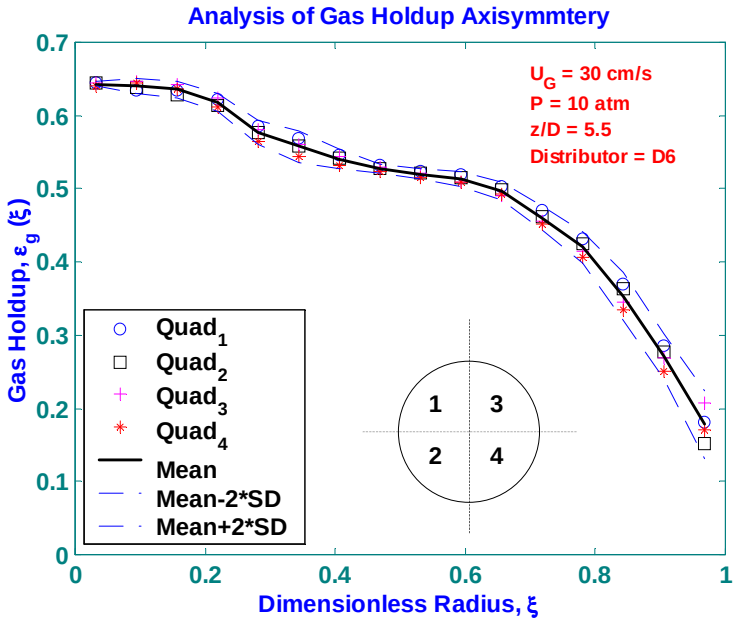

(c)

Figure 4-5. Radial gas holdup profiles in the four different quadrants of the cross-sectional gas holdup distribution: a) D4, U_g = 2 cm/s, P = 1 atm; b) D3, U_g = 30 cm/s, P = 4 atm; c) D6, U_g = 30 cm/s, P = 10 atm.

4.3. Reproducibility of CT Scans with Different Batches of Water

One last issue that needs to be addressed, before establishing the framework for the discussion of the CT measured gas holdup distribution, is the reproducibility of the experiments. To address this, the reproducibility of CT scans for gas holdup profiles at P = 1 and 4 atm at U_g = 30 cm/s was tested. Two different batches of tap water on three different days were used to obtain the gas holdup profiles using the perforated plate distributor D4 (0.15% open area, d_o = 0.5 mm) (refer to Table 3-1 and Figure 3-2 for distributor configuration). The results shown in Figure 4-6 indicate good agreement in radial holdup profiles obtained using either fresh or old batch of water. At atmospheric pressure, the bounds for the 95% confidence interval, consisting of two standard deviations on each side of the mean, are at every radial location well within ± 2%, except

at the points close to the wall which are within ± 5%. For the higher pressure of 4 atm (shown in Figure 4-6b), all points in the radial gas holdup profiles are within ± 4% of the average radial gas holdup profile which indicates very good reproducibility. It is not reasonable to expect that various distributors could produce holdup profiles within the range of reproducibility of a single distributor even when claiming the same behavior of different distributors. Hence, a band of holdup values defining the "same" behavior will have to be set, and is discussed in the subsequent sections. In conclusion, the reproducibility CT measured cross-sectional gas holdup distribution is very good.

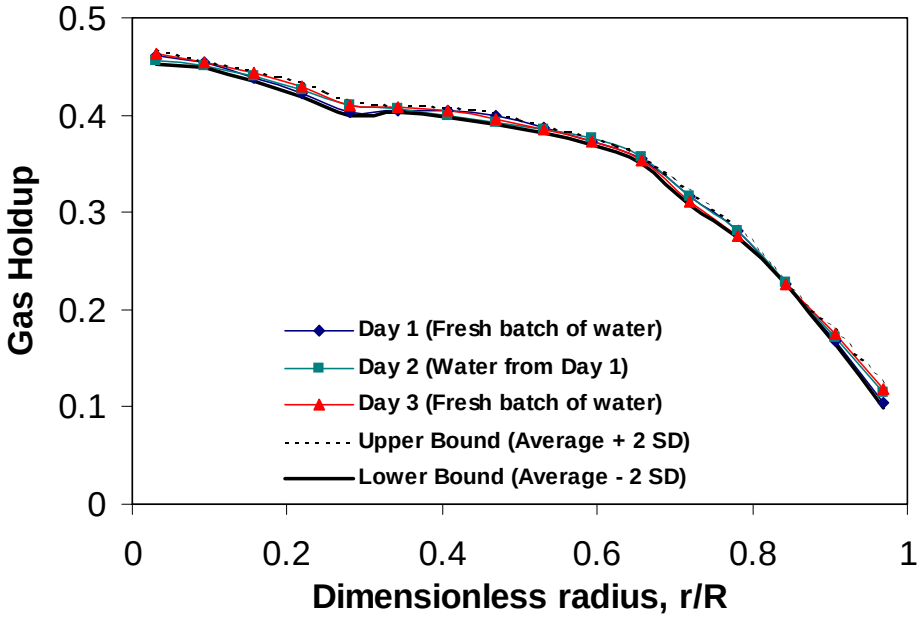

(a)

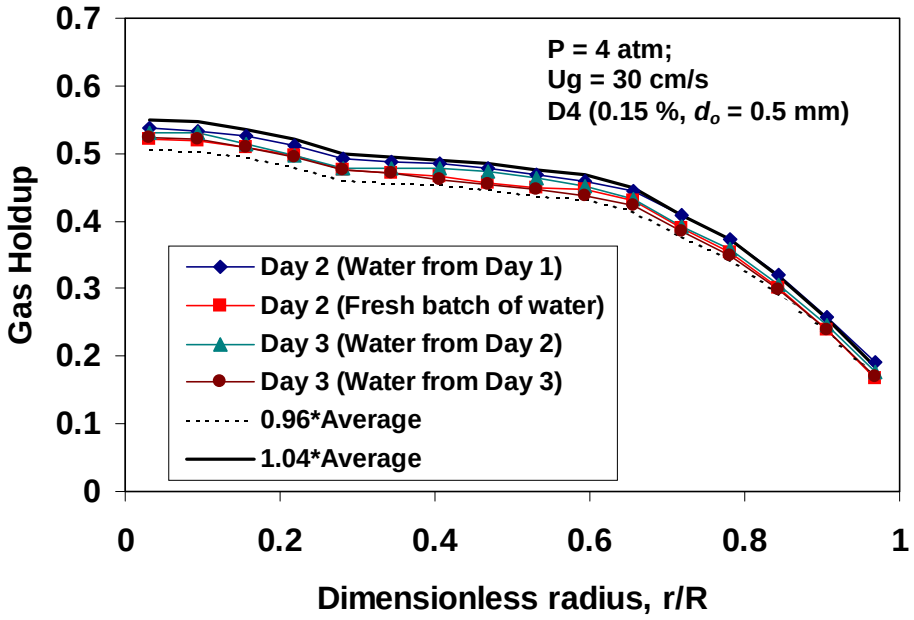

(b)

Figure 4-6. Reproducibility of the radial gas holdup profiles at superficial gas velocity of 30 cm/s at (a) P = 1 atm; and (b) P = 4 atm using two different batches of water on three different days using perforated plate distributor D4 (0.15 % open area; d_o = 0.5 mm).

4.4. Distributor Effects on Radial Gas Holdup Distribution

It is a general belief that as one moves the operation of a bubble column deep into the churn-turbulent regime, the effect of spargers on the gas holdup, its distribution and the rest of the associated hydrodynamics is confined to a region near the sparger and the hydrodynamics prevailing in most of the column is unaffected by the distributor type. For example, George *et al.* (2000[b]) found that the effect of distributors was limited to *z/D* of 2.1 in a 0.483 m diameter column at U_g of 5 to 30 cm/s at P = 0.1 to 0.5 MPa. From Table 4-2, it is clear that even for U_g as large as 30 cm/s, some spargers exhibit bubbling regime for bubble formation and are candidates for producing different gas holdup compared to other distributors. Table 4-3 shows the estimated bubble sizes at the sparger based on the propositions of Ellenberger and Krishna (1994), Leibson *et al.* (1956) and

Wallis (1969). Clearly, there is quite a discrepancy in the bubble size predicted by various correlations.

Table 4-3. Initial bubble size and penetration length for different operating conditions using different distributors.

Distributors	P, atm	U_g, cm/s	$U_{g,\,trans}$, cm/s	Initial Bubble Size, cm			$u_{o,crit}$, m/s Wallis (1969)	Penetration Length[b], cm
				Ellenberger & Krishna (1994)	Leibson *et al.* (1956)	Wallis (1969)		
D1 (0.1%, 163 orifices of 0.4 mm)	1	14	0.44	2.38	0.47	0.08	86.0	2.31
	1	30	0.44	3.25	0.45	0.08	95.3	3.84
	1	45	0.44	3.83	0.45	0.08	108	5.03
	4	30	4.27	3.07	0.42	0.08	47.6	6.09
D2 (0.1%, 4 orifices of 2.6 mm)	1	14	0.44	10.5	0.43	0.52	13.2	7.85
	1	30	0.44	14.3	0.41	0.52	14.6	13.1
	4	30	4.27	13.5	0.39	0.52	7.27	20.7
D3 (0.1%, 1 orifices of 5.1 mm)	1	14	0.44	18.2	0.42	1.02	6.74	12.6
	1	30	0.44	24.9	0.40	1.02	7.48	21.0
	4	30	4.27	23.6	0.37	1.02	3.74	33.3
D4 (0.15%, 163 orifices of 0.5 mm)	1	2	0.44	1.00	0.005	0.33	64.2	0.54
	1	8	0.44	1.88	0.008	0.52	65.5	1.37
	1	14	0.44	2.38	0.48	0.10	66.8	1.99
	1	30	0.44	3.25	0.46	0.10	71.0	3.31
	1	45	0.44	3.83	0.45	0.10	75.6	4.33
	1	60	0.44	4.30	0.44	0.10	81.3	5.25
	4	2	4.27	-	0.008	0.33	32.1	0.86
	4	8	4.27	1.42	0.46	0.10	32.7	2.17
	4	14	4.27	2.08	0.44	0.10	33.4	3.16
	4	30	4.27	3.07	0.43	0.10	35.5	5.25
	4	45	4.27	3.69	0.42	0.10	37.8	6.88
	10	2	8.79	-	0.47	0.33	20.2	1.17
	10	8	8.79	-	0.44	0.10	20.7	2.95
	10	14	8.79	1.62	0.43	0.10	21.1	4.29
D5 (0.04%, 61 orifices of 0.4 mm)	1	14	0.44	3.52	0.45	0.08	100.8	4.45
D6 (1.25%, 163 orifices of 1.25 mm)	1	30	0.44	3.25	0.48	0.25	25.9	0.30
	4	30	4.27	3.07	0.45	0.25	12.9	0.47
	10	30	8.79	2.84	0.43	0.25	8.17	0.64

[a] Wallis (1969) suggests the bubble size at the sparger to be twice the orifice diameter when $u_o > u_{o,crit}$.
[b] Banks & Chandrasekhara (1963)

The correlation for prediction of bubble sizes at the sparger from Leibson *et al.* (1956), presented in Chapter 2, have been used to calculate the initial bubble sizes for various operating conditions in Table 4-3. From the predicted initial bubble size, it can be seen that beyond a superficial gas velocity of 14 cm/s, the bubble size at the sparger decreases with pressure. Since gas holdup is known to increase with *P*, a reduction in bubble size points to the correct trend of increasing gas holdup with these operating conditions. However, for the lowest superficial gas velocity of 2 cm/s using distributor D4, one observes a contradictory increase in bubble size with pressure. One should also note that with increasing U_g, the initial bubble size either increases or remains constant.

Wallis (1969) suggested that when the orifice velocity, u_o (refer to Table 4-2) is greater than the critical orifice velocity, $u_{o,crit}$ (refer to Table 4-3), then the gas is introduced into the column as a jet and the bubble size at the sparger can be approximated as twice the orifice diameter, d_o. He, however, also cautioned against the extrapolation of this single orifice observation to the multiple orifice cases. Ellenberger and Krishna (1994), on the other hand, modified the correlation of Darton *et al.* (1977) to represent the change of the bubble size at the sparger to the equilibrium size, as presented below.

$$d_b = \begin{cases} (h + h_o)^{4/5} (U_g - U_{g,trans})^{2/5} g^{-1/5} & \text{for } h \le h^* \\ (h^* + h_o)^{4/5} (U_g - U_{g,trans})^{2/5} g^{-1/5} & \text{for } h^* \le h \le H \end{cases} \quad \text{(SI Units)} \qquad (4\text{-}1)$$

where h^* is the height above the sparger at which the bubbles after forming at the sparger attain their equilibrium size and $h_o = 4\sqrt{A_o}$; A_o is the area of the distributor plate per unit orifice. They correlated h^* with their observations as follows:

$$h^* = 0.018 + 1.05 * (U_g - U_{g,trans}) \quad \text{(SI Units)} \qquad (4\text{-}2)$$

To obtain the bubble size at the sparger, one substitutes $h = 0$ in the expression for prediction of bubble sizes valid for $h \le h^*$ in Equation (4-1). It is interesting to note that Ellenberger and Krishna's (1994) approach predicts a reduction in the size of the

bubble at the sparger with increasing pressure, an observation frequently quoted (Lin *et al.*, 1998; Letzel, 1997). However, the predicted bubble sizes appear to be very large, especially for the cross sparger (D2) and single nozzle (D3). The other point to note is that h^* decreases with increasing pressure for the same U_g since U_{gtrans} increases with pressure (Table 4-3 and Equation (4-2)). This is relatively surprising since with increasing pressure, more kinetic energy is carried by the gas jets into the column and one would expect a higher equilibration height. Banks and Chandrasekhara (1963) proposed the following correlation to predict the jet penetration length in liquids.

$$L_j = \left(\frac{2K_2^2 M}{\pi \rho_l g} \right)^{1/3} \tag{4-3}$$

where K_2 has a value of 8.0 (Banks and Chandrasekhara, 1963) and $M = \pi \rho_g d_o^2 u_o^2 / 4$. The above expression was derived via stagnation pressure analysis, which related the depth of the surface depression or cavity to the stagnation pressure based on the centerline velocity of the jet in the neighborhood of the surface. In spite of the above analysis being developed for air jets shooting downwards vertically into stagnant liquid pools, its applicability to the case of bubble columns is justifiable since the velocity head of the jets formed at the sparger is much larger than the gravity head.

The predictions from the above equation are also presented in Table 4-3 and one can see that the jet penetration length does indeed increase with U_g and pressure. But even for the highest pressure and U_g combination for the single nozzle sparger (D3), the predicted jet penetration seems to be confined to within *z/D* of 2.25. However, since these predictions are based on independently developed theory and experiments, it is advisable that based on the range of jet penetration lengths in Table 4-3, the presence of spargers effect on holdup and subsequently liquid turbulence and recirculation are not outright discarded for the cross and single nozzle spargers. Further discussion of the axial variation of gas holdup is provided in Section 4.5. In view of the above discussion, it would be fair to expect that in truly churn-turbulent regime, the sparger effects are not significant beyond a *z/D* of 2.5 or greater.

Figures 4-7 and 4-8 show the radial gas holdup profiles, $\varepsilon_{gi}(r)$, for each distributor (i = 1, 2, 3, 4, 5 or 6) taken at z/D = 5.5, for superficial gas velocities of 14 and 30 cm/s, respectively, at atmospheric pressure. Since the perforated plate distributor (D1), cross sparger (D2) and single nozzle (D3) have the same open area, at a given axial elevation, z, the mean holdup profile at each radial location, $\varepsilon_g(r,z) = \sum_{i=1}^{N} \varepsilon_{gj}(r,z) \Big/ N$ (where j = 1, 2, 3), is calculated and the distributor effect is considered insignificant if $\varepsilon_{gi}(r,z)$ lies within the range from 0.95 $\varepsilon_g(r,z)$ to 1.05 $\varepsilon_g(r,z)$. This represents a narrow (less than ± 5%) band around the mean. Figures 4-5 and 4-6 also display the lower bound of the allowable band at 0.95 $\varepsilon_g(r,z)$ and the upper bound at 1.05 $\varepsilon_g(r,z)$. At U_g = 14 cm/s (Figure 4-7), not all the distributors generate a gas holdup profile in that band. These differences are notable not only near the distributor zone (not shown here), but also throughout the column. There are significant differences in gas holdup profile produced by different distributors at dimensionless radii r/R < 0.8 in the core of the column.

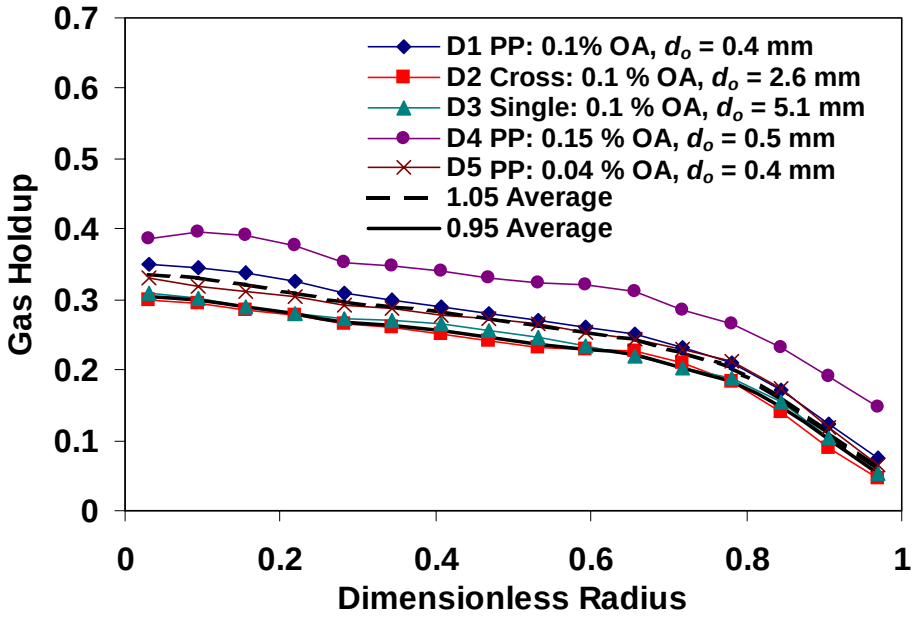

Figure 4-7. Effect of spargers at U_g = 14 cm/s at scan level z/D = 5.5 (P = 1 atm).

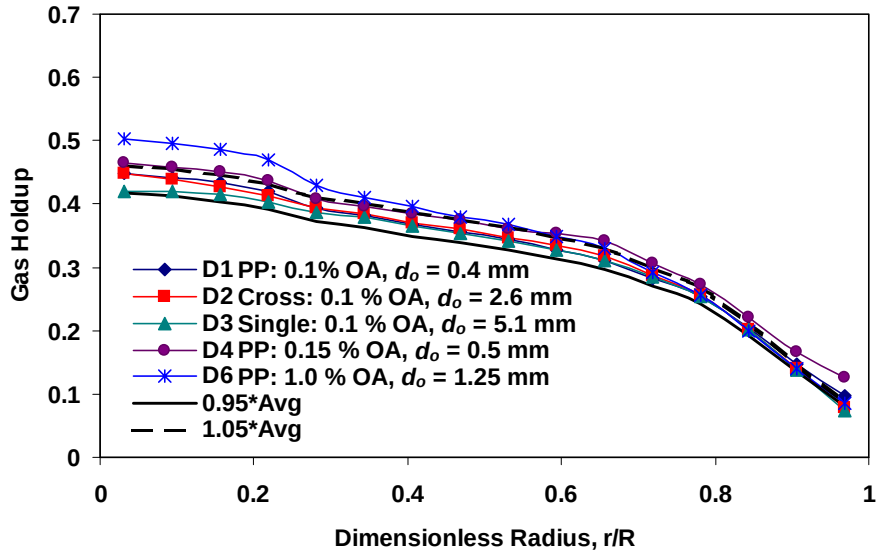

Figure 4-8. Effect of spargers at U_g = 30 cm/s at scan level z/D = 5.5 (P = 1 atm).

Examination of Figure 4-7 reveals that, for a U_g of 14 cm/s and atmospheric pressure, the cross and single nozzle spargers produce the lowest radial gas holdup profile, whereas the perforated plate distributors produce higher holdups which are proportional to their percentage open area (POA). In other words, for the perforated plate distributors, the holdup is the largest for D4 (0.15 POA), followed by D1 (0.1 POA) and lastly D5 (0.04 POA). In spite of these differences in gas holdup profiles measured using the perforated plate distributor, distributors D2 and D3, which are the cross and the single nozzle spargers, respectively, generate almost identical gas holdup profiles. The behavior of D2 and D3 is significantly different even from distributor D1, which has the same percent open area, but is a perforated plate. Kumar (1994) also observed a similar trend in measured gas holdup profiles using a slightly larger column (19-cm diameter) with a perforated plate (166 holes of 0.33 mm ID, square pitch, 0.05 POA), bubble cap and cone distributor. One possible explanation for the observed differences may lie in the bubble formation regimes of the different spargers. Because of the significantly stronger jetting/dispersed jetting mode of gas introduction by spargers D2 and D3, it is likely that the stable bubble structure produced by perforated plates cannot be maintained and one transitions early to churn-turbulent flow. It is likely then that the perforated plate distributors induce a very stable bubble structure in the column that suppresses

coalescence of bubbles and leads to higher gas holdups. This is confirmed from Table 4-2 since gas introduction by distributors D4 and D1 at U_g = 14 cm/s and P = 1 atm is in the bubbling regime based on Idogawa *et al.* (1987[b]). These observations indicate that transition to churn-turbulent flow is indeed dependent on the sparger type, and few of the previously reported studies seem to consider this effect. This can be seen from Table 4-3, which lists the estimated transition velocity for each sparger and one can see that the existing procedures do not account for the effect of distributors on transition velocity. Similar observation can be made regarding the equilibrium bubble size. Barring the correlation of Kumar *et al.* (1976), it is evident from Table 4-4 that the current state of the art for predicting bubble sizes assumes that the stable bubble size is independent of distributor. The above observations expose the limitations of the existing body of literature and provide potential opportunities for future investigations. However, it should be kept in mind that perforated plates are rarely employed for industrial systems, with spargers similar to D2 and D3 being preferred. It can therefore be said that for industrially important spargers, the effect of sparger design can be considered negligible for superficial gas velocities exceeding 14 cm/s at P = 1 atm.

As mentioned earlier, at P = 1 atm and U_g = 14 cm/s, when one compares the radial gas holdup distributions for the perforated plate distributors (D1 - 0.1 POA; D4 - 0.15 POA; D5 - 0.04 POA), one sees that the gas holdup obtained using D4 is systematically higher than that for D1 at all radial locations (Figure 4-7). The reason for this could be the larger size of the orifice holes for distributor D4 (0.5-mm) as compared to D1 (0.4-mm). Therefore, in spite of the same distribution of orifices for these two spargers, the same bubble number density (per unit sparger cross section) with larger bubble diameter will result in greater gas holdup for distributor D4. A larger orifice diameter implies a lower orifice velocity, hence slightly larger bubbles are formed with lower ejection velocity and a lower frequency of bubbling. Also, with similar bubble number density, larger bubbles would produce greater hindrance to the rise of individual bubbles, implying a larger holdup. If this distribution of bubbles does not undergo coalescence as the bubble swarm rises up, larger gas holdup for D4 could be maintained along the entire column length as compared to gas holdup obtained using D1.

Table 4-4. Equilibrium bubble size (cm) calculations for different operating conditions using correlations in Table 2-6.

	P, atm	U_g, m/s	Equilibrium bubble size, cm				Maximum stable bubble size, cm			$d_{b,large}$,cm
			Akita & Yoshida (1973)	Kumar *et al.* (1976)	Wilkinson (1991)	Ellenberger and Krishna (1994)	Hinze[†]	Walter & Blanch (1986)	Lin *et al.* (1998)	Krishna (2000)
D1 (0.1%, 163 orifices of 0.4 mm)	1	0.14	0.49	0.39	0.45	8.03	0.21	0.39	1.48	3.02
	1	0.3	0.45	0.29	0.44	17.7	0.15	0.28	1.09	4.22
	1	0.45	0.42	0.24	0.44	27.6	0.13	0.24	0.93	4.98
	4	0.3	0.45	0.16	0.38	15.3	0.15	0.28	0.83	4.12
D2 (0.1%, 4 orifices of 2.6 mm)	1	0.14	0.49	0.48	0.45	15.0	0.21	0.39	1.48	3.02
	1	0.3	0.45	0.35	0.44	26.4	0.15	0.28	1.09	4.22
	4	0.3	0.45	0.20	0.38	23.6	0.15	0.28	0.83	4.12
D3 (0.1%, 1 orifices of 5.1 mm)	1	0.14	0.49	0.50	0.45	22.2	0.21	0.39	1.48	3.02
	1	0.3	0.45	0.37	0.44	35.8	0.15	0.28	1.09	4.22
	4	0.3	0.45	0.21	0.38	32.6	0.15	0.28	0.83	4.12
D4 (0.15%, 163 orifices of 0.5 mm)	1	0.02	0.62	0.49	0.47	1.58	0.46	0.84	3.22	-
	1	0.08	0.52	0.88	0.45	4.74	0.26	0.48	1.85	2.25
	1	0.14	0.49	0.48	0.45	8.03	0.21	0.39	1.48	3.02
	1	0.3	0.45	0.35	0.44	17.7	0.15	0.28	1.09	4.22
	1	0.45	0.42	0.30	0.44	27.6	0.13	0.24	0.93	4.98
	1	0.6	0.41	0.27	0.43	38.2	0.12	0.22	0.83	5.59
	4	0.02	0.62	0.88	0.40	-	0.46	0.84	2.44	-
	4	0.08	0.52	0.34	0.39	2.73	0.26	0.48	1.40	1.94
	4	0.14	0.49	0.27	0.38	5.90	0.21	0.39	1.12	2.84
	4	0.3	0.45	0.20	0.38	15.3	0.15	0.28	0.83	4.12
	4	0.45	0.42	0.17	0.38	25.0	0.13	0.24	0.70	4.91
	10	0.02	0.62	0.41	0.36	-	0.46	0.84	2.03	-
	10	0.08	0.52	0.24	0.35	-	0.26	0.48	1.17	1.71
	10	0.14	0.49	0.19	0.35	3.50	0.21	0.39	0.93	2.72

[†] As reported in Wallis (1969)

Table 4-4. Equilibrium bubble size (cm) calculations for different operating conditions using correlations in Table 2-6 – Cont'd

	P, atm	U_g, m/s	Equilibrium bubble size, cm				Maximum stable bubble size, cm			$d_{b,large}$,cm
			Akita & Yoshida (1973)	Kumar *et al.* (1976)	Wilkinson (1991)	Ellenberger and Krishna (1994)	Hinze[†]	Walter & Blanch (1986)	Lin *et al.* (1998)	Krishna (2000)
D5 (0.04%, 61 orifices of 0.4 mm)	1	0.14	0.49	0.26	0.45	8.90	0.21	0.39	1.48	3.02
D6 (1.25%, 163 orifices of 1.25 mm)	1	0.3	0.45	0.80	0.44	17.7	0.15	0.28	1.09	4.22
	4	0.3	0.45	0.46	0.38	15.3	0.15	0.28	0.83	4.12
	10	0.3	0.45	0.32	0.34	12.5	0.15	0.28	0.69	4.07

[†] As reported in Wallis (1969)

The observations above regarding the gas holdup distributions obtained using spargers D1 and D4 are contrary to the findings of Tsuchiya and Nakanishi (1992) who concluded that the average gas holdup decreases with increasing orifice diameter when keeping the number of holes on the perforated plate fixed. However, their measurements were made in a very tall column of 14.8-cm ID and 8.0-m high resulting in L/D = 55. Perhaps a much higher L/D ratio of 55 in their study, as opposed to 15 in this study, is the source of these different findings. In other words, they might have experienced a slugging flow pattern not seen in this investigation. The holdup obtained with D5 is lower than that obtained with D1 probably due to a lower percent open area (POA); however, there is no clear trend in the differences at various radial locations. Nevertheless, considering all the spargers evaluated in this study, sparger design does appear to have an influence on gas holdup even at operating conditions which are normally taken to be in the churn-turbulent regime such as U_g = 14 cm/s at P = 1 atm. However, as shown in Figure 4-8, deep in the churn-turbulent regime, at a superficial gas velocity of 30 cm/s, sparger effect on holdup distribution is small but not insignificant, which is in agreement with other reported studies (Mikkilineni and Knickle, 1987; Tsuchiya and Nakanishi, 1992; Krishna and Ellenberger, 1996).

From Figure 4-8, in addition to the observation that gas holdup values are higher and that the difference in gas holdups for the different spargers is much narrower as compared to the results at U_g = 14 cm/s, one also sees that spargers D4 and D6, which experience the bubbling regime of bubble formation, produce higher gas holdups in the center of the column while the single nozzle sparger (D3) produces the lowest. This implies that for the perforated plate spargers, the bubble number density of the smaller bubbles is larger in the column center (more so for D6, followed by D4, then D1) as compared to the cross and single nozzle spargers. Therefore, even though it might be tempting to conclude that for practical engineering purposes, the effect of distributors on gas holdup is insignificant at U_g = 30 cm/s and at P = 1 atm, the Computed Tomographic measurements from this study indicate that the detected differences are small but larger than expected due to the usual band of reproducibility. It should, however, still be emphasized that distributor effect on gas holdup profile remains small even when the

open area of the distributors is changed from 0.1 % (perforated plate D1, cross sparger D2, single nozzle D3) to 1.0 % (perforated plate D6). Only slightly higher holdups at *r/R* greater than 0.9 were observed for perforated plate distributor, D4 with 0.15 % open area and at *r/R* less than 0.2 for perforated plate distributor, D6 with 1.0 % open area than for D1, D2, and D3 with 0.1 % open area. Therefore, at atmospheric pressure and deep in the churn-turbulent regime for tall columns, it may be reasonable to assume insignificant distributor effects on gas holdup.

The results presented until now were for different U_g and spargers at atmospheric pressure. It is, however, important to investigate the effect of spargers on gas holdup at higher operating pressure. Figure 4-9 displays the radial gas holdup profiles for distributors D1, D2, D3, D4 and D6 measured at a superficial gas velocity of 30 cm/s at z/D = 5.5 at P = 4 atm. As shown in Figure 4-9, the radial gas holdup profiles for perforated plate distributor D1 and cross sparger D2 fall within the 10 % band around the mean, whereas holdup profiles generated by D3 (single nozzle of 0.1% porosity) and D6 (perforated plate of 1% porosity) lie above and below the 10% band, respectively. If one considers all the distributors other than D3 (single nozzle), at P = 4 atm and U_g = 30 cm/s one can conclude that there is not a significant distributor effect on radial gas holdup profile, except near the column walls. Figure 4-9 also shows that the radial gas holdup exhibited using D3 (single nozzle) is comparatively much higher as compared to the rest of the distributors. This could be explained from the studies conducted by Kling (1962) and La Nauze and Harris (1974) who used nozzles of various orifice diameters. They reported that upon increasing the pressure, the gas jet produced by the nozzle disperses and breaks up more rapidly and forms more numerous small bubbles. In this case, the level of liquid turbulence generated using a single nozzle might be so much greater than turbulence generated by the perforated plate and cross distributors that the gas holdup increases substantially for the single nozzle sparger.

In summary, though small, the effect of distributors on gas holdup deep in the churn-turbulent regime should not be entirely ignored during reactor design and scale-up. For estimation of bubble sizes, it appears from Table 4-4 that the correlations of Kumar *et al.* (1976) and Wilkinson (1991) provide the most reasonable estimate of equilibrium

bubble sizes while capturing the effect of a decrease in bubble size with an increase in pressure. Interestingly, the prediction of the size of "large" bubbles based on Krishna's (2000) approach also indicates a decrease in bubble size with pressure.

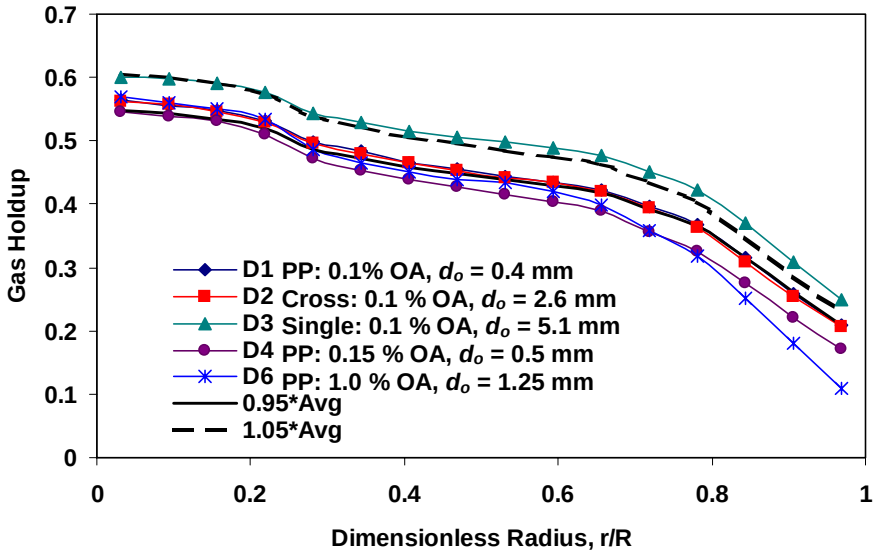

Figure 4-9. Effect of spargers at U_g = 30 cm/s at scan level z/D = 5.5 (P = 4 atm).

4.5. Axial Variation of Gas Holdup

As was shown in the last section, the perforated plate distributors generate higher gas holdup than cross and single nozzle spargers at atmospheric pressure. This could be due to the presence of distributor effects in the middle portion of the column. Figures 4-10 and 4-11 show the axial variation of the radial holdup profile, $\varepsilon_{gi}(r,z)$, for perforated plate distributor, D1 and for single nozzle sparger, D3 at U_g = 14 cm/s at atmospheric pressure, respectively. From Figure 4-10, which is for a uniform perforated plate distributor, D1, one can clearly see a significant axial variation of gas holdup. One also observes a consistent trend for this perforated plate distributor (D1), where the gas holdup uniformly decreases with height. This implies that at this superficial gas velocity the primary bubble size at the distributor is smaller than the secondary (stable) bubble

size (Joshi *et al*., 1998), which can also be seen from Tables 4-3 and 4-4. Similar conclusions regarding the axial variation of the radial gas holdup profiles are reached for other perforated plate distributors D4 and D5.

For a single nozzle distributor D3, as displayed in Figure 4-10, there is relatively small but finite axial variation of the radial gas holdup profile. It can be seen from the figure that gas holdup marginally increases with height, which implies that the average bubble size at the sparger is slightly larger than the equilibrium bubble diameter. These findings are in agreement with studies of Shollenberger *et al*. (2000). The same observation holds for the cross sparger, D2, and can be explained in terms of the stable bubble size, which is attained relatively close to the sparger, implying that the sparger zone for these two distributors is confined to less than two column diameters.

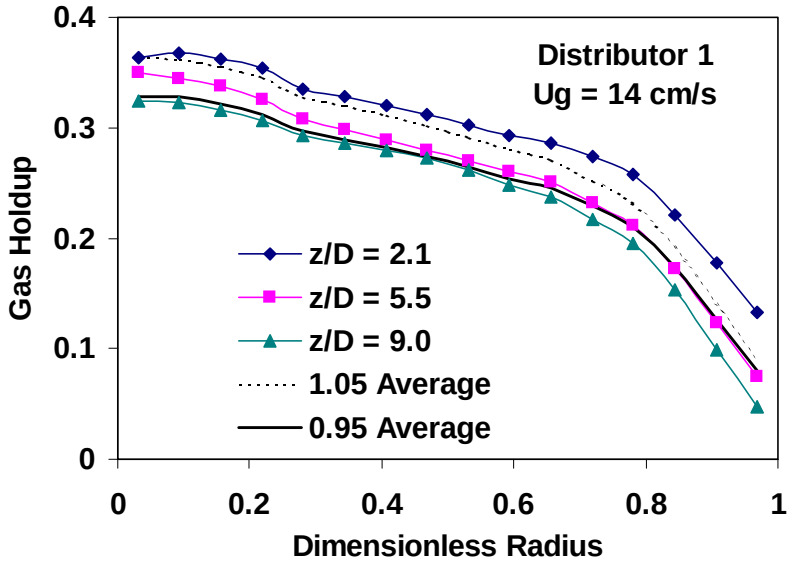

Figure 4-10. Axial variation of gas holdup for perforated plate distributor D1 (0.1% open area; d_o = 0.4 mm) at U_g = 14 cm/s (P = 1 atm).

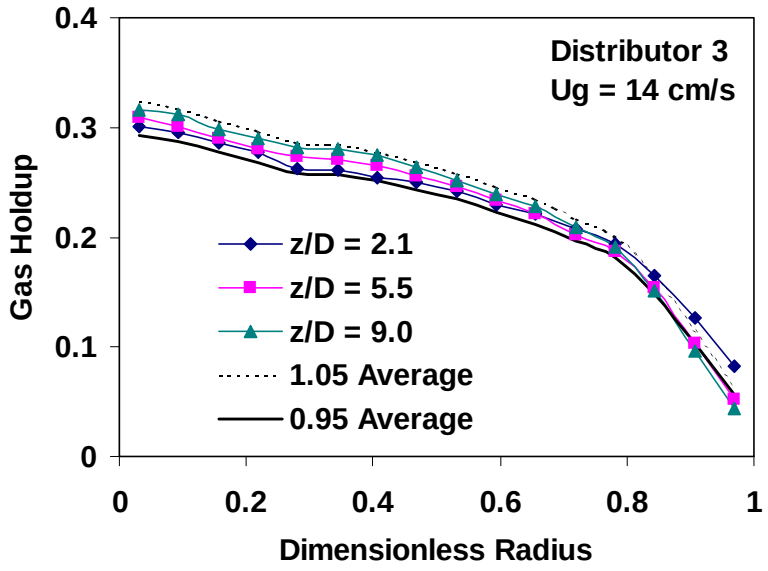

Figure 4-11. Axial variation of gas holdup for single nozzle sparger D3 (0.1% open area; d_o = 5.1 mm) at U_g = 14 cm/s (P = 1 atm).

At U_g = 30 cm/s and at P = 1 atm, the radial gas holdup profiles for all distributors investigated are not a function of axial position (except for points at r/R > 0.85 at z/D = 2.1) as shown in Figure 4-12 for D2 (cross sparger) and D4 (perforated plate distributor). This implies that the entry region is confined to about two column diameters, which is in agreement with the findings of Shollenberger *et al*. (2000).

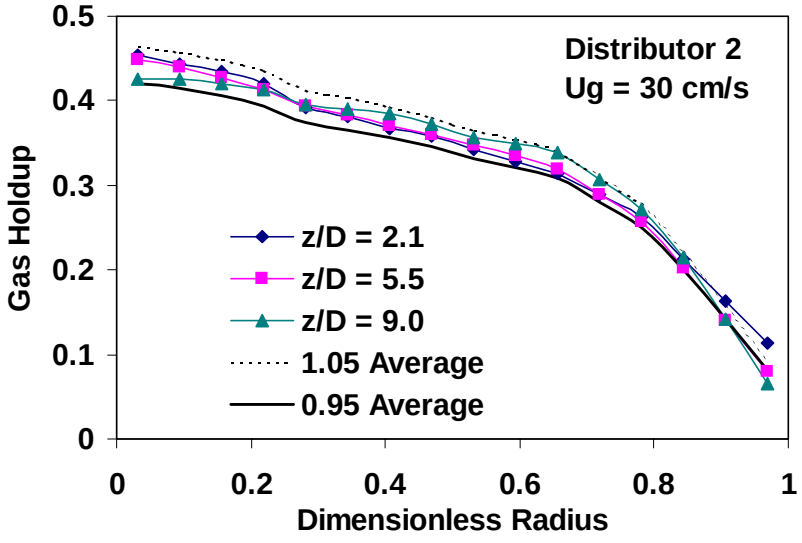

(a)

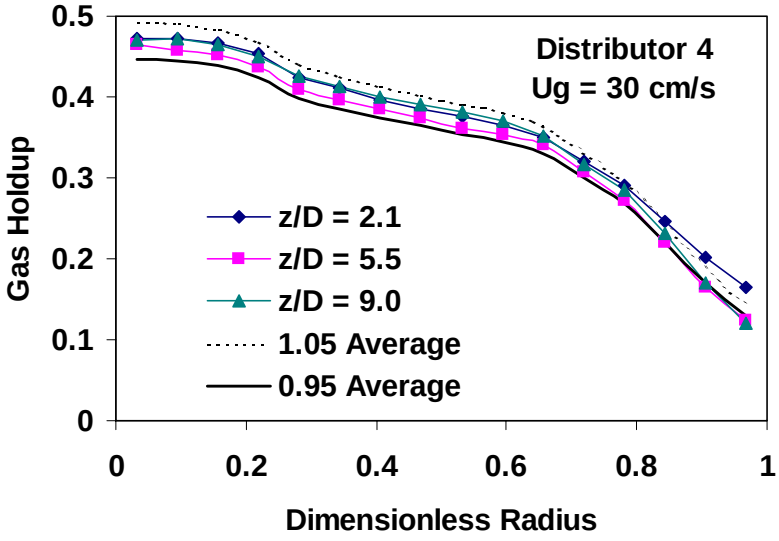

(b)

Figure 4-12. Axial variation of gas holdup for a) cross sparger D2 (0.1% open area; d_o = 2.6 mm) and b) perforated plate D4 (0.15% open area; d_o = 0.5 mm) at U_g = 30 cm/s (P = 1 atm).

Figure 4-13 displays the cross-sectional average gas holdup as a function of *z/D* for different distributors at different operating conditions. There are several trends for the axial variation of gas holdup and this can be explained in terms of primary and secondary bubble sizes (Joshi *et al.*, 1998), which are described in the beginning of this section for uniform perforated plate distributor, D1. There are some interesting observations that can be extracted from Figures 4-13d and 4-13e for the uniform perforated plate distributor, D4 at a superficial gas velocity of 8 and 14 cm/s. At a superficial gas velocity of 8 cm/s at atmospheric pressure (refer to Figure 4-13d), gas holdup increases with axial position along the column. That is to say, the primary bubble size formed at the distributor is larger than the secondary (equilibrium) bubble size in the latter sections of the column. This is possible since this condition might be within the range where transition from homogeneous regime to churn-turbulent flow occurs. At a higher pressure of 4 atm, it was found that gas holdup for U_g = 14 cm/s is lower than that at U_g = 8 cm/s for all axial locations (refer to Figure 4-13e). The reason might be that at U_g = 14 cm/s, the flow is

still not deep in the churn-turbulent regime and also at U_g = 8 cm/s, the flow is in the transition regime going through a maximum in the variation of gas holdup with U_g.

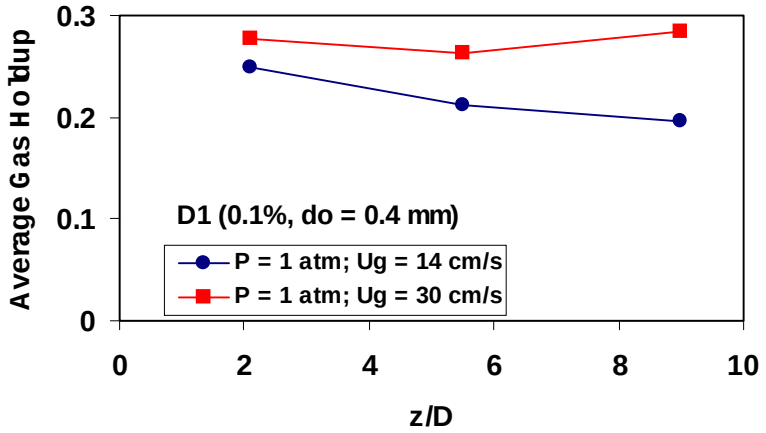

(a)

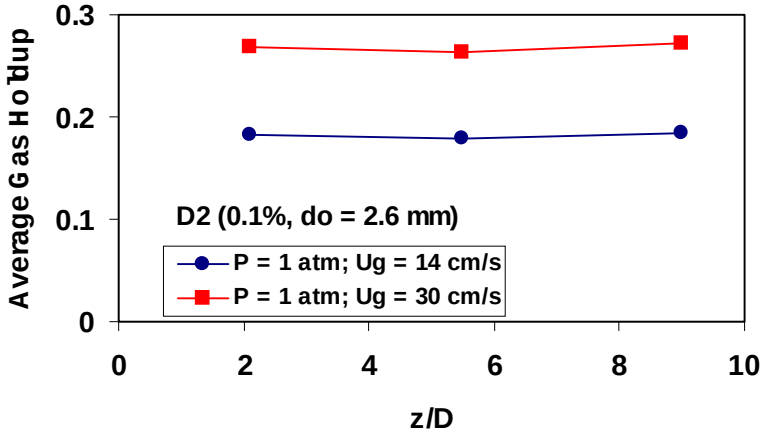

(b)

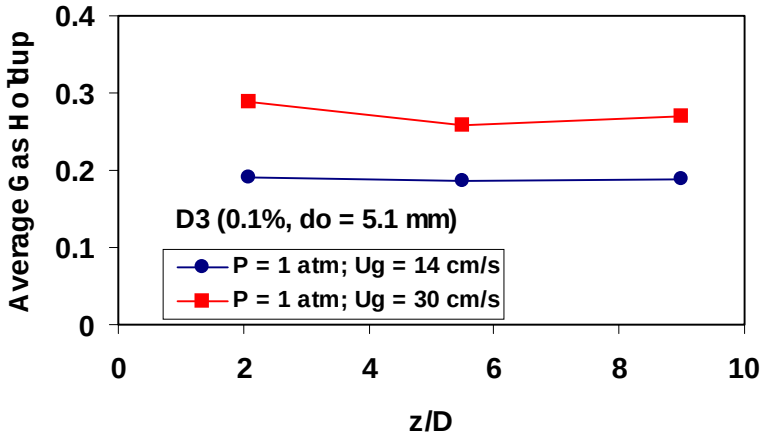

(c)

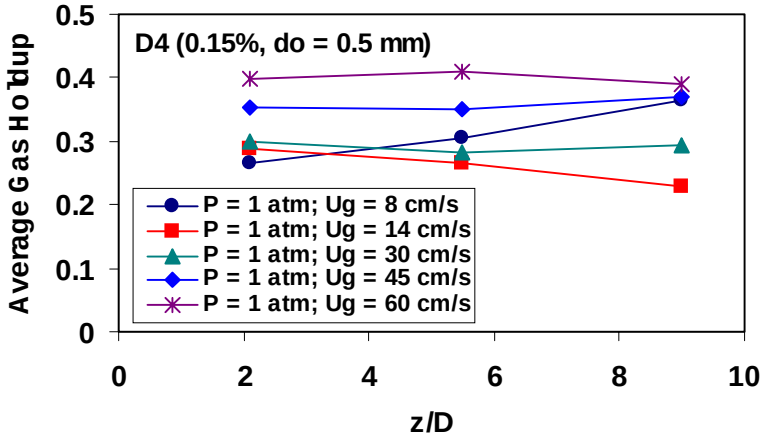
D4 (0.15%, do = 0.5 mm)
Average Gas Holdup
z/D
P = 1 atm; Ug = 8 cm/s
P = 1 atm; Ug = 14 cm/s
P = 1 atm; Ug = 30 cm/s
P = 1 atm; Ug = 45 cm/s
P = 1 atm; Ug = 60 cm/s

(d)

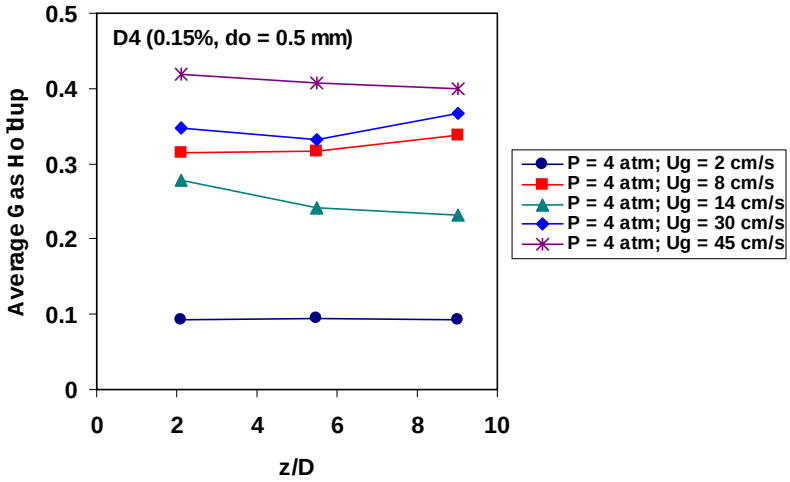
D4 (0.15%, do = 0.5 mm)
Average Gas Holdup
z/D
P = 4 atm; Ug = 2 cm/s
P = 4 atm; Ug = 8 cm/s
P = 4 atm; Ug = 14 cm/s
P = 4 atm; Ug = 30 cm/s
P = 4 atm; Ug = 45 cm/s

(e)

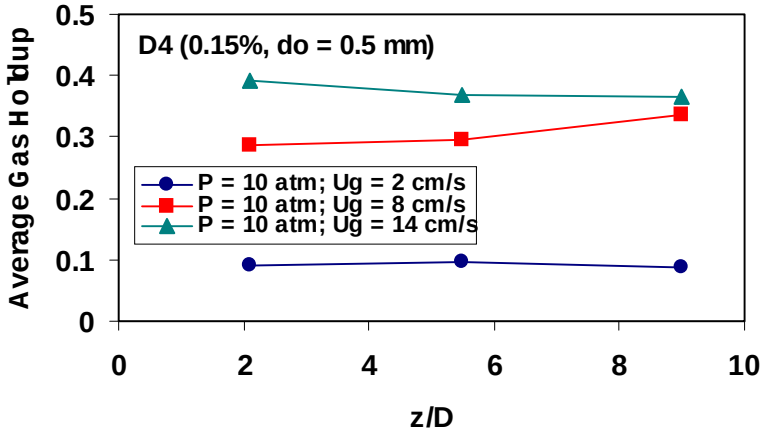
D4 (0.15%, do = 0.5 mm)
Average Gas Holdup
z/D
P = 10 atm; Ug = 2 cm/s
P = 10 atm; Ug = 8 cm/s
P = 10 atm; Ug = 14 cm/s

(f)

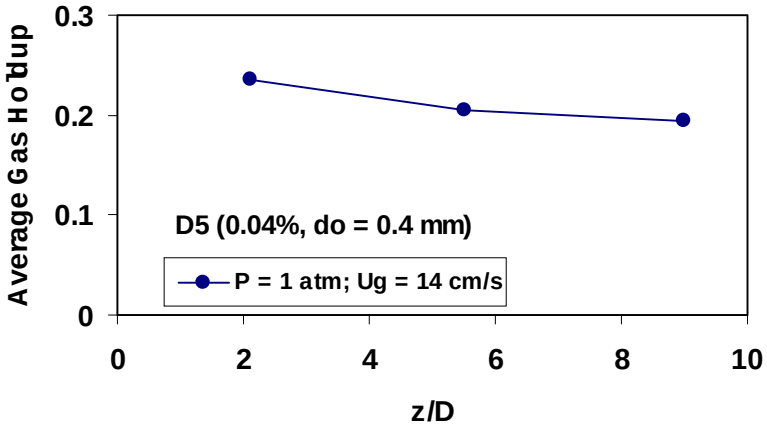

(g)

Figure 4-13. Cross-sectional average gas holdup as a function of *z/D* for (a) uniform perforated plate distributor D1; (b) cross sparger, D2; (c) single nozzle, D3; (d-f) uniform perforated plate distributor, D4 for different pressures; (g) perforated plate distributor, D5.

A possible physical explanation for these observations is as follows. The increase in gas holdup along the column length for U_g = 8 cm/s could only be attributed to 1) lack of coalescence; 2) expansion of bubble volumes due to reduction of hydrostatic head as bubbles rise up the column. The combination of these two can explain the increase in gas holdup with height due to preservation of bubble number density as a result of lack of bubble coalescence. On the other hand, at U_g = 14 cm/s, the prevalent dynamics in the column are such that coalescence is probably promoted among the bubbles as they rise up the column. As a result, bubble size increases not only due to bubble volume expansion resulting from the reduction of hydrostatic head, but also due to bubble coalescence. However, in this case, the bubble number density is not preserved due to coalescence and hence, a reduction in gas holdup along the column length is observed.

4.6. Effect of Superficial Gas Velocity on Radial Gas Holdup Profiles

It has been previously well-established that the gas superficial velocity, U_g, is the primary variable that affects gas holdup profiles and that increased U_g leads to higher gas holdup and steeper radial holdup profiles (Hills, 1974; Yao *et al*., 1991; Kumar, 1994; Kemoun *et al.*, 2001). This is illustrated in Figures 4-14 and 4-15 where the variation of radial gas holdup profile with superficial gas velocity is displayed for perforated plate distributor D4 at z/D = 5.5 at atmospheric pressure and at P = 4 atm, respectively. As expected, the cross-sectional average gas holdup from the tomographic scans, as well as the radial gas holdup gradient increases as the superficial gas velocity is increased above 14 cm/s (Ueyama *et al*., 1980; Kumar, 1994; Joshi *et al*., 1998). However, at a pressure of 4 atm, the average gas holdup increases to a maximum at a superficial gas velocity of 8 cm/s, it decreases then before gradually increasing with superficial gas velocity (refer to Figure 4-15b). Further discussion on the effect of pressure on the radial gas holdup distribution is presented in Section 4.7.

One can draw some additional conclusions from Figures 4-14 and 4-15. It seems that as long as bubbly flow is maintained, the radial gas holdup profile is relatively flat as can be seen with uniform perforated plate distributor D4, where a flat holdup profile is observed even at U_g = 8 cm/s. Increasing the U_g from 2 cm/s to 8 cm/s simply raised the flat holdup profile from 0.1 to 0.4 (refer to Figure 4-15). Once instability occurs, it results in pushing more gas to the center of the column, where it moves as rapidly rising large void spaces. Thus, in transition flow, one increases the slope of the radial gas holdup profile. However, once deep in the churn-turbulent regime where the slope of the holdup profile has already been established through the transition regime, further increase in U_g results in lifting the holdup profile without pronounced changes in the radial gas holdup gradient. Similar observations are attained at z/D = 2.1 and 9.0.

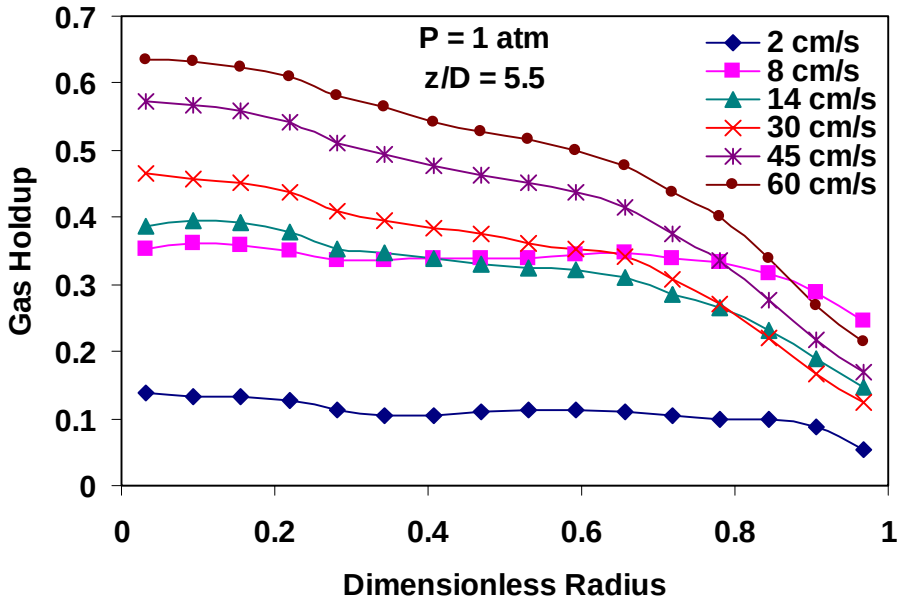

(a)

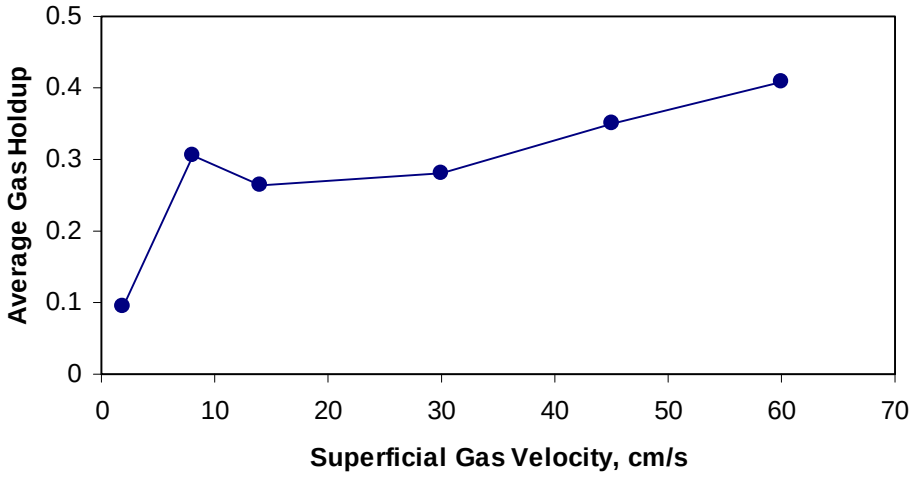

(b)

Figure 4-14. Effect of superficial gas velocity on (a) radial gas holdup; (b) cross-sectional average gas holdup from CT scans using perforated plate distributor D4 (0.15% open area; d_o = 0.5 mm) at z/D = 5.5 (P = 1 atm).

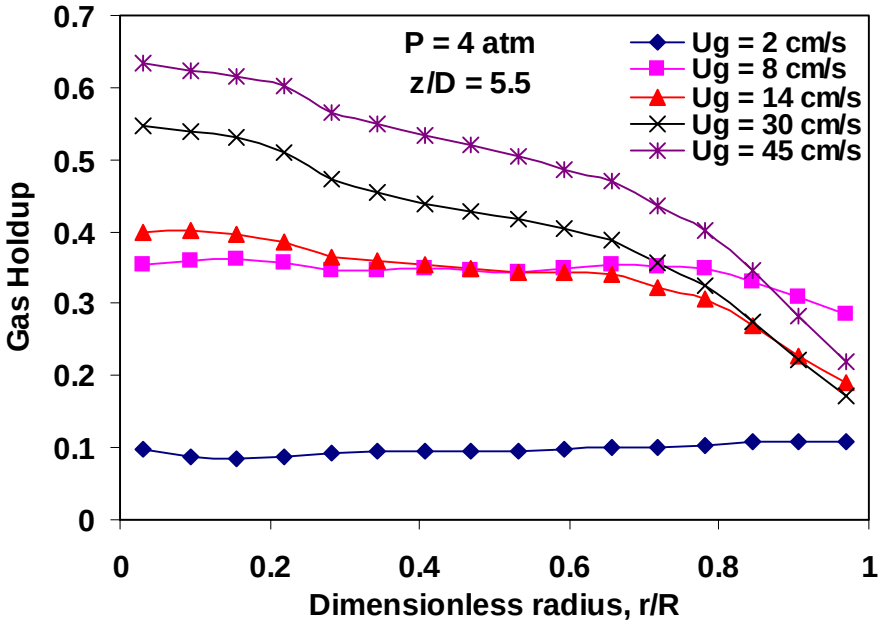

(a)

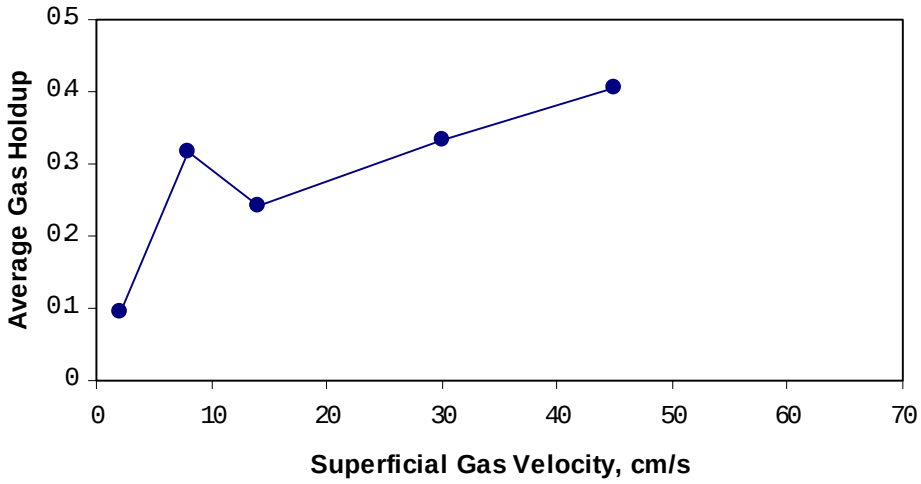

(b)

Figure 4-15. Effect of superficial gas velocity on (a) radial gas holdup; (b) cross-sectional average gas holdup from CT scans for perforated plate distributor D4 (0.15 % open area; d_o = 0.5 mm) at z/D = 5.5 (P = 4 atm).

An assessment of the steepness of the radial gas holdup profiles can be accomplished by Equation (4-4).

$$F = \left| \left(\frac{d\varepsilon_g}{d\xi} \right)_{average} \right| = \left| 2\int_0^1 \xi \frac{d\varepsilon_g}{d\xi} d\xi \right|_{average} = 2\tilde{\varepsilon}_g c \frac{m+2}{m+1} = 2\overline{\varepsilon_g} c \frac{m(m+2)}{(m+1)(m+2-2c)} \qquad (4\text{-}4)$$

Equation (4-4) is obtained by differentiating the empirical relation for the radial gas holdup (refer to Equation (4-5)) and the absolute value of the derivative is averaged over the cross-section for all scan levels. Equation (4-5) includes the possibility of finite holdup at the wall, and is used to fit the experimental radial gas holdup profiles.

$$\varepsilon_g(\xi) = \tilde{\varepsilon}_g \left(\frac{m+2}{m} \right) \left(1 - c\xi^m \right) \qquad (4\text{-}5)$$

In Equation (4-5), ξ is the dimensionless radial position, *m* is the exponent, *c* allows the possibility of nonzero gas holdup close to the wall and $\tilde{\varepsilon}_g$ is related to the cross-sectional average gas holdup, $\bar{\varepsilon}_g$, by Equation (4-6). A larger value of the exponent *m* indicates a flatter radial gas holdup profile while a smaller *m* (approaching the value of 2) indicates a more parabolic profile. The cross-sectional average gas holdup, $\bar{\varepsilon}_g$, is related to the parameters of the gas holdup expression as follows.

$$\bar{\varepsilon}_g = \tilde{\varepsilon}_g \left(\frac{m+2-2c}{m} \right) \qquad (4\text{-}6)$$

It can be seen from Equation (4-4) that a higher *F*-value, which depends on the parameters of the empirical equation for the radial gas holdup profile (refer to Equation (4-4)), i.e., $\bar{\varepsilon}_g$, *m* and *c*, represents a steeper gas holdup profile. From Equation (4-4), the following can be deduced.

- For constant *m* and *c*, *F* increases with increasing $\bar{\varepsilon}_g$.

- For constant $\bar{\varepsilon}_g$ and c, F decreases with increasing m.
- For constant $\bar{\varepsilon}_g$ and m, F increases with increasing c.

Chen *et al.* (1998) calculated the F-values and reported an increase in F-value with an increase in superficial gas velocity (for U_g in the range from 2 to 10 cm/s) in a 44-cm bubble column for both air-Drakeol (viscosity and specify gravity of Drakeol are approximately 17.7 to 20.2 cP and 0.838 to 0.864, respectively) and for air-water. F was found to be 0.052 and 0.157 for U_g = 2 and 10 cm/s, respectively in air-Drakeol and F values of 0.081 and 0.215 for U_g = 2 and 10 cm/s, respectively are reported for air-water systems at atmospheric pressure. Listed in Table 4-5 are the F values calculated using Equation (4-4) averaged over three scan levels for all experimental conditions using the perforated plate distributor D4 (0.15 % open area) as well as the standard deviation of the F-values for the three scan levels. A general conclusion from Table 4-5 is that for all pressures, as superficial gas velocity increases, the radial gas holdup profiles become steeper. Further assessment of the additional entries in Table 4-5 regarding the pressure effect on the steepness of the radial gas holdup profile are discussed in Section 4.7.

Table 4-5. Axially averaged F-values (± standard deviation) at various operating conditions using perforated distributor D4 (0.15% open area; d_o = 0.5 mm).

$$\overline{F} = abs\left(\sum_{i=1}^{3} F_i \Big/ 3\right)$$ (F_i refers to gas holdup at i axial location)

U_g, cm/s	Pressure, atm		
	1	4	10
2	0.124 ± 0.025	0.00293 ± 0.0022	0.00462 ± 0.0027
8	0.194 ± 0.059	0.129 ± 0.028	0.126 ± 0.057
14	0.348 ± 0.064	0.366 ± 0.033	0.325 ± 0.026
30	0.466 ± 0.050	0.465 ± 0.003	-
45	0.541 ± 0.032	0.542 ± 0.005	-
60	0.593 ± 0.052	-	-

4.7. Effect of Pressure on Gas Holdup

It is of particular interest to understand the pressure effect on gas holdup at high superficial gas velocity, say 30 cm/s. Since a vast amount of experiments were conducted using the uniform perforated plate distributor (D4) of 0.15 % open area (orifice diameter of 0.5 mm), it was deemed desirable to use this distributor also at this high gas velocity. Unfortunately, the maximum superficial velocity that can be reached with this perforated plate distributor at P = 10 atm is less than 30 cm/s. In order to study the effect of pressure at this high superficial gas velocity, which was our goal, the perforated plate of 1.0 % open area, D6, was used. Figure 4-16 shows the effect of pressure on the radial gas holdup for perforated plate distributor D4 for superficial gas velocities up to 14 cm/s, and for perforated plate distributor D6 for superficial gas velocity of 30 cm/s at z/D of 5.5. It can be seen from the figure that gas holdup increases with increasing pressure only in the churn-turbulent flow. This is in agreement with the observations reported in the literature (Idogawa *et al.*, 1986; Jiang *et al.*, 1995; Kojima *et al.*, 1991; Kojima *et al.*, 1997; Oyevaar *et al.*, 1989; Luo *et al.*, 1999; Kemoun *et al.*, 2001).

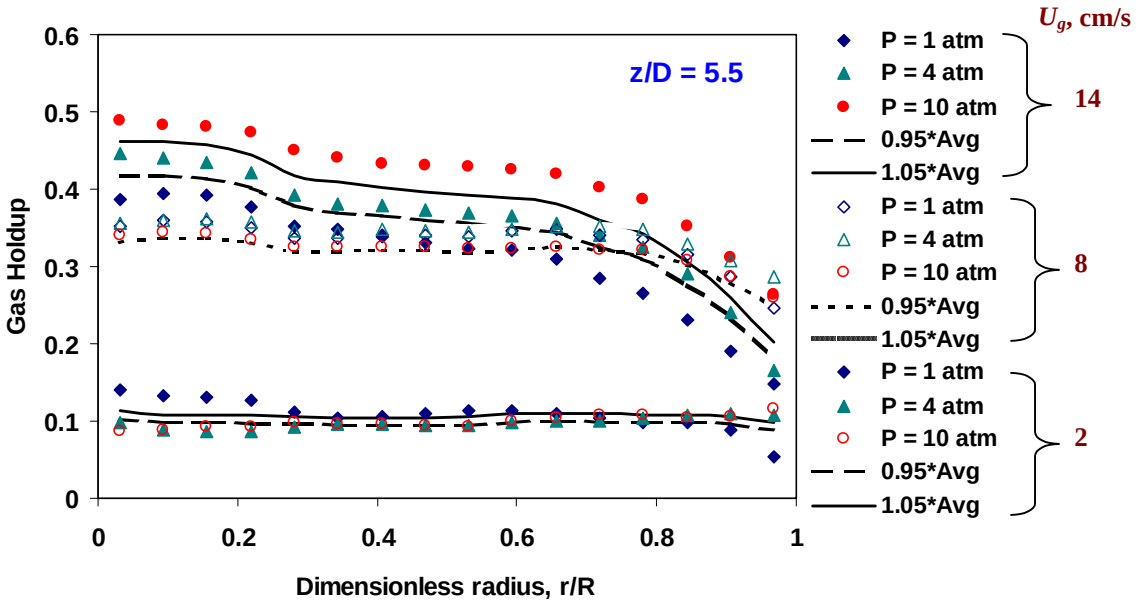

(a)

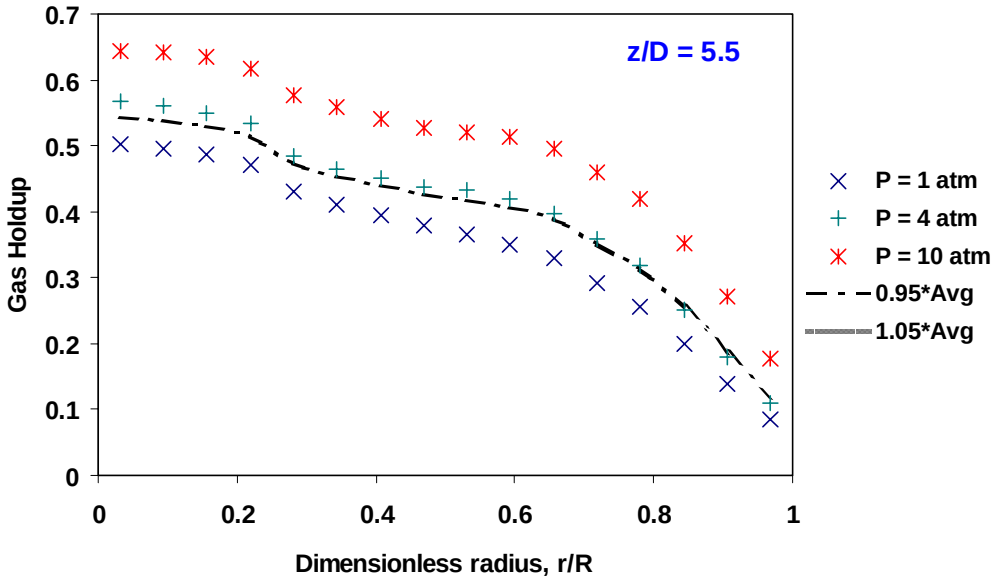

(b)

Figure 4-16. Effect of pressure on gas holdup profiles obtained at z/D = 5.5 using (a) uniform perforated distributor D4 (0.15% open area; d_o = 0.5 mm) for superficial gas velocities up to 14 cm/s and (b) uniform perforated distributor D6 (1.0 % open area; d_o = 1.25 mm) at U_g = 30 cm/s.

From Figure 4-16, one can also see that at both superficial gas velocities of 2 cm/s and 8 cm/s for perforated plate distributor D4, there is no significant effect of pressure on holdup. This is in agreement with the findings of Letzel (1997) who reported that when bubbly flow conditions prevail gas holdup is relatively independent of pressure. The phenomena can also be explained in terms of using the gas holdup correlation developed by Krishna (2000), whose methodology involves calculating gas holdup in the small (dense) and large (dilute) bubble phases (refer to Equations (2-6) to (2-10)). Based on the definitions for the above quantities, as presented in Chapter 2, Table 4-6 shows the calculated rise velocity of dense (small) bubble phase, $V_{b,small}$, the transition velocity (superficial gas velocity at which transition from bubbly to heterogeneous regime takes place), $U_{g,trans}$, gas holdup at transition, ε_{trans}, large bubble diameter, $d_{b,large}$, and overall gas holdup, ε_g, for different operating conditions. It can be seen from Table 4-6 that at a low superficial gas velocity of 2 cm/s, though finite , there is not much change in the

overall gas holdup with increasing pressure. The relative insensitivity of gas holdup with increasing pressure at low superficial gas velocities (lower than transition superficial gas velocity) could be explained from Equations (2-7a) and (2-8). From these equations, it can be seen that the gas holdup at low superficial gas velocity depends on the value of $V^0_{b,small}$, which has a very low sensitivity to pressure ($\propto \rho_g^{-0.04}$). Hence, gas holdup does not change much with pressure at low superficial gas velocity. On the other hand, at higher superficial gas velocity, the overall gas holdup increases with pressure primarily due to decreasing $V_{b,large}$. It is interesting to note from Table 4-6 that for superficial gas velocities greater than 14 cm/s (where one expects to be in the churn-turbulent regime), the decrease in the diameter of the large bubbles with pressure is relatively small. In spite of this small change in bubble diameter, the velocity of the large bubbles decreases significantly with pressure. This is due to the strong influence of the density correction factor (*DF*) presented in Equation (2-10) which shows an inverse proportionality to the square root of gas density as was developed by Letzel (1997) based on the Kelvin-Helmholtz instability analysis.

The cross-sectional average gas holdup can be computed from the radial holdup profile as follows.

$$\bar{\varepsilon}_{g,scan}(z) = \frac{2}{R^2}\int_0^R r\,\varepsilon_g(r,z)\,dr \tag{4-7}$$

Table 4-6. Predicted parameters using the gas holdup correlation developed by Krishna *et al.* (2000).

P, atm	U_g, m/s	$V_{b,small}$, m/s	ε_{trans}	$U_{g,trans}$, m/s	$d_{b,large}$, cm	$V_{b,large}$, m/s	ε_g
1	0.02	0.255	0.131	0.0291	-	-	0.0858
	0.08	0.255	0.131	0.0291	2.25	1.007	0.175
	0.14	0.255	0.131	0.0291	3.02	1.213	0.211
	0.3	0.255	0.131	0.0291	4.22	1.629	0.276
	0.45	0.255	0.131	0.0291	4.98	1.977	0.316
	0.6	0.255	0.131	0.0291	5.59	2.311	0.346
4	0.02	0.241	0.256	0.0459	-	-	0.0913
	0.08	0.241	0.256	0.0459	1.94	0.463	0.311
	0.14	0.241	0.256	0.0459	2.84	0.581	0.376
	0.3	0.241	0.256	0.0459	4.12	0.794	0.494
	0.45	0.241	0.256	0.0459	4.91	0.969	0.566
	0.6	0.241	0.256	0.0459	5.53	1.137	0.619
10	0.02	0.232	0.397	0.0557	-	-	0.0951
	0.08	0.232	0.397	0.0557	1.71	0.278	0.450
	0.14	0.232	0.397	0.0557	2.72	0.357	0.539
	0.3	0.232	0.397	0.0557	4.06	0.495	0.695
	0.45	0.232	0.397	0.0557	4.86	0.606	0.789
	0.6	0.232	0.397	0.0557	5.49	0.712	0.858

Figure 4-17 shows the cross-sectional average gas holdup obtained from Computed Tomography (Equation (4-7)) as a function of superficial gas velocity for uniform perforated plate distributor D4 at different pressures at z/D = 5.5. Gas holdup is rather insensitive to pressure at low superficial gas velocities (below 5 cm/s) as reported by Kölbel *et al*. (1961), Deckwer *et al*. (1980) and Letzel (1997). With increasing U_g, the average gas holdup increases initially, drops at a critical U_g value, and then gradually increases again. A transition from homogeneous (bubbly flow) to heterogeneous (churn-turbulent flow) regime is indicated by a sudden drop in gas holdup (Joshi *et al*., 1998). As shown in Figure 4-17, this regime transition seems to occur at a U_g between 8 and 14 cm/s at atmospheric pressure, as gas holdup exhibits a dip, levels off and then increases again at higher U_g. It can also be seen from comparison of the data for P = 1 atm and P = 10 atm in Figure 4-17 that the transition from homogeneous to heterogeneous regime is shifted towards higher U_g at higher pressures. At higher pressure, homogeneous regime

seems to prevail at higher gas superficial velocities, and hence, the flow regime transition is shifted to higher superficial gas velocity as pressure increases. This is in agreement with the observations of Oyevaar *et al*. (1989), Wilkinson *et al*. (1992), Letzel (1997) and Lin *et al*. (1999).

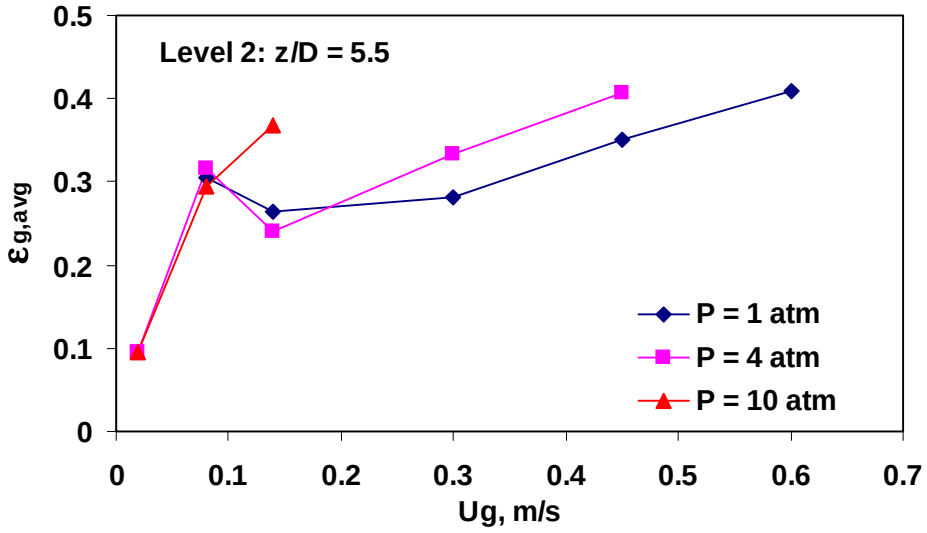

Figure 4-17. Cross-sectional average gas holdup as a function of superficial gas velocity at different pressures for perforated plate distributor D4 (0.15% open area; d_o = 0.5 mm) at z/D = 5.5.

Until now, the discussion primarily focused on the cross-sectional average gas holdup since comparison with trends reported in the literature on overall gas holdup could be readily made. As was pointed out earlier, few studies (Kemoun *et al.*, 2001) exist in the literature which address the radial distribution of gas holdup as a function of pressure. Since a complete cross-sectional distribution of gas holdup is available from Computed Tomographic scans, it is possible to address the effect of pressure on the distribution of gas holdup. As was discussed earlier, the radial gas holdup distribution in a bubble column can be expressed via Equation (4-5). Figure 4-18 shows the plot of the gas holdup profile exponent, m (Equation (4-5)) as a function of superficial gas velocity for perforated plate distributor D4 at different pressures at z/D = 5.5. Chen *et al.* (1998)

had reported that *m* is a function of column diameter, and Kumar (1994) has shown that *m* is a function of U_g. Figure 4-18 indicates that pressure also affects the values of exponent *m*. However, in the 6.4" column studied, it can be said that the value *m* = 6.5 seems to hold for all three pressures, 1, 4 and 10 atm, at U_g less than 8 to 10 cm/s. Then *m* falls precipitously and is essentially equal to 2 at high pressure for U_g greater than 20 cm/s.

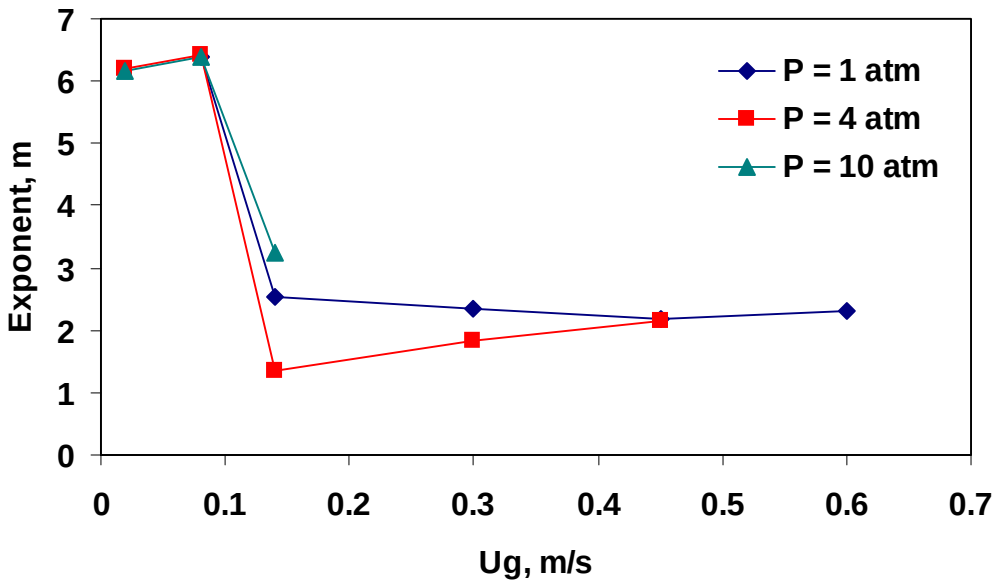

Figure 4-18. Plot of *m* values as a function of superficial gas velocity for uniform perforated plate distributor D4 (0.15% open area; d_o = 0.5 mm) at different pressures and at *z*/*D* = 5.5.

It was shown in the previous section that the exponent *m* alone is not a clear indicator of the gradient of gas holdup. Therefore, the effect of pressure on the gradient of the radial gas holdup profiles is evaluated based on Equation (4-4) and shown in Table 4-5 (refer to the Section 4.6). At the superficial gas velocity of 2 cm/s, *F* values are very low indicating bubble flow at *P* = 4 and 10 atm, and a slightly higher *F* value is seen at atmospheric pressure but still indicative of bubbly flow. At this particular operating condition of 1 atm, lower gas holdup value near the wall of the column is obtained as

compared to higher pressures (refer to Figures 4-14 and 4-15), thus, yielding a higher *c* value leading to a higher *F* value. At U_g = 2 cm/s, *F* initially decreases with pressure and levels off at high pressure indicating more stable bubbly flow at higher pressure (the accuracy of the holdup measurements is insufficient to distinguish *F* values of 0.00293 and 0.00462 since they are very much smaller than 0.1). The same trend in *F* with pressure is observed at U_g = 8 cm/s. At U_g = 14 cm/s, there is no pronounced trend in the slope of the profile, *F*, indicating that one may be close to flow regime transition at *P* = 1 atm and 4 atm at this gas velocity. Beyond a superficial gas velocity of 14 cm/s (U_g = 30 cm/s and U_g = 45 cm/s, one can see from Table 4-5 that there is insignificant change in the slope of the radial gas holdup profile.

Table 4-7 listed the *F* values calculated using Equation (4-4) for all pressures employed using uniform perforated plate distributor D6 (1.0 % open area) at a gas superficial velocity of U_g = 30 cm/s. As evident, the steepness of the radial gas holdup increases somewhat with increasing pressure, although $\bar{\varepsilon}_g$ and *m* increase with pressure while *c* displays the opposite trend with pressure. The effect of pressure on $\bar{\varepsilon}_g$ has a stronger effect on the *F*-value as compared to an increase in *m* value and a decrease in *c* value, hence, causing a significant increase in *F*-value. At these conditions, it is likely that one is deep in churn-turbulent flow and a small increase in the steepness of the holdup profile may reflect the increase in gas momentum with increased pressure. This is contradictory to the reports in the literature (Idogawa *et al*., 1986; Shollenberger *et al*., 2000; Kemoun *et al*., 2001) which indicate that the radial gas holdup profile at higher pressure is flatter, compared to that at atmospheric pressure, and that this increased flatness is to be expected since the flow regime transition from homogeneous to heterogeneous is delayed at increased pressure. In other words, based on the observations reported in the literature, one would expect the calculated *F*-values to decrease with increasing pressure. A possible explanation for this discrepancy may be that the literature observations refer to mainly bubbly, transitional and mildly churn-turbulent flows. At a given superficial gas velocity, the flow may be transitional or barely churn-turbulent at atmospheric pressure and clearly in bubbly flow at elevated pressure with transition being

delayed (Oyevaar *et al*., 1989; Wilkinson *et al*., 1992; Krishna *et al*., 1994; Letzel, 1997; Lin *et al*., 1999). Under such circumstances the holdup profile would be steeper at lower pressure, (characteristic of churn-turbulent flow which has close to parabolic holdup profiles) than at high pressure where in bubbly flow a relatively flat holdup profile prevails. However, when the superficial gas velocity is so high that at all pressures studied the flow is clearly churn-turbulent, then the effect of increasing pressure at constant gas superficial velocity is equivalent to increasing the gas momentum which leads to steeper holdup profiles. It is well known at constant pressure that an increase in gas velocity, which increases momentum, leads to steeper holdup profiles. Hence, when churn-turbulent flow is established at a given fixed gas superficial gas velocity at all pressures studied, the results of our current study indicate that at such conditions the gas holdup profiles became somewhat steeper with increased pressure.

Table 4-7. *F*-values for uniform perforated plate distributor D6 (1.0 % open area; d_o = 1.25 mm) at a superficial gas velocity of 30 cm/s for all pressures measured at *z/D* = 5.5.

P, atm	$\tilde{\varepsilon}_g$	*m*	*c*	*F*
1	0.241	1.96	0.837	0.540
4	0.289	2.29	0.811	0.611
10	0.359	2.82	0.730	0.660

4.8. Overall Gas Holdup

In majority of the studies reported in the literature, gas holdup is measured based on the bed expansion method (Equation (4-10)). It is therefore interesting to compare the CT results with those obtained via the bed expansion method. To accomplish this, the overall holdup was obtained in two ways. Radial gas holdup profiles at which CT scans were performed for each distributor (i = 1, 2, 3, 4, 5 and 6) are averaged in a cross-section to obtain a cross-sectionally averaged holdup, $\bar{\varepsilon}_{gi}(z)$ at three z elevations.

$$\bar{\varepsilon}_{gi}(z) = \frac{2}{R^2}\int_0^R r\varepsilon_{gi}(r,z)\,dr \tag{4-8}$$

These cross sectional average values are interpolated between z/D = 2.1 to z/D = 9.0 using cubic splines and are axially averaged to obtain the average total holdup.

$$\varepsilon_{gi,CT} = \frac{1}{(9.0-2.1)} \int_{z/D=2.1}^{z/D=9.0} \bar{\varepsilon}_{gi}(z)\, d(z/D) \tag{4-9}$$

Listed in Tables 4-8 and 4-9 are the cross-sectional averaged holdups at three elevations, average holdups for the fully developed flow zone determined from CT scans and overall holdup obtained by level measurement at atmospheric pressure using uniform perforated plate distributor D4 for U_g = 14 cm/s and U_g = 30 cm/s, respectively. The overall (average) holdup was obtained by dividing the difference in the dynamic height of the two-phase mixture and static liquid height by the dynamic liquid height (Equation (4-10)).

$$\varepsilon_{gi} = \frac{H_{di} - H_s}{H_{di}} \tag{4-10}$$

Table 4-8. Cross-sectional averaged and overall gas holdup at U_g = 14 cm/s and atmospheric pressure.

Sparger	Cross-sectional averaged gas holdup			$\varepsilon_{g,CT}$	ε_g	% difference $\left\lvert\frac{\varepsilon_{g,CT}-\varepsilon_g}{\varepsilon_{g,CT}}\right\rvert \times 100\%$
	z/D = 2.1	z/D = 5.5	z/D = 9.0			
D1 (PP)	0.249	0.211	0.196	0.215	0.225	4.7
D2 (Cross)	0.183	0.180	0.184	0.181	0.179	1.1
D3 (Single)	0.170	0.187	0.189	0.188	0.180	4.1
D4 (PP)	0.288	0.264	0.229	0.262	0.277	5.7
D5 (PP)	0.236	0.205	0.193	0.208	0.224	7.8
Avg. ± 2SD	0.229 ± 0.086	0.209 ± 0.067	0.198 ± 0.036	0.211 ± 0.074	0.207 ± 0.049	4.7 ± 4.9

*D1: 0.1% open area; d_o = 0.4 mm; D2: 0.1% open area; d_o = 2.6 mm; D3: 0.1% open area; d_o = 5.1 mm; D4: 0.15% open area; d_o = 0.5 mm; D5: 0.04% open area; d_o = 0.4 mm

Table 4-9. Cross-sectionally averaged and overall gas holdup at U_g = 30 cm/s and atmospheric pressure.

Sparger	Cross-sectional averaged gas holdup			$\varepsilon_{g,CT}$	ε_g	% difference $\left\|\frac{\varepsilon_{g,CT}-\varepsilon_g}{\varepsilon_{g,CT}}\right\|\times 100\%$
	z/D = 2.1	z/D = 5.5	z/D = 9.0			
D1 (PP)	0.277	0.263	0.285	0.269	0.293	9.0
D2 (Cross)	0.268	0.263	0.272	0.265	0.281	5.9
D3 (Single)	0.289	0.259	0.270	0.266	0.284	7.0
D4 (PP)	0.300	0.282	0.292	0.287	0.300	4.7
D6 (PP)	-	0.275	-	0.275	0.267	2.9
Avg. ± 2SD	0.283 ± 0.028	0.268 ± 0.019	0.280 ± 0.022	0.272 ± 0.018	0.285 ± 0.025	5.9 ± 4.6

*D1: 0.1% open area; d_o = 0.4 mm; D2: 0.1% open area; d_o = 2.6 mm; D3: 0.1% open area; d_o = 5.1 mm; D4: 0.15% open area; d_o = 0.5 mm; D6: 1.0% open area; d_o = 1.25 mm

Due to the inherent inaccuracies in determining the fluctuating free surface of the gas-liquid mixture at the top of the column, the overall gas holdup measurements could be subject to ± 10% error. Tables 4-8 and 4-9 show that the difference between CT determined average holdup, $\varepsilon_{g,CT}$ in the fully developed flow zone, and overall (average) column holdup, ε_g, is always well within 10% for all distributors. By comparison of columns 5 and 6 in Table 4-8 at U_g = 14 cm/s and atmospheric pressure, one can see that the CT determined average is a little higher than the column average for the cross and single nozzle spargers (D2 and D3). This is to be expected since the CT determined average is based on holdup values outside the distributor region. In contrast, the CT determined column average holdup for all the perforated plate distributors is lower than the column average holdup, which implies that the bubble size in the distributor region is smaller leading to higher gas holdup in that region and consequently to higher column average gas holdup.

However, at U_g = 30 cm/s and at P = 1 atm, by comparison of columns 5 and 6 in Table 4-9, the average column holdup is always somewhat higher than the CT estimated average for all distributors investigated in this study except for D6. The holdup in the sparger region, which is not measured by CT, is expected to be higher than the holdup in the fully developed flow region. In other words, our CT measurements were performed at

such elevations that they capture only the holdup in the fully developed zone, while the overall column holdup contains the contribution of all the zones.

Table 4-10 displays a similar analysis for different distributors at U_g = 30 cm/s and P = 4 atm, where the CT scans were obtained at z/D = 5.5. This table reveals that the difference between CT determined average holdup and average column holdup is always well within 20 %, which is larger as compared to the maximum 10 % difference obtained at the same superficial gas velocity at atmospheric pressure. It should be, however, pointed out that at atmospheric pressure, a relatively accurate measurement of the fluctuating gas-liquid surface was possible. Such was not the case with high pressure measurements since the top of the column was sealed for pressurizing the column and, therefore, an indirect assessment of the gas-liquid interface was obtained using the gamma-ray source and one scintillation detector. Table 4-10 also indicates a higher cross-sectional average gas holdup obtained using CT as compared to overall gas holdup for the single nozzle, D3. The single nozzle produces a jet, which penetrates into the pool of water and hence, increases the entrance length, *i.e.*, the length beyond which flow is fully developed. It can also be seen from Table 4-4 that at this operating condition, the penetration length predicted using Banks and Chandrasekhara's (1963) formula for the single nozzle is larger than for any other distributor. Hence, gas holdup is lower for a single nozzle in the entry region than in the fully developed zone, which results in the observed lower overall holdup (which accounts for the entry and fully developed zone) than the CT average holdup (which accounts only for the fully developed zone).

Table 4-10. Comparison of CT and overall gas holdup (z/D = 5.5; U_g = 30 cm/s; P = 4 atm).

Sparger	Cross-sectional averaged gas holdup, $\bar{\varepsilon}_g$	ε_g	% difference between $\bar{\varepsilon}_g$ & ε_g $\left(\%\ diff. = \frac{\bar{\varepsilon}_g - \varepsilon_g}{\bar{\varepsilon}_g} \times 100\%\right)$
D1 (PP)	0.364	0.392	7.6
D2 (Cross)	0.362	0.389	7.5
D3 (Single)	0.413	0.357	13.4
D4 (PP)	0.333	0.382	14.7
D6 (PP)	0.328	0.326	0.6
Avg. ± 2SD	0.360 ± 0.067	0.369 ± 0.055	8.8 ± 11.2

*D1: 0.1% open area; d_o = 0.4 mm; D2: 0.1% open area; d_o = 2.6 mm; D3: 0.1% open area; d_o = 5.1 mm; D4: 0.15% open area; d_o = 0.5 mm; D6: 1.0% open area; d_o = 1.25 mm

4.9. Comparison with Existing Gas Holdup Correlations

Numerous correlations for overall gas holdup in bubble columns have been reported and those that seem applicable to the conditions investigated in this study are summarized in Table 2-2. Kumar (1994) has shown that the cross-sectional average holdup measured at heights above the distributor larger than 4 to 5 column diameters is in close agreement with the overall gas holdup in the column. In addition, Tables 4-8, 4-9 and Table 4-10 confirm that the two averages are within 9% and 20 % at atmospheric pressure and P = 4 atm, respectively. Hence, the cross sectional average holdup determined in this study at the middle elevation of the column was chosen for comparison with the prediction for overall gas holdup obtained from the reported correlations. Figure 4-19 provides such a comparison, at P = 4 atm at z/D = 5.5.

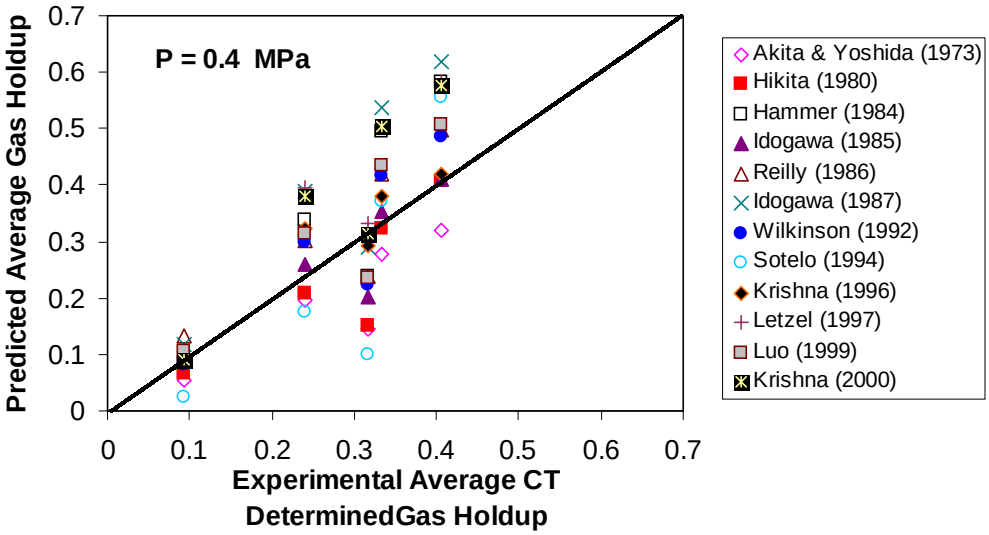

Figure 4-19. Predicted cross-sectional average gas holdup as a function of observed cross-sectional average gas holdup at P = 4 atm for perforated distributor D4 (0.15% open area; d_o = 0.5 mm).

Excellent predictions should line up as closely as possible along the diagonal of this parity plot. However, it can be seen from the figure that the predictions of the gas holdup based on literature correlations show a wide spread as compared to the CT data. Similar trends are observed at P = 1 atm and 10 atm. To quantitatively assess the discrepancies between the measured and predicted gas holdup values, Table 4-11 displays the error analysis of the overall gas holdup using different correlations for the perforated plate distributor D4 at z/D = 5.5 for all pressures studied. It can be concluded from Table 4-11 that correlations proposed by Krishna and Ellenberger (1996), Letzel (1997) and Reilly *et al.* (1986) agree the best with our experimental data followed by the correlation of Idogawa *et al.* (1985), and Wilkinson *et al.* (1992). However, at U_g = 8 cm/s, the above mentioned predictions of all correlations deviate from the observed holdup (refer to Table 4-11).

Table 4-12 lists the estimated transition superficial gas velocity using the correlation proposed by Krishna and Ellenberger (1996) for the three pressures investigated in this study. This correlation was developed based on data measured at

atmospheric pressure with gases of different densities. As shown in Table 4-12, the predicted transition velocity for all operating pressures is lower than 8 cm/s, which implies that the heterogeneous regime should prevail at a superficial gas velocity above 8 cm/s. This, however, contradicts the findings in this study, where at the superficial gas velocity of 8 cm/s, a stabilized bubbly flow exists as indicated by the flatness of the radial gas holdup profile. It is also possible that at superficial gas velocity of 8 cm/s, the system is in the transition regime, which might explain the higher gas holdup observed. Furthermore, the stabilized bubbly flow at a relatively high superficial gas velocity could also result from the extreme rigidity of the experimental apparatus as well as the immaculate smoothness of the column internal surface. It is also observed that the experimental holdup value at U_g = 8 cm/s at P = 1 atm is considerably higher than the value predicted by any of the correlations, which indicates perhaps a different flow regime (i.e. bubbly flow) during our experiment than observed in the studies used to develop these correlations. In summary, one can say that at atmospheric pressure, the correlations of Krishna and Ellenberger (1996) and Letzel (1997) result in the best prediction of gas holdup with an average deviation of 14.6 % for the five superficial gas velocities investigated in this study and a maximum deviation of 38.4% at U_g = 8 cm/s. The predicted values of transition velocity are not confirmed by our findings.

Table 4-11. Error analysis of gas holdup using different correlations (% error is reported) for perforated plate distributor D4 (0.15% open area; d_o = 0.5 mm) at z/D = 5.5.

$$\text{Absolute Relative Error} = \left|\frac{\text{Measured Value} - \text{Predicted Value}}{\text{Measured Value}}\right| \text{x}100\%$$

U_g, cm/s	Akita (1973)	Hikita (1980)	Hammer (1984)	Idogawa (1985)	Reilly (1986)	Idogawa (1987)	Wilkinson (1992)	Sotelo (1994)	Krishna (1996)	Letzel (1997)	Luo (1999)	Krishna (2000)
P = 1 atm												
8	52.8	54.9	35.3	49.4	39.4	20.6	47.2	74.6	38.4	38.4	44.4	42.0
14	25.7	28.0	8.3	23.6	11.3	26.4	16.1	48.9	16.4	16.4	12.4	19.1
30	1.9	4.9	55.3	0.3	15.0	70.3	13.7	1.8	0.2	0.2	20.0	0.2
45	8.5	6.4	49.6	5.3	9.9	59.7	8.0	22.1	7.0	7.0	14.9	7.9
60	13.6	7.9	43.6	9.4	6.8	50.8	3.6	39.4	10.9	10.9	10.6	13.4
Avg.	20.5	20.4	38.4	**17.6**	**16.5**	45.5	**17.7**	37.4	**14.6**	**14.6**	20.5	16.5
P = 4 atm												
2	42.9	28.5	9.4	8.4	41.8	25.3	13.6	73.0	3.2	3.2	12.4	3.1
8	54.5	52.7	25.0	36.1	24.8	9.0	29.8	68.3	7.6	4.8	25.5	1.4
14	18.6	14.0	39.6	7.9	25.4	61.0	23.7	27.5	34.5	63.8	29.8	58.0
30	17.0	3.3	49.0	6.2	25.9	61.8	25.1	11.7	13.9	51.6	30.9	51.0
45	21.1	0.02	43.4	0.5	22.7	51.8	19.2	36.5	2.7	43.1	24.3	41.9
Avg.	30.8	**19.7**	33.3	**11.8**	28.1	41.8	22.3	43.4	**12.4**	33.3	24.6	38.1
P = 10 atm												
2	43.7	25.5	2.8	41.3	64.4	41.3	12.6	68.4	0.7	0.7	40.8	0.6
8	51.0	46.1	9.3	12.1	4.3	9.2	3.6	59.5	42.7	61.9	1.8	53.5
14	46.6	40.3	1.3	11.4	2.6	15.8	3.6	43.5	21.8	53.5	2.0	48.2
Avg.	47.1	37.3	**4.5**	21.6	23.8	22.1	**6.5**	57.1	21.7	38.7	**14.9**	34.1

*Values in bold indicate the best agreement.

Table 4-12. Transition superficial gas velocity estimated using Wikinson *et al*. (1992) and Krishna and Ellenberger (1996).

Pressure, atm	$U_{g,trans}$ using Wilkinson *et al.* (1992), cm/s	$U_{g,trans}$ using Krishna and Ellenberger (1996), cm/s
1	0.209	2.89
4	2.10	4.57
10	4.35	5.55

Among the correlations listed in Table 2-2 those of Idogawa *et al.* (1985; 1987[a]), Wilkinson *et al*. (1992), Krishna and Ellenberger (1996), Letzel (1997) and Luo *et al.* (1999) were developed by considering high-pressure data also. As evident from Table 4-11 therefore, for P = 4 atm, the gas holdup correlations developed by Idogawa *et al*. (1985) followed by those of Krishna and Ellenberger (1996), Hikita *et al.* (1980), Wilkinson *et al.* (1992), and Luo *et al.* (1999) are in good agreement with the observed cross-sectional gas holdup. However, for P = 10 atm, the predictions made by Hammer *et al.* (1984) fit best the experimental data, followed by correlations of Wilkinson *et al.* (1992) and Luo *et al.* (1999). In conclusion, for all pressures, Wilkinson *et al.* (1992) correlation has the best overall agreement with data followed by the correlations of Krishna and Ellenberger (1996) and Idogawa *et al*. (1985). The correlation developed by Wilkinson *et al.* (1992) yields an average deviation of about 15.5 % for all operating conditions, whereas the correlations developed by Krishna and Ellenberger (1996) and Idogawa *et al.* (1985) yield an average deviation of 16.2 % and 17.0%, respectively.

In addition to the gas holdup value, which determines the amount of space available for reaction (i.e. the liquid holdup), the radial gas holdup profile is critical in determining liquid recirculation and mixing. It is the gradient of the radial gas holdup profile which is the primary factor in driving liquid recirculation and subsequently governing the state of mixing of the liquid phase. The liquid recirculation velocity profile can be predicted from the simplified one-dimensional two-fluid model (Gupta *et al*., 2001) based on the knowledge of the radial gas holdup profile. Recently, Wu *et al.*

(2001) made use of the gas holdup database generated as part of this study to develop a correlation for predicting the parameters *m* and *c* of the radial gas holdup profile shown in Equation (4-5). The correlations developed by them are displayed as Equations (4-11) and (4-12).

$$m = 2.188\times10^{3}\ Re_G^{-0.598}\ Fr^{0.146} Mo_L^{-0.004} \tag{4-11}$$

$$c = 4.32\times10^{-2}\ Re_G^{0.249} \tag{4-12}$$

where *Fr* is Froude Number $\left(U_g^2/gD_c\right)$; Mo_L is Morton Number $\left(g\mu_l^4/\left(\rho_l-\rho_g\right)\sigma^3\right)$; and Re_G is Reynolds Number $\left(U_g\left(\rho_l-\rho_g\right)D_c/\mu_l\right)$.

Figure 4-20 shows the parity plots of the predicted (using Equations (4-11) and (4-12)) versus actual *m* and *c* values obtained from this study. Clearly, discrepancies exist between the predicted and actual *m* and *c* values. The reason might be due to the fact that the correlation developed by Wu *et al.* (2001) does not account for the effect of distributors on gas holdup (refer to Equations (4-11) and (4-12)), which has significant influence at low superficial gas velocities. It should be noted that flatter gas holdup profiles are usually observed at low U_g and are characterized by higher values of *m* and lower values of *c*. Additionally, many of the aforementioned discrepancies are found to be at those conditions that are close to the flow transition, where the correlations fail to predict the *m* and *c* values accurately. It should be mentioned that Wu *et al.* (2001) only used some of the measurements from this study to obtain the correlation.

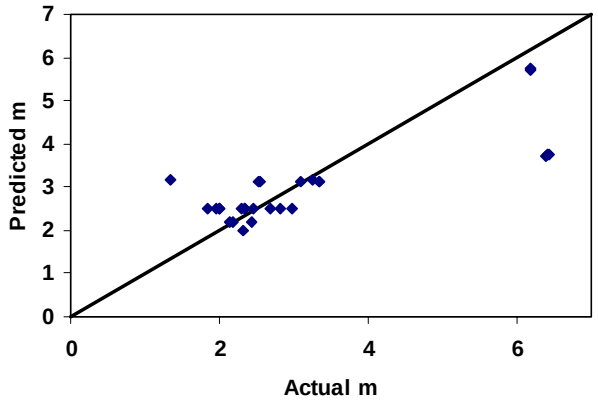

(a)

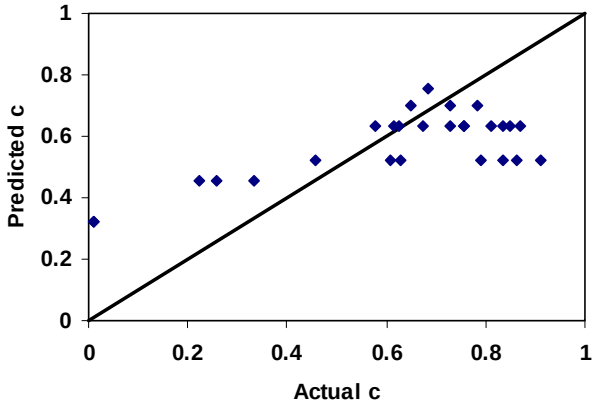

(b)

Figure 4-20. Parity plots of a) *m* and b) *c* parameters used in empirical equation for radial gas holdup represented in Equation (4-2).

Based on the analysis above, it is evident that there are no universal correlations for prediction of the overall gas holdup as well as its radial distribution. While the database on the overall gas holdup studies is large, there exist wide discrepancies in the measured and correlated data. It is only with the use of precise and accurate measurement techniques like Computed Tomography that one can overcome the lack of reliability present in the vast majority of reported data. It has been shown in this study that controlled experimentation with accurate measurements leads to observation of phenomena that previously remained undetected due to inaccuracies in experimental methods. The database presented in this study coupled with the few others existing in the literature should therefore serve as a starting point for development of correlation for prediction of gas holdup and its radial distribution. To begin with, the effect of gas distributor on gas holdup should be incorporated in any future efforts for development of a universal correlation. Secondly, many more data points would be required to really capture the effect of very high superficial gas velocities (greater than 30 cm/s) on gas holdup.

4.10. Final Remarks

The following conclusions can be drawn from this work:

1. At atmospheric pressure, effects of some distributors are observed on radial gas holdup profiles even at gas superficial velocities as high as U_g = 14 cm/s although at this superficial gas velocity, the flow is usually considered to be in churn-turbulent regime. Much smaller almost negligible effect of distributor on radial gas holdup profile is observed at very high U_g of 30 cm/s. At a higher pressure of 4 atm and U_g of 30 cm/s, there still exists some distributor effect on gas holdup for dramatically different distributor types.
2. If the radial gas holdup profiles at different axial locations fall within ±5% of the average profile, one can deem that the effect of axial location along the column is insignificant, which is observed at U_g = 30 cm/s at atmospheric pressure.
3. Gas holdup in churn-turbulent flow increases with pressure. The transition flow regime is shifted to higher superficial gas velocity.
4. The values of the overall gas holdup obtained using the dynamic height measurement and the axially cross-sectional average gas holdup evaluated using CT measurements are within 10 % for each distributor at U_g = 14 cm/s and 30 cm/s at atmospheric pressure. This difference increases to 20 % at U_g = 30 cm/s and at P = 4 atm. This might due to the fact that the CT measurements at 4 atm were performed only at one elevation away from the sparger and disengagement region while the overall gas holdup contains the contribution from all the zones.
5. There is no universal correlation for overall gas holdup that can predict well all the operating conditions in this work. The correlation of Wilkinson *et al.* (1992) yields the best agreement with our data followed by the correlation of Krishna and Ellenberger (1996) and Idogawa *et al*. (1985).
6. The correlation for predicting the radial gas holdup profile developed by Wu *et al.* (2001) does not yield a good estimation at all the operating conditions performed in this study. The discrepancies occur due to the fact that the correlation developed by Wu *et al. (*2001)

- does not account for the difference in distributor type;
- was developed based on a limited set of data;
- does not account for the transition regime.

To account for the shortcomings of the correlation of Wu *et al.* (2001), one of the first possible things that could be done is to develop separate correlations for m and c in the bubbly, transition and churn-turbulent regimes (much on the lines of the overall holdup correlation of Krishna (2000)). Secondly, the effect of distributor on these parameters could be captured by incorporation of an additional parameter based on distributor (example the Reynolds number based on orifice diameter and velocity, Re_o). Lastly, the effects of the physical properties of liquid and gas as well as the operating conditions need to be accounted for not only in the correlation for m but also for c. It is also noteworthy that Wu *et al.* (2001) did not propose a correlation for overall gas holdup. Therefore, with an expanding database of CT measurements of gas holdup distribution, it may become possible to also develop a correlation for overall gas holdup. The task of developing correlations has not been attempted in this study, as sufficient data points especially at high U_g and pressure do not yet exist.

Having observed and discussed the effect of various operating and geometric variables on gas holdup and its distribution, it is next of interest to assess the effect of these parameters on liquid recirculation and turbulence. Specifically, issues like whether there is any significant distributor effect on liquid velocity and turbulence at high pressure and whether similar gas holdup profiles indicate similar liquid flow structure and turbulence are discussed in Chapter 5.

Chapter 5. Study of Liquid Phase Hydrodynamics in Churn-Turbulent Bubble Columns Using CARPT

One of the main conclusions from Chapter 4 was that gas holdup and its mean gradient in the radial direction increases with pressure and superficial gas velocity in a stainless steel air-water bubble column. Furthermore, it was found that often the radial gas holdup profiles are within ±5% of the average radial gas holdup in the churn-turbulent region at atmospheric pressure indicating no apparent effect of distributors on gas holdup. However, some distributor effects on radial gas holdup distribution were found to exist at a higher pressure of 4 atm, although one can conclude that for distributors of industrial interest, their effect on gas holdup is almost negligible. Since radial gas holdup profiles drive liquid recirculation, the same radial holdup profiles should cause the same recirculation pattern provided the turbulence structure, represented in the simplest fashion by a mixing length or turbulent kinematic viscosity, is the same. Therefore, to substantiate the findings in Chapter 4, Computer Automated Radioactive Particle Tracking (CARPT) studies were conducted to investigate whether similar radial holdup distributions result in similar liquid recirculation and turbulence structure. This chapter presents the findings from the hydrodynamic study conducted using CARPT, and the chapter is organized as follows. First, a short discussion on the sampling compartments of the bubble column and a brief description of the methodology of processing CARPT data is provided. As mentioned in Chapter 3, the raw position data has to be filtered using the wavelet methodology before the turbulence characteristics of the bubble column hydrodynamics can be computed. Section 5.2 discusses the selection

of the parameters for wavelet filtering of the instantaneous position data. The rest of the chapter describes qualitatively and quantitatively the observations made based on the measurements and results computed from them.

5.1. Sampling Compartments

The precursor to processing the data acquired from a CARPT experiment is the notional compartmentalization of the three-dimensional space inside the column. There are several methods of discretization as discussed by Degaleesan (1997). In her study, she suggested an optimal discretization depending on the column size. Based on her recommendation, the compartmentalization chosen for this study is shown in Figure 5-1.

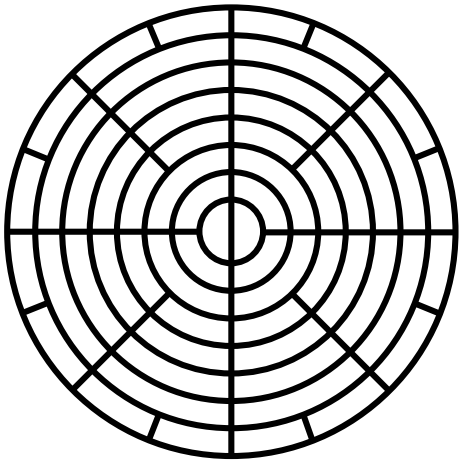

Parameters	
N_r	8
$N_{\theta,max}$	16
N_z	100
Δr, cm	1.01
Δz, cm	1.8

Figure 5-1. Compartment discretization for 6.4” (16.2 cm) bubble column.

As evident from Figure 5-1, the radial divisions are kept constant while the angular divisions are varied with radial position in the column. This discretization is used to maintain reasonably uniform particle occurrence statistics in each compartment (Degaleesan, 1997). Similar to the radial divisions, the axial compartments are also constant along the column length. For the current study, the number of radial and axial compartments are 8 and 100, respectively (refer to Figure 5-1) and the maximum number of angular compartments used is 16.

5.2. Data Processing

As mentioned in Chapter 3, Computed Automated Radioactive Particle Tracking (CARPT) experiments were performed using four different distributors in a 6.4" (16.2 cm) diameter air-water, stainless steel, bubble column at high superficial gas velocities (U_g = 30 and 45 cm/s) at atmospheric and at higher pressures of 4 and 10 atm (refer to Table 3-3). Once the data is acquired, the next step involves processing the data to obtain the time series for the instantaneous particle positions for each operating condition using the column discretization shown in Figure 5-1. The algorithm proposed by Degaleesan (1997) was used first to analyze the CARPT data. Two issues arise. First, because of the column wall being made of stainless steel, there is an additional attenuation and scattering in the registered counts as compared to those encountered by Devanathan (1991), Degaleesan (1997) and Chen *et al.* (1999) as the column walls in those earlier studies were made of Plexiglas. Second, in this study, the detectors were positioned only in the fully developed region, where acceleration and deceleration effects were negligible as compared to the distributor and exit regions. Because of these issues, the algorithm proposed by Degaleesan (1997) leads to a considerable number of reconstructed particle positions, especially close to the distributor and exit regions, that lie outside the column specification. To resolve this, a full Monte Carlo simulation was used (Gupta, 2002). Further details on the Monte Carlo method will not be discussed here and the interested reader can obtain more information from Gupta (2002).

The performance of these two algorithms were compared using data acquired from a bubble column equipped with a uniform perforated plate, D4, (163 holes of 0.5 mm, porosity of 0.15%) (refer to Figure 3-2 for the schematic diagram) and operated at U_g = 30 cm/s at P = 1 atm. Figures 5-2 to 5-4 display the time-averaged liquid velocity and turbulence parameters averaged over z level of 54 to 136.8 cm. The error bars shown in each plot represent a standard deviation in each direction from the plotted average variable. Once should be aware of a much different scale of the ordinate in Figures 5-2b and 5-2c compared to Figures 5-3b and 5-3c, respectively. Same is true of scales in Figures 5-4a and 5-4b. As evident from Figures 5-2 to 5-4, it was found that the particle position reconstruction for this study using the Monte Carlo algorithm yields much better

results with less spread in the quantities derived from the reconstructed instantaneous positions as compared to the algorithm proposed by Degaleesan (1997).

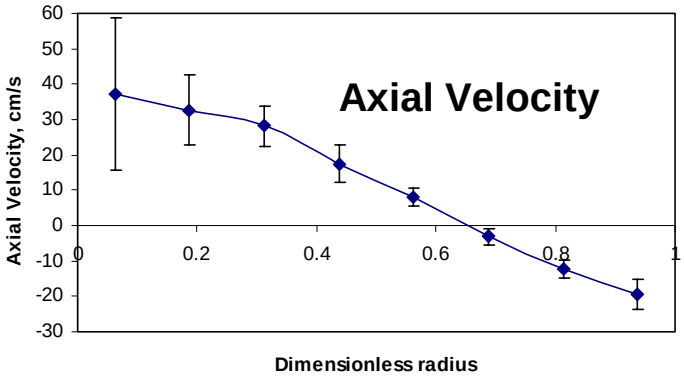

(a)

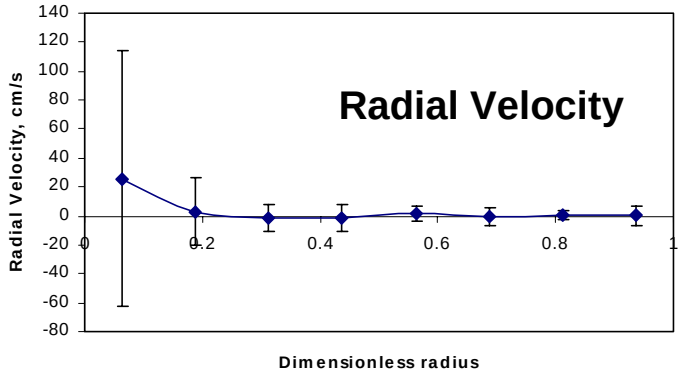

(b)

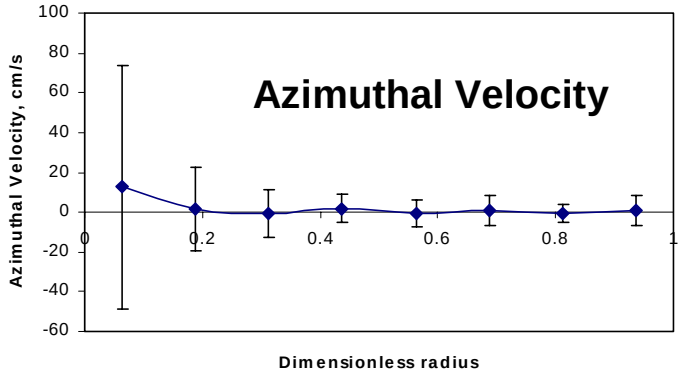

(c)

Figure 5-2. Velocity profiles using *unfiltered instantaneous positions* based on Degaleesan's algorithm (1997): a) axial velocity; b) radial velocity; c) azimuthal velocity.

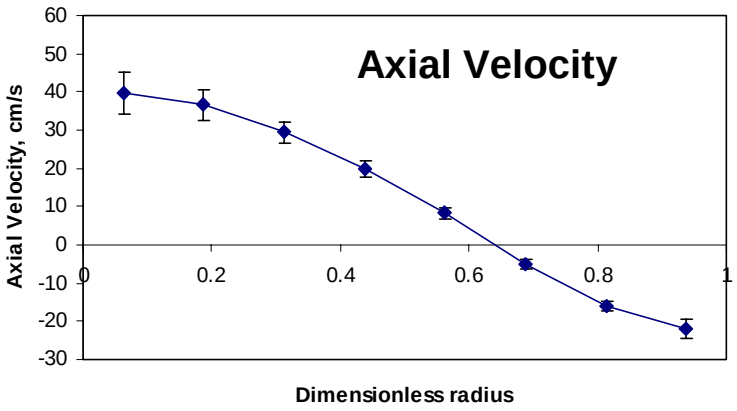

(a)

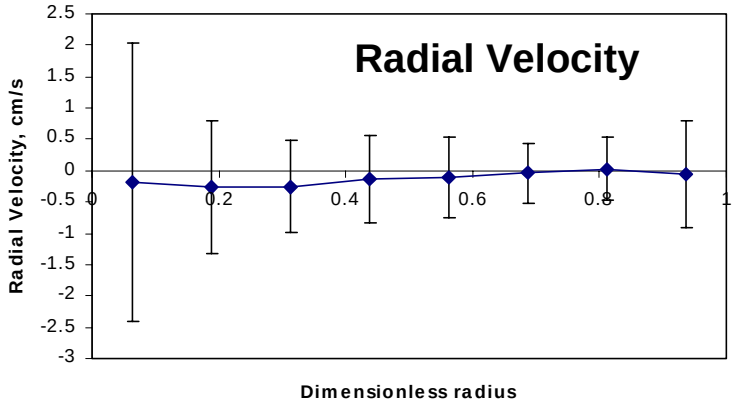

(b)

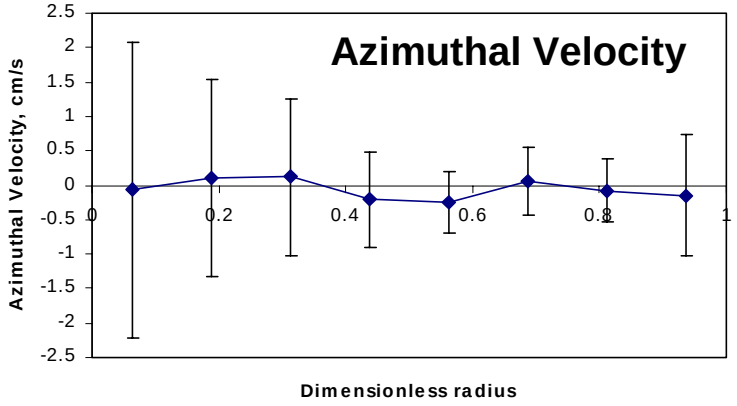

(c)

Figure 5-3. Velocity profiles using *unfiltered instantaneous positions* based on Monte Carlo Method (Gupta, 2002): a) axial velocity; b) radial velocity; c) azimuthal velocity.

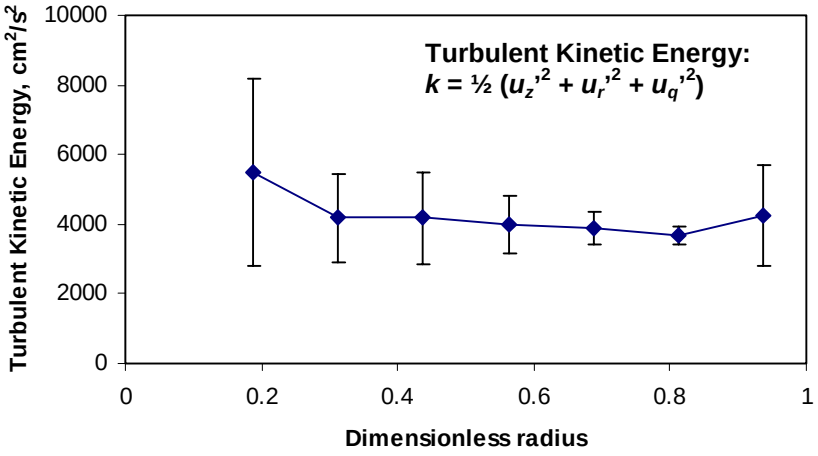

(a)

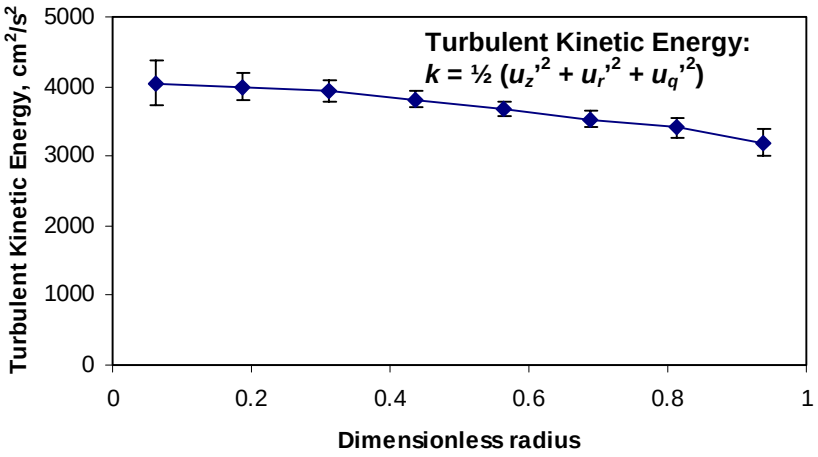

(b)

Figure 5-4. Turbulent kinetic energy profiles using *unfiltered instantaneous positions* based on a) Degaleesan's algorithm (1997); b) Monte Carlo Method (Gupta, 2002).

As can be seen from the above figures, the improved position estimates using the Monte Carlo method result in significantly reduced error bars, especially at the center of the column, in the computed time-averaged liquid circulation velocity and turbulent kinetic energy. Another observation from Figure 5-2 is that the range of radial and

azimuthal velocity components close to the column center obtained using Degaleesan's method (1997) is two orders of magnitude higher than those obtained using Monte Carlo method. Since in the long-time average sense, the radial and azimuthal velocities are expected to be not far removed from zero, the better performance of the Monte Carlo method is clearly evident. Thus, for this study, the Monte Carlo method has been used to compute the instantaneous positions of the particle for all operating conditions.

5.3. Wavelet Filtering Methodology

As was discussed in detail by Degaleesan (1997), it is necessary to filter the instantaneous particle-position data from a CARPT experiment in order to eliminate the contribution of the spurious velocities to the measured instantaneous velocities, hence yielding better and accurate estimates of the turbulence parameters. She proposed using the wavelet-filtering algorithm to eliminate the noise in the instantaneous position data. To achieve wavelet filtering, CARPT data is first divided into sets of length $N = 2^L$ (L = 10, N = 1024). Then, the wavelet packet decomposition using Daubechies' (1988) is employed on a randomly selected data set to obtain the best basis representation based on minimizing the entropy of the coefficients (Degaleesan, 1997). A signal threshold for the wavelet packet coefficients, *st*, is then selected in such a way that the noise filtered from the data satisfies the characteristics of white noise. The choice of *st* depends on the extent of noise in the data, x(t), y(t) and z(t). Further discussion on the wavelet filtering method, analysis and implementation is described elsewhere (Degalessan, 1997; Degaleesan *et al.*, 2002). In the earlier work by Degaleesan (1997), an initial estimate of *st* is first obtained using the experimental data for a stationary particle measured during the calibration. Fine-tuning of the threshold is performed using power spectral density to ensure that the noise filtered represents white noise, i.e., white noise has a uniform distribution of energy over all the frequencies sampled. This process is repeated with several randomly chosen data sets to arrive at the final value of *st* for the data, which is then used to filter the entire instantaneous position data.

The procedure described above has been used to process the CARPT data obtained in this work. However, the problem of not being able to achieve the uniform power spectral density for the filtered noise irrespective of the value of *st* sometimes arises. In this section, another approach of obtaining the filtering parameters is described. The unfiltered instantaneous position data was further processed to obtain the Lagrangian correlation coefficients, thereby ignoring the filtering step. Figure 5-5 displays these Lagrangian correlation coefficients at various radial positions obtained from the unfiltered instantaneous position data generated by Degaleesan (1997) in a 6" (14.0 cm) bubble column operating at a superficial gas velocity of 9.6 cm/s at atmospheric pressure. Clearly the artificial kinks appear in the radial, azimuthal and axial autocorrelation profiles.

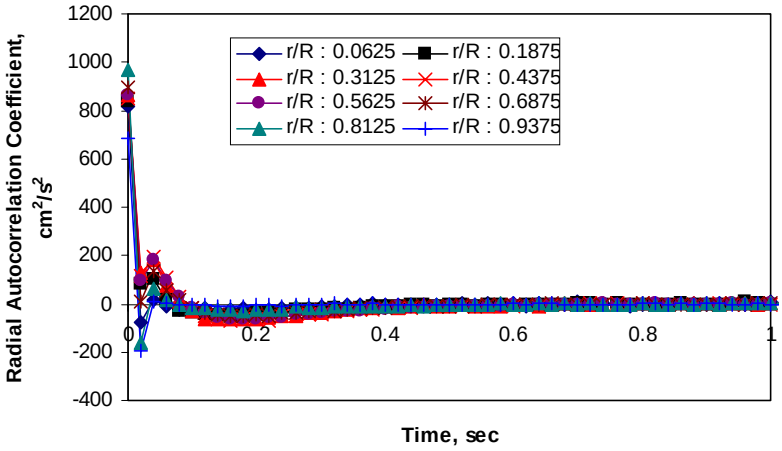

(a)

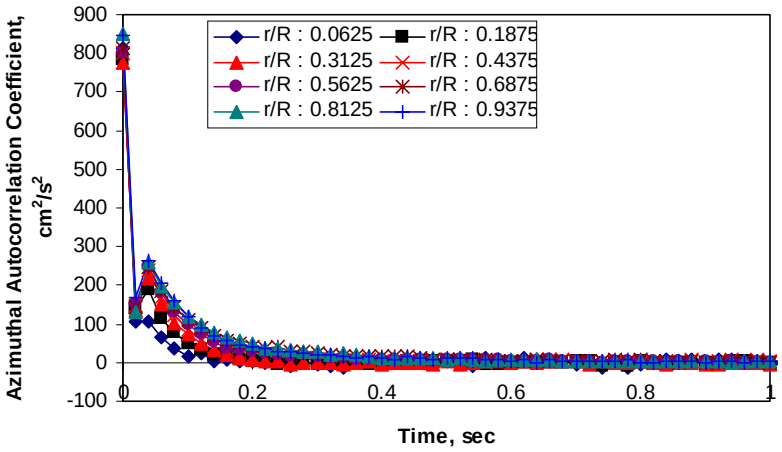

(b)

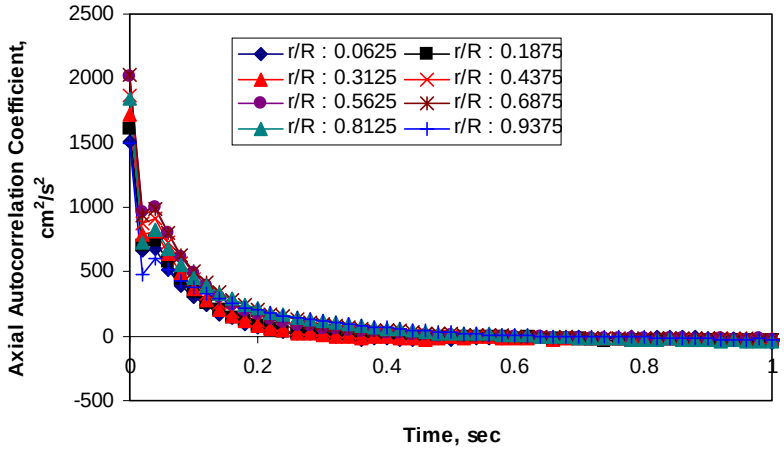

(c)

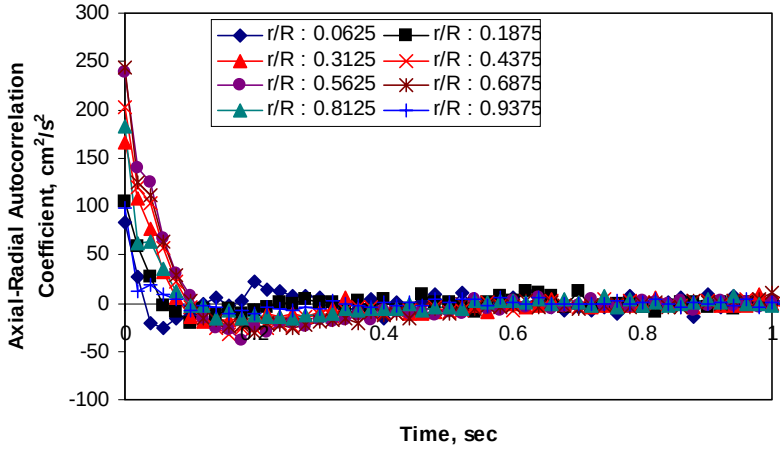

(d)

Figure 5-5. Lagrangian correlation coefficient at various radial positions using *unfiltered instantaneous position data* from Degaleesan (1997) in a 6" bubble column operating at U_g = 9.6 cm/s: a) radial; b) azimuthal; c) axial; d) axial-radial.

Next, the unfiltered data was filtered using the wavelet filtering methodology described in Degaleesan (1997). The Lagrangian correlation coefficient profiles for this case are displayed in Figure 5-6. It can be readily seen that the artificial kinks are eliminated and the profiles are much smoother as compared to those in Figure 5-5.

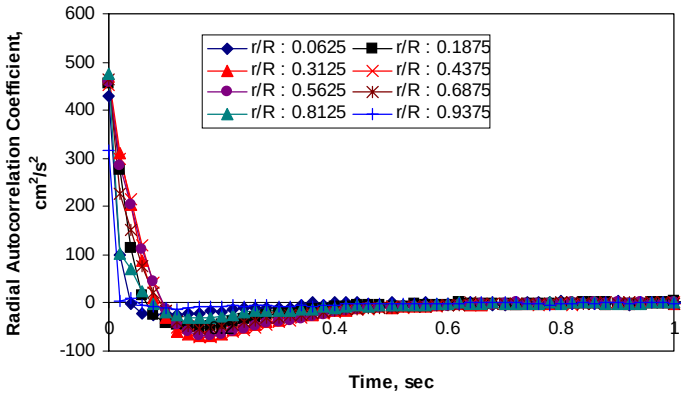
r/R : 0.0625
r/R : 0.1875
r/R : 0.3125
r/R : 0.4375
r/R : 0.5625
r/R : 0.6875
r/R : 0.8125
r/R : 0.9375
Radial Autocorrelation Coefficient, cm²/s²
Time, sec

(a)

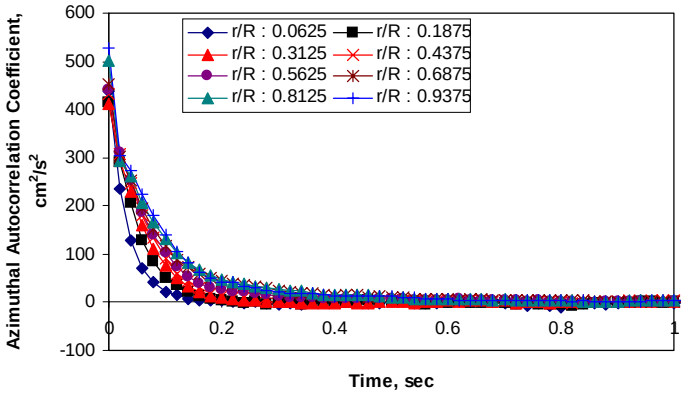
r/R : 0.0625
r/R : 0.1875
r/R : 0.3125
r/R : 0.4375
r/R : 0.5625
r/R : 0.6875
r/R : 0.8125
r/R : 0.9375
Azimuthal Autocorrelation Coefficient, cm²/s²
Time, sec

(b)

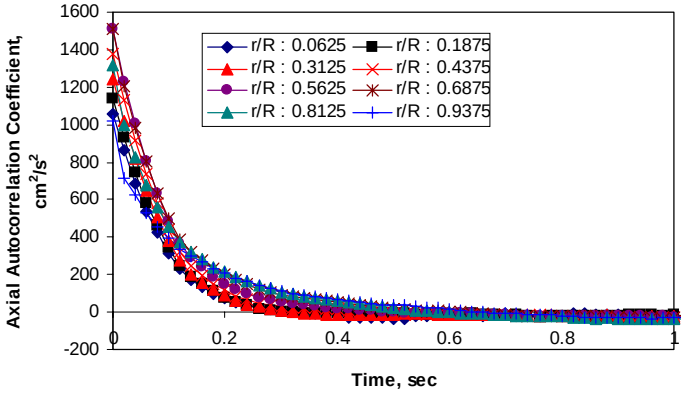
r/R : 0.0625
r/R : 0.1875
r/R : 0.3125
r/R : 0.4375
r/R : 0.5625
r/R : 0.6875
r/R : 0.8125
r/R : 0.9375
Axial Autocorrelation Coefficient, cm²/s²
Time, sec

(c)

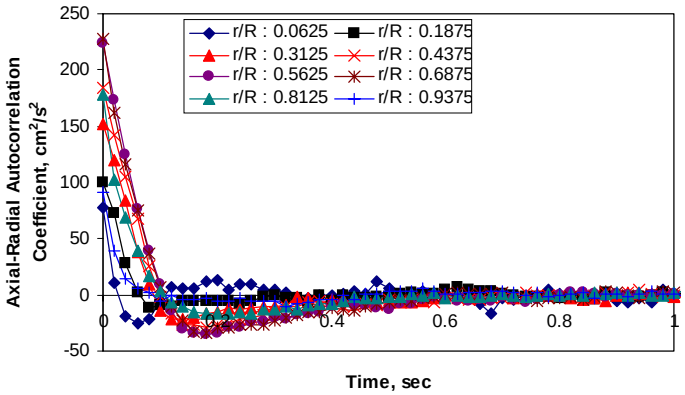

(d)

Figure 5-6. Lagrangian correlation coefficient at various radial positions using *filtered instantaneous position data* from Degaleesan (1997) in a 6" bubble column operating at U_g = 9.6 cm/s: a) radial; b) azimuthal; c) axial; d) axial-radial.

Hence, from Figures 5-5 and 5-6, it can be concluded that improper filtering of the instantaneous position data yields artificial kinks in the Lagrangian correlation coefficient profiles. Therefore, for this study, a stepwise increment of the filtering parameters was implemented and the procedure of obtaining liquid velocity components, turbulence parameters and Lagrangian correlation coefficients was repeated until the Lagrangian correlation coefficient profiles no longer show any kinks. The question arises whether overfiltering of the instantaneous position data occurs if this procedure is used. Table 5-1 displays the various incremented *st* values for *x*, *y* and *z* positions (st_x, st_y, st_z) employed for processing the experimental data acquired using the uniform perforated plate distributor, D4, at a superficial gas velocity of 30 cm/s at atmospheric pressure. Subsequently, Figure 5-7 shows the effect of the *st* values for *x*, *y* and *z* positions for the nine different cases that were tested (refer to Table 5-1). Also displayed in Figure 5-7a to 5-7j are the average profile for all cases and a standard deviation from the average profile. The average profile was calculated by averaging the respective quantities at each radial location to provide the average value at that location. Similarly, the standard deviations were calculated at each radial location, which are shown in the figure as the bounds of variation with ±1 standard deviation.

Table 5-1. Threshold values for *x*, *y* and *z* positions for different cases.

Case	st_x	st_y	st_z
1	0.8	0.8	0.85
2	1.1	1.1	1.2
3	1.2	1.2	1.3
4	1.3	1.3	1.4
5	1.3	1.3	1.5
6	1.3	1.3	1.6
7	1.3	1.3	1.7
8	1.3	1.3	1.8
9	1.3	1.3	1.9

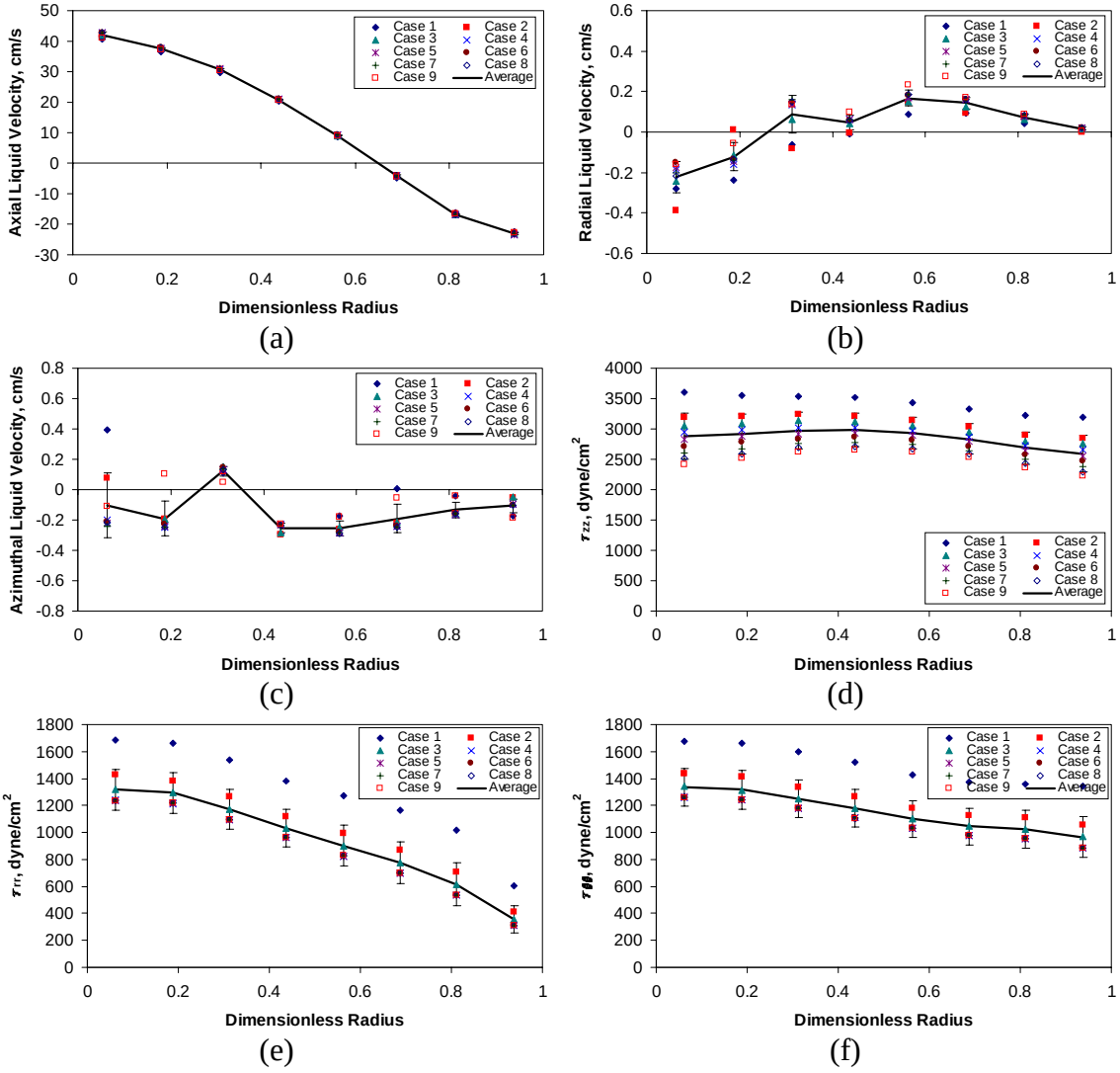

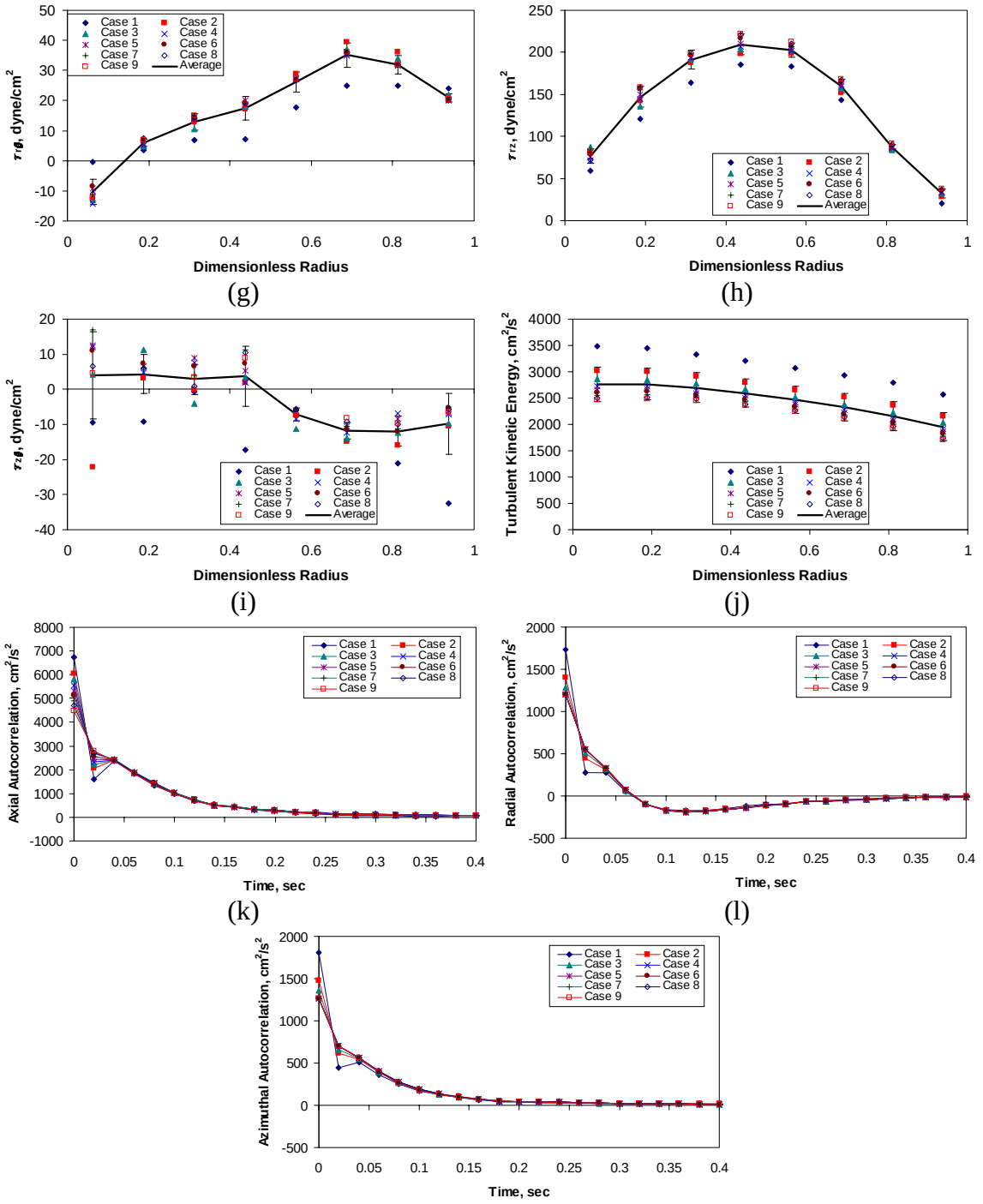

Figure 5-7. Effect of *st* for uniform perforated plate, D4, operating at U_g = 30 cm/s at atmospheric pressure on: a) u_z; b) u_r; c) u_θ; d) τ_{zz}; e) τ_{rr}; f) $\tau_{\theta\theta}$; g) $\tau_{r\theta}$; h) τ_{rz}; i) $\tau_{z\theta}$; j) turbulent kinetic energy; k) R_{zz} for r/R = 0.4375; l) R_{rr} for r/R = 0.4375; m) $R_{\theta\theta}$ for r/R = 0.4375.

As can be seen from Figure 5-7, as *st* values for *x* and *y* positions change from 0.8 to 1.3 and from 0.85 to 1.9 for *z* position, the liquid velocities and turbulence profiles are still within a standard deviation from the average profile. In addition, the artificial kinks appearing in the axial, radial and azimuthal autocorrrelation plots diminish (refer to Figure 5-7k to 5-7m). Similar analysis is performed for all conditions investigated in this study. It was found that other than at P = 10 atm and U_g = 30 cm/s, the wavelet filtering parameters for *x*, *y* and *z* positions of 1.3, 1.3 and 1.9, respectively, provide suitable data filtering. At P = 10 atm and U_g = 30 cm/s, higher wavelet filtering parameters for *x*, *y* and *z* positions had to be used (1.5, 1.5 and 1.9, respectively) most likely due to higher gas volume fraction at these operating conditions. For all conditions, the liquid velocities and turbulence profiles are within a standard deviation from the average profile.

5.4. Reproducibility of CARPT Data

Before proceeding any further, it was desirable to check the repeatability of the data acquired during the CARPT experiments. In order to analyze the CARPT reproducibility, the first 12 hours of a particular run (the whole experiment takes 24 hours) for uniform perforated plate D4 operating at P = 1 atm and U_g = 30 cm/s is denoted as Run1 and the second half of the experiment as Run2. Both sets of data were processed using the Monte Carlo method (Gupta, 2002) and filtered according to the wavelet filtering parameters suggested in Section 5.3. Figure 5-8 displays the time-averaged, axially and azimuthally averaged liquid velocities and turbulence parameters obtained for uniform perforated plate distributor D4 at P = 1 atm and U_g = 30 cm/s. The error bars shown in Figure 5-8 represent the standard deviation from the average of each plotted variable over the *z*-levels of 54 cm to 136.8 cm.

As shown in Figure 5-8, the reproducibility of CARPT data is pretty reasonable. Based on the axial liquid velocity information, the maximum deviation occurs near the center of the column (refer to Figure 5-8a) and has a value of ±5.7 % from the average.

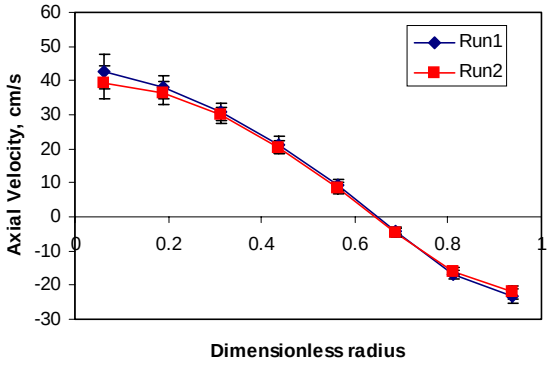
Axial Velocity, cm/s
Dimensionless radius
Run1
Run2

(a)

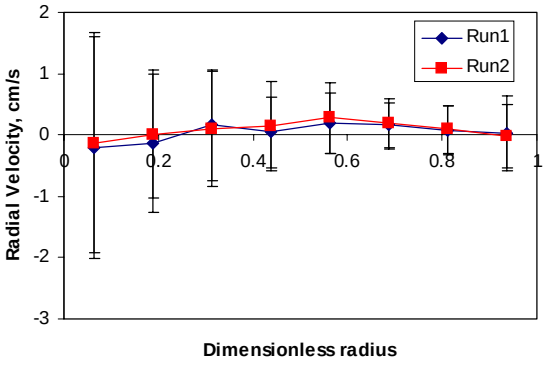
Radial Velocity, cm/s
Dimensionless radius
Run1
Run2

(b)

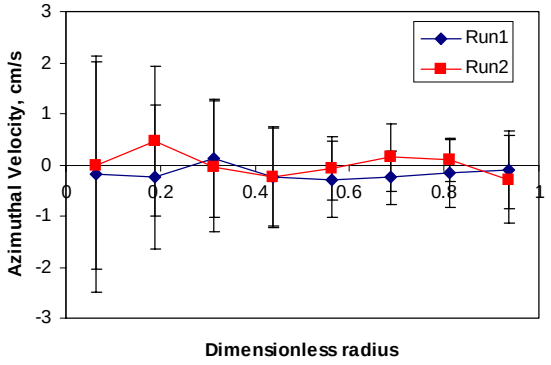
Azimuthal Velocity, cm/s
Dimensionless radius
Run1
Run2

(c)

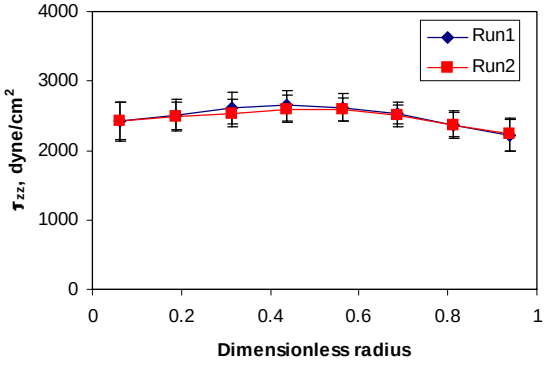
τzz, dyne/cm2
Dimensionless radius
Run1
Run2

(d)

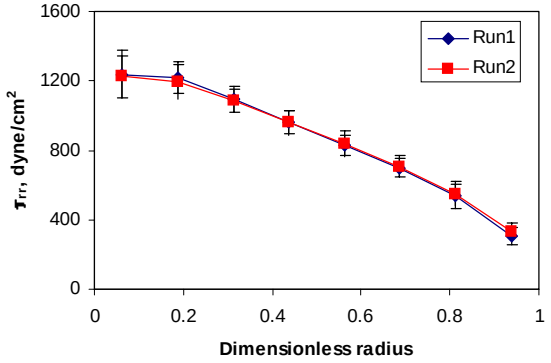
τrr, dyne/cm2
Dimensionless radius
Run1
Run2

(e)

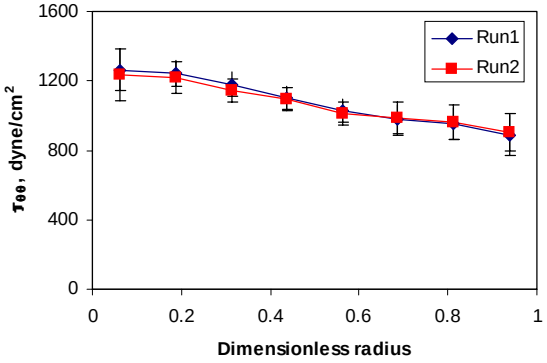
tθθ, dyne/cm2
Dimensionless radius
Run1
Run2

(f)

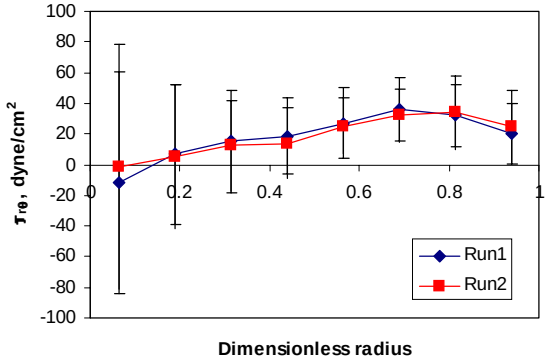
trθ, dyne/cm2
Dimensionless radius
Run1
Run2

(g)

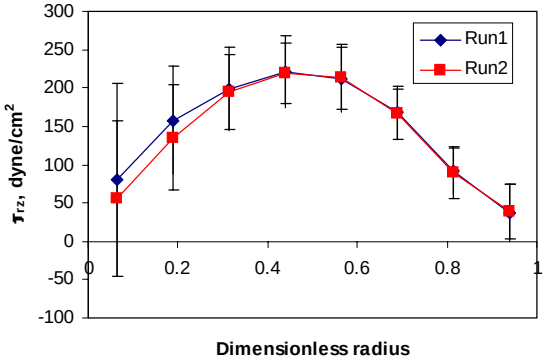
trz, dyne/cm2
Dimensionless radius
Run1
Run2

(h)

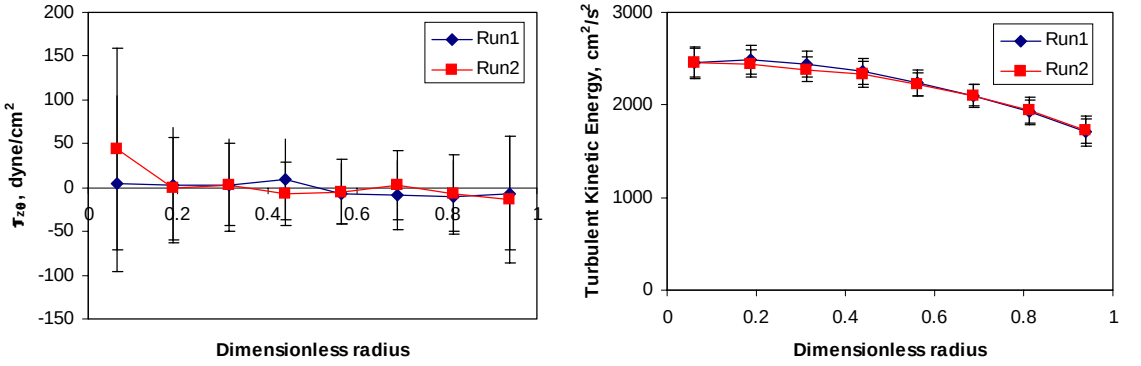

(i) (j)

Figure 5-8. Time-averaged, axially and azimuthally averaged liquid velocity and turbulence parameters using uniform perforated plate D4 at P = 1 atm and U_g = 30 cm/s. a) axial velocity; b) radial velocity; c) azimuthal velocity; d) τ_{zz}; e) τ_{rr}; f) $\tau_{\theta\theta}$; g) $\tau_{r\theta}$; h) τ_{rz}; i) $\tau_{z\theta}$; j) turbulent kinetic energy.

5.5. Time-Averaged Flow Pattern and Liquid Velocity Profiles

5.5.1. Velocity Vector Plots

It is widely know that in the time averaged sense liquid flows upwards in the center and downwards near the column wall and that the flow is symmetric (Devanathan, 1991; Degaleesan, 1997; Chen *et al.*, 1999). In this section, the velocity vector plots representing the local time-averaged liquid velocities are displayed so as to observe whether there exists an axisymmetric flow pattern in a fully three-dimensional bubble column. The plots are presented for axial locations from 20 to 140 cm since the detectors are not positioned anywhere near the distributor and disengagement regions (refer to Chapter 3). The display of the velocity vector plots were obtained using the TECPLOT software. Both longitudinal and lateral projections are made to interpret all the three components of the velocity vectors. The longitudinal sections are made through the center of the column at four different angles, namely, 0-180°, 45-225°, 135-315° and 90-270° while the cross-sectional views are obtained by visualizing the flow pattern at four selected z locations.

Figures 5-9 to 5-10 display the longitudinal and lateral views of the bubble column for uniform perforated plate distributor D4 (0.15%, 163 orifices of 0.15 mm)

operating at a superficial gas velocity of 30 cm/s at atmospheric pressure. As evident from these figures, the time-averaged flow pattern seems to be symmetric about the center of the bubble column at the axial position between 50 to 130 cm. In addition, Figure 5-9 indicates that the liquid flows upwards at the center and downwards near the wall, an observation which is frequently reported (Hills, 1974; Menzel *et al.* 1990; Yao *et al*., 1991; Devanathan, 1991; Mudde *et al.*, 1997[a, b]; Degaleesan, 1997; Vial *et al*., 2001). Figure 5-10 establishes that the radial and angular components of the time-averaged velocity are very small (compared to axial component) and that indeed the time-averaged flow pattern is basically representative of "fully developed flow". Similar observations are seen for all other operating conditions except for single nozzle distributor D3 (0.1%, 5.1 mm) at a pressure of 4 atm and superficial gas velocity of 30 cm/s (Figure 5-11). To recall, this distributor at this operating condition is studied due to the highest gas holdup obtained using CT as compared to other distributors (refer to Chapter 4). Figures 5-11 to 5-12 show the two different views of the flow pattern existing in the column for distributor D3 operating at a superficial gas velocity of 30 cm/s at a pressure of 4 atm. As evident from Figure 5-11b, which displays the azimuthally averaged liquid velocity vector plot, a liquid jet seems to persist in the liquid even at an axial location of 30 cm. This jet is not observed at other operating conditions and for other distributors. Hence, the entrance length for distributor D3 is longer than for any other distributor operating at different conditions. This might explain the higher gas holdup obtained with this distributor as the liquid jet induces higher turbulence in the liquid, hence, promotes more bubble breakup leading to smaller bubbles. Also, recall that the bubble formation for this distributor is in the dispersed jetting regime (Chapter 4). Figure 5-12 seems to indicate slightly higher radial and azimuthal velocity components than observed at other conditions.

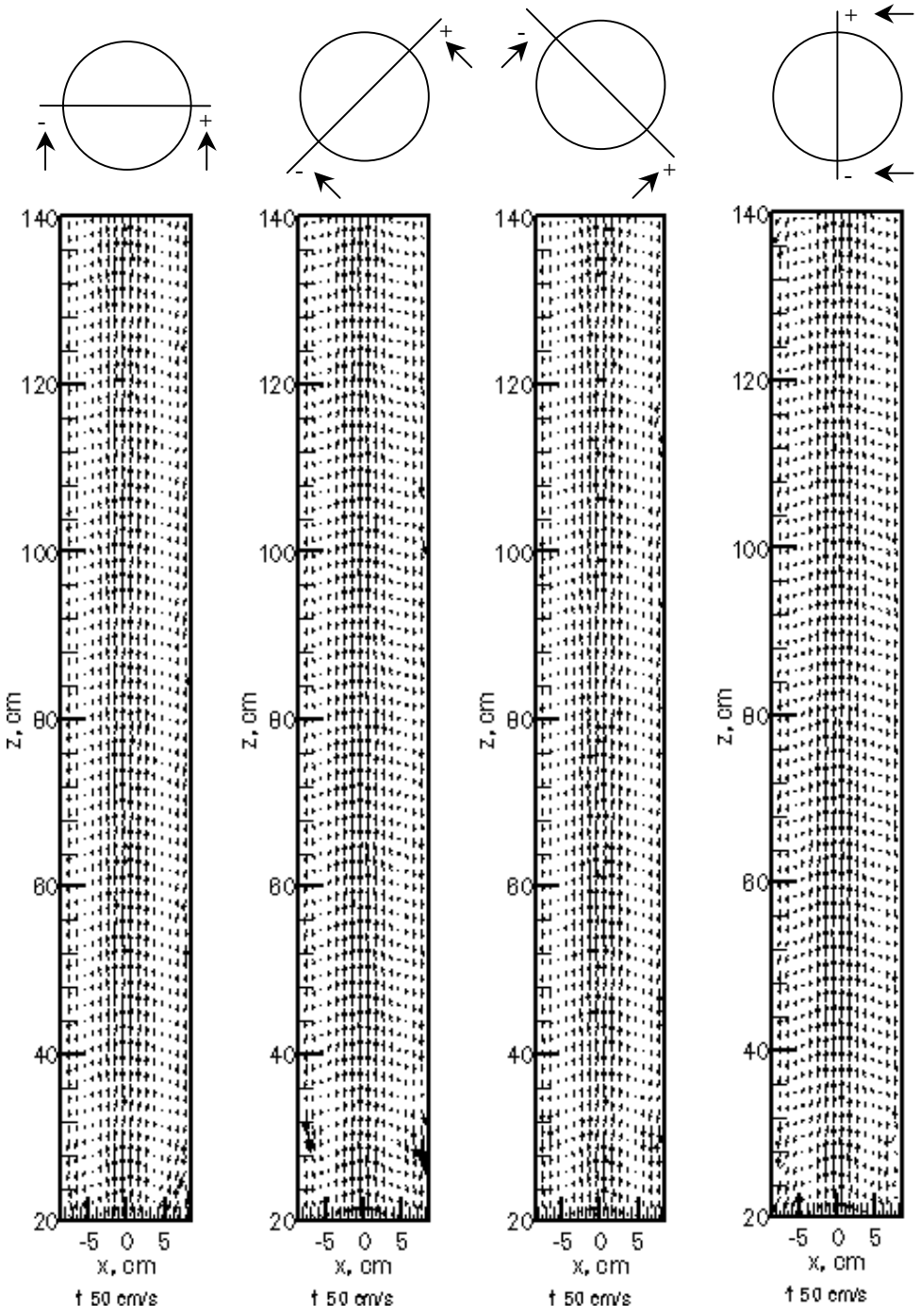

(a)

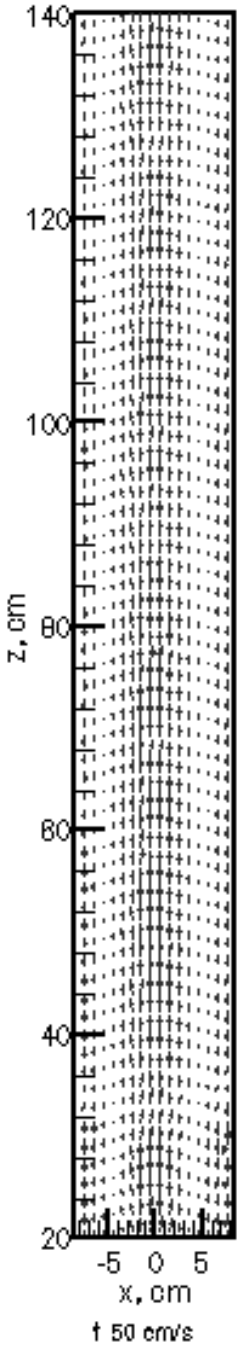

(b)

Figure 5-9. Velocity vector plots in the *r*-*z* plane for distributor D4 (0.15%, 163 orifices of 0.5 mm) at U_g = 30 cm/s at atmospheric pressure (a) Longitudinal views; (b) Azimuthally averaged view.

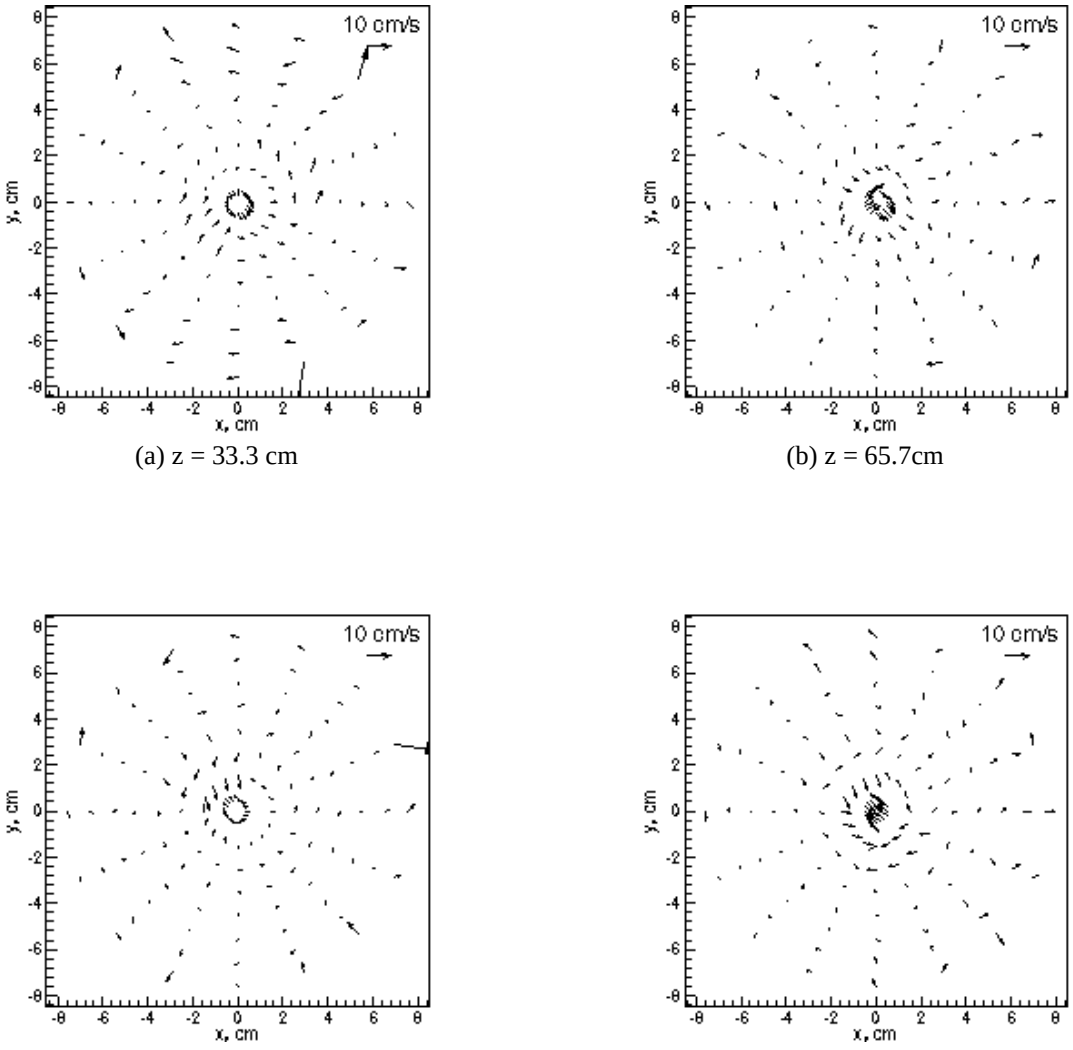

(a) z = 33.3 cm

(b) z = 65.7cm

(c) z = 101.7 cm

(d) z = 134.1cm

Figure 5-10. Velocity vector plots (cross-sectional views) for distributor D4 (0.15%, 163 orifices of 0.5 mm) at U_g = 30 cm/s at atmospheric pressure.

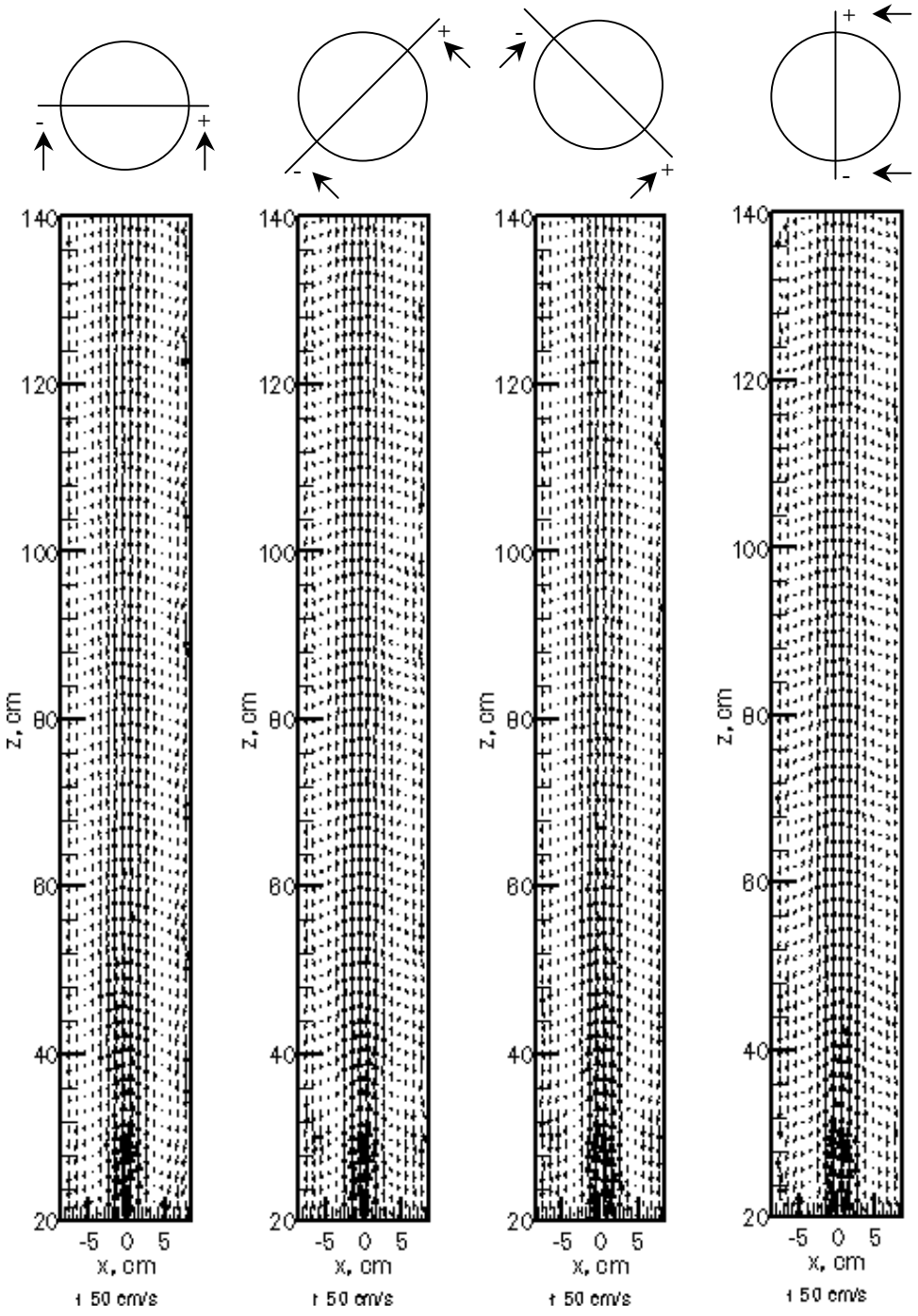

(a)

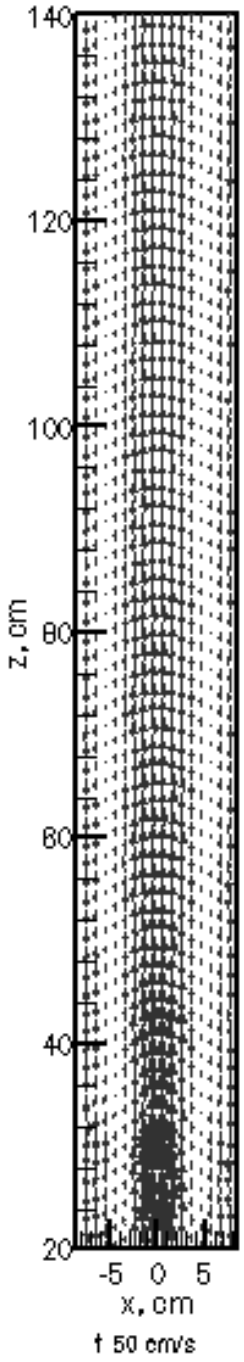

(b)

Figure 5-11. Velocity vector plots in the *r*-*z* plane for distributor D3 (0.1%, an orifice of 5.1 mm) at U_g = 30 cm/s at P = 4 atm (a) Longitudinal views; (b) Azimuthally averaged view.

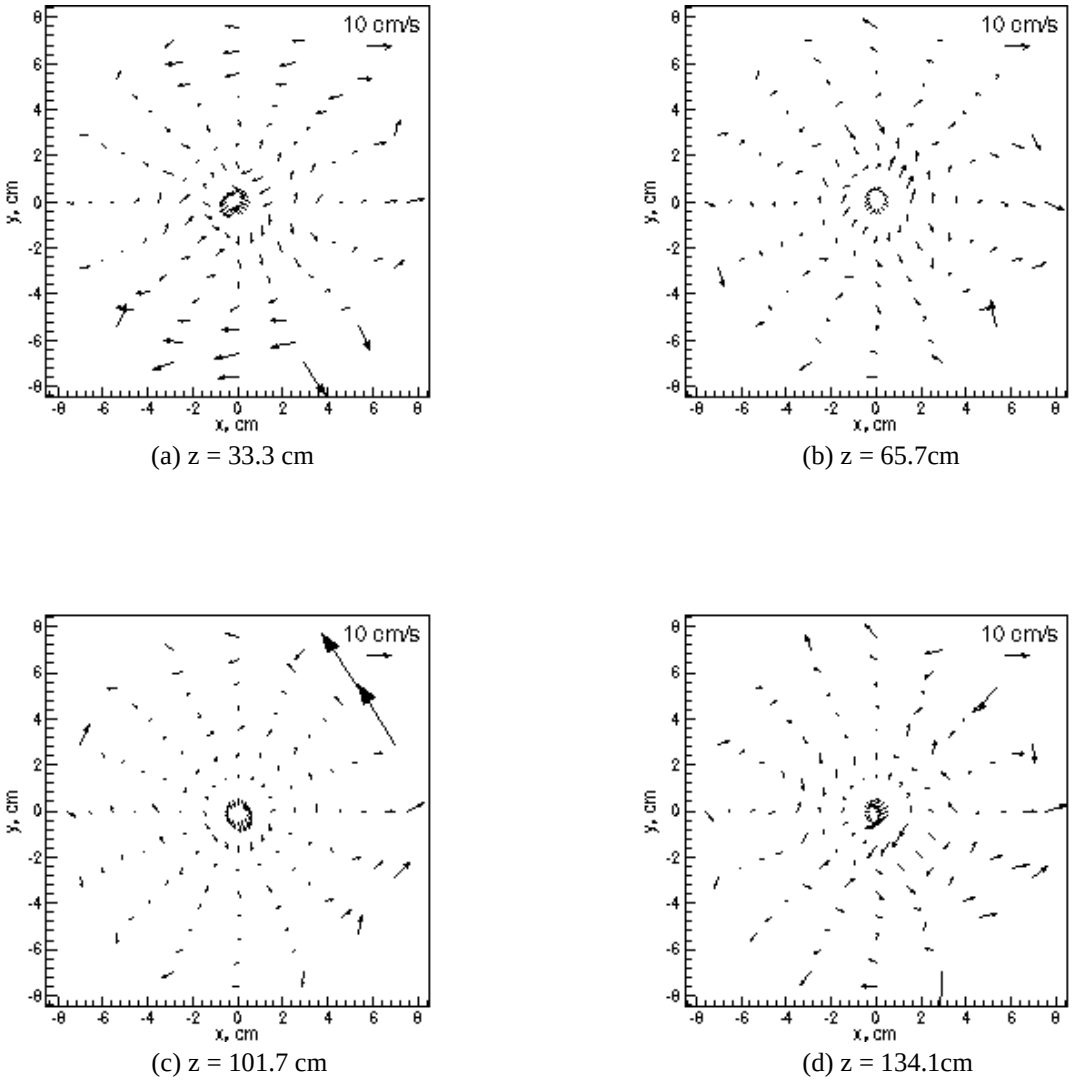

(a) z = 33.3 cm

(b) z = 65.7cm

(c) z = 101.7 cm

(d) z = 134.1cm

Figure 5-12. Velocity vector plots (cross-sectional views) for distributor D3 (0.1%, an orifice of 5.1 mm) at U_g = 30 cm/s at P = 4 atm.

5.5.2 Turbulent Stresses and Kinetic Energy Contour Plots

It is possible to evaluate the turbulent stresses and kinetic energy in the entire three-dimensional flow field of a bubble column using the CARPT technique (Devanathan, 1991; Degaleesan, 1997). Before presenting the details of the observed turbulence flow field for one of the operating conditions, a brief discussion on evaluating the liquid turbulence parameters is provided. It is known that turbulence is characterized by random fluctuations and statistical characterization of the flow parameters leads to important information about the flow (Monin and Yaglom, 1965; Wilcox, 1994). Such a characterization not only yields the time-averaged hydrodynamic information but also information on the instantaneous behavior of the system. The instantaneous information is usually obtained from higher order correlations of the fluctuating quantities that represent the turbulent interactions. One of the turbulent interactions, as shown by Equation (5-1a), is the turbulent stress tensor in cylindrical coordinates.

$$\tau = \rho_l \begin{pmatrix} \overline{u_r' u_r'} & \overline{u_r' u_\theta'} & \overline{u_r' u_z'} \\ \overline{u_\theta' u_r'} & \overline{u_\theta' u_\theta'} & \overline{u_\theta' u_z'} \\ \overline{u_z' u_r'} & \overline{u_z' u_\theta'} & \overline{u_z' u_z'} \end{pmatrix} \tag{5-1a}$$

$$\tau = \begin{pmatrix} -\frac{2}{3}\rho k & 0 & -\mu_{eff}\,\partial u_z/\partial r \\ 0 & -\frac{2}{3}\rho k & 0 \\ -\mu_{eff}\,\partial u_z/\partial r & 0 & -\frac{2}{3}\rho k \end{pmatrix} \text{ for bubble columns} \tag{5-1b}$$

where $\overline{u_i' u_j'}$ can be defined as the transport of momentum due to turbulent velocity fluctuations along the i^{th} direction due to the instantaneous flow in the j^{th} direction or vice versa. In this case, the negative sign is omitted since the present work emphasizes the experimental measurements and the understanding of some of the mechanisms involved in gas-liquid flows in bubble columns (Menzel *et al.*, 1990). Since the stress tensor shown in Equation (5-1) is symmetric, the nine unknown components reduce to six, namely, $\rho_l \overline{u_r' u_r'}$, $\rho_l \overline{u_\theta' u_\theta'}$, $\rho_l \overline{u_z' u_z'}$, $\rho_l \overline{u_r' u_\theta'}$, $\rho_l \overline{u_r' u_z'}$ and $\rho_l \overline{u_\theta' u_z'}$. Equation (5-1b) shows the representation of the turbulent stress tensor after applying Bousinessq's

approximation for bubble columns. This representation implies isotropic turbulence should be observed in bubble column since the turbulence normal stresses are similar. As shown in the earlier studies (Degaleesan, 1997; Chen *et al.*, 1999) and later in this chapter (Section 5.6), it is evident that bubble columns exhibit anisotropic turbulence (i.e., $\tau_{rr} \neq \tau_{\theta\theta} \neq \tau_{zz}$). Nevertheless, since Bousinessq's hypothesis is widely utilized in the field of CFD, it will be used as the first attempt to understand the bubble columns hydrodynamics in this study although more complex anisotropic models for turbulent stress are available elsewhere (Speziale, 1987; Lander, 1993; Craft *et al.*, 1993).

Another characterization of the liquid turbulence is the turbulent kinetic energy, k (defined per unit mass), which is related to the turbulent normal stresses (refer to Equation (5-2)).

$$k = \frac{1}{2}\left(\overline{u_r'^2} + \overline{u_\theta'^2} + \overline{u_z'^2}\right) \tag{5-2}$$

Contour plots for turbulent stresses and turbulent kinetic energy were obtained using MATLAB for four different views, 0-180°, 45-225°, 135-315° and 90-270°, for axial locations between 20 and 140 cm from the distributor. Figures 5-13 to 5-15 show the contour plots for the normal stresses, τ_{rr}, τ_{zz} and $\tau_{\theta\theta}$, respectively, for uniform perforated plate distributor D4 (0.15%, 163 orifices of 0.5 mm) operating at a superficial gas velocity of 30 cm/s at atmospheric pressure. The figures show reasonable symmetry about the center of the bubble column. All these figures show a maximum magnitude of the stresses at the center of the column. The axial normal stress has the highest magnitude as compared to the rest. Similarly, Figures 5-16 to 5-18 display the contour plots of the turbulent shear stresses, $\tau_{r\theta}$, τ_{rz}, and $\tau_{z\theta}$, respectively for the same operating condition described as above.

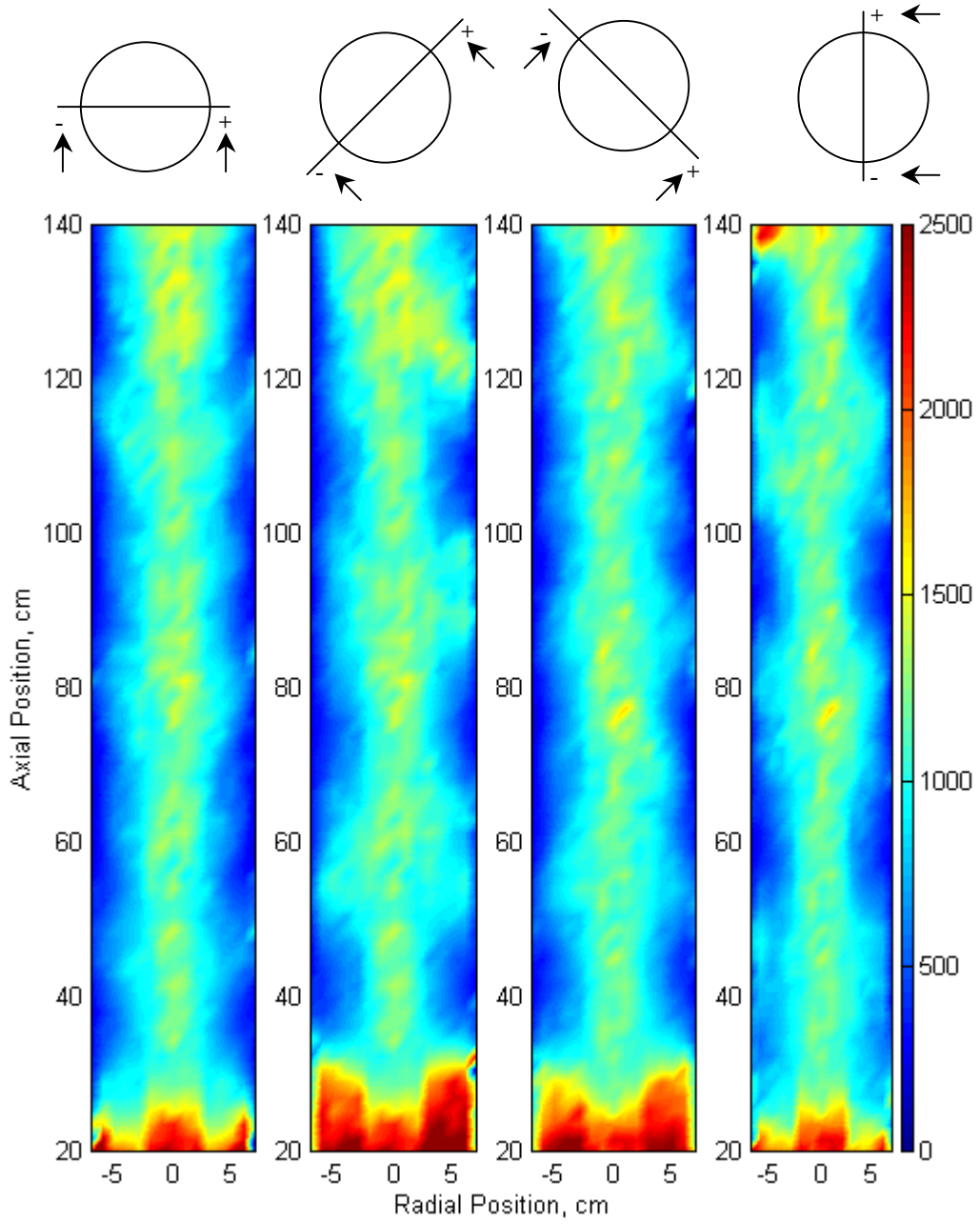

Figure 5-13. Radial turbulent normal stress (longitudinal views), τ_{rr}, for distributor D4 (0.15%, 163 orifices of 0.5 mm) at U_g = 30 cm/s at P = 1 atm.

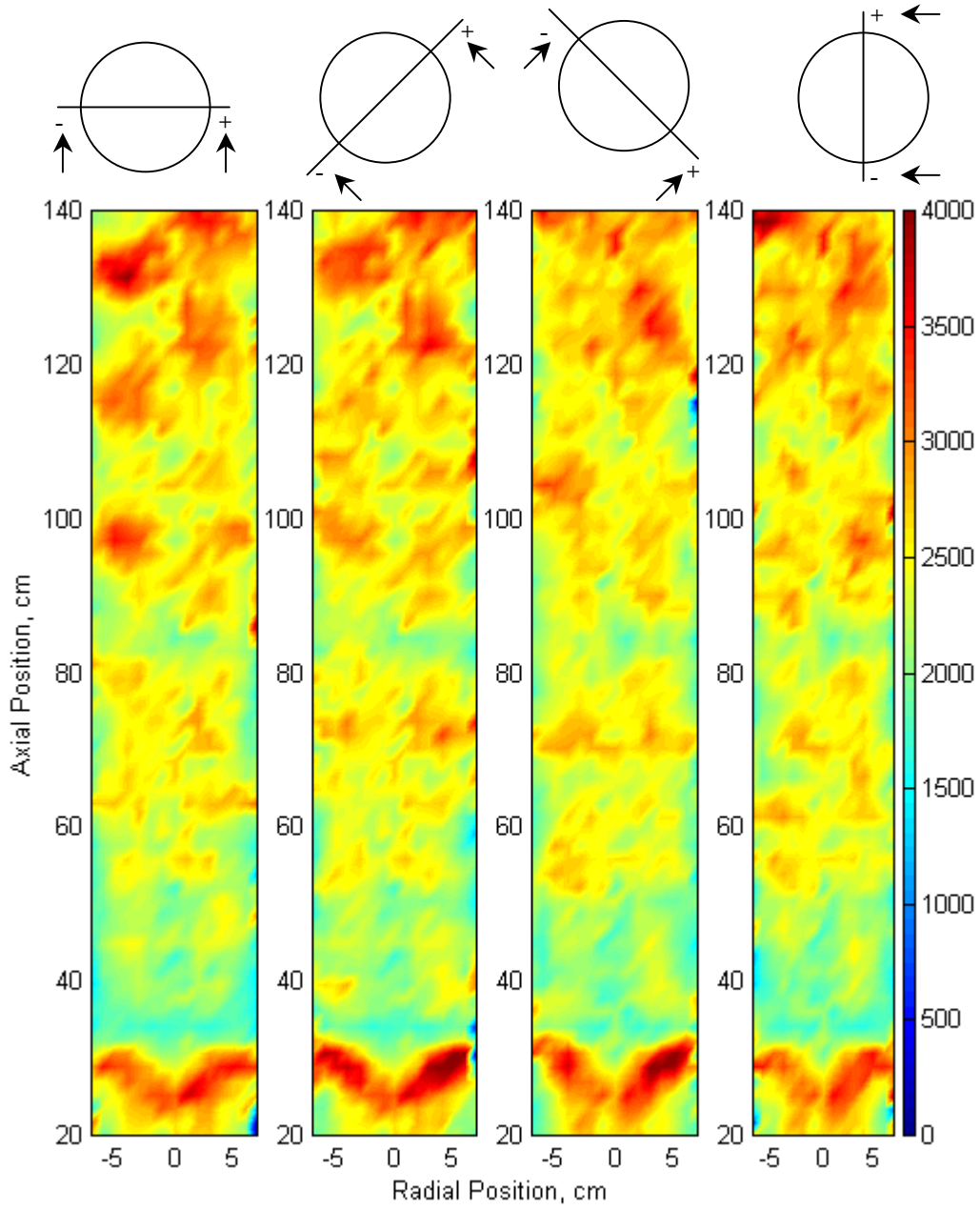

Figure 5-14. Axial turbulent normal stress (longitudinal views), τ_{zz}, for distributor D4 (0.15%, 163 orifices of 0.5 mm) at U_g = 30 cm/s at P = 1 atm.

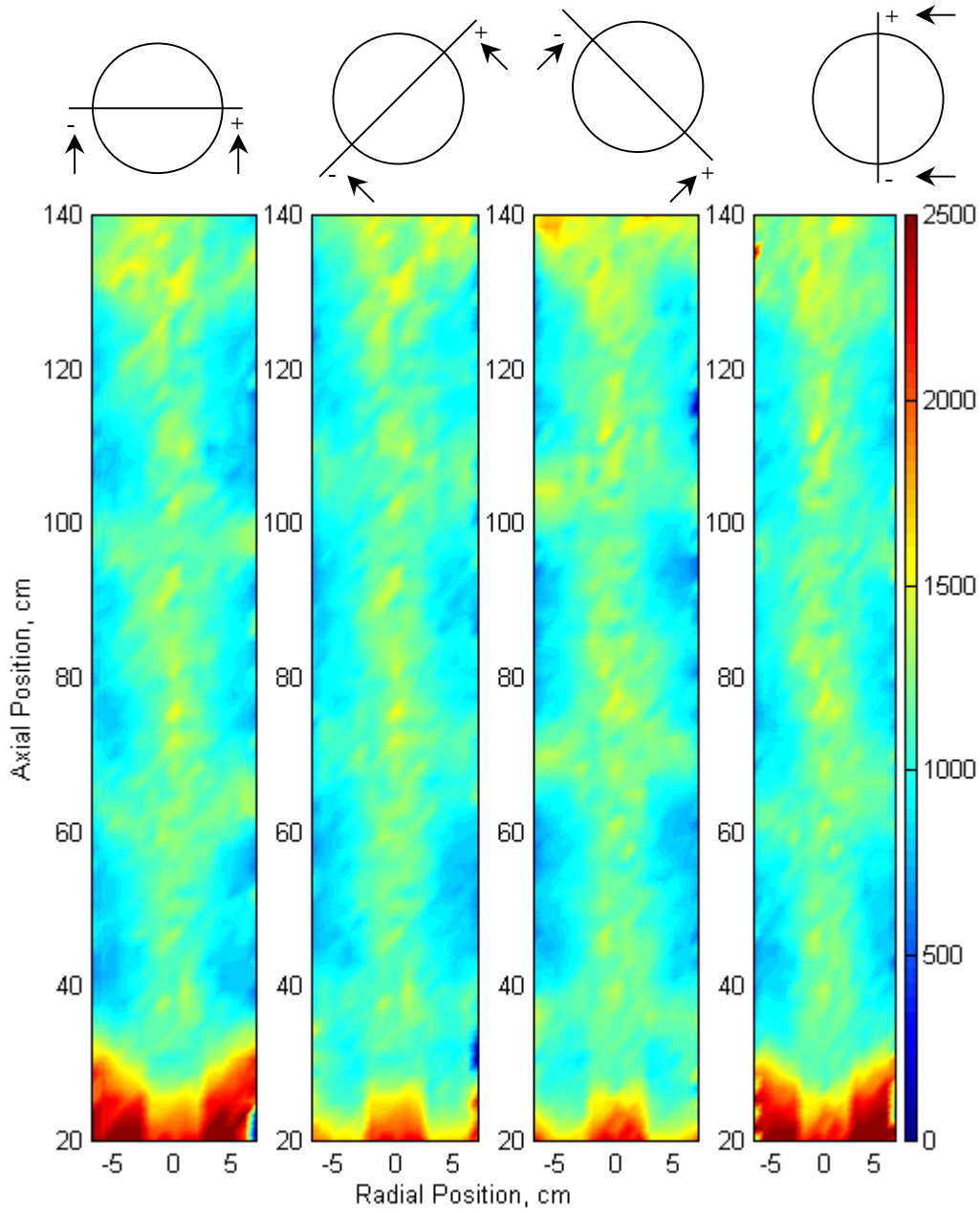

Figure 5-15. Azimuthal turbulent normal stress (longitudinal views), $\tau_{\theta\theta}$, for distributor D4 (0.15%, 163 orifices of 0.5 mm) at U_g = 30 cm/s at P = 1 atm.

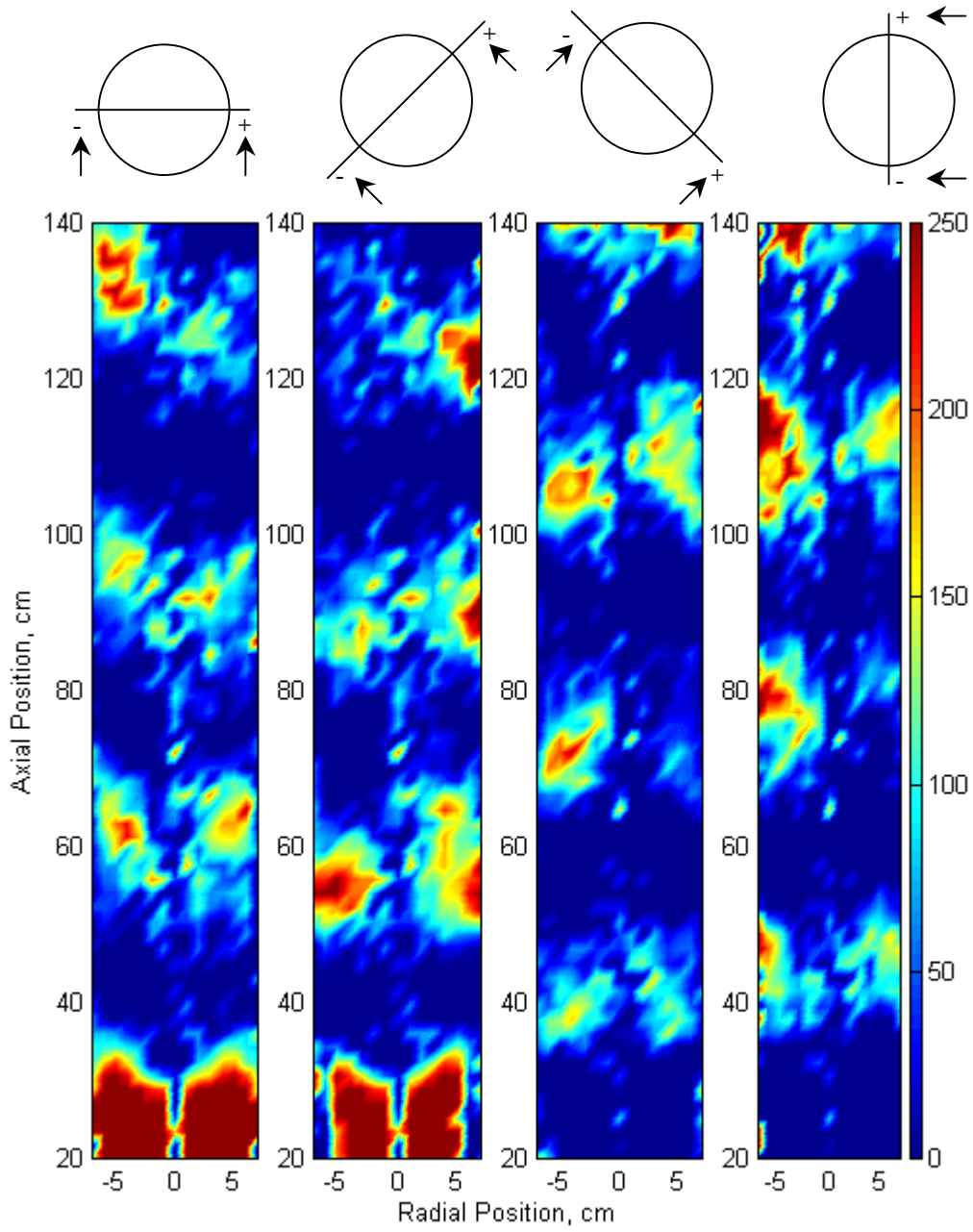

Figure 5-16. Radial-azimuthal turbulent stress (longitudinal views), $\tau_{r\theta}$, for distributor D4 (0.15%, 163 orifices of 0.5 mm) at U_g = 30 cm/s at P = 1 atm.

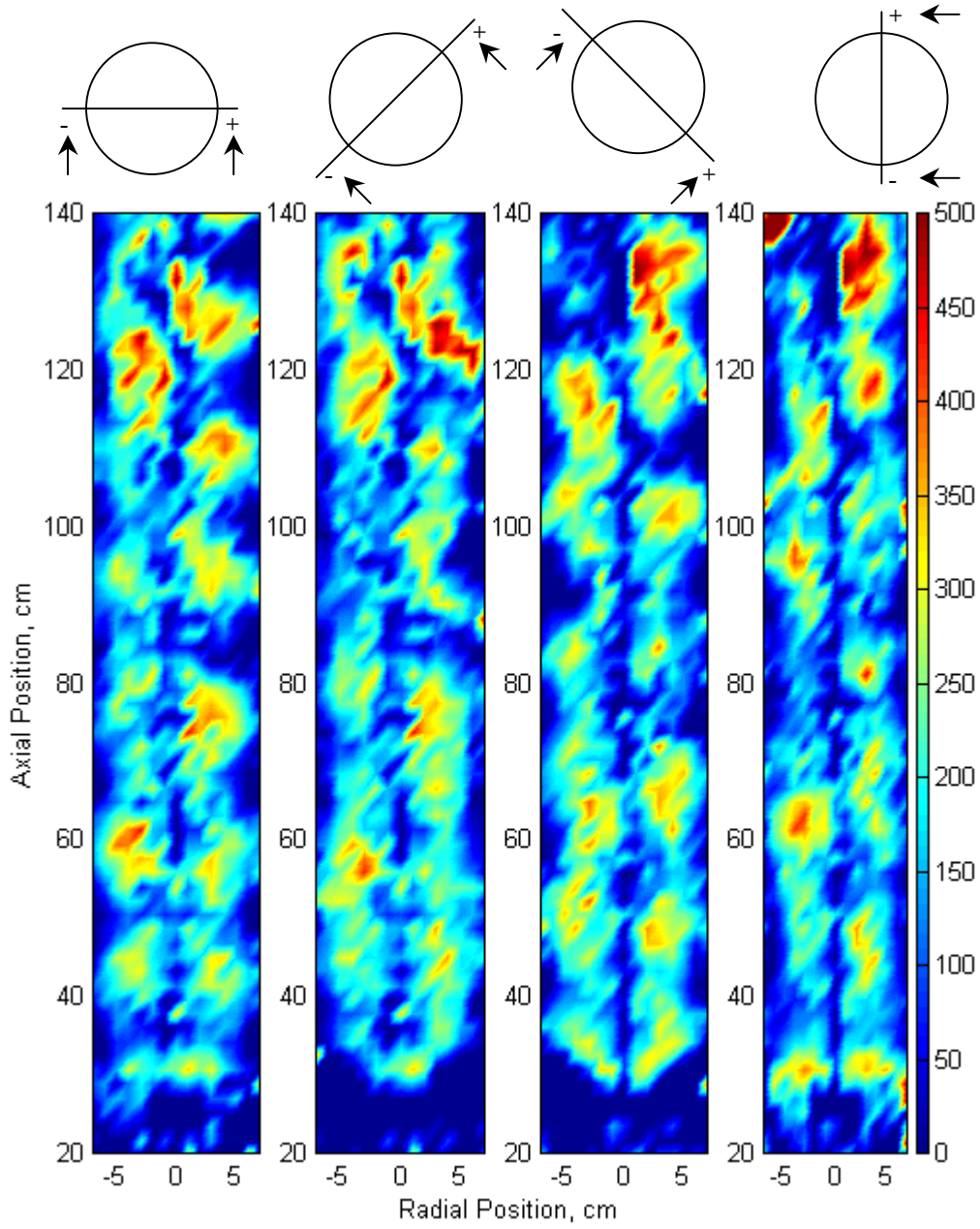

Figure 5-17. Radial-axial turbulent stress (longitudinal views), τ_{rz}, for distributor D4 (0.15%, 163 orifices of 0.5 mm) at U_g = 30 cm/s at P = 1 atm.

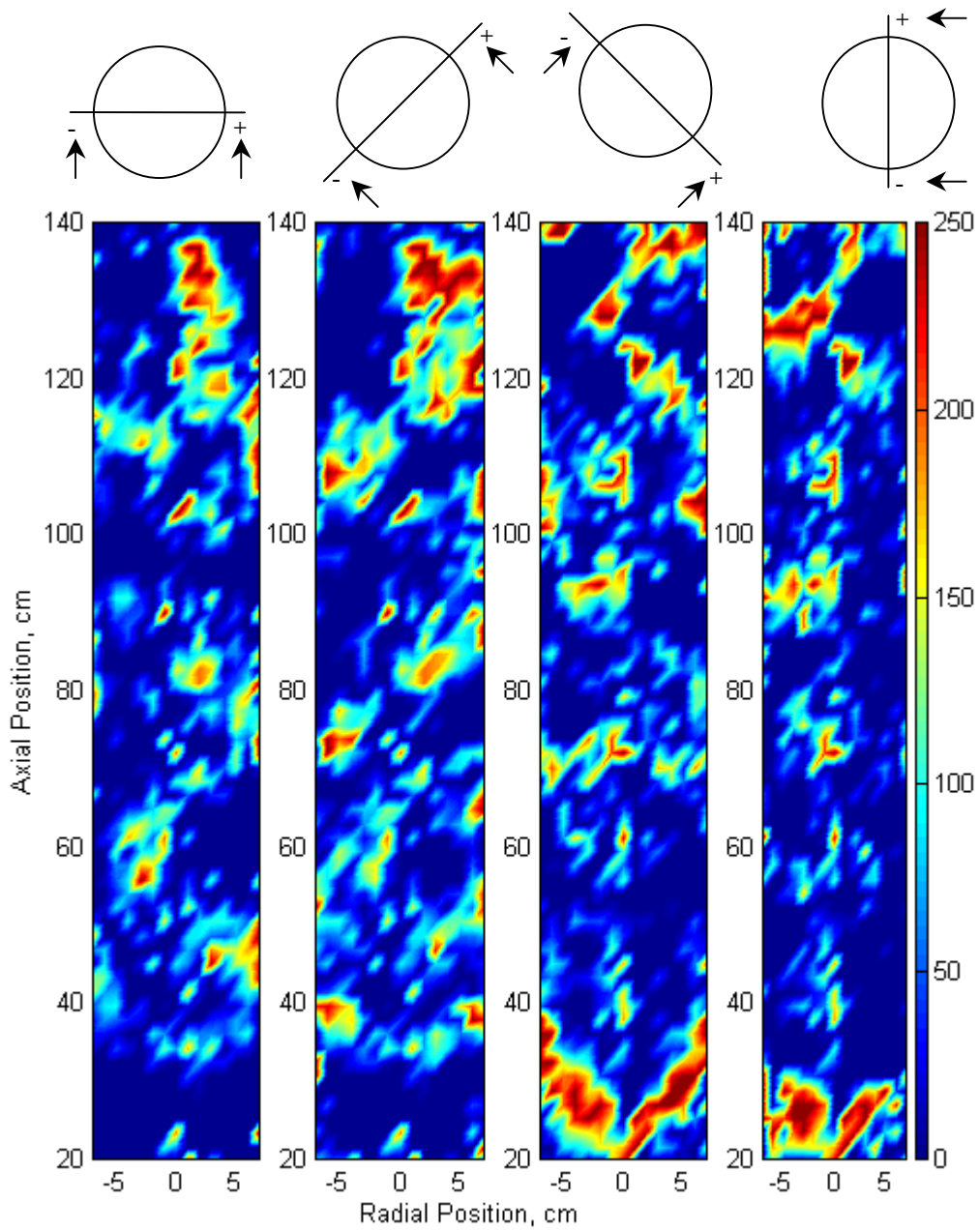

Figure 5-18. Axial-azimuthal turbulent stress (longitudinal views), $\tau_{z\theta}$, for distributor D4 (0.15%, 163 orifices of 0.5 mm) at U_g = 30 cm/s at P = 1 atm.

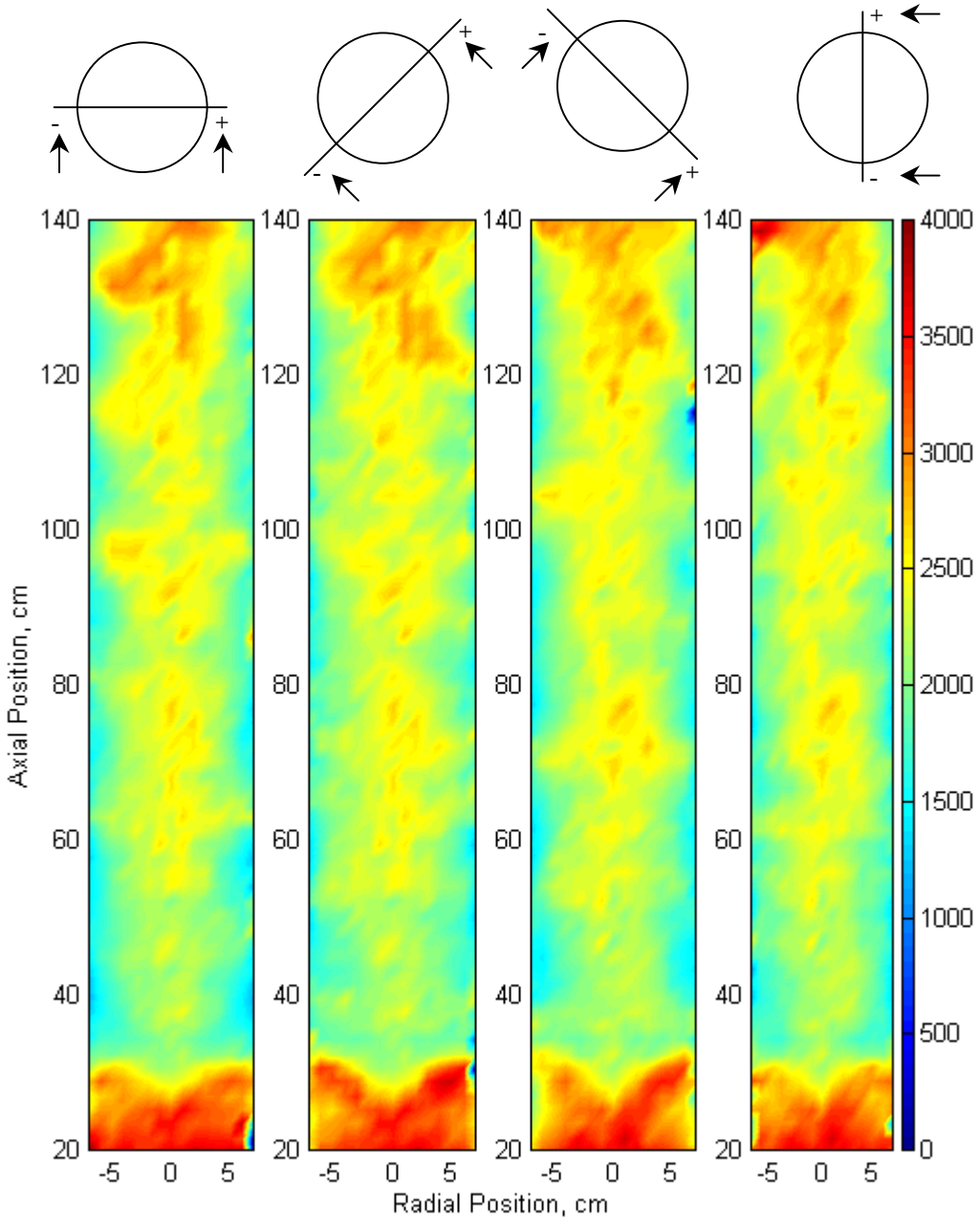

Figure 5-19. Turbulent kinetic energy (longitudinal views) for distributor D4 (0.15%, 163 orifices of 0.5 mm) at U_g = 30 cm/s at P = 1 atm.

Further, Figure 5-19 shows the turbulent kinetic energy contour plot for uniform perforated plate distributor D4 at the same operating conditions as those for Figures 5-13 to 5-18. It can be readily seen from Figures 5-16 and 5-18 that $\tau_{r\theta}$ and $\tau_{z\theta}$ are relatively small in magnitude as compared to τ_{rz} and the plots do not indicate any particular symmetry trends. Also, τ_{rz} shows a peak in the annular region of the column (refer to Figure 5-17). Figure 5-19 indicates higher values at an axial position of 20-30 cm from the distributor, which implies high degree of turbulence in the inlet section. In addition, the plot exhibits symmetry about the column center. Based on the symmetry in most of these observations, the three-dimensional velocity data are averaged azimuthally and axially (54-136.8 cm from the distributor) to obtain the one-dimensional variation of liquid velocity and turbulence fields along the radial dimension.

5.6. One-Dimensional Analysis of Liquid Velocity and Turbulence Parameters

As mentioned in the previous section, the flow is fairly symmetric about the central axis and becomes fully developed at a *z* level above 50 cm. Therefore, further analysis of the data has been restricted to discussion of the azimuthally, axially and time-averaged flow quantities. Hence, the time-averaged and azimuthally-averaged liquid velocity and turbulence profiles presented in the figures in subsequent sections were axially averaged from z = 54 to 136.8 cm and the error bars on each profile represent the range of values encountered for all z levels.

Before further discussing the effects of distributor, pressure and superficial gas velocity on the axially, azimuthally and time-averaged liquid velocity and turbulence profiles, it is interesting to review the turbulent shear stress in the *r*-*z* plane (τ_{rz}) and its relationship to the gradient of the mean axial liquid velocity as per the Boussinesq's hypothesis. The reason for only modeling τ_{rz} is that in the long time-averaged sense, based on the experimental measurements of the velocity cross correlations and the velocity gradients, the shear stresses in the r-θ and z-θ directions are negligible.

The relationship between τ_{rz} and the gradient of the mean axial liquid velocity based on the Boussinesq's hypothesis is shown in Equation (5-3), which also forms the

closure relationship in the frequently employed one-dimensional liquid recirculation model (Kumar, 1994; Gupta *et al.*, 2001; Gupta, 2002). Further details on the one-dimensional liquid recirculation model can be found in Appendix A. One may question the validity of the Boussinesq's hypothesis to describe the Reynolds shear stress. However, not many alternatives are available, and the approach has even been used in the framework of Large Eddy Simulation-LES (Deen *et al.*, 2001; Deen, 2001) to simulate hydrodynamics in a square bubble column. As a result, the experimental observations in this study have been evaluated assuming the validity of the Boussinesq's hypothesis, which will be addressed in Section 5.7.

$$\tau_{l,rz} = \begin{cases} \rho_l \overline{u_r' u_z'} = -\rho_l \dfrac{\nu_{eff}}{R}\dfrac{du_z}{d\xi} & for\ \xi \le \lambda \\ -\rho_l \dfrac{\nu_m}{R}\dfrac{du_z}{d\xi} & for\ \xi > \lambda \end{cases} \qquad (5\text{-}3a, b)$$

In the above equation, ξ is the dimensionless radius and λ is that value of ξ at which one observes the maximum downward liquid velocity. The effective kinematic viscosity, ν_{eff}, is frequently reported to be the sum of the contributions from molecular (ν_m), shear-induced turbulent (ν_{SIT}) and bubble-induced turbulent (ν_{BIT}) kinematic viscosities (Deen *et al.*, 2001; Deen, 2001; Ohnuki and Akimoto, 2001) as shown in Equation (5-4). The eddy viscosity due to bubble-induced turbulence is computed based on the model proposed by Sato and Sekoguchi (1975) (refer to Equation (5-4b)). On the other hand, the eddy viscosity due to shear-induced turbulence is represented in a fashion similar for single-phase isotropic turbulence (refer to Equation (5-4c)).

$$\nu_{eff} = \nu_m + \nu_{SIT} + \nu_{BIT} \qquad (5\text{-}4a)$$

$$\nu_{BIT} = C_{\mu,BIT}\varepsilon_g d_b \left|u_{slip}\right| \qquad C_{\mu,BIT} = 0.6 \qquad (5\text{-}4b)$$

$$\nu_{SIT} = C_\mu \left\{ \begin{array}{ll} \dfrac{k^2}{\varepsilon} & Deen\ et.\ al.\ (2001) \\ \dfrac{k_{SIT}^2}{\varepsilon} & Ohnuki\ and\ Akimoto\ (2001) \end{array} \right\} \qquad (5\text{-}4c)$$

$$where,\ C_\mu = 0.09$$

In Equation (5-4c), ε refers to the energy dissipation rate per unit mass of liquid. However, in this study, ε is estimated to be equal to gU_g (Deckwer and Schumpe, 1987; Rubio *et al.*, 1999; Camacho *et al.*, 2001), which represents the upper bound of the total dissipation rate. Hence, ν_{SIT} represents the lower bound due to the contribution of shear-induced turbulence while k_{SIT} is the portion of the total turbulent kinetic energy resulting from shear-induced turbulence.

Based on the relative magnitudes of τ_{rr}, $\tau_{\theta\theta}$ and τ_{zz} as shown earlier (Figure 5-7), it is clear that the turbulent kinetic energy is not evenly distributed along the r, θ, and z-directions and therefore the turbulence structure is anisotropic, which contradicts with Equation (5-1b) that states the normal stresses are similar (i.e. $\tau_{rr} = \tau_{\theta\theta} = \tau_{zz}$). Nevertheless, Bousinessq's hypothesis will still be used as a simple approach to explain the experimental observations. The turbulent eddy viscosity resulting from shear-induced turbulence, ν_{SIT}, is inversely proportional to the gradient of axial liquid velocity, whereas the eddy viscosity from bubble-induced turbulence, ν_{BIT}, is proportional to the bubble size as well as the slip velocity between the liquid and bubbles. In this section, Equations (5-3) and (5-4) will mostly be used to discuss the experimental results.

5.6.1 Distributor Effects on Liquid Recirculation and Turbulence Parameters

A) P = 1 atm; U_g = 30 cm/s

At atmospheric pressure, the effect of distributors on liquid velocity and turbulence parameters is investigated using distributors D2 (0.1% cross sparger), D4 (0.1% uniform perforated plate) and D6 (1.0% uniform perforated plate) (refer to Figure 3-2 for the schematic diagram of the distributors). A note to remember is that the orifices of distributor D2 is facing downwards. Figure 5-20 displays the effect of distributors on radial profiles of the axial liquid velocity at U_g = 30 cm/s and at atmospheric pressure. Despite the different configurations of the distributors, there appears to be no significant difference in the measured time-averaged liquid velocity profiles, which should not be surprising since this operating condition is representative of the churn-turbulent regime.

This is also in agreement with the trends observed in the radial gas holdup profiles measured using Computed Tomography reported in Chapter 4 (refer to Figure 4-8).

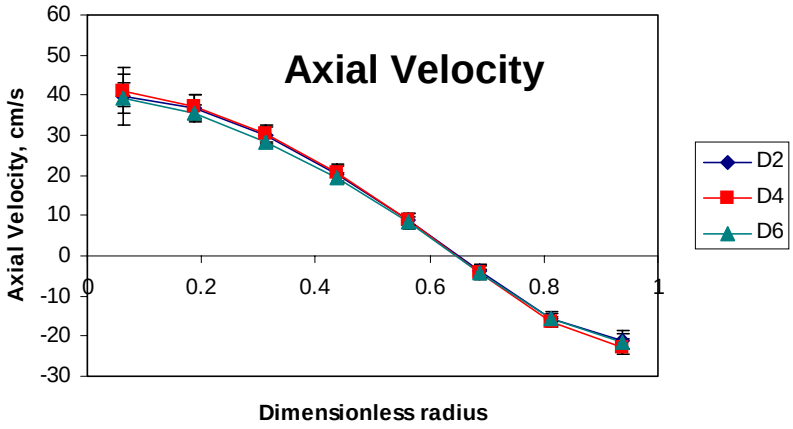

(a) Axial liquid velocity

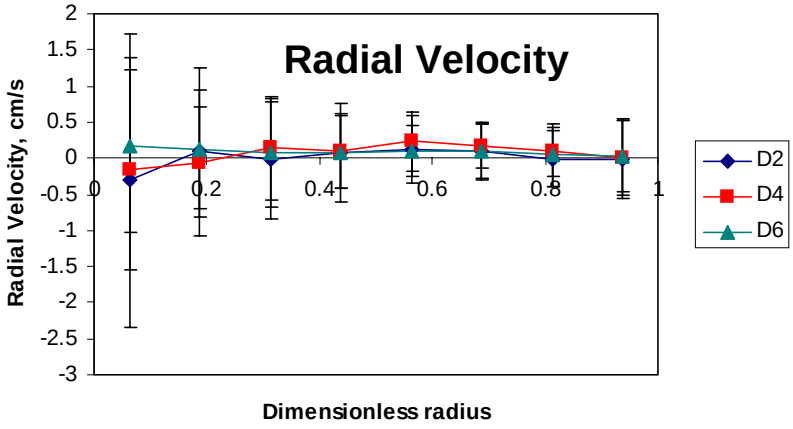

(b) Radial liquid velocity

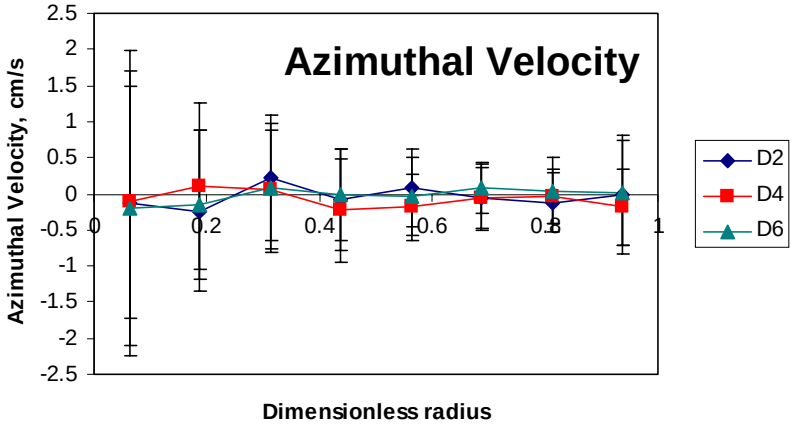

(c) Azimuthal liquid velocity

Figure 5-20. Effect of distributors on velocity profiles (U_g = 30 cm/s, P = 1 atm).

Figures 5-21 and 5-22 show the effect of distributor on the turbulence stresses and turbulent kinetic energy, respectively. As can be seen from Figure 5-21a to 5-21c, the axial normal stress is about two times larger than the radial and angular normal stresses. This is in agreement with what was observed by Degaleesan (1997). Since gas holdup profiles for these distributors are similar (refer to Figure 4-8) along with the liquid recirculation profiles (refer to Figure 5-20), the similar profiles of shear stress in *r*-*z* direction, τ_{rz}, as shown in Figure 5-21e, imply similar ***effective*** turbulent eddy viscosity (these arguments can be made based on the one-dimensional liquid recirculation model). Clearly a similar effective turbulent eddy viscosity implies similar sum of shear-induced and bubble-induced turbulent contributions. Since the equilibrium bubble size is likely to be similar when using the three distributors, at this operating condition the bubble induced turbulence is similar. For shear-induced turbulent eddy viscosity to be also similar for different distributors, Equation (5-4c) implies that the total turbulent kinetic energy should be the same as well (Deen *et al.*, 2001). However, from Figure 5-22, it is clear that the turbulent kinetic energy for distributor D2 (cross sparger) is distinctly higher than that for distributors D4 and D6 (perforated plates). The higher turbulent kinetic energy obtained for cross sparger, D2, is due to the higher normal stresses obtained in r and θ directions, τ_{rr} and $\tau_{\theta\theta}$, which do not contribute to axial liquid recirculation. As can be seen from Figure 5-21a, even though the magnitudes of τ_{zz} for different distributors have a similar trend as for τ_{rr} and $\tau_{\theta\theta}$, the band of variation is larger for τ_{zz}. Hence, the normal stress in the z direction (τ_{zz}) for the three distributors could be considered identical within the bounds of experimental uncertainty (error bars). Therefore, the only explanation for a similar shear-induced eddy viscosity for the three spargers can be obtained if one considers the anisotropic nature of turbulence. Thus, neglecting the anisotropy of the turbulent structure in bubble columns leads to unreliable results.

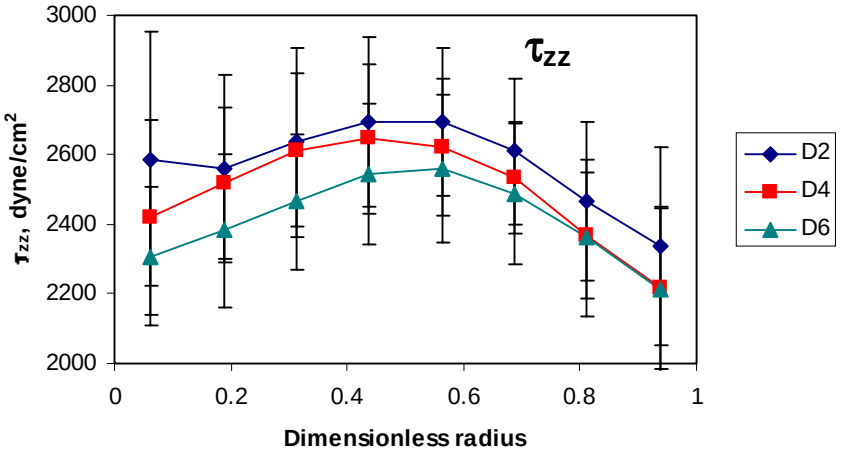
τzz
τzz, dyne/cm2
3000
2800
2600
2400
2200
2000
0
0.2
0.4
0.6
0.8
1
Dimensionless radius
D2
D4
D6

(a)

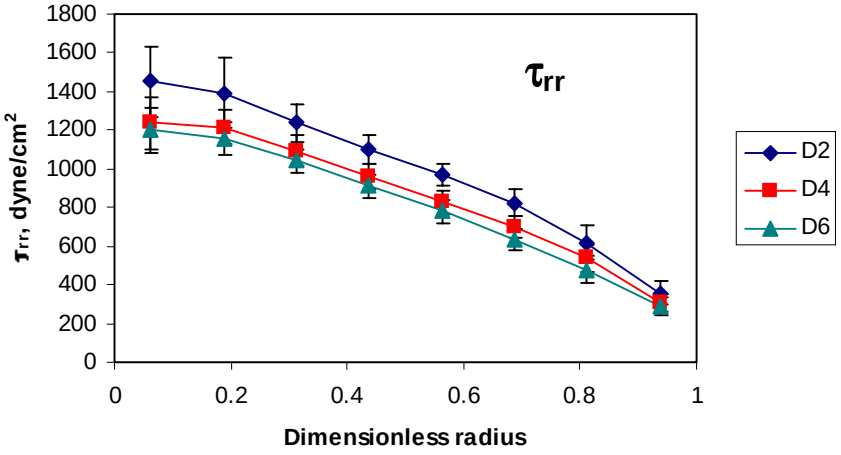
τrr
τrr, dyne/cm2
1800
1600
1400
1200
1000
800
600
400
200
0
0
0.2
0.4
0.6
0.8
1
Dimensionless radius
D2
D4
D6

(b)

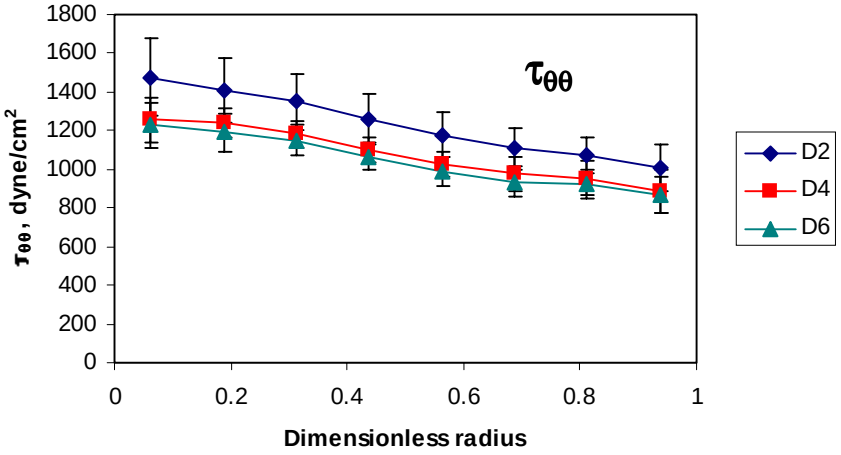
τθθ
τθθ, dyne/cm2
1800
1600
1400
1200
1000
800
600
400
200
0
0
0.2
0.4
0.6
0.8
1
Dimensionless radius
D2
D4
D6

(c)

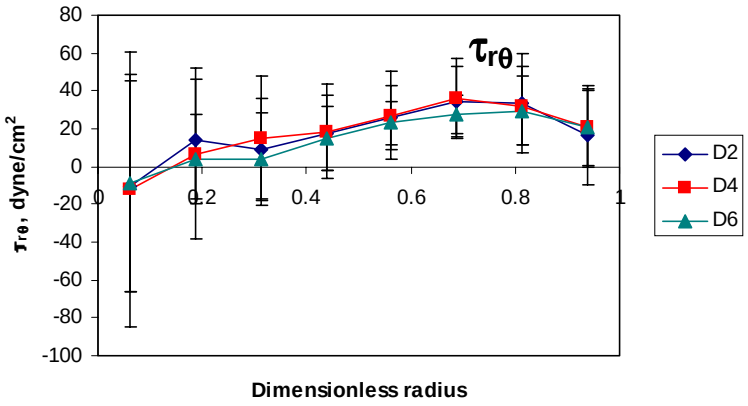

(d)

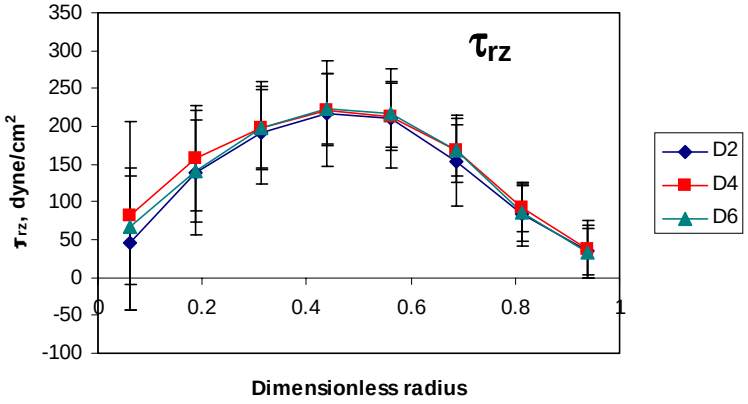

(e)

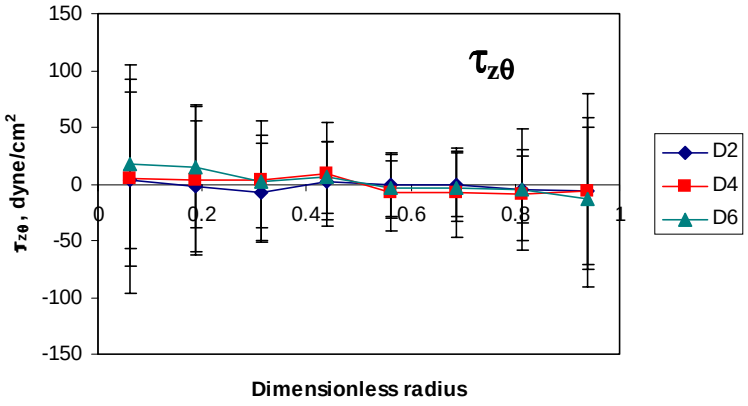

(f)

Figure 5-21. Effect of distributors on turbulent stresses (U_g = 30 cm/s, P = 1 atm).

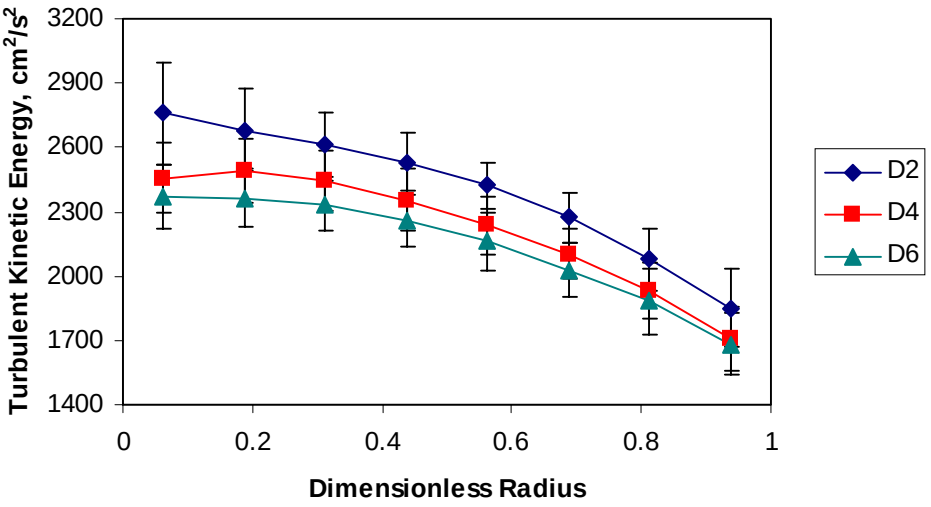

Figure 5-22. Effect of distributors on turbulent kinetic energy profiles (U_g = 30 cm/s, P = 1 atm).

As was mentioned earlier, the turbulent stress profiles presented in Figure 5-21 for the cross sparger, D2 indicate higher turbulent normal stresses in the radial and azimuthal directions as compared to the other two distributors. One possible explanation for these observed differences could be developed based on the bubble formation regimes prevalent for these three spargers (refer to Table 4-2). From the table, it is seen that the uniform perforated plate spargers D4 and D6 are in the "bubbling" regime of bubble formation, whereas cross sparger D2 lies in the dispersed jetting regime. Since the dispersed jetting regime is characterized by turbulent gas jets, from which small bubbles keep shearing off into the liquid phase, it is not surprising that the level of liquid turbulence is higher for cross sparger D2 than those measured with uniform perforated plate distributors D4 and D6. It was argued earlier that the equilibrium bubble size generated by these three spargers is similar so as to result in similar bubble-induced eddy viscosity. Due to different regimes of bubble formation, one can expect significantly different bubble structure in the sparger region with strong gas jets emanating from the orifices of distributor D2. Thus, the transition from the distributor to the fully developed region of the column might require complex bubble coalescence and break-up events

contributing to liquid phase turbulence in the well-developed flow region. For example, it is possible that the bubble size formed at the distributor D6 is close to the equilibrium bubble size. Then, fewer coalescence and breakup events of the bubbles formed at the orifice are needed to reach this equilibrium bubble size, which would result in the reduced fluctuations leading to the lowest level of τ_{zz}, τ_{rr}, $\tau_{\theta\theta}$ for D6.

One should take note that CARPT experiments for two other distributors (D1: uniform perforated plate, 163 orifices of 0.4 mm; and D3: single nozzle of 5.1 mm) of the same porosity as D2 (0.1%) were not performed due to the hypothesis made based on radial gas holdup measured using Computed Tomography (refer to Section 4.2.1) that uniform perforated plate distributor, D1 would exhibit the CARPT profiles of uniform perforated plate distributor, D4 (0.15%, d_o = 0.5 mm), and single nozzle, D3 those of cross sparger, D2.

B) P = 4 atm; U_g = 30 cm/s

Similar analysis, as presented above for atmospheric pressure condition, is performed at a higher pressure of 4 atm. In this case, distributors D3 (0.1% single nozzle), D4 (0.15% uniform perforated plate) and D6 (1.0% uniform perforated plate) were used to investigate the distributor effect on liquid velocity and the turbulence parameters. Figures 5-23 to 5-25 display the effect of distributors on the liquid velocity and turbulence parameters at a superficial gas velocity of 30 cm/s and at a pressure of 4 atm. Although at atmospheric pressure, the axial liquid velocity profiles fall on top of each other (refer to Figure 5-20a), at P = 4 atm, the axial liquid velocity profiles are slightly different for the three distributors investigated, whereas the radial and azimuthal liquid velocity profiles can be assumed negligible (refer to Figure 5-23). As evident from Figure 5-23, the liquid velocity profile for the uniform perforated plate distributor, D4 is slightly lower than the profile obtained by the other two distributors. In Chapter 4, it was reported that gas holdup was highest for D3, followed by D6 and then D4. On the other hand, the mean gradient of the radial gas holdup profile (F) was highest for D6 (0.611), followed by D3 (0.475) and then D4 (0.465). Since it is the gradient of the radial gas

holdup distribution that drives liquid recirculation, one would expect highest axial liquid velocity for distributor D6 followed by D3 and then D4. While the trend predicted for D4 based on these arguments is evident from Figure 5-23a, a clear difference is not seen for the axial liquid velocity measured using D3 and D6. A possible explanation could be the opposite effects of the higher gas holdup and lower gas holdup gradient obtained with distributor D3 that prevents a significantly lower axial liquid velocity compared to that obtained using D6.

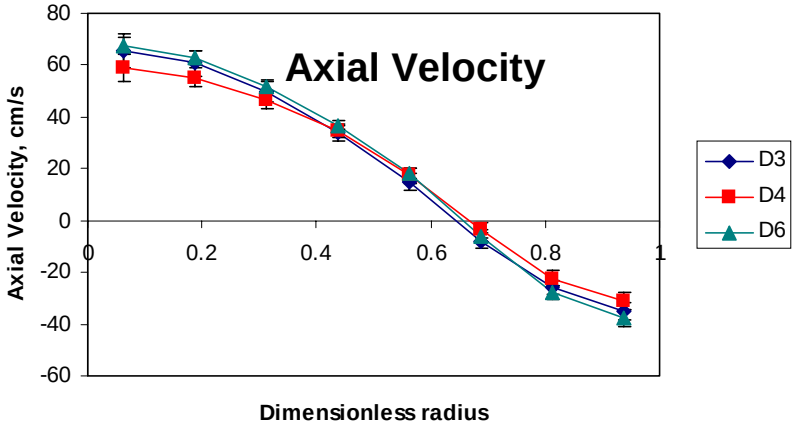

(a) Axial liquid velocity

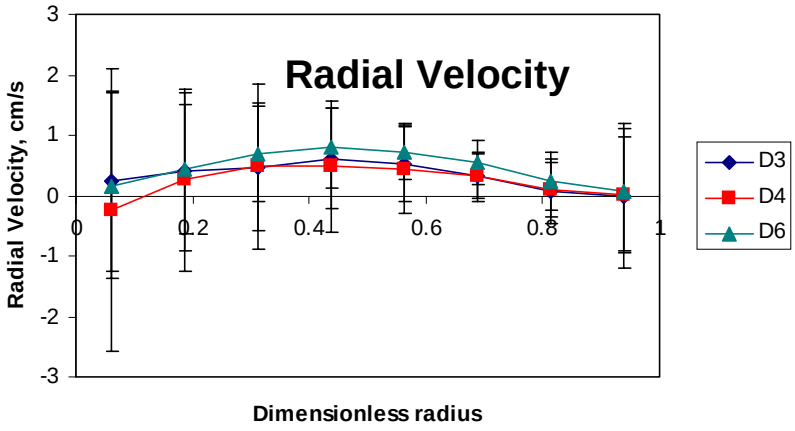

(b) Radial liquid velocity

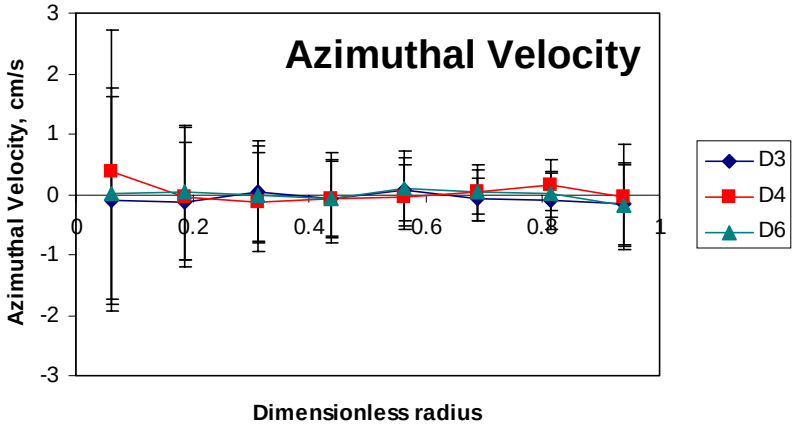

(c) Azimuthal liquid velocity

Figure 5-23. Effect of distributors on velocity profiles (U_g = 30 cm/s, P = 4 atm).

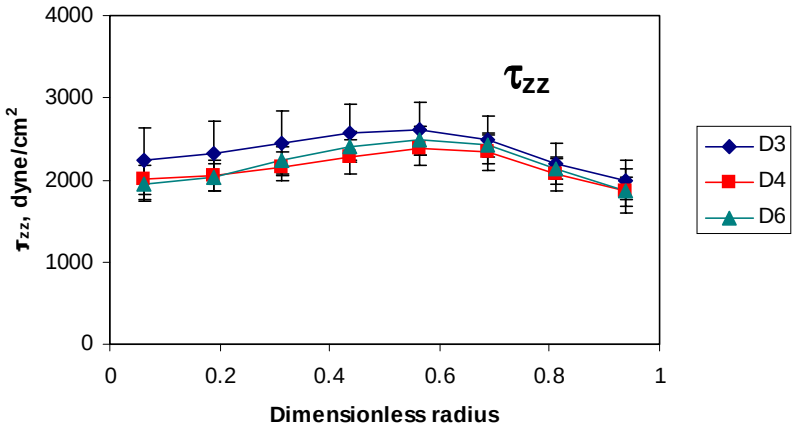

(a)

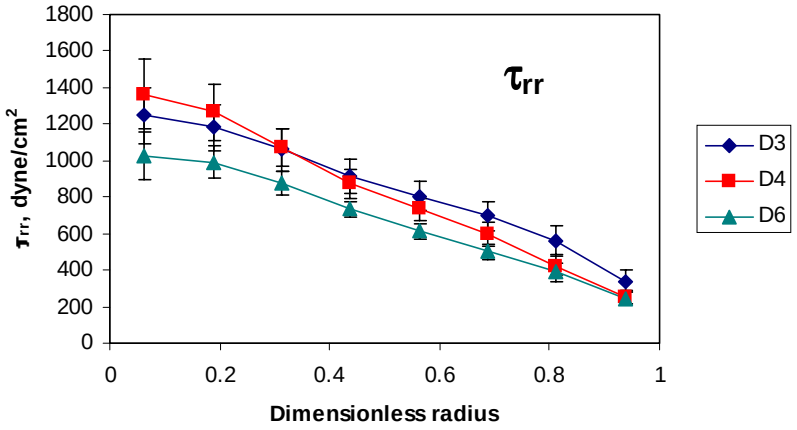

(b)

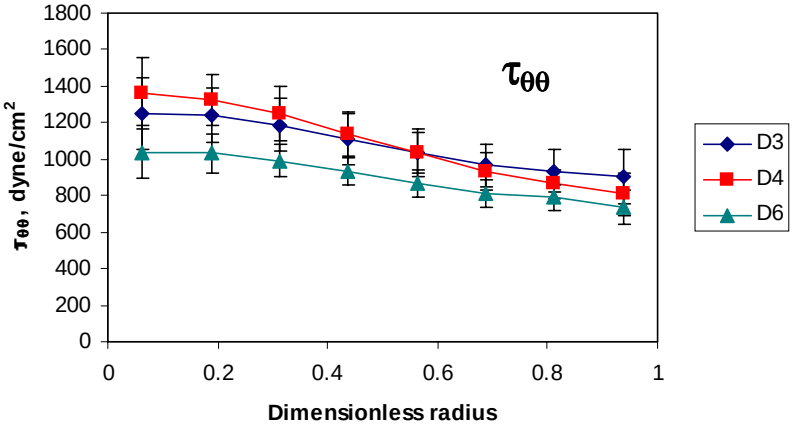
τθθ
τθθ, dyne/cm2
Dimensionless radius
D3
D4
D6

(c)

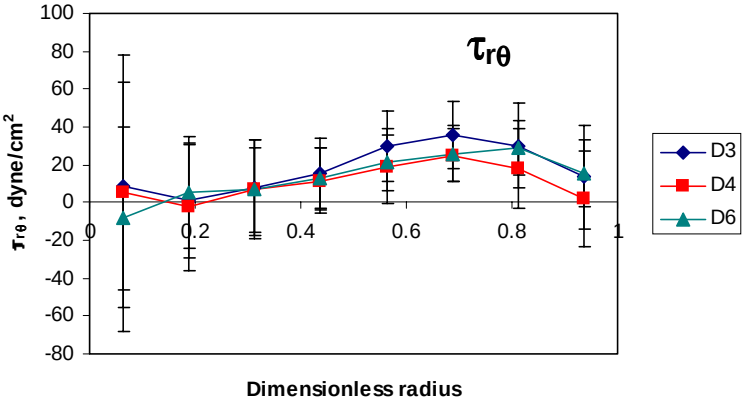
τrθ
τrθ, dyne/cm2
Dimensionless radius
D3
D4
D6

(d)

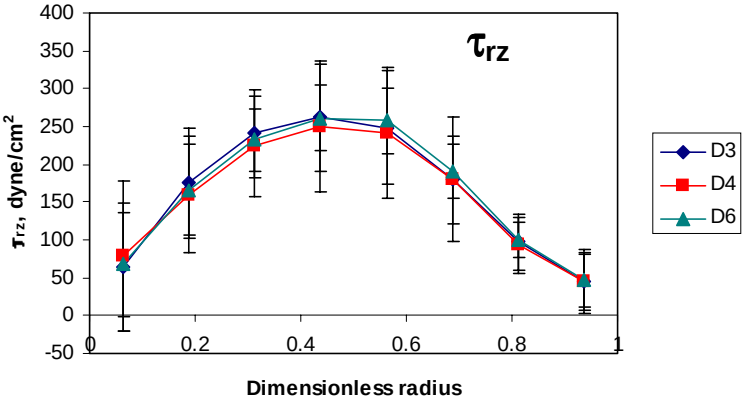
τrz
τrz, dyne/cm2
Dimensionless radius
D3
D4
D6

(e)

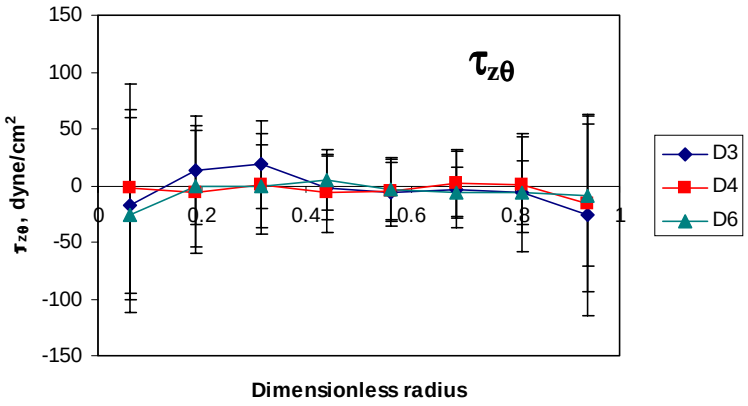

(f)

Figure 5-24. Effect of distributors on turbulent stresses (U_g = 30 cm/s, P = 4 atm).

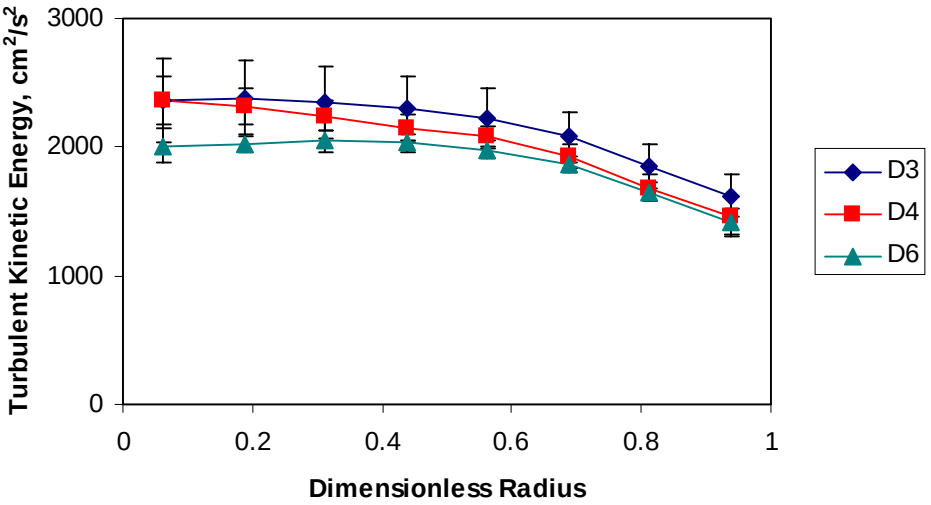

Figure 5-25. Effect of distributors on turbulent kinetic energy profiles (U_g = 30 cm/s, P = 4 atm).

Another observation is that despite the differences in the gas holdup (Figure 4-9) and liquid velocity profiles (Figure 5-23a), the shear stresses in the r-z direction, τ_{rz} (Figure 5-24e) are almost the same. This could be explained using Equations (5-3) and (5-4). The axial liquid velocity for each distributor is somewhat different as evident from Figure 5-23a. For τ_{rz} to be the same, ν_t must be different and the effect of ν_t on τ_{rz} must

be opposite to that of the axial liquid velocity gradient, thus, eliminating the distributor effect on τ_{rz}. Figure 5-26 shows the axial velocity gradient for three different distributors at a superficial gas velocity of 30 cm/s and at a pressure of 4 atm. The axial velocity gradient is obtained approximately via backward difference (refer to Equation (5-5)).

$$\left(\frac{du_z}{dr}\right)_i = \frac{u_{z,i} - u_{z,i-1}}{r_i - r_{i-1}} \tag{5-5}$$

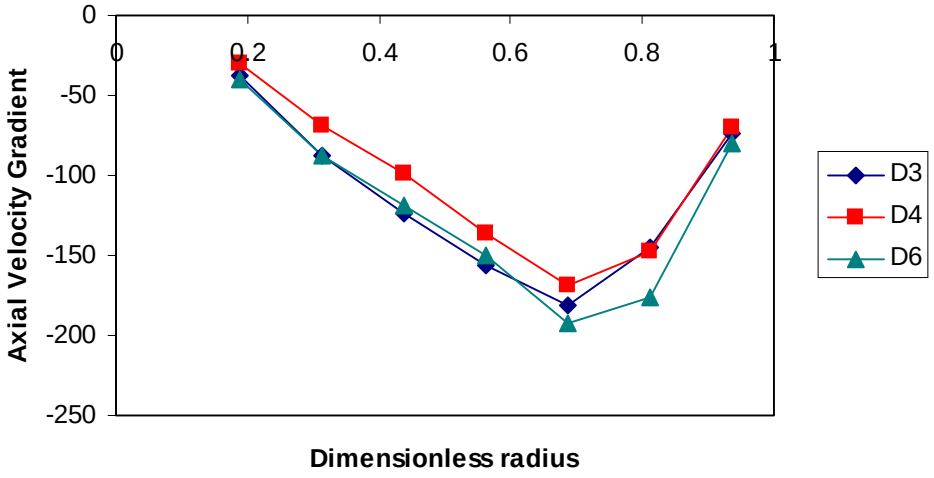

Figure 5-26. Effect of distributors on axial velocity gradient profiles (U_g = 30 cm/s, P = 4 atm).

Based on Equation (5-4) and (5-5), the trends for ν_{SIT} and the axial liquid velocity gradient for three distributors are represented as follows.

ν_{SIT}: D6 < D4 < D3

$\frac{du_z}{dr}$: D4 < D3 < D6

As evident from the above trends and also from Figure 5-26, the absolute value of the radial gradient of axial velocity is the highest for the uniform perforated plate distributor D6 compared to the other two distributors and lowest ν_{SIT}. This implies that the radial gradient of axial velocity and turbulent eddy viscosity have an opposite effect on τ_{rz} considering all distributors. However, this is not true for distributors D3 and D4. Distributor D3 has a higher ν_{SIT} and the liquid velocity gradient as compared to D4.

Hence, distributor D3 should exhibit a higher turbulence shear stress than distributor D4. From Figure 5-24e, although one see that τ_{rz} is almost similar for all distributors, a closer look at the graph indicates that τ_{rz} is slightly higher for D3 than for D4. In addition, as shown in Chapter 4, the gas holdup profile is the highest for distributor D3 than any other distributors (refer to Figure 4-9), thus, a higher τ_{rz} is generated. The dependence of gas holdup on τ_{rz} is not clearly seen from the 1-D model shown in Appendix A, however, the dependency can be seen from a simplified version of the 1-D model developed by Kumar (1994) (refer to Equation (5-6)).

$$\tau_{rz}(\xi) = \begin{cases} \rho_l gR/2 \left(2\tilde{\varepsilon}/m\lambda^2\right) \xi\, c\left[1-\left(\xi/\lambda\right)^m\right] & \xi \le \lambda \\ \rho_l gR/2 \left(\bar{\varepsilon}/\lambda^2\right)\left[\dfrac{\lambda^2-\xi^2}{\xi}\right] & \xi \ge \lambda \end{cases} \tag{5-6}$$

Figure 5-25 shows that the turbulent kinetic energy profile for distributor D3 is marginally higher as compared to the other two distributors. This somewhat higher turbulent kinetic energy exhibited using the single nozzle distributor (D3) could be explained based on the regime of bubble formation. As shown in Table 4-2, at this operating condition, the single nozzle, D3 is in the dispersed jetting regime whereas the remaining two distributors are in the jetting regime. Since numerous fine bubbles along with the larger ones from the gas jets are generated in the distributor region when a distributor is operating in the dispersed jetting regime, it implies that a multitude of coalescence/breakup events would be required to attain the equilibrium bubble size in the column. These would in turn result in higher levels of turbulent fluctuations of the liquid phase as well (refer to Figure 5-11). It is interesting to note that the enhanced level of liquid turbulence seen with D3 primarily contributes to higher normal stress in the *z* direction with the remaining contributions in *r* and θ directions being marginally similar for distributors D3 and D4 and significantly lower for D6. Thus, more complex bubble coalescence and breakup events might occur during the transition from one distributor region to the fully-developed region, resulting in higher levels of liquid turbulence as compared to other distributors.

5.6.2 Pressure Effects on Liquid Recirculation and Turbulence Parameters

A) D6; U_g = 30 cm/s

The effect of pressure on liquid velocity and turbulence parameters is investigated using distributor D6, which has a 1.0 % open area, operating at a superficial gas velocity of 30 cm/s. The results are shown in Figures 5-27 to 5-29. As evident from Figure 5-27, higher pressure leads to higher axial liquid velocity due to increased gas holdup (refer to Figure 4-16b).

Figures 5-28b,c and 5-29 indicate that the radial and azimuthal normal turbulent stresses, and subsequently the turbulent kinetic energy are higher at atmospheric pressure and are reduced (up to 20%) as pressure increases. A possible explanation for this phenomenon could be as follows. Because of the larger bubble size at the atmospheric conditions (lower pressure), it is likely that the bubbles formed at the sparger are substantially larger in size than the equilibrium bubble size. As a result, the bubble structure may undergo frequent coalescence and breakup to attain the equilibrium bubble size. This probably results in a generation of velocity fluctuations emanating from bubble rupture. These velocity oscillations get superimposed on the mean flow structure inside the column, which is predominantly in the axial direction. Thus, the effect is mainly seen in the radial and azimuthal components of the normal turbulent stress. Additionally, a larger bubble size at lower pressure also probably leads to a more spiraling flow structure that leads to higher values of the root mean square fluctuating velocities. On the other hand, as operating pressure increases, the bubble size formed at the sparger, as well as those prevalent in the column are smaller (Fan and Tsuchiya, 1990; Luo *et al.*, 1999). As a result, the transition of the bubble size from that at the sparger to the equilibrium size probably leads to fewer and less energetic bubble breakup events. This subsequently leads to reduction in the level of liquid phase turbulence in the column (Lee *et al.*, 2001). Additionally, because of the smaller bubble sizes, the structure of the gas phase is possibly more uniform, thereby leading to a reduction in the vortical (helical) motion. This is reflected in the lower values of radial and azimuthal normal turbulent stresses as compared to those at lower pressure.

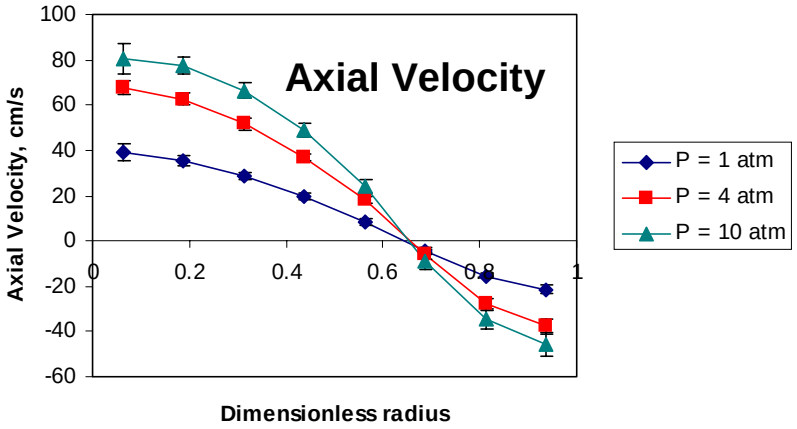

(a) Axial liquid velocity

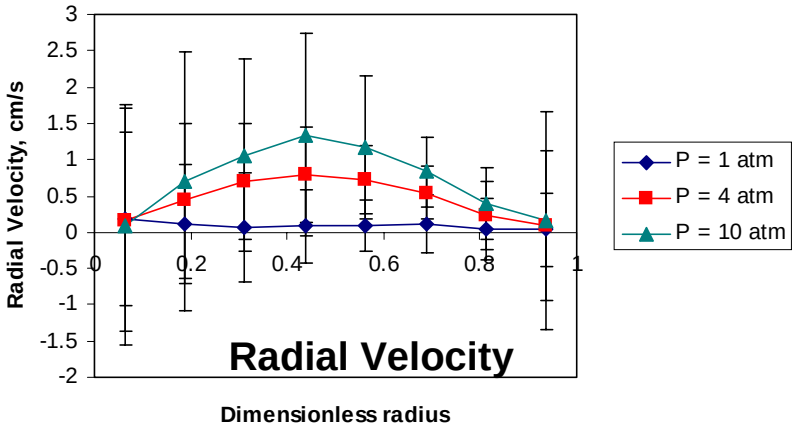

(b) Radial liquid velocity

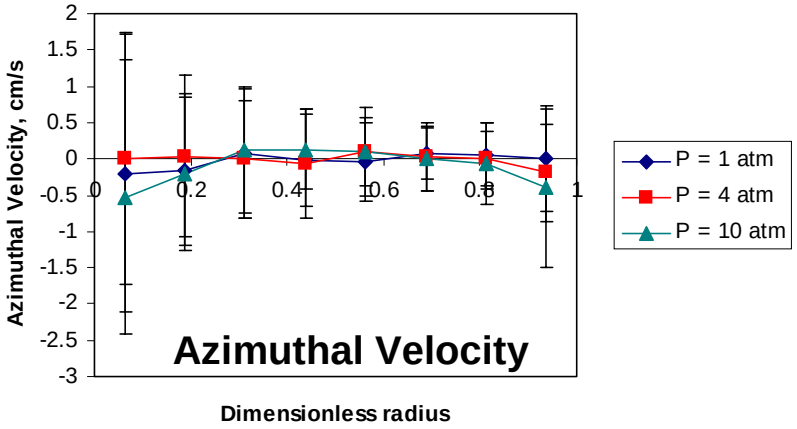

(c) Azimuthal liquid velocity

Figure 5-27. Effect of pressure on velocity profiles for distributor D6 (1.0 POA) at U_g = 30 cm/s.

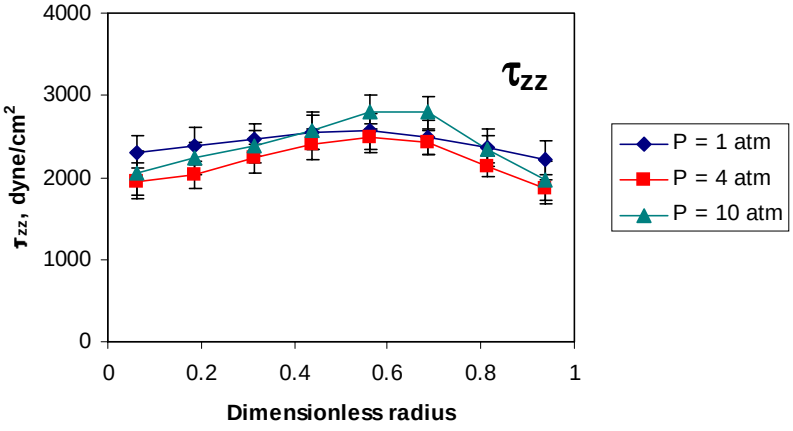
τzz
τzz, dyne/cm2
4000
3000
2000
1000
0
0
0.2
0.4
0.6
0.8
1
Dimensionless radius
P = 1 atm
P = 4 atm
P = 10 atm

(a)

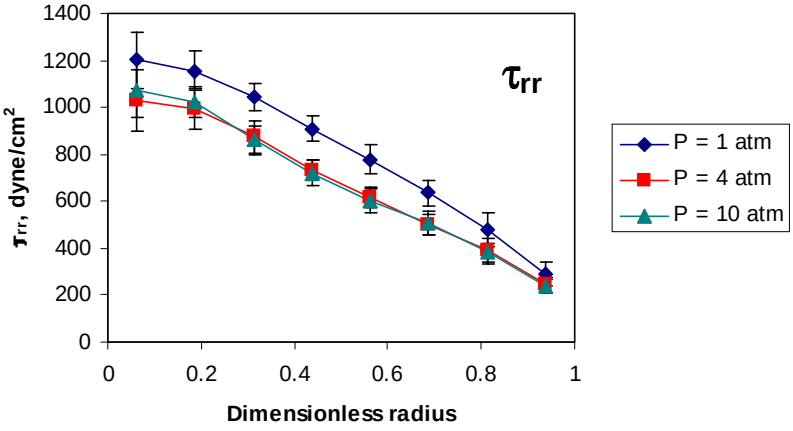
τrr
τrr, dyne/cm2
1400
1200
1000
800
600
400
200
0
0
0.2
0.4
0.6
0.8
1
Dimensionless radius
P = 1 atm
P = 4 atm
P = 10 atm

(b)

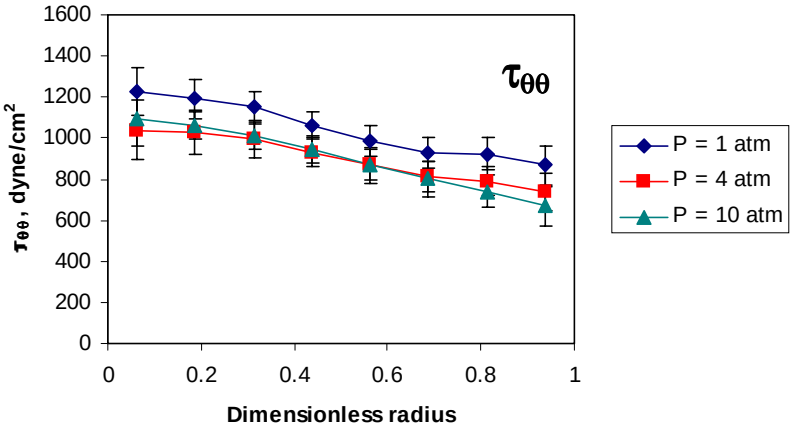
τθθ
τθθ, dyne/cm2
1600
1400
1200
1000
800
600
400
200
0
0
0.2
0.4
0.6
0.8
1
Dimensionless radius
P = 1 atm
P = 4 atm
P = 10 atm

(c)

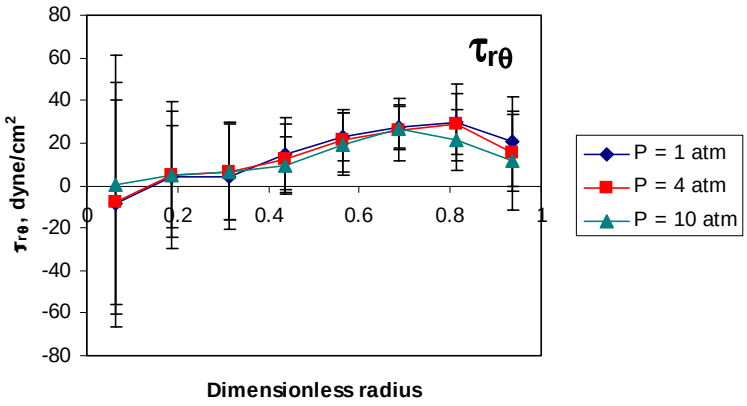

(d)

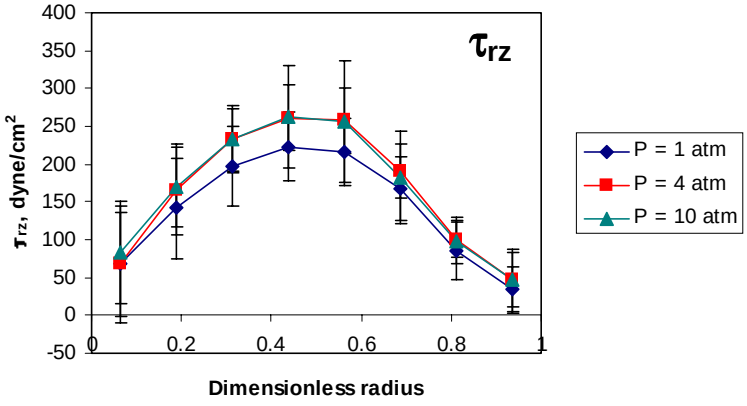

(e)

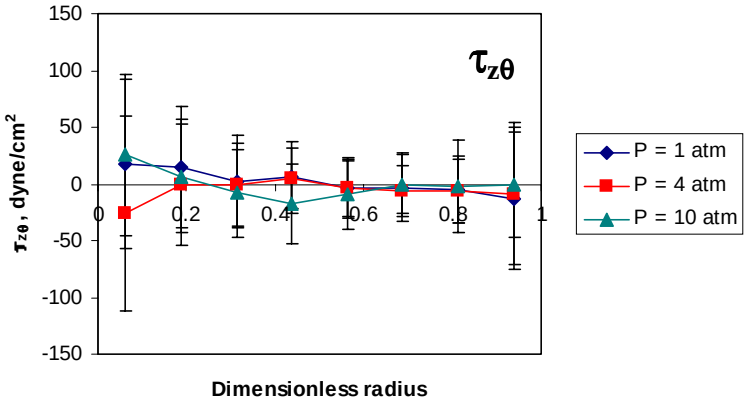

(f)

Figure 5-28. Effect of pressure on turbulent stresses for distributor D6 (1.0 POA) at U_g = 30 cm/s.

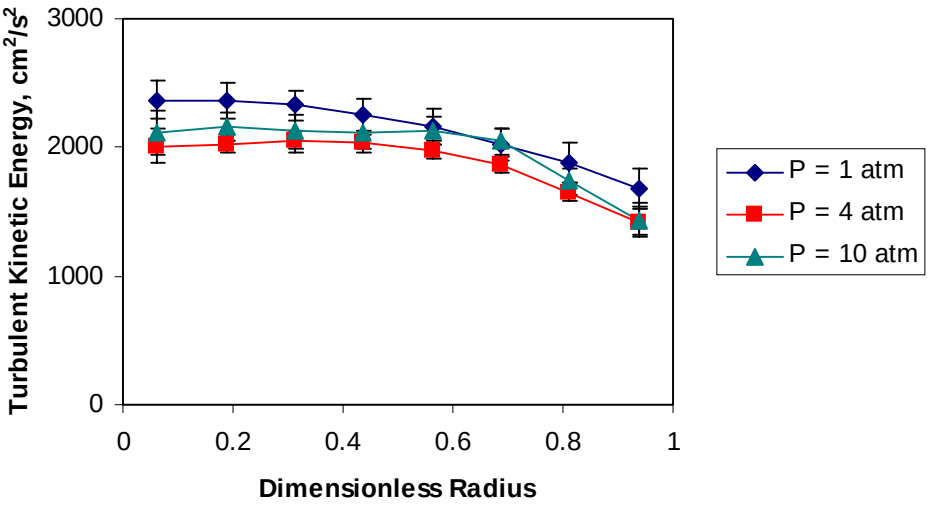

Figure 5-29. Effect of pressure on turbulent kinetic energy profiles for distributor D6 (1.0 POA) at U_g = 30 cm/s.

A few more observations can be made based on Figures 5-27 and 5-28. From Figure 5-27, one can see that the azimuthal velocity is very close to zero across the entire column cross-section implying that in a time-averaged sense, there is no net azimuthal flow. However, the radial velocity seems to become increasingly non-negligibly positive with increase in pressure. Since mass conservation requires that the net radial flow be zero, the positive radial velocities could, therefore be attributed to experimental errors at high pressure due to increasing volume fraction of the gas phase. However, compared to the magnitudes of the axial liquid velocities, the radial velocity component can still be considered to be negligible.

The next observation is regarding τ_{zz} (refer to Figure 5-28a). While there exist a finite effect of pressure on τ_{rr} and $\tau_{\theta\theta}$ as discussed before, a clear trend does not exist for τ_{zz}. It appears that in the column center τ_{zz} is higher at atmospheric pressure than at P = 4 or 10 atm. Close to inversion point, it always exhibits a maximum in its radial profile at which is most pronounced at P = 10 atm, less at P = 4 atm and least at P = 1 atm. Unfortunately, the arguments developed for explanation of the trends in τ_{rr} and $\tau_{\theta\theta}$ do not

yield any plausible explanation for the observed behavior of τ_{zz}. From Figure 5-28d and 5-28f, one can conclude that there is negligible effect of pressure on radial-azimuthal ($\tau_{r\theta}$) and axial-azimuthal ($\tau_{z\theta}$) shear stresses. Furthermore, the radial-axial (τ_{rz}) shear stress is found to be lower at atmospheric pressure as compared to that at high pressures. This in turn along with higher gas holdup leads to stronger liquid recirculation at higher pressures.

The observed lower liquid phase turbulent kinetic energy for higher operating pressure at the same superficial gas velocity (refer to Figure 5-29) may appear counter-intuitive at first since the rate of energy input by the gas phase can be approximated by $\rho_g U_g^2$, implying that with increasing pressure the energy input increases which should eventually result in higher liquid phase turbulence. It should be noted that since the rate of total energy dissipation is given by $\rho_l U_g g$, it is independent of pressure. Thus, an increase in kinetic energy input into the column due to increased pressure (larger ρ_g) should indicate a higher level of liquid turbulence. However, an additional parameter governing the liquid phase turbulence is the bubble size. It was shown by Lin *et al.* (1998) that an increase in gas density causes instability of the large bubble structure, which leads to a reduction in bubble size. Therefore, the controlling phenomena for the observed liquid phase turbulence are probably both the bubble size as well as the incoming gas momentum. Depending on the specific operating condition, the effect of either of the above factors maybe more dominant. If the dominant controlling factor is the bubble size, it implies that the excess kinetic energy input into the column by the gas phase at higher operating pressure is imparted to the liquid phase to drive the mean liquid recirculation. This is clearly seen from Figure 5-27a where for higher operating pressure, one sees an increase in mean liquid recirculation. Since bubble size decreases with pressure while gas holdup increases, the interfacial surface area for momentum transfer to the liquid phase increases, thereby leading to higher liquid recirculation. Additionally, a smaller bubble size implies lower intensity of bubble fluctuations leading to lower levels of liquid turbulence (for example when comparing data for P = 1 and 4 atm in Figure 5-29).

On the other hand, one observes from Figure 5-29 that the turbulent kinetic energy for P = 10 atm is higher than that for P = 4 atm. In addition, from Figure 5-28e, the shear stress in *r-z* direction is the same for P = 4 and 10 atm. One can attempt to explain this observation based on Equation (5-3). As the shear stress in *r-z* direction is the same for these two pressures, and the magnitude of the gradient of the axial liquid velocity is higher for P = 10 atm than for P = 4 atm or P = 1atm (refer to Figure 5-27), this implies that the eddy viscosity is the smallest at P = 10 atm. As mentioned earlier, the evaluation of turbulent eddy viscosity consists of two parts: shear-induced and bubble-induced turbulence. Further discussion based on decomposing the turbulence kinetic energy measured with CARPT into bubble-induced and shear-induced components in presented in Section 5.7 based on the model of Ohnuki and Akimoto (2001). For the current discussion, it is sufficient to note that as the pressure increases, smaller bubbles are generated, which decreases the turbulent eddy viscosity computed from bubble-induced turbulence. In addition, the axial liquid velocity gradient is the highest at P = 10 atm and since the shear-induced turbulence are almost similar (refer to Figure 5-28e), the turbulent eddy viscosity should decrease as pressure increases from P = 4 atm to 10 atm. As can be seen from Equation (5-4), eddy viscosity is proportional to the square of the turbulent kinetic energy. Hence, theoretically, the turbulent kinetic energy should be lower at P = 10 atm as compared to P = 4 atm. This is contradictory with what is observed in Figure 5-29. Thus, further investigation of the hydrodynamics at this pressure condition and probably even higher pressure conditions in terms of bubble size and rise velocity measurements would need to be made to fully comprehend the complexity of the phenomenon depicted by the curves shown in Figure 5-29.

B) D4; U_g = 45 cm/s

Important issue addressed in this study is whether there is a noticeable pressure effect on liquid recirculation velocity and turbulence parameters at very high superficial gas velocity of 45 cm/s. To accomplish this task, the uniform perforated plate distributor D4 was used, as the gas holdup data measured using CT was available for this operating

condition. Since an operating pressure of 10 atm could not be achieved for this distributor, due to the limitation of the air compressor capacity, the experiment was carried out at P = 1 and 4 atm. The results from these measurements are shown in Figures 5-30 to 5-32. Figure 5-30 shows that the gas holdup and consequently the axial liquid recirculation velocity increase with increased pressure and so does the turbulent shear stress, τ_{rz} (Figure 5-31). However, the normal stress components are reduced slightly (Figure 5-31a to 5-31c) resulting in somewhat reduced turbulent kinetic energy (Figure 5-32). As mentioned above and shown in Figure 5-30, gas holdup increases with pressure due to a reduction in bubble size with pressure. Hence, the increase in liquid recirculation velocity and gas holdup with pressure does not contradict the fact that gas holdup drives liquid recirculation in bubble columns. The increase in τ_{rz} with pressure is directly explained in the framework of one-dimensional liquid recirculation model (refer to Equation (5-6) for a simplified expression for turbulent shear stress developed by Kumar (1994)) which indicates an increase in τ_{rz} with an increase in gas holdup. Therefore an increase in gas holdup with pressure leads to an increase in the turbulent shear stress with pressure. Additionally, from Figure 5-30, one can observe that the radial gradient of axial liquid velocity increases with pressure. Referring to Equation (5-3), it can be implied that unless the turbulent eddy viscosity decreases significantly with pressure, an increase in pressure translates into an increase in the turbulent shear stress, τ_{rz} as shown in Figure 5-31e.

To discuss further the decrease in turbulent kinetic energy with pressure (refer to Figure 5-32), one observes from Figure 5-31d to 5-31f that other than τ_{zz}, which is almost constant for both pressures, τ_{rr} and $\tau_{\theta\theta}$ decrease with increasing pressure, hence, leading to a decrease in turbulent kinetic energy. This effect of pressure on turbulence structure was also observed at a superficial gas velocity of 30 cm/s (refer to Figures 5-28 and 5-29). Therefore, the underlying physical phenomena governing the structure of liquid recirculation and turbulence at these two high superficial gas velocities (30 and 45 cm/s) can be hypothesized to be similar. Consequently, as for U_g = 30 cm/s, a reduction in bubble size with pressure would be primary factor leading to lower levels of normal turbulent stresses at U_g = 45 cm/s also.

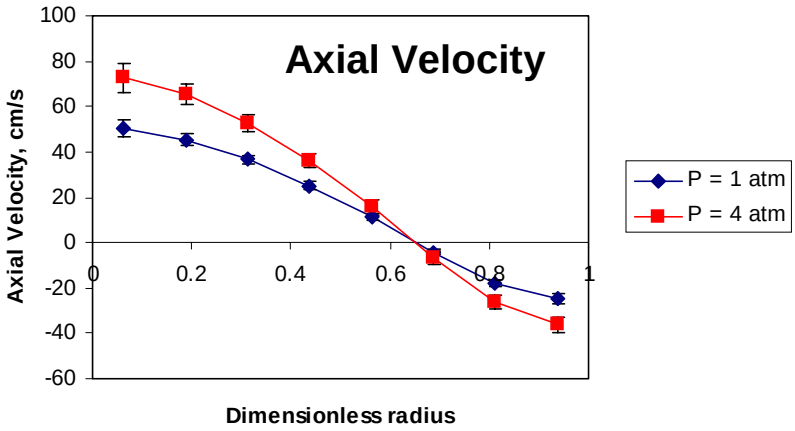

(a) Axial liquid velocity

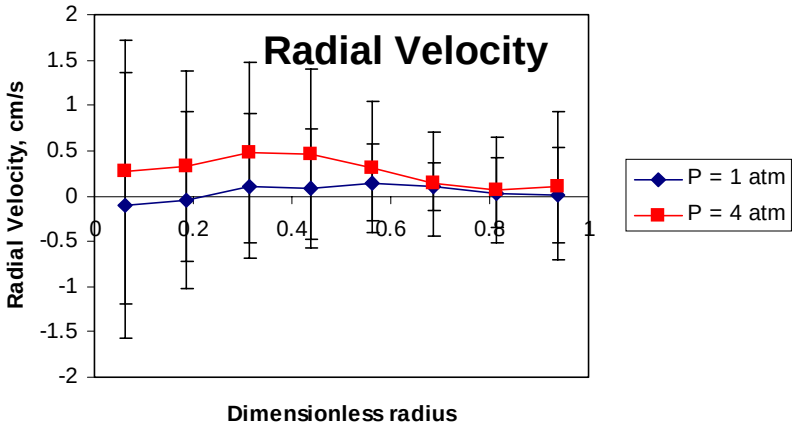

(b) Radial liquid velocity

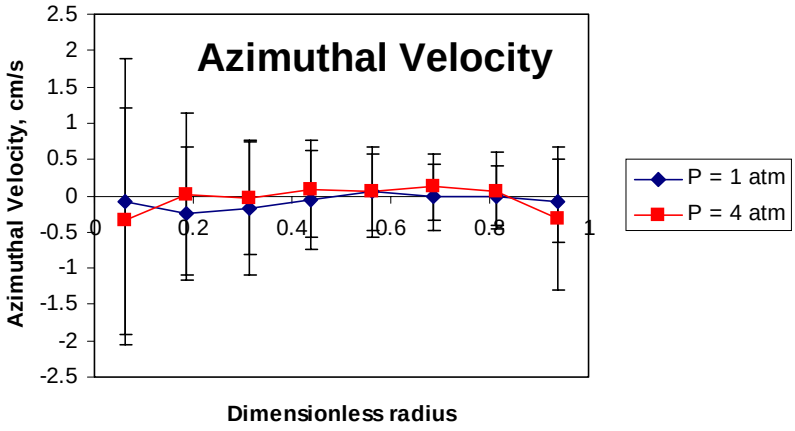

(c) Azimuthal liquid velocity

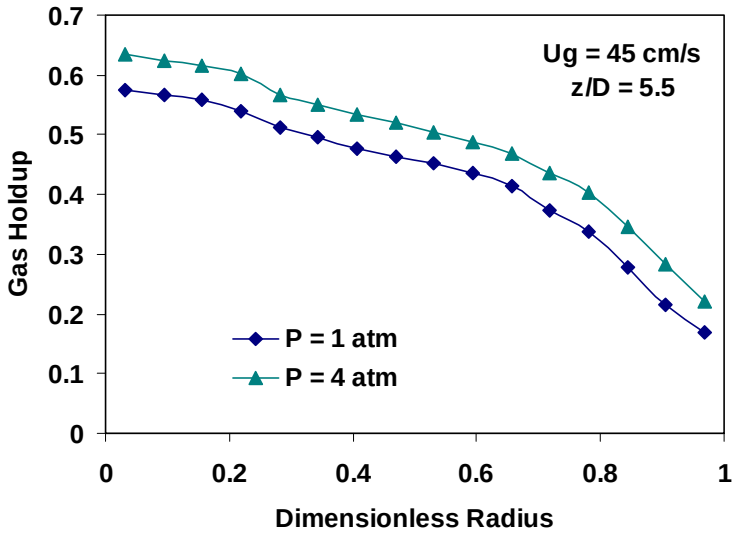

Figure 5-30. Effect of pressure on velocity and gas holdup profiles for distributor D4 (0.15 POA) at U_g = 45 cm/s.

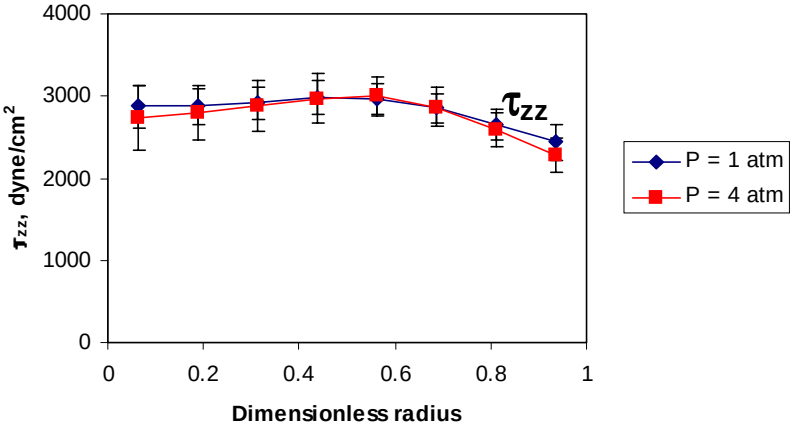

(a)

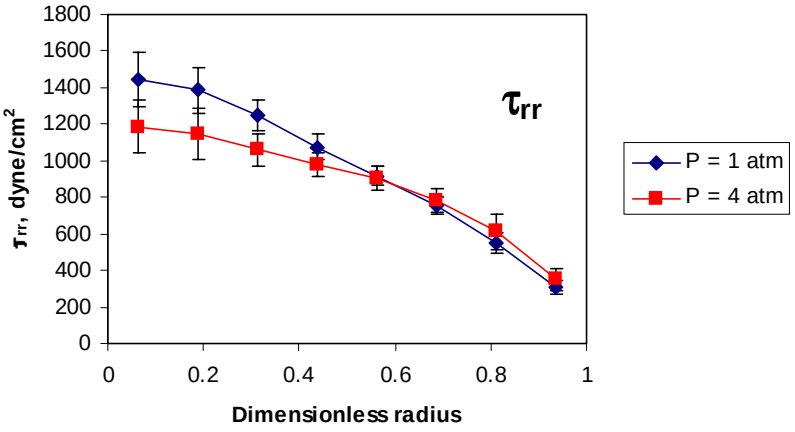

(b)

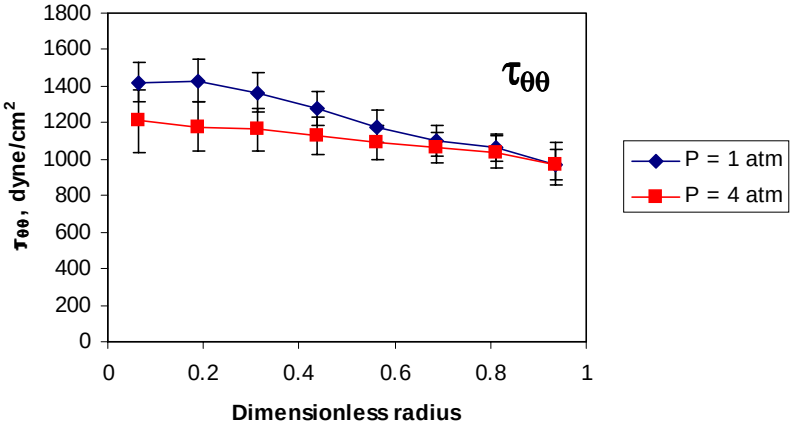
τθθ
τθθ, dyne/cm2
Dimensionless radius
P = 1 atm
P = 4 atm

(c)

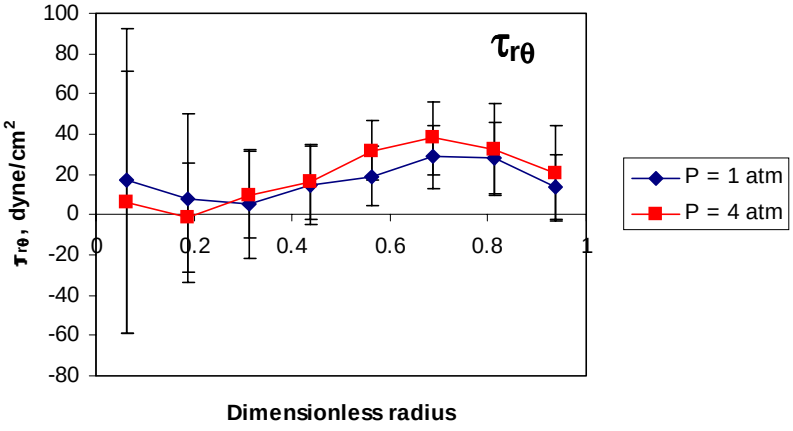
τrθ
τrθ, dyne/cm2
Dimensionless radius
P = 1 atm
P = 4 atm

(d)

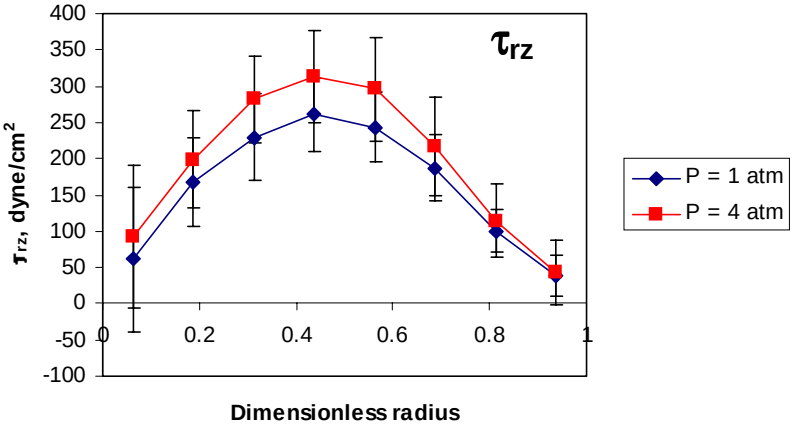
τrz
τrz, dyne/cm2
Dimensionless radius
P = 1 atm
P = 4 atm

(e)

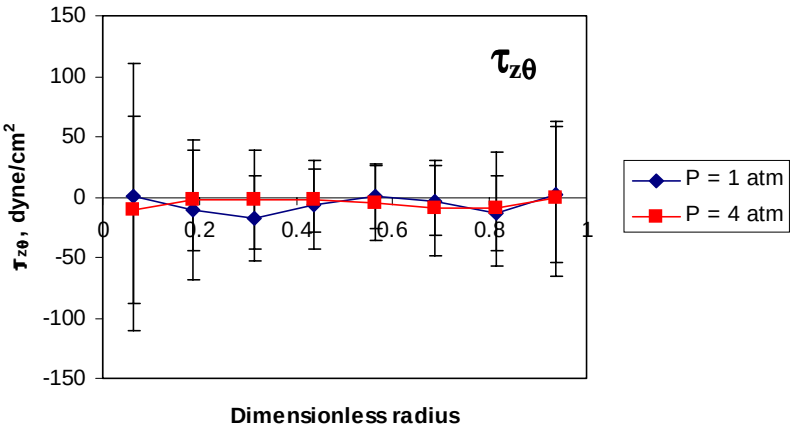

(f)

Figure 5-31. Effect of pressure on turbulent stresses for distributor D4 (0.15 POA) at U_g = 45 cm/s.

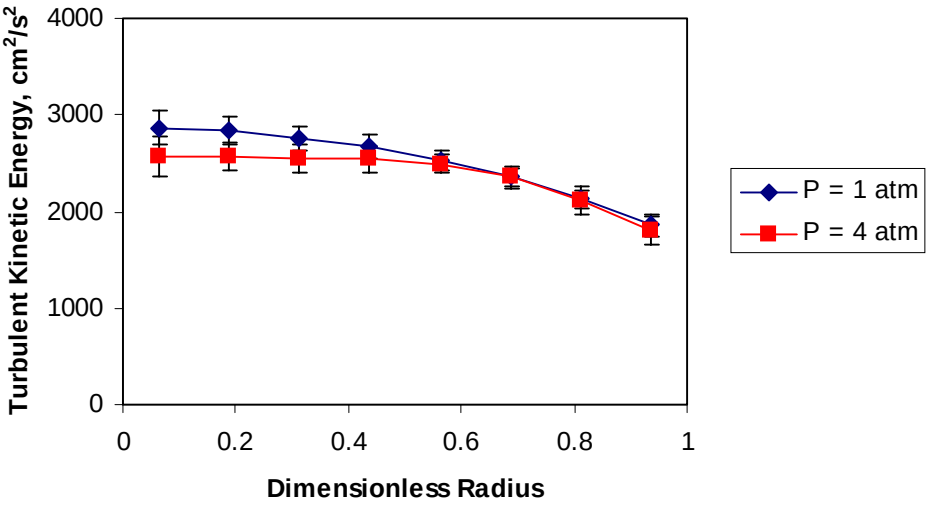

Figure 5-32. Effect of pressure on turbulent kinetic energy profiles for distributor D4 (0.15 POA) at U_g = 45 cm/s.

5.6.3. Effect of Superficial Gas Velocity on Liquid Recirculation and Turbulence Parameters

In this section, the effect of superficial gas velocity on the liquid phase velocity and turbulence parameters is discussed. For the purpose of this investigation, the uniform

perforated plate distributor D4 (0.15%, d_o = 0.5 mm) was used and CARPT experiments were performed using air as the gas phase and water as batch liquid. Very high superficial gas velocities of 30 cm/s and 45 cm/s at two operating pressures of P = 1 and 4 atm were employed (refer to Table 3-3 for details of the operating conditions). As mentioned earlier, the experimental data were then processed using the Monte Carlo algorithm (Gupta, 2002) to obtain the instantaneous position data. Since liquid recirculation and turbulence is intricately linked to the gas holdup distribution, the results from the gas holdup measurements using CT are reported first. Figure 5-33 shows the effect of superficial gas velocity on gas holdup at P = 1 and 4 atm using the uniform perforated plate distributor D4. It can be seen from the figure that gas holdup increases both with superficial gas velocity as well as with pressure. The holdup at P = 1 atm and U_g = 45 cm/s is somewhat higher than the holdup at P = 4 atm and U_g = 30 cm/s but considerably lower than holdup at P = 4 atm and U_g = 45 cm/s.

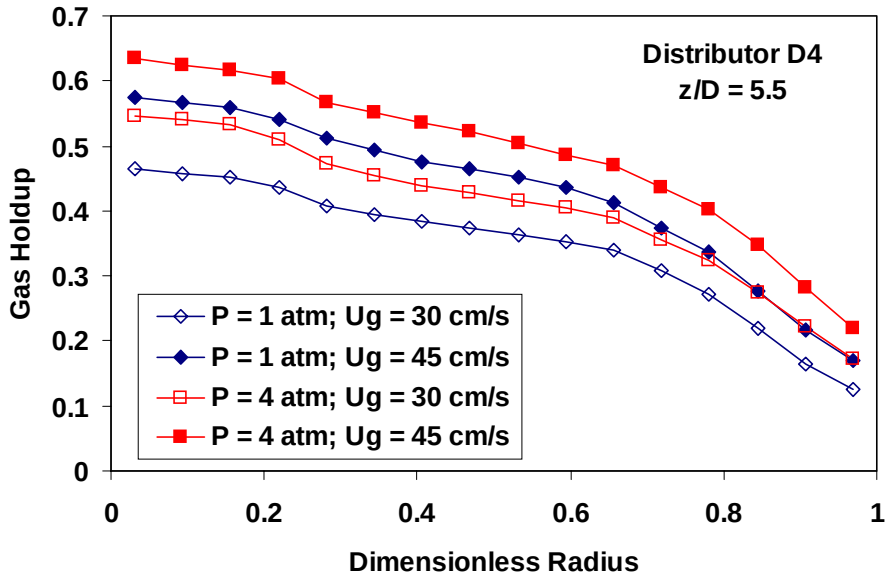

Figure 5-33. Effect of superficial gas velocity on gas holdup at P = 1 and 4 atm.

Upon examination of the results from the CARPT measurements, it was found that the trends in the variation of hydrodynamic quantities with superficial gas velocity were similar at the two operating pressures. Hence, only the results from atmospheric pressure conditions are presented here to elucidate the effect of superficial gas velocity.

Figures 5-34 to 5-36 display the time-averaged velocity profiles, turbulent stresses and kinetic energy obtained at superficial gas velocities of 30 cm/s and 45 cm/s at P = 1 atm, respectively. These profiles were obtained via averaging over z = 54 to 136.8 cm and the bars on each profile represent the range of values encountered. The liquid velocity profile obtained at a superficial gas velocity of 45 cm/s is higher than that at a U_g = 30 cm/s (Figure 5-34). Also, its centerline velocity is about 21% higher than that at U_g = 30 cm/s. This is to be expected since at U_g = 45 cm/s, the measured gas holdup is higher than at a U_g of 30 cm/s, as shown in Figure 5-33. The same conclusions are reached for the turbulent stresses and turbulent kinetic energy (Figures 5-35 and 5-36), indicating greater turbulence in liquid phase at higher gas velocity. The centerline turbulent kinetic energy for U_g = 45 cm/s is about 10% higher than that at a U_g = 30 cm/s. The higher liquid phase turbulence could also be attributed to the regime of bubble formation as can be seen from Table 4-2 where at a U_g of 45 cm/s, the flow is in the jetting regime, whereas at U_g = 30 cm/s, it is in the bubbling regime. Hence, with superficial gas velocity, the intensity of liquid turbulence increases, as shown in Figures 5-35 and 5-36.

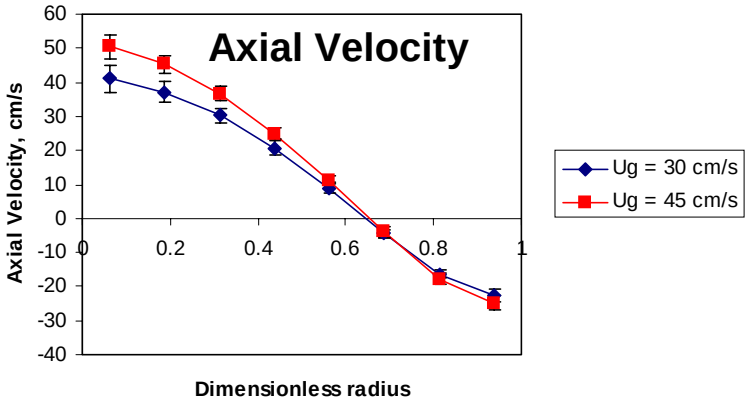

(a) Axial liquid velocity

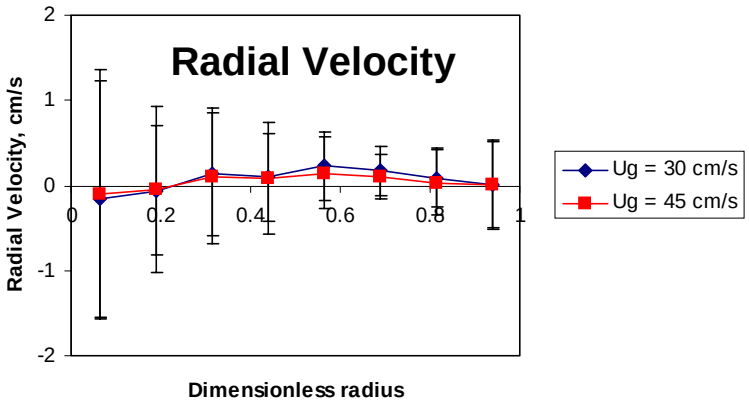

(b) Radial liquid velocity

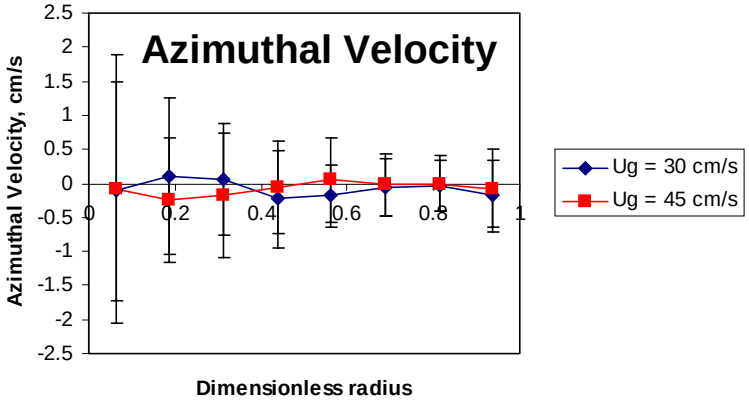

(c) Azimuthal liquid velocity

Figure 5-34. Effect of superficial gas velocity on velocity profiles at atmospheric pressure using distributor D4.

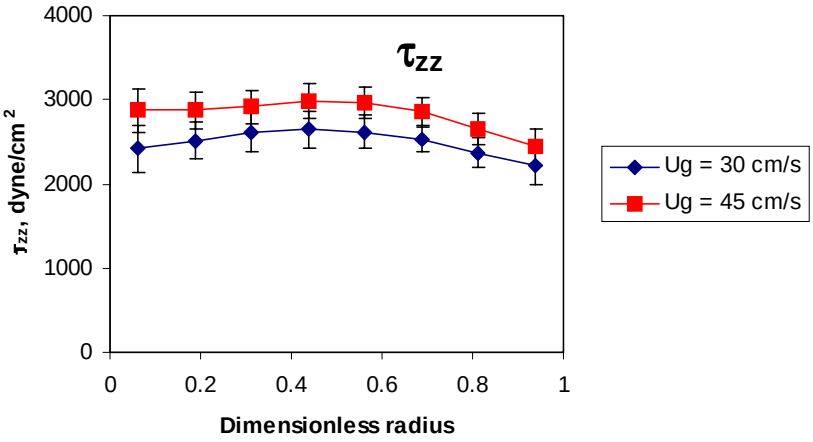

(a)

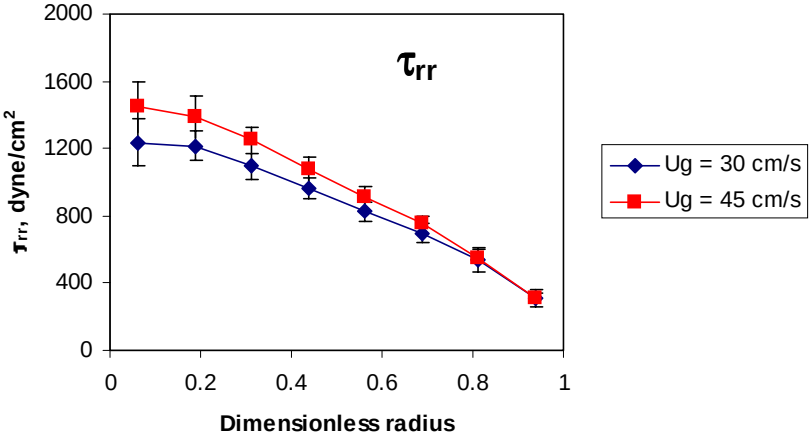
τrr
τrr, dyne/cm2
2000
1600
1200
800
400
0
0
0.2
0.4
0.6
0.8
1
Dimensionless radius
Ug = 30 cm/s
Ug = 45 cm/s

(b)

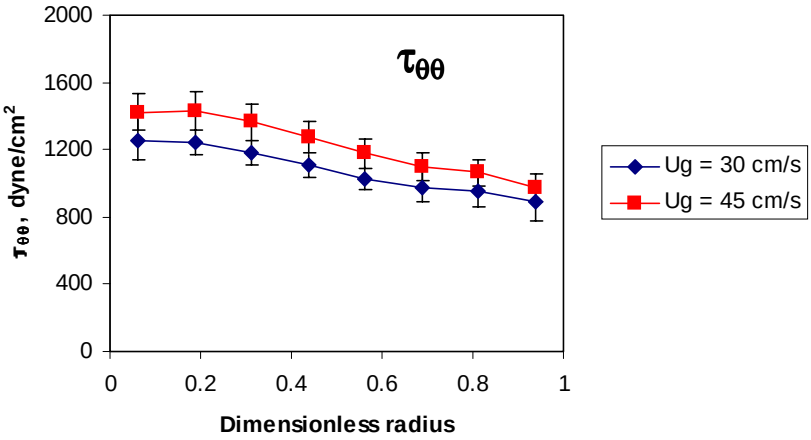
τθθ
τθθ, dyne/cm2
2000
1600
1200
800
400
0
0
0.2
0.4
0.6
0.8
1
Dimensionless radius
Ug = 30 cm/s
Ug = 45 cm/s

(c)

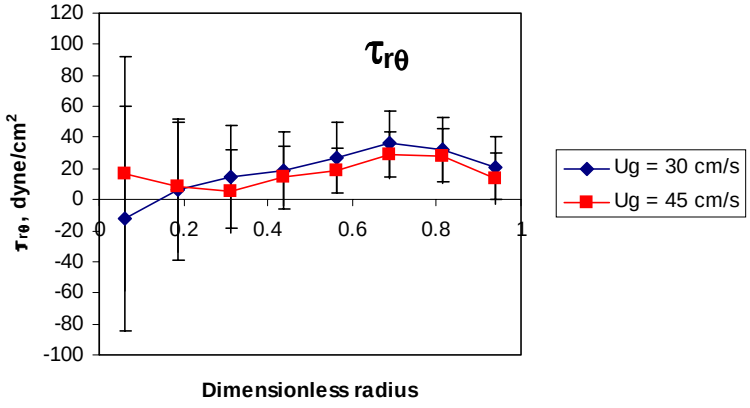
τrθ
τrθ, dyne/cm2
120
100
80
60
40
20
0
-20
-40
-60
-80
-100
0
0.2
0.4
0.6
0.8
1
Dimensionless radius
Ug = 30 cm/s
Ug = 45 cm/s

(d)

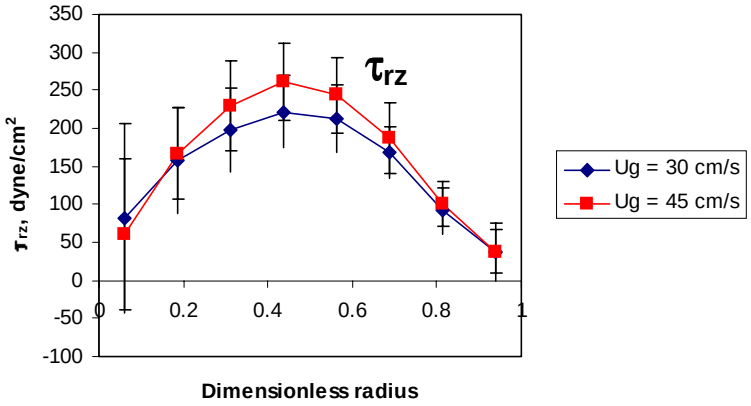

(e)

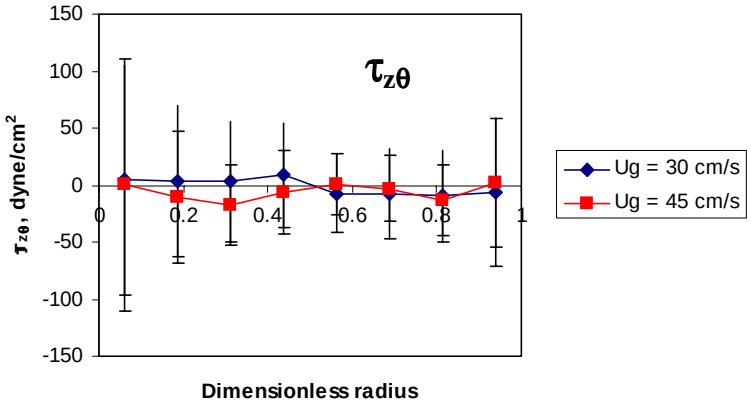

(f)

Figure 5-35. Effect of superficial gas velocity on turbulent stresses using distributor D4.

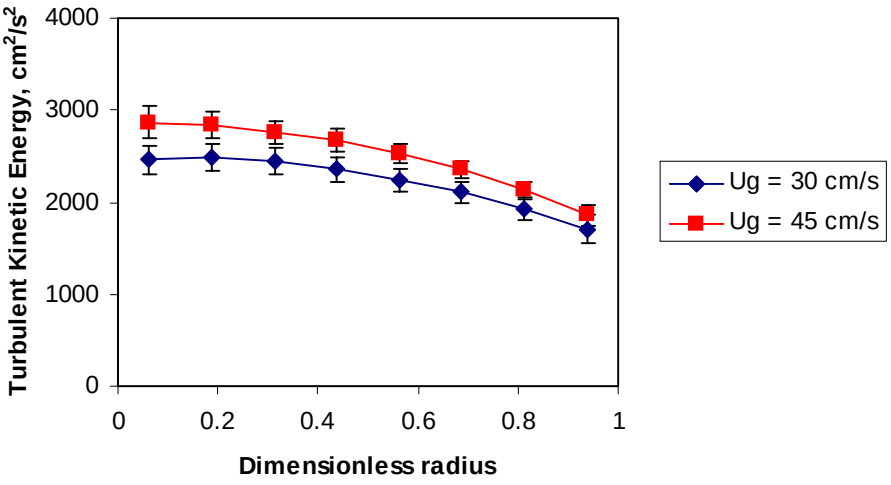

Figure 5-36. Effect of superficial gas velocity on turbulent kinetic energy profiles using distributor D4.

It is interesting to note from Figures 5-35 and 5-36 that the turbulent normal stresses and the shear stress, τ_{rz} all increase with superficial gas velocity. The trend of increasing τ_{rz} with superficial gas velocity is the same as observed with increasing operating pressure. Since both pressure and superficial gas velocity lead to an increase in gas holdup, it can therefore be concluded that the magnitude of τ_{rz} is primarily dependent on the magnitude of the gas holdup and its distribution. As mentioned earlier, confirmation of this explanation also falls out directly from the one-dimensional model presented in Appendix A. However, the trends in the variation of the turbulent normal stresses with superficial gas velocity are opposite to those that are observed with increasing operating pressures (refer to Figures 5-31 and 5-35). While an increase in pressure leads to stabilization of the flow via smaller bubble sizes and consequently, lowering of the normal turbulent stresses, an increase in superficial gas velocity leads to an increase in turbulent normal stresses. In terms of the momentum ($\propto \rho_g U_g^2$) and energy ($\propto \rho_g U_g^3$) inputs into the column, at a constant U_g, an increase in pressure implies proportionately equivalent increase in both the momentum and energy inputs into the column. On the other hand, at a constant pressure, an increase in superficial gas velocity implies a proportionately larger increase in energy input to the column as compared to the momentum input. It is probably this difference in the mode of momentum and energy input that causes the opposite trends in the variation of the turbulent normal stresses with pressure and superficial gas velocity.

Lastly, it is also worthwhile to compare the liquid phase hydrodynamic trends observed with variation of superficial gas velocity in the study with those obtained by Degaleesan (1997). Since her study is limited to atmospheric pressure and a superficial gas velocity of up to 12 cm/s, it is relevant to only compare the results of the measurements performed at atmospheric pressure in this study. As with the results shown in Figures 5-34 to 5-36, Degaleesan's findings (1997) also indicate that increasing the superficial gas velocity increases liquid velocity as well as the ensuing turbulence.

5.6.4. Cross-Sectional Averaged Turbulent Stresses

Based on the turbulent stresses profiles obtained from CARPT, the cross-sectional averaged turbulent stresses for all operating conditions are evaluated (refer to Equation 5-7)) and shown in Table 5-2. It can be concluded that the normal stress in the *z*-direction is at least two times higher than the remaining cross-sectional averaged quantities. This is in agreement with the findings of Degaleesan (1997).

$$\overline{\tau_{ij}} = 2\int_0^1 \xi\, \tau_{ij}(\xi)\, d\xi \qquad i, j = r, \theta, z \tag{5-7}$$

As shown in Table 5-2, at a fixed pressure, as superficial gas velocity increases, the cross-sectional averaged turbulent stresses increase. This is due to the increasing level of liquid turbulence with increasing superficial gas velocities. Another observation from Table 5-2 is that at a fixed superficial gas velocity, as pressure increases, all cross-sectional averaged quantities decrease with pressure except the shear stress in the *r*-*z* direction, τ_{rz}. This can also be seen from Figures 5-28 and 5-31. Explanation of these effects of pressure and superficial gas velocity on turbulent quantities was discussed in the previous sub-sections (5.6.1 to 5.6.3).

Table 5-2. Cross-sectionally averaged turbulent stresses for all operating conditions.

U_g (cm/s)	P (atm)	Sparger	$\overline{\tau_{zz}}$ (dyne/cm^2)	$\overline{\tau_{rr}}$ (dyne/cm^2)	$\overline{\tau_{\theta\theta}}$ (dyne/cm^2)	$\overline{\tau_{rz}}$ (dyne/cm^2)
30	1	D2	2534	787	1141	126
30	1	D4	2450	679	1004	133
30	1	D6	2400	633	969	131
45	1	D4	2744	739	1132	149
45	4	D4	2690	723	1061	177
30	4	D3	2323	679	1005	151
30	4	D4	2136	606	975	146
30	4	D6	2188	516	838	155
30	10	D6	2398	514	814	153

5.7. Turbulent Eddy Viscosity

The above sections describe the results obtained using CARPT and provide the possible explanations for the observed phenomenon at high pressure and at high superficial gas velocity for different distributors. In this section, first an approach for obtaining the turbulent eddy viscosity is discussed. Then, a discussion on the decomposition of the turbulent eddy viscosity based on Ohnuki and Akimoto (2001) will be provided.

5.7.1. Evaluation of Turbulent Eddy Viscosity

First, the methodology for obtaining the turbulent eddy viscosity is described. Assuming negligible molecular viscosity and for dimensionless radius less than the radial position of maximum downflow, λ, Equation (5-3a) becomes

$$\tau_{l,rz} = -\frac{\rho_l \, \nu_{eff}}{R} \frac{du_l}{d\xi} \tag{5-8}$$

The shear stress in *r*-*z* direction, τ_{rz}, and the radial gradient of the time-average axial liquid velocity are obtained from CARPT measurements and the turbulent eddy viscosity profile, ν_t, is assumed to have the form of Equation (5-9).

$$\nu_t(\xi) = \nu_{t0} \, (1.0 - k\xi^{\alpha}) \tag{5-9}$$

where ν_{t0}, k and α are the fitted parameters. The form of equation is chosen based the following explanation. Since liquid recirculation is strongly dependent on the gradient of the radial gas holdup and closure for liquid turbulence, it was conjectured that a form for ν_t similar to radial gas holdup profile would offer the best possibility of fitting the CARPT data. It should, however, be mentioned that other forms for ν_t like a constant eddy viscosity ($k = \alpha = 0$) or a linearly varying form ($k = \alpha = 1$) were also tried but did not fit the experimental data well at all operating conditions. Therefore, the form

presented in Equation (5-9) was used and found to fit the experimental data very well. For each operating condition, the fitted parameters are optimized to fit the relationship shown in Equation (5-8) and then, the line-averaged and cross-sectional averaged turbulent eddy viscosities are evaluated using Equation (5-10), respectively.

$$\overline{\nu_{t,CSA}} = \int_0^1 \xi \nu_t \, d\xi = \nu_{t0}\left(1 - \frac{2k}{\alpha + 2}\right) \tag{5-10}$$

Figure 5-37 displays the fitted and experimentally measured radial profile of the shear stress in *r*-*z* direction for uniform perforated plate, D4, at a superficial gas velocity of 30 cm/s and at atmospheric pressure. The fitted shear stress, τ_{rz}, is obtained by the fitting the turbulent eddy viscosity profile (Equation (5-9) in Equation (5-8) to the CARPT τ_{rz} data. As evident from Figure 5-37, the fit of the shear stress profiles is excellent. Similar procedure is carried out for the remaining operating conditions and similar plots are shown in Appendix B. The fitted parameters, ν_{t0}, k and α as well as the average turbulent eddy viscosity for each operating condition are listed in Table 5-3. The cross-sectional average turbulent eddy viscosity is used further to explain the effect of distributors, pressure and velocity on liquid velocity and turbulence where the physical explanation is provided earlier in Section 5.6.

A. Distributor effects at P = 1 atm; U_g = 30 cm/s

At atmospheric pressure, from Table 5-3, the average turbulent eddy viscosity for uniform perforated plate, D4 is the highest, followed by uniform perforated plate D6 and cross sparger D2. Earlier in Section 5.6.1A, it was mentioned that there is minimal effect of spargers on liquid recirculation and turbulent shear stress. However, if one looks carefully at the shear stress profile, τ_{rz} (Figure 5-21e), one notices that towards the center of the column, the uniform perforated plate D4 has the highest shear stress, followed by uniform perforated plate D6 and cross sparger D2. Since the gradient of the axial velocity profile is almost identical (refer to Figure 5-20) therefore, based on Equation (5-3), D4 must have the highest turbulent eddy viscosity.

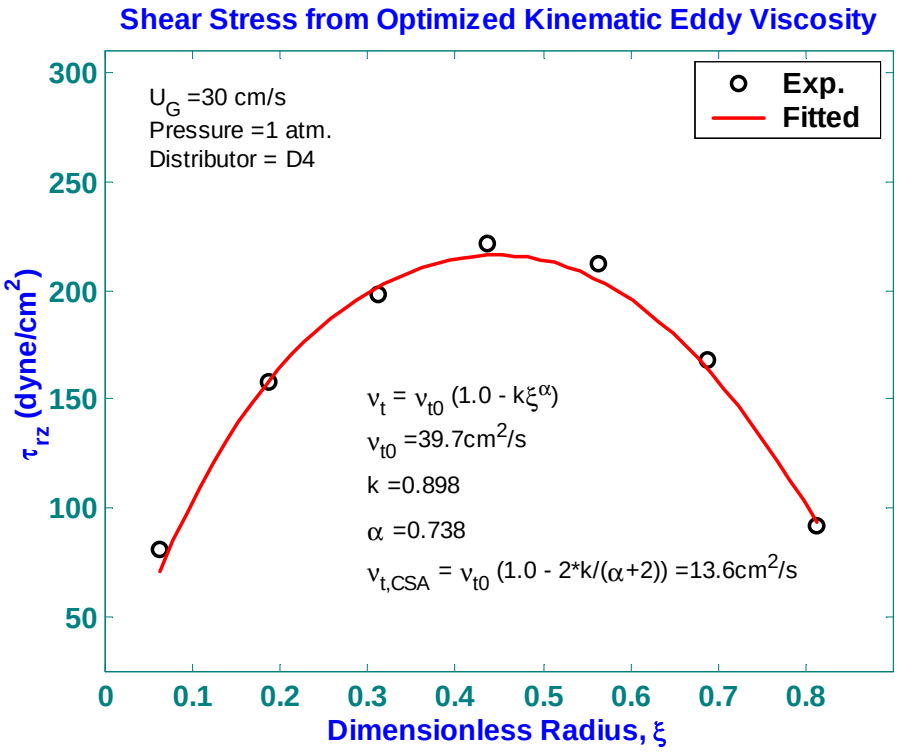

Figure 5-37. Comparison of experimental and optimized shear stress profile for uniform perforated plate distributor, D4 (0.15%, d_o = 0.5 mm) at a superficial gas velocity of 30 cm/s at atmospheric pressure.

Table 5-3. Optimized parameters of the eddy viscosity profile (Equation 5-9)) and cross-sectional $\left(\overline{\nu_{t,CSA}}\right)$ averaged eddy viscosity (Equation (5-10)).

Sparger	U_g (cm/s)	P (atm)	ν_{t0}, cm^2/s	k	α	$\overline{\nu_{t,CSA}}$, cm^2/s
D2	30	1	29.6	0.975	1.400	12.6
D3	30	4	27.6	0.915	0.812	9.61
D4	30	1	39.7	0.898	0.738	13.6
	45	1	24.3	1.000	2.000	12.1
	30	4	43.2	0.969	0.544	10.3
	45	4	21.6	0.961	1.650	10.2
D6	30	1	28.0	0.986	1.760	13.3
	30	4	23.1	1.000	1.220	8.75
	30	10	440.1	0.997	0.0303	7.95

B. Distributor effects at P = 4 atm; U_g = 30 cm/s

At a higher pressure of 4 atm, one could see that the average turbulent eddy viscosity is the lowest for the uniform perforated plate, D6 and the highest for uniform perforated plate, D4. In addition, from Figure 5-26, D6 has the highest absolute axial liquid velocity gradient. Based on Equation (5-3), if the turbulent eddy viscosity decreases, and the axial liquid velocity gradient increases, the shear stress in *r*-*z* plane should be more or less equal. This is evident from Figure 5-24e, where the shear stresses in *r*-*z* plane for D4 and D6 are almost similar.

C. Pressure effects at U_g = 45 cm/s using uniform perforated plate distributor, D4

At a superficial gas velocity of 45 cm/s, as pressure increases, the average turbulent eddy viscosity decreases (refer to Table 5-3), but not as much as the increase in axial liquid velocity gradient. Thus, the net effect is an increase in shear stress in *r*-*z* plane, τ_{rz} (refer to Figure 5-31e).

The above analysis of evaluating the overall turbulent eddy viscosity from the CARPT measurements contains the contributions both from shear-induced as well as bubble-induced turbulence. Recently, Ohnuki and Akimoto (2001) presented a model for decomposing the relative contributions of shear and bubble interactions towards the overall turbulent kinetic energy. This model is described in the following section along with an analysis of the CARPT eddy viscosity data.

5.7.2. Decomposition of Eddy Viscosity

As presented in Section 5.6, the total kinematic eddy viscosity can be broken into contributions from bubble-induced and shear-induced turbulence (refer to Equation (5-4)). This framework can be used to explain the eddy viscosity computed from CARPT measurements. To accomplish this, the total turbulent kinetic energy is first decomposed into contributions due to shear-induced and bubble-induced components using the approach of Ohnuki and Akimoto (2001) (refer to Equation (5-11)).

$$k_{tot} = k_{SIT} + k_{BIT} \tag{5-11}$$

where $k_{BIT} = \varepsilon_g \left| u_{slip} \right|^2$. As mentioned previously, the total turbulent kinetic energy is obtained from CARPT measurements. Hence, the turbulent kinetic energy due to shear-induced can be estimated from Equation (5-11) when k_{tot} is measured and k_{BIT} is estimated. The slip velocity, u_{slip}, is evaluated using the Richardson-Zaki correlation shown in Equation (5-12) with n = 2.39.

$$u_{slip} = U_{b\infty} (1 - \varepsilon_g)^{n-1} \tag{5-12}$$

where $U_{b\infty}$ is obtained using the correlation developed by Fan and Tsuchiya (1990) (refer to Table 2-7). To calculate $U_{b\infty}$, an estimate of the bubble size is needed. Since there is a wide discrepancy in the bubble size predictions computed from various correlations, two different correlations were tested to assess how much difference does this make. Thus, the bubble size is evaluated using the correlations of Lee and Meyrick (1970) and Wilkinson (1991) (refer to Table 2-6a).

In summary, with the knowledge of slip velocity and gas holdup, one can readily evaluate the turbulent kinetic energy due to bubble-induced turbulence. Subtracting k_{BIT} from the total turbulent kinetic energy as measured from CARPT, the turbulent kinetic energy due to shear-induced turbulence (k_{SIT}) is obtained. Subsequently, Equation (5-4c) is used to calculate the turbulent eddy viscosity due to shear-induced turbulence. Additionally, knowing the bubble size and slip velocity, the eddy viscosity due to bubble-induced turbulence can be estimated from Equation (5-4b). Tables 5-4a and 5-4b display the values evaluated from the above analysis. From these table, the following conclusions.

1. The kinematic eddy viscosity contribution from bubble-induced turbulence is strongly dependent on bubble size, rise (slip) velocity and gas holdup. Comparison of values between Tables 5-4a and 5-4b reveals an order of magnitude difference in the eddy viscosity due to bubble-induced turbulence (ν_{BIT}) when using two different correlations mentioned above to compute bubble

size. Clearly when the estimated bubble size differs by an order of magnitude so does bubble-induced eddy viscosity. Hence, knowledge of bubble size is essential for this estimation.

2. The total turbulent kinetic energy is predominantly due to shear-induced turbulence since the magnitude of the turbulent kinetic energy due to bubble-induced turbulence is at least an order of magnitude smaller than the turbulent kinetic energy due to shear-induced turbulence (as shown in Table 5-4, $k_{SIT} >> k_{BIT}$). Therefore, there is only a small effect of the choice of bubble size on the estimate of the kinematic eddy viscosity due to shear-induced turbulence.
3. Comparison of the effective kinematic eddy viscosity estimated from the model of Ohnuki and Akimoto (2001) with experimentally measured values from the CARPT measurements indicate that the estimations based on the bubble size correlation of Wilkinson (1991) yields a much superior agreement with data. This implies that bubble size estimation based on Wilkinson (1991) are closer to the prevalent bubble sizes at various operating conditions used in this study.
4. Additionally, it can be seen from Table 5-4b that using Wilkinson approach for bubble size estimation, the relative contribution of bubble-induced turbulence to the total kinematic eddy viscosity is less than 10%. Therefore, though the bubble-induced turbulence may be important, its contribution is relatively small as compared to the generation of turbulence from the shearing action of the fluid. This observation is in line with the findings of Deen *et al.* (2001) who found that when all the momentum exchange terms are accounted for (drag, virtual mass and lift), large eddy simulation of bubble column hydrodynamics is insensitive to whether or not one explicitly accounts for bubble-induced turbulence.

Table 5-4a. Eddy viscosity analysis using the bubble size correlation developed by Lee and Meyrick (1970).

Error Analysis based on $\overline{\nu_{t,CSA}}$: $\%\,diff = \frac{\nu_{tot} - \overline{\nu_{t,CSA}}}{\overline{\nu_{t,CSA}}} \times 100\%$; Error Analysis based on $\overline{\nu_{t,LA}}$: $\%\,diff = \frac{\nu_{tot} - \overline{\nu_{t,LA}}}{\overline{\nu_{t,LA}}} \times 100\%$

Distributor	P, atm	U_g, cm/s	ε_g	d_b, cm	$U_{b\infty}$, cm/s	Average turbulent kinetic energy, cm^2/s^2 and specific energy dissipation rate, cm^2/s^3				Computed Viscosity, cm^2/s			Error Analysis based on	
						k_{tot} (from CARPT)	k_{BIT}	k_{SIT}	ε	ν_{BIT}	ν_{SIT}	ν_{eff}	$\overline{\nu_{t,CSA}}$	$\overline{\nu_{t,LA}}$
D2 (cross sparger, 0.1%)	1	30	0.263	2.94	38.4	2289	166	2123	29430	11.7	13.8	25.5	102.1	45.5
D3 (single nozzle, 0.1%)	4	30	0.413	3.66	42.6	2063	171	1892	29430	18.4	11.0	29.4	205.8	116.1
D4 (perforated plate, 0.15%)	1	30	0.282	3.04	39.1	2122	171	1950	29430	12.7	11.6	24.3	78.8	26.7
	1	45	0.351	2.89	38.1	2377	153	2224	44145	12.7	10.1	22.8	88.6	40.9
	4	30	0.333	3.30	40.5	1918	177	1741	29430	15.2	9.3	24.5	137.7	52.1
	4	45	0.407	3.11	39.4	2307	148	2159	44145	14.5	9.5	24.0	134.9	73.6
D6 (perforated plate, 1.0%)	1	30	0.275	3.01	38.8	2050	170	1880	29430	12.3	10.8	23.1	74.0	28.6
	4	30	0.328	3.28	40.4	1827	177	1650	29430	15.0	8.3	23.3	166.4	83.6
	10	30	0.415	3.67	42.5	1932	169	1763	29430	18.5	9.5	28.0	251.7	95.5

Table 5-4b. Eddy Viscosity analysis using the bubble size correlation developed by Wilkinson (1991).

Error Analysis based on $\overline{\nu_{t,CSA}}$: $\%\,diff = \frac{\nu_{tot} - \overline{\nu_{t,CSA}}}{\overline{\nu_{t,CSA}}} \times 100\%$; Error Analysis based on $\overline{\nu_{t,LA}}$: $\%\,diff = \frac{\nu_{tot} - \overline{\nu_{t,LA}}}{\overline{\nu_{t,LA}}} \times 100\%$

Distributor	P, atm	U_g, cm/s	ε_g	d_b, cm	$U_{b\infty}$, cm/s	Average turbulent kinetic energy, cm^2/s^2 and specific energy dissipation rate, cm^2/s^3				Computed Viscosity, cm^2/s			Error Analysis based on	
						k_{tot} (from CARPT)	k_{BIT}	k_{SIT}	ε	ν_{BIT}	ν_{SIT}	ν_{eff}	$\overline{\nu_{t,CSA}}$	$\overline{\nu_{t,LA}}$
D2 (cross sparger, 0.1%)	1	30	0.263	0.44	22.2	2289	55.5	2234	29430	1.01	15.3	16.3	29.1	-7.0
D3 (single nozzle, 0.1%)	4	30	0.413	0.38	22.1	2063	46.0	2017	29430	0.99	12.44	13.4	39.7	-1.3
D4 (perforated plate, 0.15%)	1	30	0.282	0.44	22.2	2122	55.4	2067	29430	1.04	13.1	14.1	3.7	-26.5
	1	45	0.351	0.44	22.2	2377	52.0	2325	44145	1.12	11.0	12.1	0.3	-25.0
	4	30	0.333	0.38	22.1	1918	52.9	1865	29430	0.95	10.6	12.0	12.6	-28.0
	4	45	0.407	0.37	22.1	2307	46.6	2260	44145	0.98	10.4	11.4	11.7	-17.4
D6 (perforated plate, 1.0%)	1	30	0.275	0.44	22.2	2050	55.5	1994	29430	1.03	12.2	13.2	-0.8	-26.7
	4	30	0.328	0.38	22.1	1827	53.1	1774	29430	0.95	9.62	10.6	20.8	-16.8
	10	30	0.415	0.34	22.0	1932	45.4	1886	29430	0.89	10.9	11.8	48.1	-17.7

5.8. Centerline Velocity Correlation

As mentioned earlier in Chapter 2, there are two correlations, developed by Riquarts (1981) and Zehner (1986), that predict the centerline liquid velocity (refer to Equations (2-29) and (2-30) which are being reported here again for completeness).

Riquarts (1981):

$$u_{o,Riquarts} = 0.21(gD_c)^{1/2}\left(\frac{U_g^3\rho_l}{g\mu_l}\right)^{1/8} \tag{2-29}$$

Zehner (1986):

$$u_{o,Zehner} = 0.737\, g^{1/3} D_c^{1/3} U_g^{1/3} \tag{2-30}$$

It should be noted that the correlation for centerline velocity obtained by Riquarts (1981) has its basis in the recirculation model of Ueyama and Miyauchi (1979). Riquarts (1981) neglected the effect of wall friction on the axial pressure gradient and simplified the model of Ueyama and Miyauchi (1979) to obtain a closed form expression for the centerline velocity which contains the average gas holdup as well as the turbulent eddy viscosity. Using a theoretical derived relationship for eddy viscosity and an empirical correlation for average gas holdup, Riquarts (1981) obtained the expression shown in Equation (2-29) for the centerline velocity. On the other hand, the physical basis for the expression in Equation (2-30) from Zehner (1986) lies in the cell model with cell dimensions being that of the column diameter. Zehner (1986) derived a pressure gradient based on the difference in the gas holdup in the upflow and downflow sections of the cells and equated it to an equivalent liquid phase velocity head, finally leading to Equation (2-30).

The usefulness of the centerline velocity becomes evident when one considers the correlation developed by Wu and Al-Dahhan (2001) for the radial profile of axial liquid velocity (refer to Equation (2-31) in Chapter 2). To obtain the radial profile of liquid recirculation velocity, Wu and Al-Dahhan (2001) recommend the use of their correlation in conjunction with a literature correlation for centerline liquid velocity like that of Riquarts (1981) and Zehner (1986).

In Table 5-5, the correlations developed by Riquarts (1981) and Zehner (1986) are used to predict the axial liquid velocity at the center of the column and to compare

them to CARPT determined data. The predicted centerline liquid velocity at atmospheric pressure computed using Zehner's (1986) approach are consistently in better agreement with data than the predictions using Riquarts's (1981) method. However, the data is overpredicted by 25% to 42%.

Table 5-5. Percentage error for the predicted centerline velocity computed using Equations (2-29) and (2-30) obtained in this work for all operating conditions.

U_g (cm/s)	P (atm)	Sparger*	Experimental u_{l0} (cm/s)	$\frac{(u_{l,pred} - u_{l0})}{u_{l0}} \times 100\%$		
				Riquarts (1981)	Zehner (1986)	Fitted
30	1	D2	40.5	75.6	41.9	41.9
30	1	D4	43.0	65.7	33.9	33.9
30	1	D6	41.1	73.3	40.0	40.0
45	1	D4	52.7	57.2	24.9	24.9
45	4	D4	75.6	9.6	-13.0	3.9
30	4	D3	66.9	6.4	-14.0	2.6
30	4	D4	61.7	15.4	-6.8	11.3
30	4	D6	71.6	-0.6	-19.7	-4.2
30	10	D6	83.4	-14.6	-31.0	-7.4

*D2: Cross sparger (0.1%, d_o = 2.6 mm); D3: Single nozzle (0.1%, d_o = 5.1 mm); D4: Uniform perforated plate (0.15%, d_o = 0.5 mm); D6: Uniform perforated plate (1.0%, d_o = 1.25 mm)

At higher pressure both Riquarts and Zehner's correlations predict the centerline velocity within 20%. The tendency is now to underpredict, accurately for Zehner' correlation. To account for the effect of pressure on centerline velocity, the correlation developed by Zehner (1983) is further modified as shown in Equation (5-13).

$$u_{o,pred} = 0.737 g^{1/3} D_c^{1/3} U_g^{1/3} \left(\frac{\rho_g}{\rho_{g,atm}} \right)^a \tag{5-13}$$

where $\rho_{g,atm}$ is the gas density at atmospheric pressure and a is the parameter to be fitted. Basically, Equation (5-13) still captures the predictions by Zehner (1986) at atmospheric pressure and the incorporation of the pressure ratio term is to reduce the errors as shown in Table 5-5 at higher pressures. Using MATLAB, the fitted parameter a was found to be 0.128. Hence, Equation (5-13) becomes

$$u_{o,pred} = 0.737 g^{1/3} D_c^{1/3} U_g^{1/3} \left(\frac{\rho_g}{\rho_{g,atm}} \right)^{0.128} \quad (5\text{-}14)$$

The percentage errors for centerline liquid velocity computed using Equation (5-14) is also shown in Table 5-5. As shown in Table 5-5, the percentage errors are reduced at higher pressures indicating the usefulness of the proposed correction to the correlation of Zehner (1986). As shown in Equation (5-14), the modified correlation is not able to capture the distributor effect on the centerline liquid velocity, thus, it is best to determine the number of standard deviations that the modified correlation yields. To achieve this, the average and standard deviations for the u_{l0}, for the two different operating conditions (U_g = 30 cm/s at P = 1 and 4 atm) are obtained and shown as follows:

P = 1 atm; U_g = 30 cm/s Average = 41.5; Standard Deviation = 1.27

P = 4 atm; U_g = 30 cm/s Average = 66.7; Standard Deviation = 4.98

The modified Zehner's correlation yields values of 57.5 and 68.6 cm/s for P = 1 and 4 atm, respectively. Hence, it was found that the number of standard deviations is 1.38 and 1.03 for P = 1 and 4 atm, respectively and a conclusion can be made that the modified correlation for distributor effect is approximately within 95% confidence interval.

5.9. Eddy Diffusivity

An important quantity that can be obtained directly from CARPT measurements is the turbulent eddy diffusivity evaluated from the Lagrangian autocorrelation function. Since most other experimental techniques employed for studying bubble column hydrodynamics do not provide Lagrangian data, estimation of eddy diffusivities is therefore unique to CARPT. Degaleesan (1997) discussed in detail the procedure for obtaining eddy diffusivities from CARPT data and only a brief summary of the governing equations for calculating diffusivities is provided below. As indicated by Degaleesan (1997), one of the issues with evaluating eddy diffusivity in bubble columns is the anisotropic nature of the flow. The issue has been addressed in her thesis. Equations (5-15) to (5-17) are used to obtain the radial, axial and tangential eddy diffusivities (Degaleesan, 1997).

$$D_{rr}(t) = \frac{1}{2}\frac{d}{dt}\overline{y_r^2(t)} = \int_0^t \overline{u_r'(t)u_r'(\tau)}d\tau \tag{5-15}$$

$$D_{\theta\theta}(t) = \frac{1}{2}\frac{d}{dt}\overline{y_\theta^2(t)} = \int_0^t \overline{u_\theta'(t)u_\theta'(\tau)}d\tau \tag{5-16}$$

$$D_{zz}(t) = \frac{1}{2}\frac{d}{dt}\overline{y_z^2(t)} = \int_0^t \left\{ \overline{\left.\frac{\partial U_z}{\partial r}\right|_{y_r(t')} \left(\int_0^{t'} u_z'(t)u_r'(\tau)d\tau \right)} + \overline{u_z'(t)u_z'(t')} \right\} dt' \tag{5-17}$$

The presence of the extra term in the *z* direction in Equation (5-17) is due to the presence of the significant axial liquid velocity gradient. The above equations are related to the Lagrangian auto-correlation coefficient, which is defined as

$$R_{ij}(\tau) = \overline{u_i'(t)\, u_j'(t+\tau)} \qquad i, j = r, \theta, z \tag{5-18}$$

where $i = j$ defines the auto-correlation coefficient. Similarly, the other components of the eddy diffusivity, D_{rz}, $D_{r\theta}$ and $D_{z\theta}$ can be calculated from Equations (5-19) to (5-21).

$$\begin{aligned} D_{rz}(t) &= \frac{1}{2}\frac{d}{dt}\overline{y_r(t)y_z(t)} \\ &= \frac{1}{2}\left\{ \int_0^t \left\{ \overline{\left.\frac{\partial U_z}{\partial r}\right|_{y_r(t')} \left(\int_0^{t'} u_r'(t)u_r'(\tau)d\tau \right)} + \overline{u_r'(t)u_z'(t')} \right\} dt' + \int_0^t u_r'(t')u_z'(t)dt' \right\} \end{aligned} \tag{5-19}$$

$$D_{r\theta}(t) = \frac{1}{2}\frac{d}{dt}\overline{y_r(t)y_\theta(t)} = \int_0^t \overline{u_r'(t)u_\theta'(\tau)}d\tau \tag{5-20}$$

$$\begin{aligned} D_{z\theta}(t) &= \frac{1}{2}\frac{d}{dt}\overline{y_r(t)y_\theta(t)} \\ &= \frac{1}{2}\left\{ \int_0^t \left\{ \overline{\left.\frac{\partial U_z}{\partial r}\right|_{y_r(t')} \left(\int_0^{t'} u_\theta'(t)u_r'(\tau)d\tau \right)} + \overline{u_\theta'(t)u_z'(t')} \right\} dt' + \int_0^t u_\theta'(t')u_z'(t)dt' \right\} \end{aligned} \tag{5-21}$$

Using these equations, various correlation coefficients can be calculated from CARPT experimental data, which can then be used to compute the components of the eddy diffusivity tensor. In the sections below, a discussion of the autocorrelation function, integral time scales, eddy diffusivities as well as the characteristic turbulent length scale is provided.

5.9.1. Autocorrelation

Figure 5-38 displays typical correlation coefficient plots for various radial positions in the column for uniform perforated plate distributor D4 (0.15 %, 163 orifices of 0.5 mm) at a superficial gas velocity of 30 cm/s at atmospheric pressure. The figures represent axially and azimuthally averaged data in the fully developed region (z = 54 to 136.8 cm). Figures 5-38a to 5-38d indicate that there is a radial variation of the autocorrelation coefficients and the correlation coefficient in the r and z directions. On the other hand, the correlation coefficient for the z-θ and r-θ direction are found to be approximately zero (refer to Figures 5-38e and 5-38f). Hence, the one-dimensional plots for axial-azimuthal and radial-azimuthal cross-correlations will not be further described in this work.

As mentioned by Degaleesan (1997), there are two types of functional forms that can be fitted to an autocorrelation coefficient. A general functional form (the second type) which includes the negative loops and oscillations as observed for $R_{rr}(\tau)$, is represented as in Equation (5-22).

$$R_L(\tau) = exp\left\{-\frac{\tau}{(m^2+1)\tau_L}\right\} cos\left\{\frac{m\tau}{(m^2+1)\tau_L}\right\} \qquad (5\text{-}22)$$

A value of m = 0 leads to the first type of exponentially decaying correlation coefficients, as is the case with $R_{zz}(\tau)$ and $R_{\theta\theta}(\tau)$. This type of correlation coefficients are usually observed in homogeneous isotropic turbulence (Snyder and Lumley, 1971) while the second type of correlation coefficient has been found in flows of heavy particles in turbulent gases (Mei *et al.*, 1991).

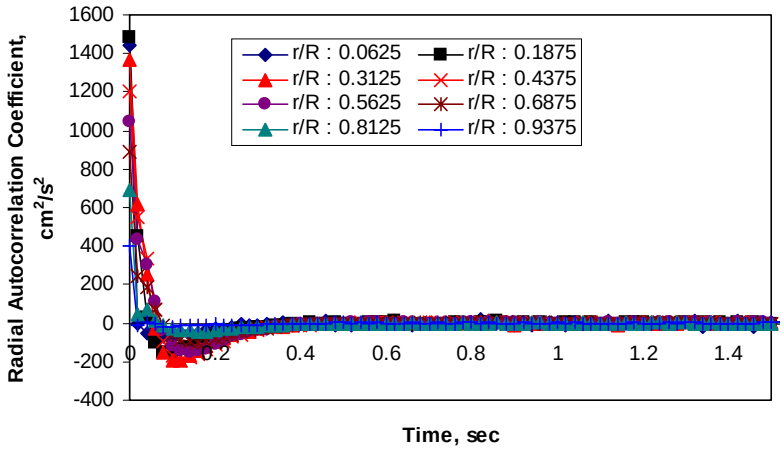
Radial Autocorrelation Coefficient, cm²/s²
1600
1400
1200
1000
800
600
400
200
0
-200
-400
0
0.2
0.4
0.6
0.8
1
1.2
1.4
Time, sec
r/R : 0.0625
r/R : 0.1875
r/R : 0.3125
r/R : 0.4375
r/R : 0.5625
r/R : 0.6875
r/R : 0.8125
r/R : 0.9375

(a)

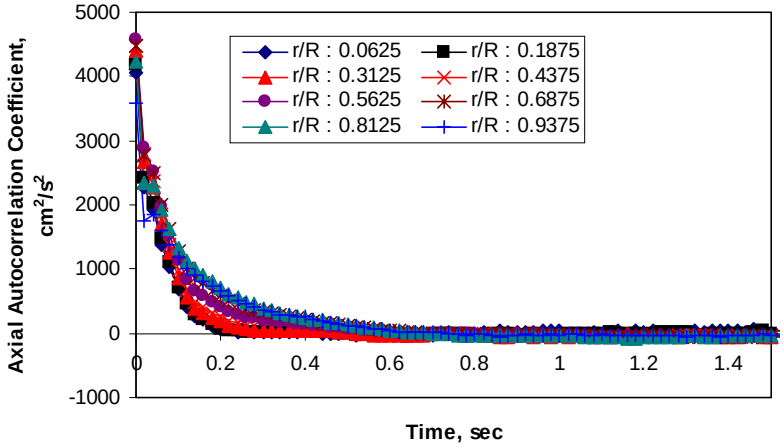
Axial Autocorrelation Coefficient, cm²/s²
5000
4000
3000
2000
1000
0
-1000
0
0.2
0.4
0.6
0.8
1
1.2
1.4
Time, sec
r/R : 0.0625
r/R : 0.1875
r/R : 0.3125
r/R : 0.4375
r/R : 0.5625
r/R : 0.6875
r/R : 0.8125
r/R : 0.9375

(b)

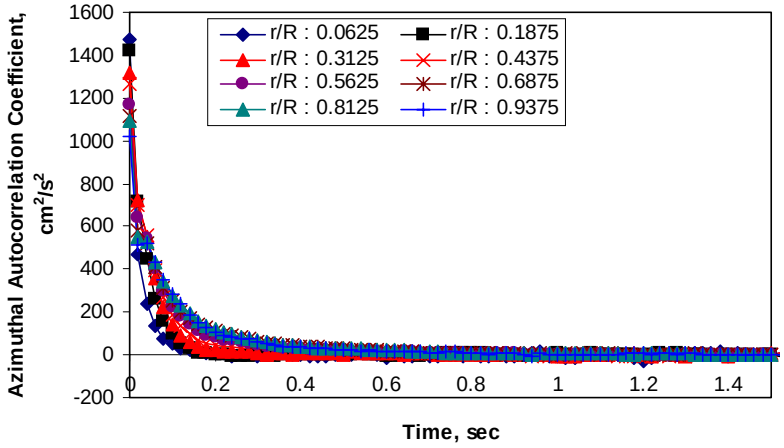
Azimuthal Autocorrelation Coefficient, cm²/s²
1600
1400
1200
1000
800
600
400
200
0
-200
0
0.2
0.4
0.6
0.8
1
1.2
1.4
Time, sec
r/R : 0.0625
r/R : 0.1875
r/R : 0.3125
r/R : 0.4375
r/R : 0.5625
r/R : 0.6875
r/R : 0.8125
r/R : 0.9375

(c)

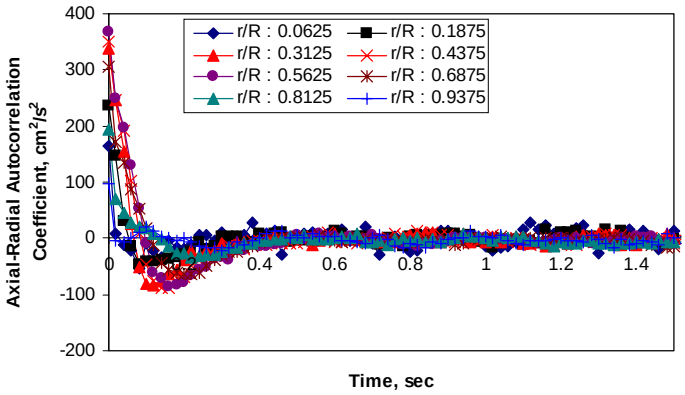

(d)

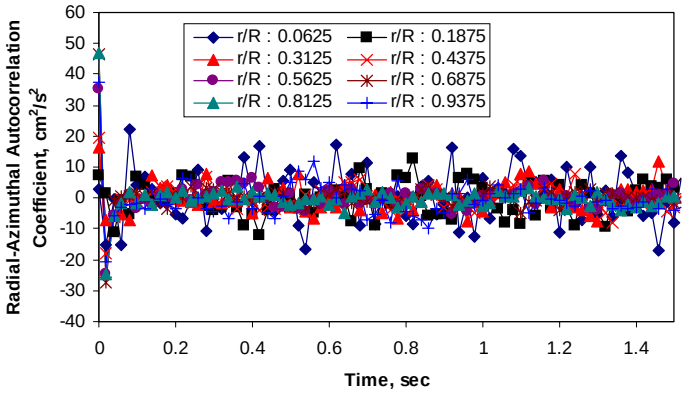

(e)

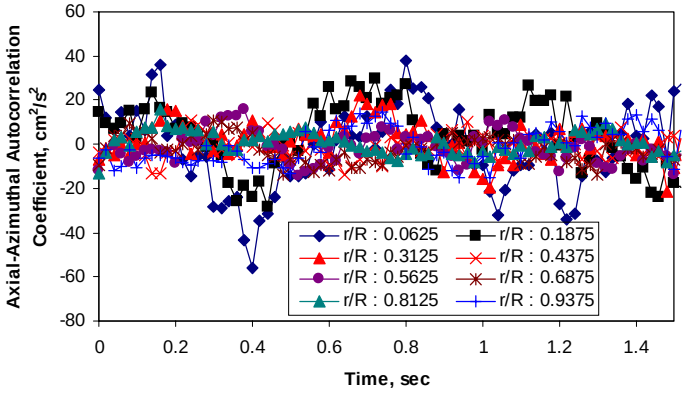

(f)

Figure 5-38. Lagrangian correlation coefficients at various radial positions for distributor D4 (0.15%, 163 orifices of 0.5 mm) at a U_g = 30 cm/s at P = 1 atm: a) radial; b) axial; c) azimuthal; d) axial-radial; e) radial-azimuthal; f) axial-azimuthal.

Another feature that can be extracted from the Lagrangian autocorrelation coefficient is the Lagrangian integral time scale (refer to Equation (5-23)), which represents the time over which the fluid element is correlated with itself (Bendat and Piersol, 1986). The earlier the autocorrelation drops to zero, the smaller is the Lagrangian integral time scale.

$$\tau_{L,i} = \frac{\int_0^\infty \left| \overline{u_i'(t) u_i'(t+t')} \right| dt'}{\overline{u_i'^2}}, \; i \equiv r, \theta, z \tag{5-23}$$

Equation (5-23) is evaluated for all operating conditions considered in this study for each radial compartment from the axially and azimuthally averaged autocorrelation functions. The radial profiles of the integral time scales are further cross-sectionally averaged and the results are shown in Table 5-6. It is evident from Table 5-6 that the integral time scale along the axial direction is much larger than that along the radial direction and is consistent with the observations of Degaleesan (1997). Additionally, while the axial Lagrangian integral time scales decreases with both P and U_g, no clear trend is seen for radial integral time scales. The trend of axial Lagrangian integral time scales with U_g agrees with that obtained from Degaleesan (1997) at atmospheric pressure conditions.

Table 5-6. Cross-sectionally averaged Lagrangian integral time scales from CARPT.

U_g (cm/s)	P (atm)	Sparger	τ_{rL} (sec)	τ_{zL} (sec)
30	1	D2	0.0587	0.0681
30	1	D4	0.0624	0.0738
30	1	D6	0.0676	0.0749
45	1	D4	0.0602	0.0631
45	4	D4	0.0594	0.0523
30	4	D3	0.0613	0.0628
30	4	D4	0.0650	0.0653
30	4	D6	0.0712	0.0676
30	10	D6	0.0682	0.0425

In the following sections, the Lagrangian correlation coefficients presented above have been used to evaluate all six components of the eddy diffusivity tensor. As with the three components of the velocity vector and the six components of the turbulent stress

tensor, the Lagrangian correlation coefficients as well as all the six components of the eddy diffusivity tensor are also available in each of the notional cells into which the three-dimensional vessel domain is compartmentalized. Traditionally, however, both the correlation coefficients as well as the eddy diffusivities have been evaluated from azimuthally and axially averaged data in order to improve the occurrence statistics (Degalessan, 1997; Chen *et al.*, 1999). The same procedure has been adopted here, as a result of which bars indicating the bounds of variation of the eddy diffusivities are not available and are therefore not shown in the radial profiles of the eddy diffusivities presented subsequently in this chapter. However, Appendix C shows the comparison of the eddy diffusivity tensors evaluated with and without axially averaging the correlation functions for one operating condition. The figures presented in Appendix C indicate that the effect of axially averaging the data has an insignificant effect on all three diagonal components of the diffusivity tensor (D_{rr}, D_{zz} and $D_{\theta\theta}$) and the off-diagonal component (D_{rz}). Such is however not the case with $D_{z\theta}$ and $D_{r\theta}$ which show a substantial difference even in the mean with large standard deviation when evaluated from averaged data and data from each individual z level. Therefore, in the graphical presentation of the radial profiles of eddy diffusivity, only D_{rr}, D_{zz}, $D_{\theta\theta}$, and D_{rz} have been reported. One should note that for D_{rz} profiles, the presence of kinks at the center and near the wall of the column may be due to insufficient statistics or occurrences.

5.9.2. Distributor Effects on Eddy Diffusivity Profiles

All the profiles shown in the following section were obtained by averaging the eddy diffusivity data from z = 54 to 136.8 cm since it was shown earlier that the flow becomes fully developed beyond a z level of 50 cm.

A) P = 1 atm; U_g = 30 cm/s

Figure 5-39 displays the effect of distributors on eddy diffusivity profiles at U_g = 30 cm/s and at atmospheric pressure for distributor D2 (0.1% cross sparger), D4 (0.1% uniform perforated plate) and D6 (1.0% uniform perforated plate). Despite the different

configurations of the distributors (refer to Figure 3-2 for the specification of the distributors), there is no significant difference in the eddy diffusivity plots. Eddy diffusivity relates to the mixing of the scalar quantities in the liquid phase in the context of Boussinesq's approximation. The calculation procedure for the eddy diffusivity tensor in bubble column from the lagrangian particle trajectory has been explained elsewhere (Degaleesan, 1997) and is followed for the estimation of quantities reported herein.

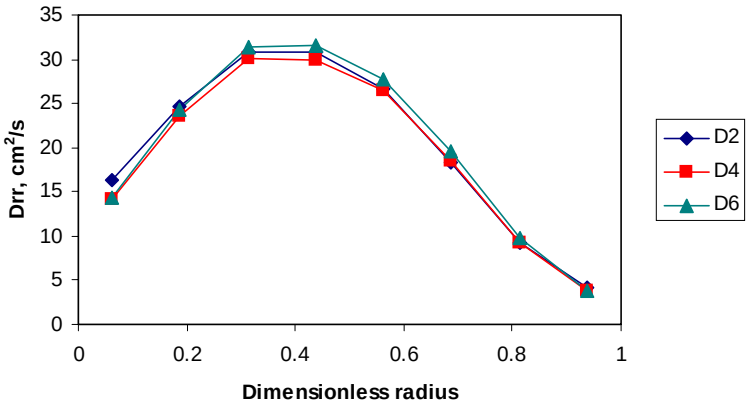

(a)

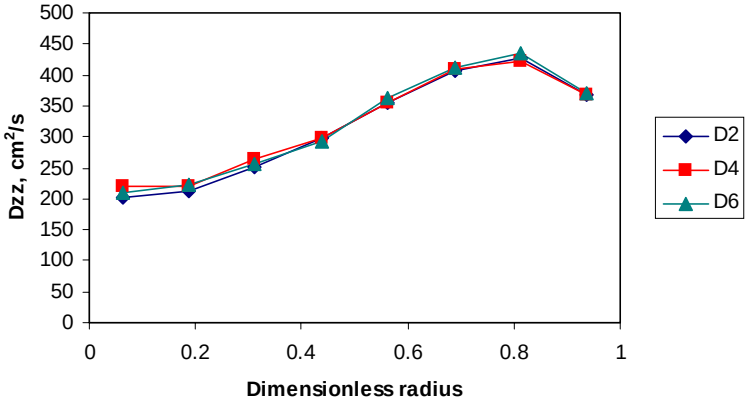

(b)

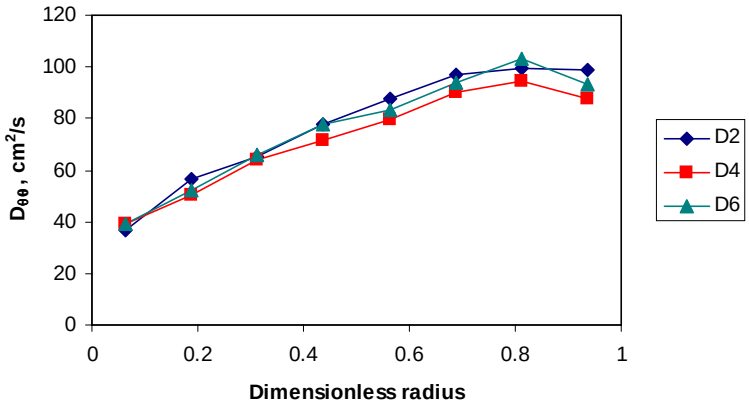

(c)

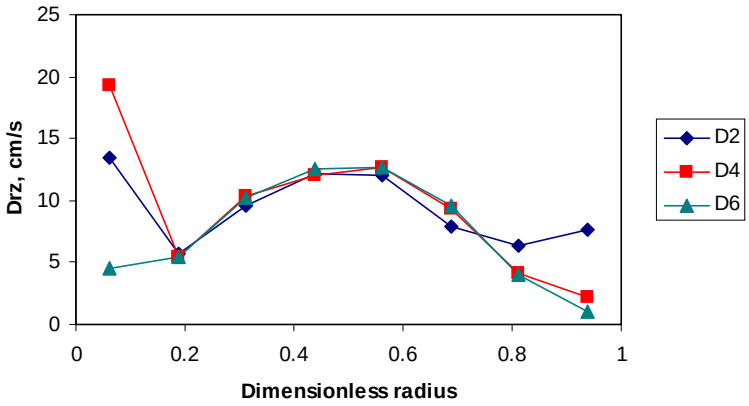

(d)

Figure 5-39. Effect of distributors on eddy diffusivity at P = 1 atm and U_g = 30 cm/s: a) D_{rr}; b) D_{zz}; c) $D_{\theta\theta}$; d) D_{rz}.

B) P = 4 atm; U_g = 30 cm/s

Similar analysis of the effect of distributor on eddy diffusivity is performed at a higher pressure of 4 atm using distributors D3 (0.1% single nozzle), D4 (0.15% uniform perforated plate) and D6 (1.0% uniform perforated plate). Figure 5-40 displays the effect of distributors on the eddy diffusivity at a superficial gas velocity of 30 cm/s and a pressure of 4 atm. It can be seen from this figure that only the axial eddy diffusivity for distributor D3 (single nozzle) shows a significantly higher value as compared to the other

two distributors since D3 is in the dispersed jetting regime whereas the other two distributors are in the jetting regime (refer to Table 4-2).

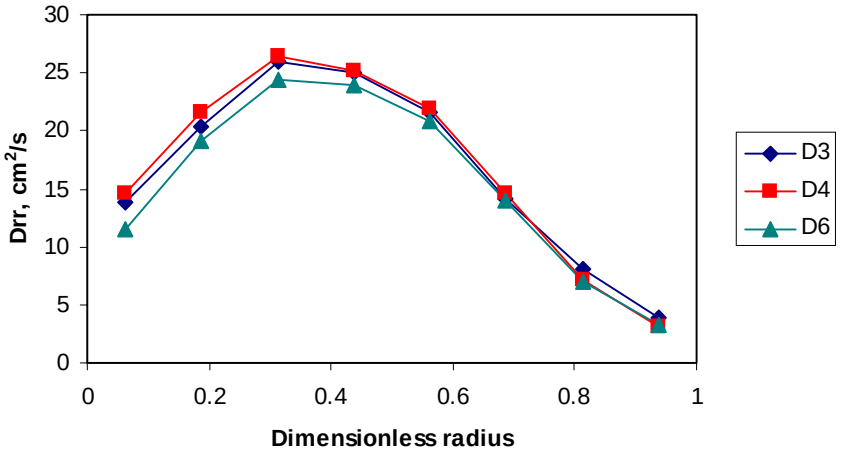

(a)

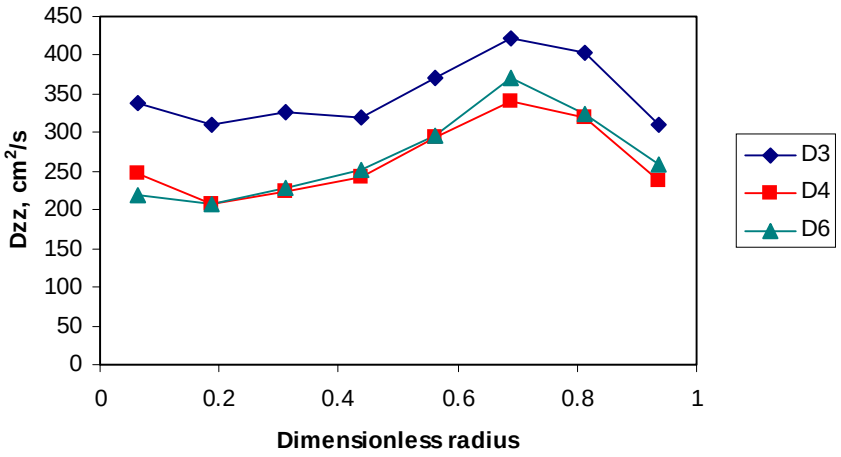

(b)

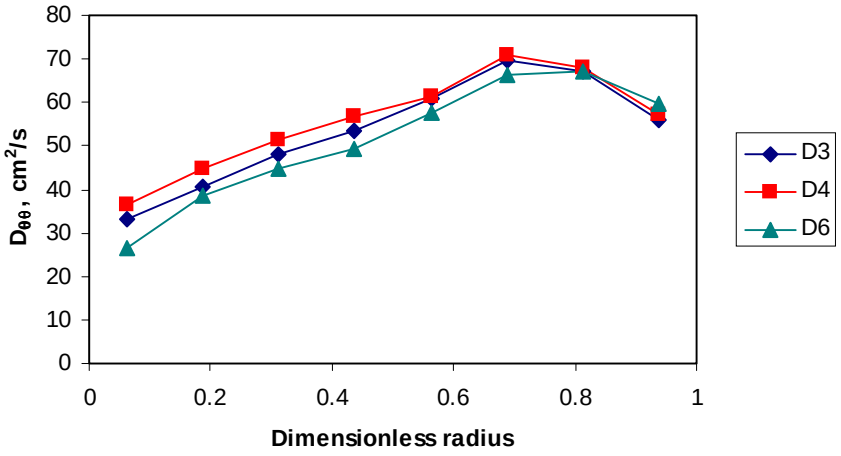

(c)

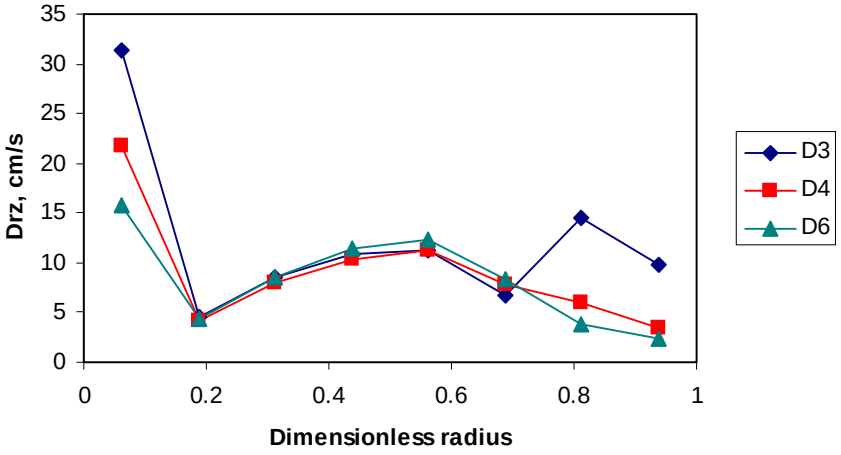

(d)

Figure 5-40. Effect of distributors on eddy diffusivity at P = 4 atm and U_g = 30 cm/s: a) D_{rr}; b) D_{zz}; c) $D_{\theta\theta}$; d) D_{rz}.

5.9.3. Pressure Effects on Eddy Diffusivity Profiles

A) D6; U_g = 30 cm/s

Figure 5-41 shows the effect of pressure on eddy diffusivity profiles at a superficial gas velocity of 30 cm/s using distributor D6 (1.0%, 163 orifices of 1.25 mm). As evident from this figure, the eddy diffusivities are reduced with increased pressure. A similar trend was also seen for the radial and azimuthal normal turbulent stresses as well

as for the turbulent kinetic energy (refer to Figure 5-28b, c and Figure 5-29). This trend can again be attributed to the reduction in bubble size with pressure.

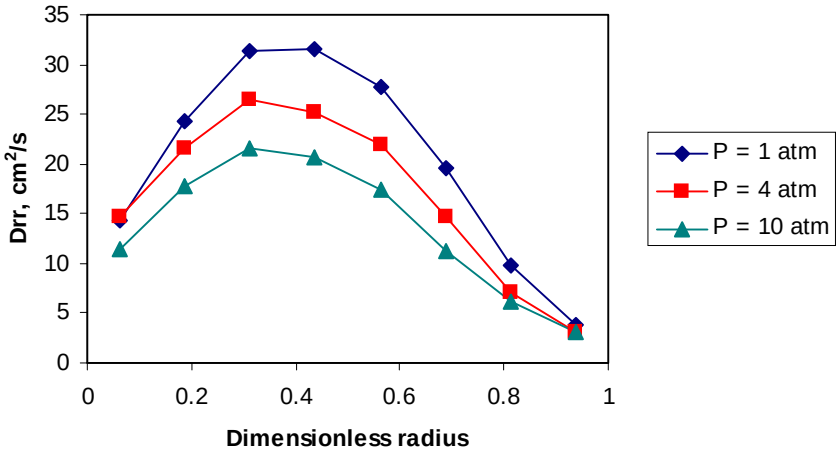

(a)

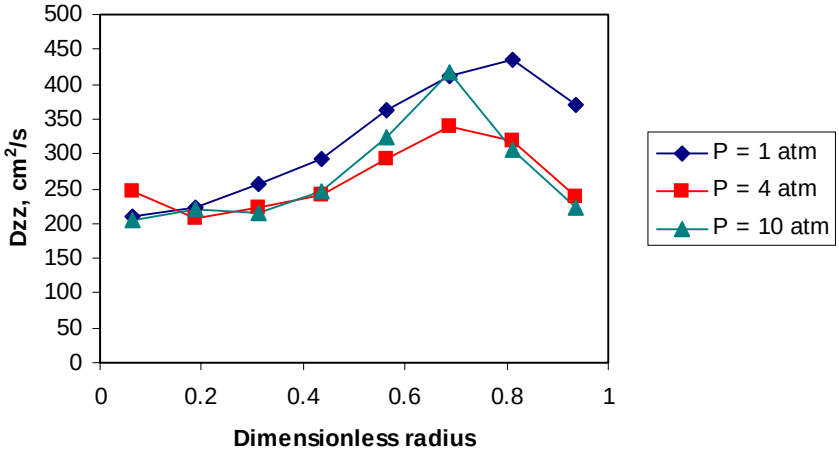

(b)

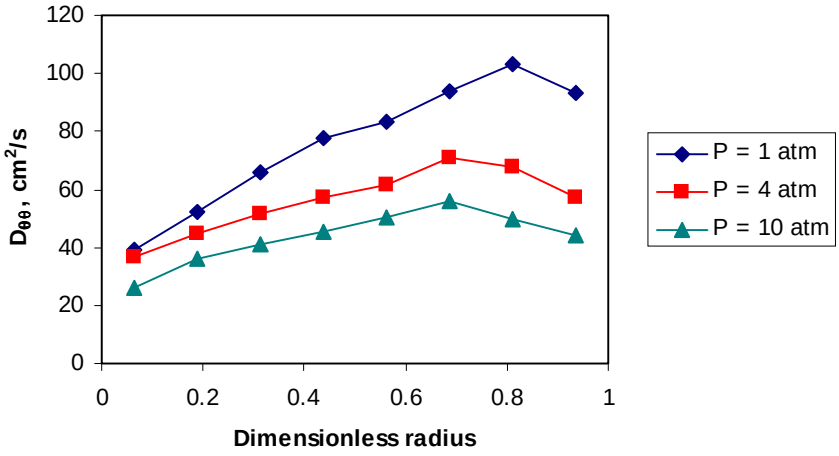

(c)

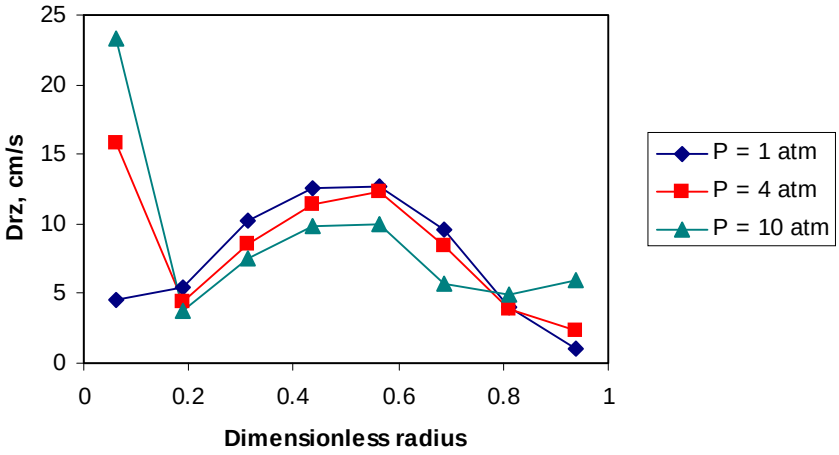

(d)

Figure 5-41. Effect of pressure on eddy diffusivity for distributor D6 (1.0%, 163 orifices of 1.25 mm) at U_g = 30 cm/s: a) D_{rr}; b) D_{zz}; c) $D_{\theta\theta}$; d) D_{rz}.

B) D4; U_g = 45 cm/s

Similar conclusions as those for distributor D6 are reached using distributor D4 (0.15%, 163 orifices of 0.5 mm) operating at a superficial gas velocity of 45 cm/s. Figure 5-42 illustrates the increase in the eddy diffusivity values as pressure decreases even at a higher superficial gas velocity.

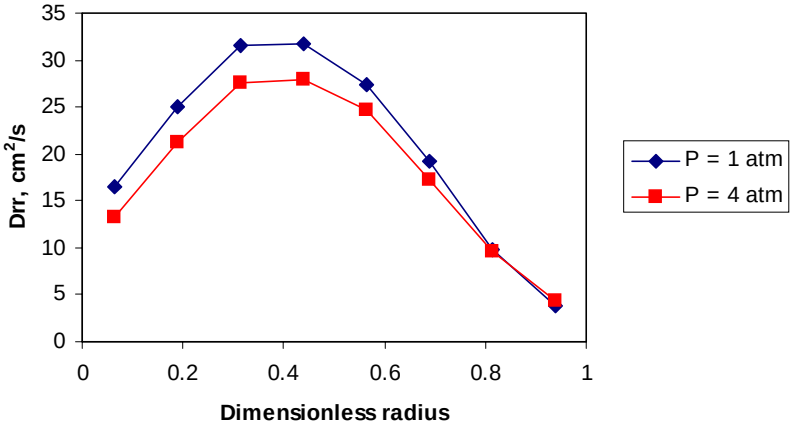
Drr, cm²/s
Dimensionless radius
P = 1 atm
P = 4 atm

(a)

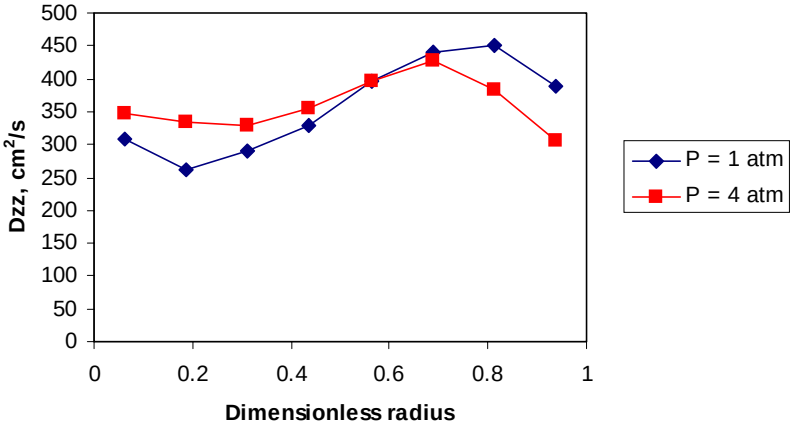
Dzz, cm²/s
Dimensionless radius
P = 1 atm
P = 4 atm

(b)

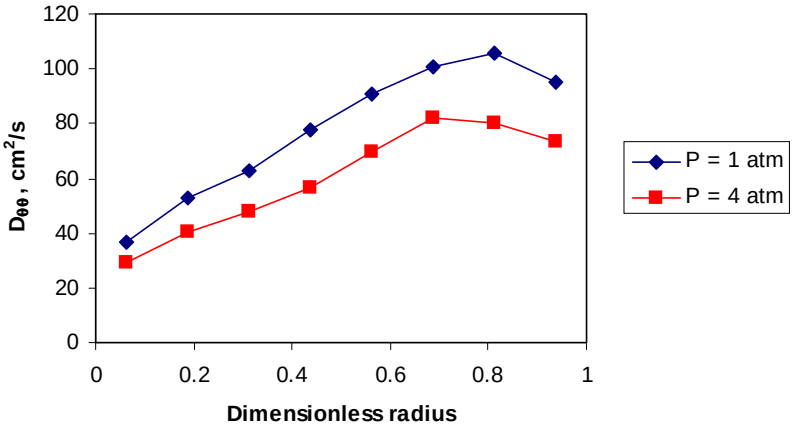
Dθθ, cm²/s
Dimensionless radius
P = 1 atm
P = 4 atm

(c)

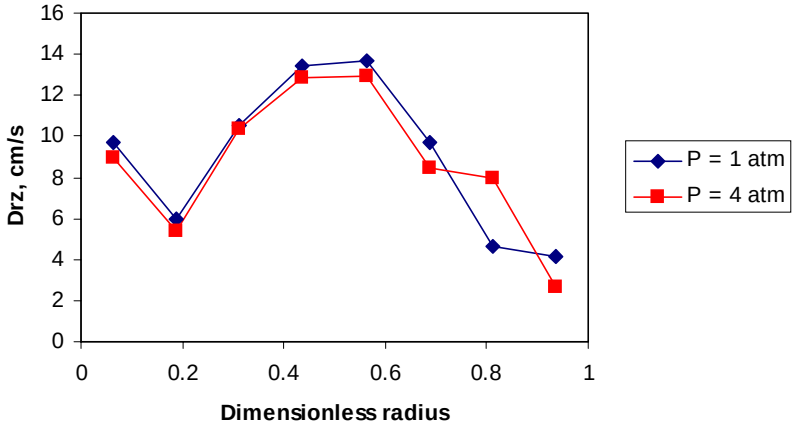

(d)

Figure 5-42. Effect of pressure on eddy diffusivity for distributor D4 (0.15%, 163 orifices of 0.5 mm) at U_g = 45 cm/s: a) D_{rr}; b) D_{zz}; c) $D_{\theta\theta}$; d) D_{rz}.

5.9.4. Effect of Superficial Gas Velocity on Eddy Diffusivity Profiles

Figure 5-43 shows the effect of superficial gas velocity on eddy diffusivity using distributor D4 (0.15%, 163 orifices of 0.5 mm) operating at atmospheric pressure for superficial gas velocities of 30 and 45 cm/s. It can be concluded from this figure that increasing superficial gas velocity increases the eddy diffusivity. Thus, higher superficial gas velocity implies enhanced mixing in the system. Figure 5-34 also indicates that the difference in the eddy diffusivity profiles for these two superficial gas velocities is much smaller than those reported by Degaleesan (1997) at lower velocities (up to 12 cm/s) and at P = 1 atm. Hence, as superficial gas velocity increases, the diffusivities tend to level off, which is similar to the behavior of the other fluid dynamic parameters (Degaleesan, 1997).

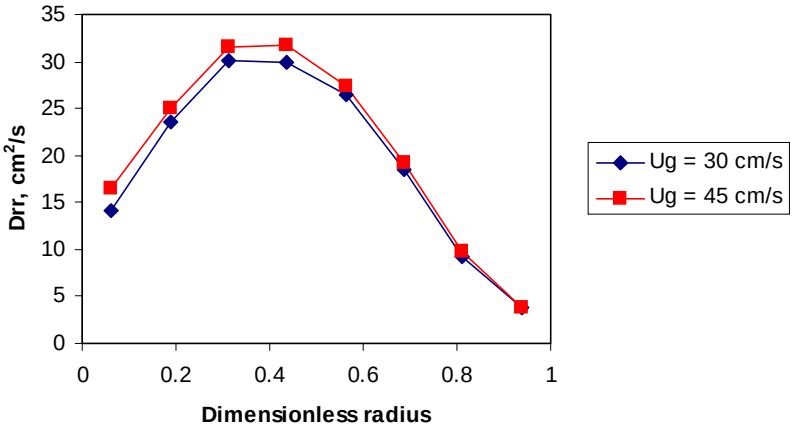
35
30
25
20
15
10
5
0
Drr, cm²/s
0
0.2
0.4
0.6
0.8
1
Dimensionless radius
Ug = 30 cm/s
Ug = 45 cm/s

(a)

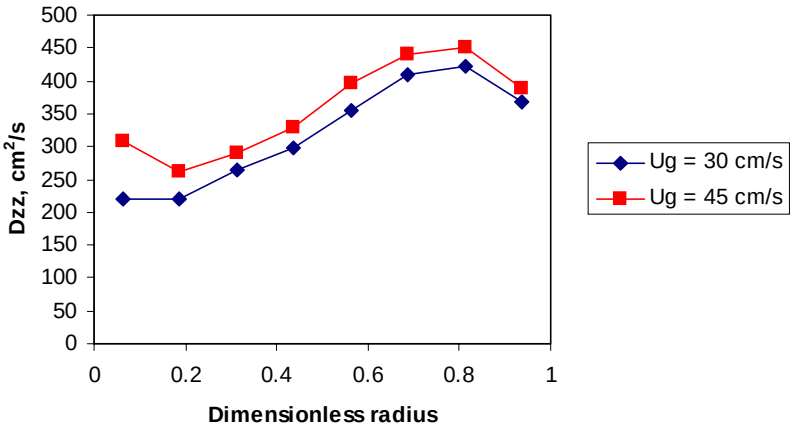
500
450
400
350
300
250
200
150
100
50
0
Dzz, cm²/s
0
0.2
0.4
0.6
0.8
1
Dimensionless radius
Ug = 30 cm/s
Ug = 45 cm/s

(b)

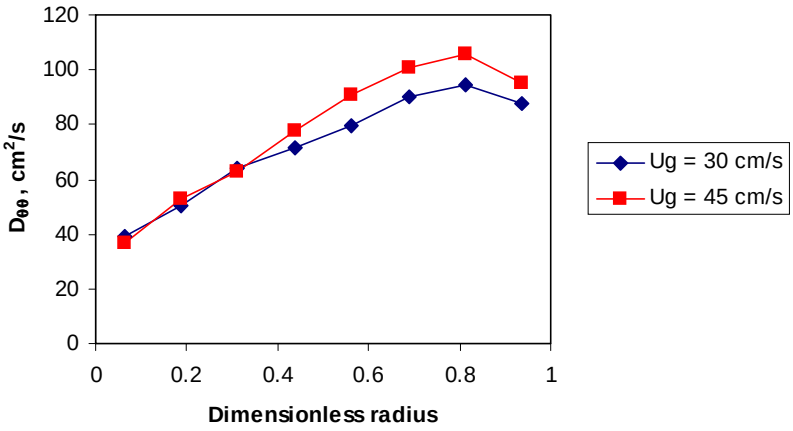
120
100
80
60
40
20
0
Dθθ, cm²/s
0
0.2
0.4
0.6
0.8
1
Dimensionless radius
Ug = 30 cm/s
Ug = 45 cm/s

(c)

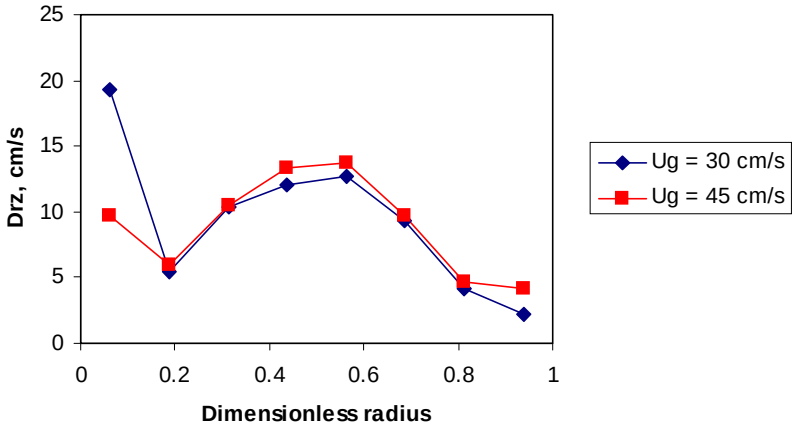

(d)

Figure 5-43. Effect of superficial gas velocity on eddy diffusivity for distributor D4 (0.15%, 163 orifices of 0.5 mm) at P = 1 atm: a) D_{rr}; b) D_{zz}; c) $D_{\theta\theta}$; d) D_{rz}.

5.9.5. Cross-Sectional Averaged Eddy Diffusivity and Turbulent Length Scales

Table 5-7 displays the cross-sectional averaged eddy diffusivity for all operating conditions investigated in this work. As shown in Table 5-7, the cross-sectional averaged axial eddy diffusivity is at least four times higher than the remaining quantities. In addition, the diffusivity, $\overline{D_{rz}}$ is found to be considerably lower than the rest. This observation is consistent with the findings of Degaleesan (1997).

Table 5-7. Cross-sectionally averaged eddy diffusivity for all operating conditions.

U_g (cm/s)	P (atm)	Sparger	$\overline{D_{zz}}$ (cm^2/s)	$\overline{D_{rr}}$ (cm^2/s)	$\overline{D_{\theta\theta}}$ (cm^2/s)	$\overline{D_{rz}}$ (cm^2/s)
30	1	D2	356	16.8	89.0	8.50
30	1	D4	357	16.5	81.9	8.06
30	1	D6	360	17.2	87.0	7.32
45	1	D4	387	17.2	89.8	8.62
45	4	D4	362	15.7	69.3	9.39
30	4	D3	357	13.9	59.0	12.5
30	4	D4	275	13.7	60.6	8.07
30	4	D6	288	13.0	58.0	8.43
30	10	D6	286	11.3	47.3	8.01

Table 5-7 also illustrates the effect of distributor, pressure and superficial gas velocity on the cross-sectional averaged eddy diffusivity. The diffusivities decrease with an increase in pressure and a decrease in superficial gas velocity. While insignificant distributor effects are seen at atmospheric pressure, at a higher pressure of 4 atm, the axial eddy diffusivity is higher for a single nozzle sparger (D3) as compared to perforated plate distributors (D4 and D6). Though more experimentation is required with the single nozzle sparger at higher pressures to understand its different behavior, overall, for engineering purposes, distributor effect on eddy diffusivities may be considered small.

A characteristic turbulent length scale can be evaluated using the turbulent eddy diffusivity and the root mean square fluctuating velocity as indicated by Equations (5-24) and (5-25) below. Alternatively, using scaling arguments, a different length scale can also be evaluated using the turbulent eddy diffusivity and the integral time scales as shown by Equations (5-26) and (5-27) based on the assumption that turbulent Schmidt Number $\left(Sc_t = \upsilon_{eff}/D\right)$ is 1.

$$\bar{l}_z \propto \frac{\overline{D}_{zz}}{\sqrt{\overline{u_z'^2}}} \tag{5-24}$$

$$\bar{l}_r \propto \frac{\overline{D}_{rr}}{\sqrt{\overline{u_r'^2}}} \tag{5-25}$$

$$\bar{l}_{zt} \propto \sqrt{\overline{D}_{zz}\tau_{zL}} \tag{5-26}$$

$$\bar{l}_{rt} \propto \sqrt{\overline{D}_{rr}\tau_{rL}} \tag{5-27}$$

Using the cross-sectionally averaged axial and radial diffusivities and normal turbulent stresses and assuming a proportionality constant of unity, the average axial and radial turbulent length scales were evaluated for all operating conditions and are reported in Table 5-8. Based on the values of the length scales shown in the table, it is clear that the length scales based on Lagrangian integral time scales are systematically lower than those based on the root mean square fluctuating velocities. However, in general, the trend in the variation of the length scales is similar to that of the turbulent stresses and diffusivities, that is the characteristic turbulent length scale increases with superficial gas velocity while it decreases with pressure. Of course, as with other turbulent quantities,

the length scales with distributor D3 at higher pressure of 4 atm is higher compared to the perforated plate distributors. Ignoring the finite but relatively small differences in the length scales observed for different operating conditions, the average length scale based on root mean square velocity is 0.6 cm in the radial direction and 6.8 cm in the axial direction.

Table 5-8. Turbulent length scales evaluated using Equations (5-24) to (5-27).

U_g (cm/s)	P (atm)	Sparger	$\bar{l}_r$, cm	$\bar{l}_z$, cm	$\bar{l}_{rt}$, cm	$\bar{l}_{zt}$, cm
30	1	D2	0.60	7.08	0.99	4.93
30	1	D4	0.63	7.22	1.01	5.13
30	1	D6	0.68	7.35	1.08	5.19
45	1	D4	0.63	7.39	1.02	4.94
45	4	D4	0.58	6.98	0.96	4.35
30	4	D3	0.53	7.41	0.92	4.73
30	4	D4	0.56	5.95	0.94	4.24
30	4	D6	0.57	6.16	0.96	4.41
30	10	D6	0.50	5.85	0.88	3.49
Average			0.59	6.82	0.97	4.60

5.10. Validity of Bousinessq's Hypothesis

Until now, the experimental observations are explained based on Bousinessq's hypothesis and the validity of the approximation to this study is provided in this section. Equation (5-28) shows the turbulent eddy viscosity can be obtained via characteristic scales arguments (Tennekes and Lumley, 1972).

$$\nu_{eff} = u_{ch} * l_{ch} = u_{ch}^2 * \tau_{ch} \tag{5-28}$$

where u_{ch}, l_{ch} and τ_{ch} are the characteristic velocity, length and integral time scales of large eddies, respectively in the direction lateral to the direction of the flow. For this study, these would mean the root mean squared velocity in the radial direction and the radial integral time scale, i.e.,

$$\nu_{eff} = \overline{u'^2_r} * \tau_{rl} \tag{5-29}$$

Using the normal stress in *r* direction and integral time scaled obtained from CARPT, Table 5-9 displays the turbulent eddy viscosity evaluated using Equation (5-29) and compares this with that from Equation (5-10b) (cross-sectional average eddy viscosity based on CARPT data). Also displayed in the table is the ratio of the cross-sectional averaged eddy viscosity and the turbulent eddy viscosity evaluated from Equation (5-29). This ratio represents a constant to Equation (5-29) for anisotropy turbulence.

Table 5-9. Validity of Bousinessq's approximation.

Sparger	P, atm	U_g, cm/s	$\overline{u'^2_r}$, cm^2/s^2	τ_{rl}, sec	ν_{eff}, cm^2/s	$\nu_{t,CSA}$, cm^2/s	$\nu_{t,CSA}/\nu_{eff}$
D2	1	30	787	0.0587	46.2	12.6	0.27
D4	1	30	679	0.0624	42.3	13.6	0.32
D6	1	30	633	0.0676	42.8	13.3	0.31
D4	1	45	739	0.0602	44.5	12.1	0.27
D4	4	45	723	0.0594	42.9	10.2	0.24
D3	4	30	679	0.0613	41.6	9.61	0.23
D4	4	30	606	0.0650	39.4	10.3	0.26
D6	4	30	516	0.0712	36.8	8.75	0.24
D6	10	30	514	0.0682	35.0	7.95	0.23
Average							0.26
Standard Deviation							0.0343

The following observations can be made from the above table:

1. $\overline{u'^2_r}$ increases with U_g and decreases with P.
2. ν_{eff} calculated from characteristic scale arguments is systematically higher than $\nu_{t,CSA}$ calculated from fitting of τ_{rz} and axial velocity gradient data. However, the magnitudes of the two values are of the same order with the average discrepancy of 74%. Of course, one should remember
3. The ratio $\nu_{t,CSA}$ / ν_{eff} decreases with both pressure and superficial gas velocity. The average ratio is 0.26 with standard deviation 0.0343.

Although the assumption of isotropic turbulence in Equation (5-1b) does not applied to bubble columns, the above analysis for CARPT data in this study still yield

eddy viscosity within 74 % or so. Of course, one should remember that the eddy viscosity computed from Equation (5-29) is just based on dimensionless scaling argument and one may actually need a constant to represent the true value for a particular flow situation of interest.

5.11. Overall Liquid Continuity

The final issue is whether the overall liquid continuity can be satisfied and this shall be discussed in this section. Since CARPT provides liquid recirculation velocities and the liquid phase holdup is available from independent measurement using CT, it is theoretically possible to evaluate the liquid phase mass balance using Equation (5-30).

$$Q = 2\pi R^2 \int_0^1 \xi\, u_l(\xi)\varepsilon_l(\xi) d\xi = 0 \qquad \text{for batch liquid} \tag{5-30}$$

Since both the axial liquid velocity as well as gas holdup consist of a mean and fluctuating part, i.e., $u_l = \bar{u}_l + u_l'$ and $\varepsilon_l = \bar{\varepsilon}_l + \varepsilon_l'$, averaging of Equation (5-30) gives

$$\bar{Q} = 2\pi R^2 \left\{ \int_0^1 \xi\, \bar{u}_l(\xi)\, \bar{\varepsilon}_l(\xi) d\xi + \int_0^1 \xi\, \overline{u_l'(\xi)\varepsilon_l'(\xi)}\, d\xi \right\} \tag{5-31}$$

The above equation contains only two terms since $\overline{\bar{u}_l(\xi)\varepsilon_l'(\xi)}$ and $\overline{u_l'(\xi)\bar{\varepsilon}_l(\xi)}$ are zero as the mean fluctuations is by definition zero.

Since both CARPT and CT measure long time-averaged quantities, the first term in Equation (5-31) can be readily evaluated. Such is not the case with the second term. If the contribution of the second term to the overall liquid recirculation is negligible, then the evaluation of the first term in Equation (5-31) would be close to zero for batch liquid. Because of the presence of high gas volume fraction under the operating conditions investigated in this study, not only does one expect the contribution of the second term in Equation (5-31) to be significant but also errors in the measurements near the wall are present as was shown in Chapter 4 for CT. Table 5-10 displays the overall liquid

continuity evaluated using only the first term in Equation (5-31) for all operating conditions. The upflow ($\overline{Q}_{up}$) and downflow ($\overline{Q}_{down}$) fluxes are obtained based on Equation (5-32).

$$\overline{Q}_{up} = 2\pi R^2 \int_0^{\xi_0} \xi\, \overline{u}_l(\xi)\, \overline{\varepsilon}_l(\xi) d\xi \tag{5-32a}$$

$$\overline{Q}_{down} = 2\pi R^2 \int_{\xi_0}^{1} \xi\, \overline{u}_l(\xi)\, \overline{\varepsilon}_l(\xi) d\xi \tag{5-32b}$$

where ξ_0 is the dimensionless radial position of liquid velocity inversion. It can be seen from the table that the overall liquid phase mass balance is not satisfied. Hence, the inclusion of the second term in Equation (5-31) may be essential to close the overall liquid continuity. One should also note from the table that the liquid recirculation increases both with pressure and superficial gas velocity. The increase in liquid recirculation with superficial gas velocity is consistent with the findings of Degaleesan (1997).

Table 5-10. Overall liquid continuity using the first term shown in Equation (5-31).

U_g (cm/s)	P (atm)	Sparger	$\overline{Q}_{up}$ (cm^3/s)	$\overline{Q}_{down}$ (cm^3/s)	$\frac{\left(Abs\left(\overline{Q}_{down}\right)-\overline{Q}_{up}\right)}{0.5\left(Abs\left(\overline{Q}_{down}\right)+\overline{Q}_{up}\right)}$, %
30	1	D2	996	-1232	21.1
30	1	D4	985	-1282	26.2
30	1	D6	900	-1241	31.9
45	1	D4	1009	-1284	24.0
45	4	D4	1267	-1739	31.5
30	4	D3	1233	-1665	29.8
30	4	D4	1442	-1597	10.2
30	4	D6	1507	-2057	30.9
30	10	D6	1595	-2284	35.5

As shown in Table 5-10, the overall liquid continuity ranges from 10 to 36%, where the highest deviation occurs at the extreme operating condition (P = 10 atm; U_g = 30 cm/s). Thus, the second term to Equation (5-31) is essential to close the liquid continuity. From Hinze (1975) and Durbin and Pettersson Reif (2001), the simplest

passive scalar flux model adopts the gradient diffusion hypothesis (refer to Equation (5-33a) and assuming that $\frac{\partial \bar{\varepsilon}_l}{\partial z} = \frac{\partial \bar{\varepsilon}_l}{\partial \theta} = 0$, the cross-correlation term applicable to this study is represented in Equation (5-33b).

$$\overline{u_l' \varepsilon_l'} = -D_{zr} \frac{\partial \bar{\varepsilon}_l}{\partial r} - D_{zz} \frac{\partial \bar{\varepsilon}_l}{\partial z} - D_{\theta\theta} \frac{\partial \bar{\varepsilon}_l}{\partial \theta} \tag{5-33a}$$

$$\overline{u_l' \varepsilon_l'} = -D_{zr} \frac{\partial \bar{\varepsilon}_l}{\partial r} \tag{5-33b}$$

As evident from Equation (5-33b), the scalar flux between the fluctuating liquid holdup and axial liquid velocity is negative since $\frac{\partial \bar{\varepsilon}_l}{\partial r} > 0$ in this study. It should be noted, however, that the *passive* scalar flux represented in Equation (5-33) is usually used based on concentration and velocity fluctuations where the concentration does not affect the velocity field (passive scalar transport). For a negative concentration gradient, the presence of the negative sign before the diffusivity is required to obtain a positive flux. However, in this study, since liquid holdup affects the liquid velocity field (i.e. active scalar) and is subjected to counter-gradient diffusion, the negative sign is omitted in Equation (5-33). Further, to fruitfully use Equation (5-33b), one needs a method for evaluation of the eddy diffusivity, D_{zr}. As mentioned earlier in Section 5.9, Degaleesan (1997) discussed the procedure for obtaining eddy diffusivities from CARPT data, however, in her formulation, the eddy diffusivity tensor is symmetric, i.e., $D_{zr} = D_{rz}$. On the other hand, Durbin and Petterson Reif (2001) concluded that the eddy diffusivity tensor is asymmetric and is shown in Equation (5-35c), which is obtained by equating Equation (5-34a) and Equation (5-34b).

$$\overline{u_i' \varepsilon_l'} = -D_{ij} \frac{\partial \varepsilon_l}{\partial x_j} \tag{5-34a}$$

$$\overline{u_i' \varepsilon_l'} = -C_c \frac{k}{\varepsilon} \left(\overline{u_i' u_j'} \frac{\partial \varepsilon_l}{\partial x_j} + \overline{u_j' \varepsilon_l'} \frac{\partial U_i}{\partial x_j} \right) \tag{5-34b}$$

$$D_{ij} = C_c \frac{k}{\varepsilon} \left(\overline{u_i' u_j'} - D_{kj} \frac{\partial U_i}{\partial x_k} \right) \tag{5-35}$$

where C_c is a constant reported to vary in the range 0.11-0.20 and a commonly used value is 0.15. As evident from Equation (5-35), the eddy diffusivity tensor is asymmetric. Hence, assuming $\frac{\partial U_z}{\partial z} = \frac{\partial U_z}{\partial \theta} = 0$, D_{zr} can be represented as

$$D_{zr} = C_c \frac{k}{\varepsilon}\left(\overline{u_z' u_r'} - C_c \frac{k}{\varepsilon}\overline{u_r' u_r'}\frac{\partial U_z}{\partial r}\right) \tag{5-36}$$

The remaining components of the eddy diffusivity tensor are shown in Equation (5-37).

$$D_{rr} = C_c \frac{k}{\varepsilon}\overline{u_r' u_r'} \tag{5-37a}$$

$$D_{\theta\theta} = C_c \frac{k}{\varepsilon}\overline{u_\theta' u_\theta'} \tag{5-37b}$$

$$D_{zz} = C_c \frac{k}{\varepsilon}\left(\overline{u_z' u_z'} - C_c \frac{k}{\varepsilon}\overline{u_r' u_z'}\frac{\partial U_z}{\partial r}\right) \tag{5-37c}$$

$$D_{r\theta} = D_{\theta r} = C_c \frac{k}{\varepsilon}\overline{u_\theta' u_r'} \tag{5-37d}$$

$$D_{rz} = C_c \frac{k}{\varepsilon}\overline{u_r' u_z'} \tag{5-37e}$$

$$D_{z\theta} = C_c \frac{k}{\varepsilon}\left(\overline{u_z' u_\theta'} - C_c \frac{k}{\varepsilon}\overline{u_r' u_\theta'}\frac{\partial U_z}{\partial r}\right) \tag{5-37f}$$

$$D_{\theta z} = C_c \frac{k}{\varepsilon}\overline{u_\theta' u_z'} \tag{5-37g}$$

Equation (5-37) has been used to calculate eddy diffusivities and compare those computed using the methodology of Degaleesan (1997) (refer to Appendix D). With D_{zr} calculated using Equation (5-36) and k obtained from CARPT experiment, the contribution of the second term in Equation (5-31) can be evaluated only if the constant C_c and the dissipation rate, ε are known. In this study, the dissipation rate is taken to be the upper bound of the dissipation, i.e., gU_g whereas the constant C_c is adjusted until the overall liquid continuity is satisfied within 1%. Table 5-11 displays the overall liquid continuity using Degaleesan's formulation of calculating eddy diffusivity, i.e., $D_{zr} = D_{rz}$ whereas Table 5-12 utilizes Equation (5-36) to evaluate D_{zr}. The values of the fluctuating

fluxes, Q_{up}' and Q_{down}' in these two tables have been evaluated using the definitions shown in Equation (5-38).

$$Q_{up}^{'} = 2\pi R^2 \int_0^{\xi_0} \xi \overline{\varepsilon_l^{'}(\xi) u_l^{'}(\xi)} d\xi = 2\pi R^2 \int_0^{\xi_0} \xi D_{zr} \frac{\partial \overline{\varepsilon}_l}{\partial \xi} d\xi \tag{5-38a}$$

$$Q_{down}^{'} = 2\pi R^2 \int_{\xi_0}^{1} \xi \overline{\varepsilon_l^{'}(\xi) u_l^{'}(\xi)} d\xi = 2\pi R^2 \int_{\xi_0}^{1} \xi D_{zr} \frac{\partial \overline{\varepsilon}_l}{\partial \xi} d\xi \tag{5-38b}$$

Table 5-11. Overall liquid continuity using D_{zr} from Degaleesan (1997).

$$\%\, Diff = \frac{abs\left(\overline{Q}_{down} + Q_{down}^{'}\right) - \left(\overline{Q}_{up} + Q_{up}^{'}\right)}{0.5 * \left(abs\left(\overline{Q}_{down} + Q_{down}^{'}\right) + \left(\overline{Q}_{up} + Q_{up}^{'}\right)\right)} \times 100$$

Sparger	P, atm	U_g, cm/s	$\overline{Q}_{up}$, cm^3/s	$\overline{Q}_{down}$, cm^3/s	Q_{up}', cm^3/s	Q_{down}', cm^3/s	% Diff
D2	1	30	996	-1232	49	68	10.8
D4	1	30	985	-1282	40	56	17.9
D6	1	30	900	-1241	44	63	22.1
D4	1	45	1009	-1284	52	71	13.4
D4	4	45	1267	-1739	51	71	23.5
D3	4	30	1233	-1665	52	74	21.3
D4	4	30	1442	-1597	40	50	4.35
D6	4	30	1507	-2057	49	65	24.5
D6	10	30	1595	-2284	50	66	29.6

Table 5-12. Overall liquid continuity using D_{zr} based on Equation (5-36).

Sparger	P, atm	U_g, cm/s	$\overline{Q}_{up}$, cm^3/s	$\overline{Q}_{down}$, cm^3/s	Q_{up}', cm^3/s	Q_{down}', cm^3/s	C_c	% Diff
D2	1	30	996	-1232	98.1	137	0.48	0.03
D4	1	30	985	-1282	122	172	0.65	0.31
D6	1	30	900	-1241	142	200	0.72	-0.12
D4	1	45	1009	-1284	120	162	0.45	-0.53
D4	4	45	1267	-1739	201	277	0.54	-0.32
D3	4	30	1233	-1665	180	254	0.67	-0.15
D4	4	30	1442	-1597	71.8	90.4	0.45	-0.46
D6	4	30	1507	-2057	233	310	0.82	0.39
D6	10	30	1595	-2284	300	399	0.78	-0.52

As can be seen from Table 5-11, the overall liquid continuity based on the eddy diffusivity (D_{zr}) calculated using Degaleesan's (1997) formulation is slightly better than that shown in Table 5-10, where the contribution from fluctuating liquid holdup and velocity is neglected. However, considering the possibility of eddy diffusivity tensor being asymmetric and using the upper bound of the dissipation ($\varepsilon = gU_g$), the overall liquid continuity can be closed within 1% by suitably adjusting the floating parameter C_c. For the range of experiments in this study, the fitted value of C_c is found to be in the range from 0.45 to 0.82. Even though this development presents a possible description of the turbulent transport of the active scalar (gas/liquid holdup), a detailed future investigation in the realm of multiphase turbulence modeling would be necessary to understand the issues related to counter-gradient diffusion as well as its applicability to CARPT data.

5.12. Summary

A systematic investigation of liquid recirculation and turbulence in a 6" bubble column has been accomplished for the first time via the Computer Automated Radioactive Particle Tracking (CARPT) technique at very high superficial gas velocities, at elevated pressures and with different gas distributors. The Monte Carlo method (Gupta, 2002) was employed for particle position reconstruction since problems with the traditional reconstruction algorithm (Deglaessan, 1997) were encountered due to excessive scattering in the measured radiation counts arising from stainless steel vessel wall. The main findings from this experimental study are summarized below.

1. The strength of the axial liquid recirculation increases with increase both in pressure as well as superficial gas velocity. This is directly related to the gas volume fraction and its radial gradient which also increases both with pressure and superficial gas velocity (at high superficial velocities indicative of churn-turbulent flow).
2. At atmospheric pressure conditions, liquid recirculation was found to be fairly independent of the choice of the distributor. However, differences were observed

in the measured turbulent quantities with the cross sparger (D2) exhibiting greater turbulent kinetic energy (TKE) as compared to the perforated plate distributors (D4 and D6).

3. At a higher pressure of 4 atm, barring the single nozzle sparger (D3) which also resulted in higher gas holdup (Chapter 4), the effect of distributors on liquid recirculation can be considered insignicant.

4. While liquid recirculation increases with increase in pressure (as a result of increase in gas holdup), the turbulent normal stresses and hence, the TKE as well as the eddy diffusivities decrease with increasing operating pressure. A reduction in bubble size with pressure is conjectured to be the most plausible explanation for these hydrodynamic observations.

5. The turbulent shear stress (τ_{rz}) and the gradient of the time averaged axial liquid velocity measured by the CARPT technique was fitted to a kinematic eddy viscosity profile of the form

$$\nu_t(\xi) = \nu_{t0}\,(1.0 - k\xi^{\alpha})$$

Based on the fitted eddy viscosity profile, the cross-sectional average eddy viscosity was evaluated for each operating condition investigated in the study. It was found that the kinematic eddy viscosity decreases both with pressure and superficial gas velocity though the change is small in churn-turbulent flow. Additionally, the effect of distributors on the estimated eddy viscosity was found to be non-negligible.

6. Based on the TKE measured by CARPT and the model presented by Ohnuki and Akimoto (2001), the relative contributions of the shear-induced and bubble-induced turbulence on the effective eddy viscosity were evaluated. It was found that when the correlation of Wilkinson (1991) is used to estimate the bubble size (which is required as an input in the model of Ohnuki and Akimoto (2001)), the comparison of the computed kinematic eddy viscosity with the kinematic eddy viscosity estimated from the CARPT data was fairly reasonable. In addition, the

contribution of bubble-induced turbulence to the effective kinematic eddy viscosity was found to be less than 10%.

7. The pressure effect on liquid recirculation has been translated into an empirical correction factor to the correlation of Zehner (1986) for predicting the centerline axial liquid velocity. The modified correlation is expressed as

$$u_{o,pred} = 0.737 g^{1/3} D_c^{1/3} U_g^{1/3} \left(\frac{\rho_g}{\rho_{g,atm}} \right)^{0.128}$$

which is valid for a column diameter of 16.2 cm, with operating pressure in the range of 1-10 atm and U_g in the range of 30-45 cm/s.

It is worth mentioning that the shape of the profiles of all the flow quantities reported in this chapter are almost identical to those reported by Degalessan (1997), which were generated from experiments in various diameter columns at lower superficial gas velocities and only at atmospheric pressure. This indicates that the mechanism of flow recirculation and turbulence generation and dissipation is very similar in the range of pressure, superficial gas velocity, column diameter and distributor investigated by the CARPT technique in this work. However, further experimentation along with bubble size measurements are needed for fully comprehending and better explaining some of the hydrodynamic phenomena observed in this study.

Chapter 6. Conclusions and Recommendations

To recapitulate, the overall objective of this study is to provide hydrodynamic data at ***high-pressure*** and at ***high superficial gas velocity*** using different ***distributors***. Such data is needed to advance the understanding and knowledge of bubble column hydrodynamics operated at such conditions. Hence, the specific goals of this work are:

- To measure radial gas holdup distribution in the fully developed region of flow using non-invasive Computed Tomography technique, at three different axial locations of the column at high pressure and high U_g conditions using different distributors.
- To determine liquid recirculation velocity profiles and turbulent parameters (Reynolds stresses, turbulent kinetic energy, turbulent eddy diffusivities, etc.), via Computer Automated Radioactive Particle Tracking (CARPT).
- To evaluate the effect of pressure and sparger design on the above-mentioned parameters at high superficial gas velocity.

An elaborate set of systematic experimental investigation was carried out to meet the objectives set for this study. The results for each of the above specific goals were previously discussed in Chapter 4 and Chapter 5. In this chapter, the main conclusions from this work are presented in the first section. Following this, the recommendations for possible future work are outlined.

6.1. Conclusions

The conclusions from this work are as follows:

1. Deep in the churn turbulent flow regime at atmospheric pressure, there are insignificant effects of the distributor and of axial locations along the bubble column on radial gas holdup profile and cross-sectional averaged gas holdup at atmospheric pressure. At higher pressure, some small distributor effects on gas holdup persist.
2. Gas holdup in churn-turbulent flow increases with pressure. The transition flow regime is shifted to higher superficial gas velocity.
3. With an increase in superficial gas velocity at constant pressure, gas holdup increases and gas holdup radial profile becomes almost parabolic.
4. Some of the radial gas holdup profiles measured using Computed Tomography technique in this work were used to develop a correlation for predicting radial gas holdup profile (Wu *et al.*, 2001), as shown below.

$$\varepsilon_g(\xi) = \tilde{\varepsilon}_g \left(\frac{m+2}{m} \right) \left(1 - c\xi^m\right)$$

where $m = 2.188\times10^3\, Re_G^{-0.598}\, Fr^{0.146} Mo_L^{-0.004}$ and $c = 4.32\times10^{-2}\, Re_G^{0.249}$

5. Similar to gas holdup, there is minimal effect of distributors on liquid recirulation deep in churn-turbulent flow at atmospheric pressure and marginal distributor effect at higher pressure. This confirms that gas holdup drives liquid recirculation and therefore, similar gas holdup structure implies similar liquid recirculation.
6. Liquid recirculation along with turbulent stresses increase with superficial gas velocity.
7. Liquid recirculation increases with pressure. As superficial gas velocity increases, the pressure effect on liquid recirculation decreases.
8. The centerline velocity obtained from this study is used to modify a correlation developed by Zehner (1986) to include the effect of pressure on centerline velocity (as shown below).

$$u_{o,pred} = 0.737 g^{1/3} D_c^{1/3} U_g^{1/3} \left(\frac{\rho_g}{\rho_{g,atm}} \right)^{0.128}$$

9. The turbulent normal stress in the axial direction is at least two times higher than the normal stresses in the radial and azimuthal directions.

10. With an increase in pressure, the level of liquid phase turbulence decreases due to a reduction of bubble size at higher pressure, leading to fewer and less energetic bubble breakup events and a reduced vortical (helical) motion.
11. An expression representing the radial profile of eddy viscosity is developed from measured shear stress and velocity gradient profile, and is shown to fit the data well.
12. Analysis of the measured eddy viscosity using the model of Ohnuki and Akimoto (2001) shows a relatively small contribution of the bubble-induced turbulence to the effective eddy viscosity as compared to that of the shear-induced turbulence.
13. Considering similar distributor configuration, the Lagrangian integral time scales increase with an increase in percentage open area of the distributor. Additionally, with an increase in pressure, the Lagrangian integral time scales increase.
14. The turbulent length scales in the radial direction are an order of magnitude smaller than in the axial direction.
15. The cross-sectional averaged turbulent axial eddy diffusivity is at least four times higher than the remaining components of the diffusivity tensor. Additionally, the cross-sectional averaged turbulent eddy diffusivities decrease with an increase in pressure or with a decrease in superficial gas velocity.

6.2. Recommendations

Suggestions for extending the work conducted in different parts of this study are listed below:

1. A vital information needed to fully comprehend the hydrodynamic observations from this study is the bubble size. Therefore, measurement of bubble size distributions, for example by using an optical probe at different pressures and superficial gas velocities would yield valuable information to further confirm the results obtained in this study.

2. Since the investigation in this study was restricted to only one column of 6.4" diameter, and since scale effects are known to be important in bubble column design (Degaleesan, 1997), a natural extension of this study would be to investigate hydrodynamics in a larger diameter column. Since a CT/CARPT database exist for an 18" diameter column for air-water and air-drakeol systems at atmospheric pressure conditions (Degaleesan, 1997; Chen *et al.*, 1998; Chen *et al.*, 1999), it is recommended that further experimentation be carried out in a 18" diameter column with water and drakeol as the liquid phases, and operating conditions representative of the ones used in this study.
3. An ad hoc criterion for choosing the threshold for wavelet filtering was used in this study so as to eliminate kinks observed in the profiles of the correlation coefficients. Therefore, it may be possible to develop a more robust filtering algorithm to filter the white noise from instantaneous position data employing a more fundamentally based criterion.
4. Results from the chaos analysis of the position-time series data from CARPT could be sought and compared against similar analysis of pressure fluctuations data to understand the chaotic nature of the bubble column hydrodynamic (Letzel, 1997) at high pressure and superficial gas velocity.
5. Few studies exist in the literature that have employed CFD to predict bubble column hydrodynamics under churn-turbulent flow conditions investigated in this study. It would therefore be interesting to perform CFD calculations of the hydrodynamics under the operating conditions of this study so as to not only benchmark the capabilities of the commercial CFD codes, but also to provide directions for the future improvements of the existing hydrodynamic models.

Appendix A. One-Dimensional Liquid Recirculation Model

The starting point in the derivation of the one-dimensional model for the radial profile of the time averaged axial liquid velocity is the two-fluid model presented below. The model equations are the result of the ensemble-averaged approach of Drew and Passman (1998). Here, the subscript '*l*' denotes the continuous liquid/slurry phase, whereas the subscript '*g*' denotes the dispersed gas phase, and both phases are considered incompressible.

Equations of Continuity

Liquid
$$\frac{\partial \varepsilon_l}{\partial t} + \nabla.\left(\varepsilon_l \boldsymbol{u}_l\right) = 0 \tag{A-1}$$

Gas
$$\frac{\partial \varepsilon_g}{\partial t} + \nabla.\left(\varepsilon_g \boldsymbol{u}_g\right) = 0 \tag{A-2}$$

Momentum Equations

Liquid
$$\rho_l \varepsilon_l \left(\frac{\partial \boldsymbol{u}_l}{\partial t} + \boldsymbol{u}_l.\nabla \boldsymbol{u}_l \right) = \rho_l \varepsilon_l \boldsymbol{g} - \varepsilon_l \nabla p - \left(\boldsymbol{M}_d + \boldsymbol{M}_{vm}\right) - \nabla.\left(\varepsilon_l \boldsymbol{\tau}_l\right) \tag{A-3}$$

Gas
$$\rho_g \varepsilon_g \left(\frac{\partial \boldsymbol{u}_g}{\partial t} + \boldsymbol{u}_g.\nabla \boldsymbol{u}_g \right) = \rho_g \varepsilon_g \boldsymbol{g} - \varepsilon_g \nabla p + \left(\boldsymbol{M}_d + \boldsymbol{M}_{vm}\right) - \nabla.\left(\varepsilon_g \boldsymbol{\tau}_g\right) \tag{A-4}$$

In the momentum balance equations, $\boldsymbol{\tau}_l$ and $\boldsymbol{\tau}_g$ are the stress tensors representing the normal and shear stresses in the liquid and gas phases, respectively, $\boldsymbol{M}_{\mathrm{d}}$ is the drag force term, and $\boldsymbol{M}_{\mathrm{vm}}$ is the virtual mass term that arises due to the relative acceleration of the two phases (Drew and Passman, 1998). The mathematical representation of these terms is shown in Equations (A-5) to (A-7).

$$\boldsymbol{M}_d = \frac{6\varepsilon_l \varepsilon_g}{\pi d_b^3} \boldsymbol{F}_d \tag{A-5}$$

$$\boldsymbol{F}_d = \frac{1}{8} \rho_l \pi d_b^2 C_D \left| \boldsymbol{u}_l - \boldsymbol{u}_g \right| \left(\boldsymbol{u}_l - \boldsymbol{u}_g \right) \tag{A-6}$$

$$\boldsymbol{M}_{vm} = \frac{1}{2} \varepsilon_l \varepsilon_g C_{vm} \left(\frac{D\boldsymbol{u}_l}{Dt} - \frac{D\boldsymbol{u}_g}{Dt} \right) \tag{A-7}$$

In the above equations, C_D is the drag coefficient and for sufficiently contaminated systems it is represented by Equation (A-8) of Tomiyama *et al*. (1995).

$$C_D = max\left[\overbrace{\frac{24}{Re}\left(1 + 0.15\, Re_b^{0.687}\right)}^{C_{D,2}}, \overbrace{\frac{8}{3}\frac{Eo}{Eo+4}}^{C_{D,1}} \right] \tag{A-8}$$

where, $Eo = g\left(\rho_l - \rho_g\right) d_b^2 / \sigma$ is the Eotvos number based on the bubble diameter and the liquid surface tension, and $Re_b = d_b \left| \boldsymbol{u}_l - \boldsymbol{u}_g \right| / \nu_l^m$ is the bubble Reynolds number. C_{vm} on the other hand is the virtual mass coefficient that has been discussed by Pan and Dudukovic' (1999).

$$C_{vm} = 1 + 3.32\varepsilon_g + O(\varepsilon_g^2) \tag{A-9}$$

In the well-developed flow region of the column, it has been extensively observed that the flow in the time-averaged sense is axisymmetric with only the axial velocities

being non-zero (Degaleesan, 1997). Hence, the time-averaged liquid flow pattern is represented by a single radial profile of the axial velocity, which is confirmed by the holdup profile database available at CREL via CT; and the liquid velocity profile database via CARPT (Devanathan *et al*., 1990; Devanathan, 1991; Kumar *et al.*, 1995; Kumar *et al.*, 1997; Degaleesan, 1997; Chen *et al*., 1998).

Under these conditions, the equations of continuity for both the phases (Equations (A-1) and (A-2)) are identically satisfied. In addition, the left hand side of the momentum equations for both the gas and liquid phases becomes zero, and so does the virtual mass term. Finally, due to no flow in the radial and azimuthal directions, the pressure is assumed to be independent of the radial and azimuthal coordinates, and the pressure gradient term in the momentum equations reduces to *dp/dz*.

After retaining the non-zero gradients and velocity components in the momentum equations for the two phases, one gets the following simplified equations.

$$\textit{Liquid} \qquad 0 = -\rho_l \varepsilon_l g - \varepsilon_l \frac{dp}{dz} - M_d - \frac{1}{r}\frac{d}{dr}\left(r\varepsilon_l \left\{\tau^m_{l,rz} + \tau^t_{l,rz}\right\}\right) \tag{A-10}$$

$$\textit{Gas} \qquad 0 = -\rho_g \varepsilon_g g - \varepsilon_g \frac{dp}{dz} + M_d - \frac{1}{r}\frac{d}{dr}\left(r\varepsilon_g \left\{\tau^m_{g,rz} + \tau^t_{g,rz}\right\}\right) \tag{A-11}$$

where

$$\tau^m_{l,rz} = -\mu^m_l \frac{du_l}{dr} \tag{A-12}$$

$$\tau^m_{g,rz} = -\mu^m_g \frac{du_g}{dr} \tag{A-13}$$

$$\tau^t_{l,rz} = \rho_l \overline{u'_{l,r}\, u'_{l,z}} \tag{A-14}$$

$$\tau^t_{g,rz} = \rho_g \overline{u'_{g,r}\, u'_{g,z}} \tag{A-15}$$

Since $\mu^m_g \approx O\left(10^{-1}\right)\mu^m_l$ and $\rho_g \approx O\left(10^{-1} - 10^{-3}\right)\rho_l$, one can neglect both the molecular as well as the turbulent shear stresses in the gas phase as compared to those in the liquid phase. Therefore, upon addition of Equations (A-10) and (A-11) one obtains

$$0 = -\left(\rho_g \varepsilon_g + \rho_l \varepsilon_l\right) g - \frac{dp}{dz} - \frac{1}{r}\frac{d}{dr}\left(r\varepsilon_l \left\{ \overbrace{\tau^m_{l,rz} + \tau^t_{l,rz}}^{\tau_{l,rz}} \right\} \right) \tag{A-16}$$

In the above equation, the superscripts "*m*" and "*t*" refer to molecular (viscous) and turbulent contributions, and ε_g is the radial gas holdup profile, which is represented in terms of the power law function given by Equation (A-17) which fits well the available experimental data (Kumar, 1994; Kumar *et al*., 1995).

$$\varepsilon_g(\xi) = \bar{\varepsilon}_g \left(\frac{m+2}{m+2-2c} \right)\left(1 - c\xi^m\right) \tag{A-17}$$

where, ξ = *r/R* is the dimensionless radius. Substituting for the radial gas holdup (Equation (A-17)) in Equation (A-16) and using $p' = -dp/dz/\rho_l g$, one gets, on integrating Equation (A-16) with boundary condition $\tau_{l,rz} = 0$ at $\xi = 0$,

$$\left(1-\varepsilon_g\right)\tau_{l,rz} = \frac{\rho_l g R \xi}{2}\left(p' - 1\right) + \frac{\left(\rho_l - \rho_g\right) g R \bar{\varepsilon}_g \xi}{2} \frac{\left(m+2-2c\xi^m\right)}{\left(m+2-2c\right)} \tag{A-18}$$

After anticipating a downward maximum liquid velocity at dimensionless radius $\xi = \lambda$, one assigns $\tau_{l,rz}\big|_{\xi=\lambda} = 0$. Applying this condition to Equation (A-18) allows one to eliminate *p'* by Equation (A-19) and yields Equation (A-20) for $\tau_{l,rz}$.

$$p' = 1 - \bar{\varepsilon}_g \left(\frac{\rho_l - \rho_g}{\rho_l} \right)\left(\frac{m+2-2c\lambda^m}{m+2-2c} \right) \tag{A-19}$$

$$\tau_{l,rz}(\xi) = \frac{\rho_l (1-\gamma) g\, R\, c\, \bar{\varepsilon}_g\, \xi\, \lambda^m}{\left(m+2-2c\right)\left(1-\varepsilon_g(\xi)\right)}\left(1 - \left(\frac{\xi}{\lambda}\right)^m\right) = \rho_l g R \beta(\xi) \tag{A-20}$$

$$\textit{where}\quad \beta(\xi) = \frac{(1-\gamma) c\, \bar{\varepsilon}_g\, \xi\, \lambda^m}{\left(m+2-2c\right)\left(1-\varepsilon_g(\xi)\right)}\left(1 - \left(\frac{\xi}{\lambda}\right)^m\right) \quad \textit{and} \quad \gamma = \frac{\rho_g}{\rho_l} \tag{A-21}$$

To obtain the liquid velocity profile from the above shear stress profile, a constitutive relationship (closure) is needed relating the turbulent shear stresses to the mean liquid velocity profile. The simplest closure in terms of turbulent kinematic viscosity is employed in Equation (A-22a) and in terms of mixing length in equation (A-22b).

$$\tau_{l,rz}(r) = -\rho_l \left(\nu_l^m + \nu_l^t\right)\frac{du_l}{dr} \tag{A-22a}$$

$$\tau_{l,rz}(r) = -\rho_l \nu_l^m \frac{du_l}{dr} - \rho_l l^2 \left|\frac{du_l}{dr}\right| \frac{du_l}{dr} \tag{A-22b}$$

Using Boussinesq's hypothesis (1896), combined with the eddy viscosity is used to describe liquid turbulence, the Reynolds shear stress, Equation (A-22a) can described as shown in Equation (A-23a).

$$\tau_{l,rz} = \begin{cases} -\rho_l \dfrac{(\nu_m + \nu_t)}{R}\dfrac{du_l}{d\xi} & for\ \xi \le \lambda \\ -\rho_l \dfrac{\nu_m}{R}\dfrac{du_l}{d\xi} & for\ \xi > \lambda \end{cases} \tag{A-23a,b}$$

If the Prandtl's mixing length is used in Equation (A-22b) for providing the constitutive equations for the turbulent shear stress, then the expression for the shear stress is shown in Equation (A-24).

$$\tau_{l,rz} = \begin{cases} \rho_l \left[-\dfrac{\nu_m}{R}\dfrac{du_l}{d\xi} + \dfrac{l^2(\xi)}{R^2}\left(\dfrac{du_l}{d\xi}\right)^2 \right] & for\ \xi \le \lambda \\ -\rho_l \dfrac{\nu_m}{R}\dfrac{du_l}{d\xi} & for\ \xi > \lambda \end{cases} \tag{A-24a,b}$$

Using Equations (A-23) or (A-24) together with Equation (A-20), Equations (A-25) or (A-26) are derived, respectively, depending on which closure is used.

$$\frac{du_l}{d\xi} = \begin{cases} -\dfrac{gR^2}{(\nu_m + \nu_t)}\beta(\xi) & for\ \xi \le \lambda \\ -\dfrac{gR^2}{\nu_m}\beta(\xi) & for\ \xi > \lambda \end{cases} \qquad \text{(A-25a,b)}$$

$$\frac{du_l}{d\xi} = \begin{cases} \dfrac{\nu_m R}{2l^2}\left[1 - \sqrt{1 + \dfrac{4gRl^2}{\nu_m^2}\beta(\xi)}\right] & for\ \xi \le \lambda \\ -\dfrac{gR^2}{\nu_m}\beta(\xi) & for\ \xi > \lambda \end{cases} \qquad \text{(A-26a,b)}$$

The needed boundary condition is that at the wall, $\xi = 1$, $u_l = 0$. The above equations require either eddy viscosity or mixing length, as well as the radial gas holdup profile of the form shown in Equation (A-17) as input. With these provided, the model is solved as follows.

Solution Procedure

The boundary conditions to be used for the solution of the above equations are $u_l = 0$ at $\xi = 1$, and $du_l/d\xi = 0$ at $\xi = 0$. Superimposed on this is the constraint that the overall continuity for the liquid phase must be satisfied (Note that the integral is split at $\xi = \lambda$ which is not the point of inversion of the liquid velocity profile, rather the point of maximum downward liquid velocity).

$$2\int_{\xi=0}^{\xi=\lambda}\left\{1-\varepsilon_g(\xi)\right\}u_l(\xi)\xi\, d\xi + 2\int_{\xi=\lambda}^{\xi=1}\left\{1-\varepsilon_g(\xi)\right\}u_l(\xi)\xi\, d\xi = U_{L,sup} \qquad \text{(A-27)}$$

It is this constraint of overall liquid continuity, as expressed by Equation (A-27), that allows one to iterate on λ to obtain a converged solution. The converged value of λ by Equation (A-28) determines *p'*. The numerical scheme for the solution is as follows.

- Guess a value for λ (generally 0.9 is a good starting point)

- Calculate $u_{l,\lambda}$ by integrating Equation (A-25b) or (A-26b) from the boundary at $\xi = 1$ to $\xi = \lambda$

$$u_{l,\lambda} = -\frac{gR^2}{\nu_l^m}\int_{\xi=1}^{\xi=\lambda}\beta(\xi)d\xi \tag{A-28}$$

- To obtain the velocity of the liquid phase in the rest of the domain, integrate Equations (A-25a) or (A-26a) from $\xi = \lambda$ towards the column center using $u_{l,\lambda}$.

$$u_l = u_{l,\lambda} + \frac{gR^2}{2(\nu_m + \nu_t)}\int_{\xi=\xi}^{\xi=\lambda}\beta(\xi)d\xi \tag{A-29}$$

$$u_l = u_{l,\lambda} - \frac{\nu_m R}{2l^2}\int_{\xi=\xi}^{\xi=\lambda}\left[1-\sqrt{1+\frac{4l^2}{\nu_m^2}\left(\frac{gR}{2}\right)\beta(\xi)}\right]d\xi \tag{A-30}$$

- Substitute the obtained radial profile of the axial liquid velocity into Equation (A-27). If Equation (A-27) is satisfied within the tolerance criterion, then the converged solution has been obtained. If the tolerance criterion is not met, then λ is incremented sequentially until convergence is achieved. A word of caution is in order at this point. The function defined by Equation (A-25) or (A-26) could have steep gradients and proper care must be taken while integrating to obtain an accurate solution.

One should note that once the liquid velocity profile is obtained by the above procedure, the pressure gradient $\frac{dP}{dz}$ can be calculated from Equation (A-19) (refer to Equation (A-31)).

$$\frac{dP}{dz} = -\rho_l g\left\{1-\bar{\varepsilon}_g\left(\frac{\rho_l-\rho_g}{\rho_l}\right)\left(\frac{m+2-2c\lambda^m}{m+2-2c}\right)\right\} \tag{A-31}$$

Appendix B. Optimized Shear Stress Profile Using Fitted Eddy Viscosity Profile

In this appendix, the fitting of the shear stress profiles using the suggested empirical form of the eddy viscosity profiles is discussed. Briefly, Equation (5-8) is obtained as closure and by assuming negligible molecular viscosity in the region of the collumn between the center and the radius of maximum downflow, λR (i.e. $\xi \leq \lambda$).

$$\tau_{l,rz} = -\frac{\rho_l \nu_t}{R}\frac{du_l}{d\xi} \tag{5-8}$$

The shear stress in *r*-*z* direction, τ_{rz}, and the radial gradient of the axial liquid velocity are obtained from CARPT measurements and the turbulent eddy viscosity profile, ν_t, is assumed to have the form represented by Equation (5-9). This empirical form is similar to that used for the radial gas holdup profile, which has been shown to fit the experimental gas holdup data well. Since liquid recirculation is strongly dependent on the gradient of the radial gas holdup and closure for liquid turbulence, it was conjectured that a form for ν_t similar to radial gas holdup profile would offer the best possibility of fitting the CARPT data. It should, however, be mentioned that other forms for ν_t like a constant eddy viscosity ($k = \alpha = 0$) or a linearly varying form ($k = \alpha = 1$) were also tried but did not fit the experimental data well at all operating conditions. Therefore, the form presented in Equation (5-9) was used and found to fit the experimental data very well as shown later in this section.

$$\nu_t = \nu_{t0}\,(1.0 - k\xi^{\alpha}) \qquad (5\text{-}9)$$

where ν_{t0}, k and α are fitting parameters. For each operating condition, the parameters are selected by fitting the shear stress profile as shown in Equation (5-8).

Figures B1 to B9 displays the fitted and experimental shear stress in *r-z* direction for all operating conditions. The fitted shear stress, τ_{rz}, is obtained by substituting the optimized turbulent eddy viscosity profile of Equation (5-9) to Equation (5-8). As evident from all the figures, the shear stress profiles are almost identical, i.e., the suggested viscosity form achieves excellent fits.

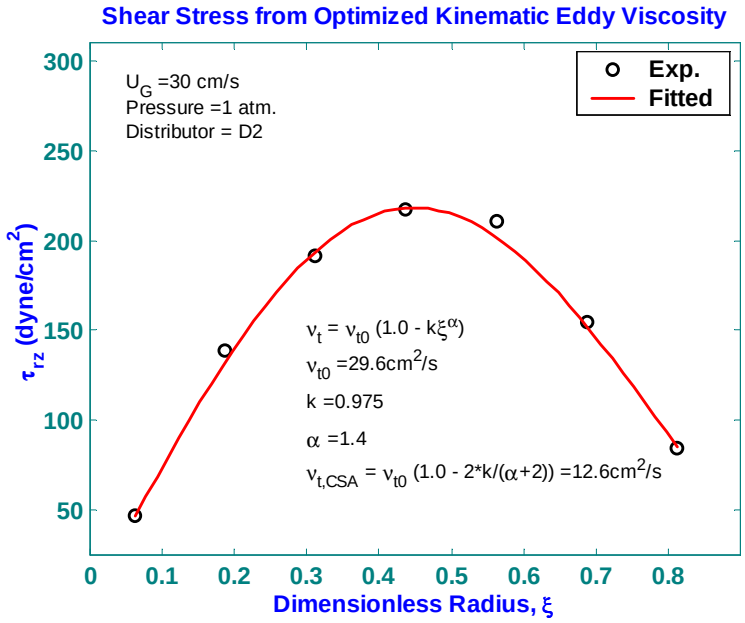

Figure B1. Comparison of experimental and optimized shear stress profile for uniform perforated plate distributor, D2 (0.1%, 2.6 mm) at a superficial gas velocity of 30 cm/s at atmospheric pressure.

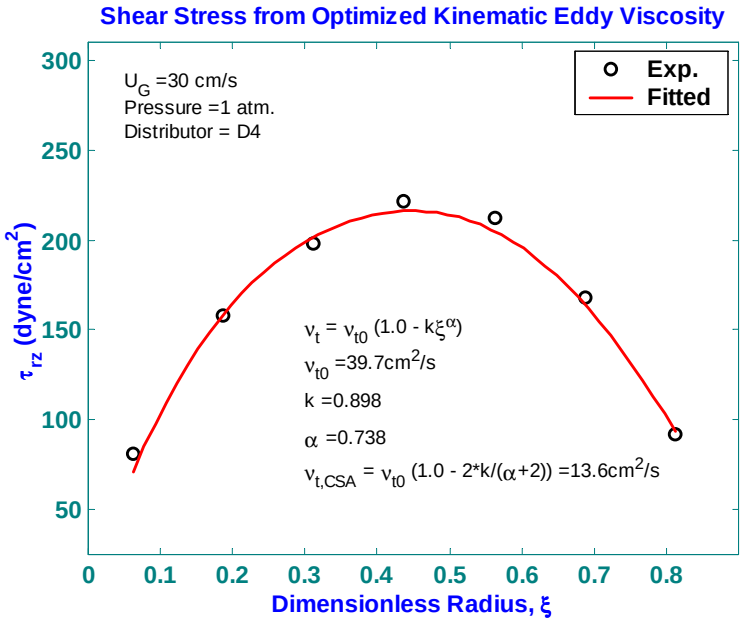

Figure B2. Comparison of experimental and optimized shear stress profile for uniform perforated plate distributor, D4 (0.15%, 0.5 mm) at a superficial gas velocity of 30 cm/s at atmospheric pressure.

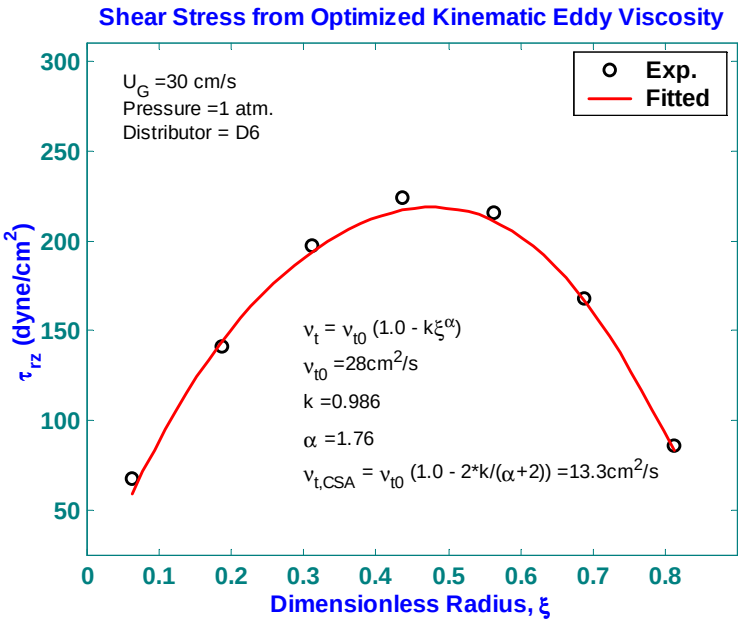

Figure B3. Comparison of experimental and optimized shear stress profile for uniform perforated plate distributor, D6 (1.0%, 1.25 mm) at a superficial gas velocity of 30 cm/s at atmospheric pressure.

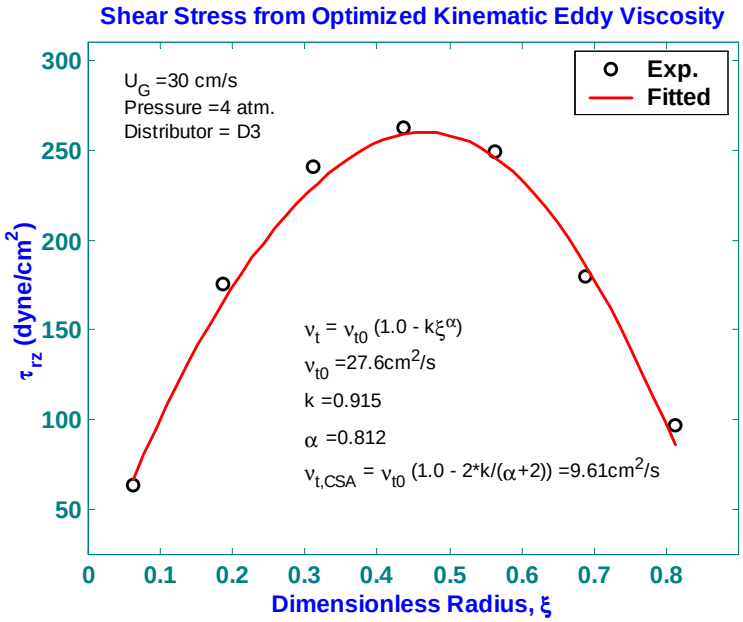

Figure B4. Comparison of experimental and optimized shear stress profile for uniform perforated plate distributor, D3 (0.1%, 2.6 mm) at a superficial gas velocity of 30 cm/s at P = 4 atm.

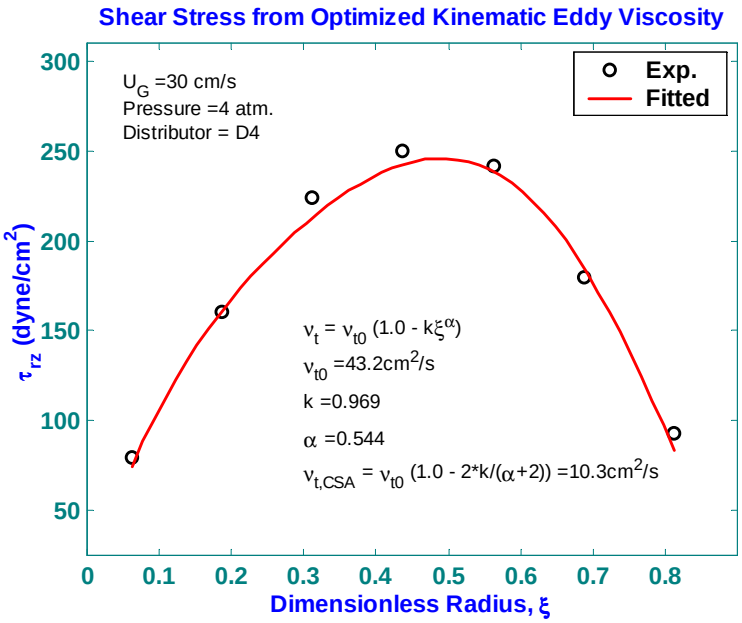

Figure B5. Comparison of experimental and optimized shear stress profile for uniform perforated plate distributor, D4 (0.15%, 0.5 mm) at a superficial gas velocity of 30 cm/s at P = 4 atm.

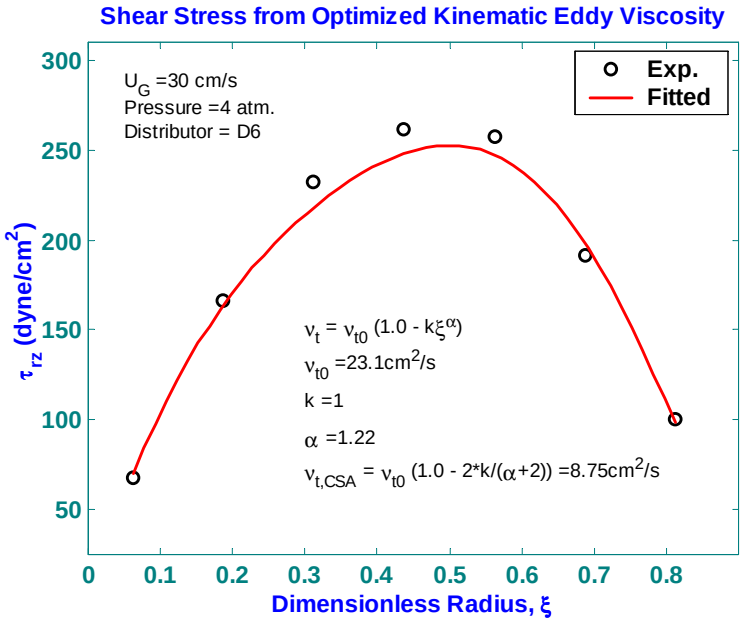

Figure B6. Comparison of experimental and optimized shear stress profile for uniform perforated plate distributor, D6 (1.0%, 1.25 mm) at a superficial gas velocity of 30 cm/s at P = 4 atm.

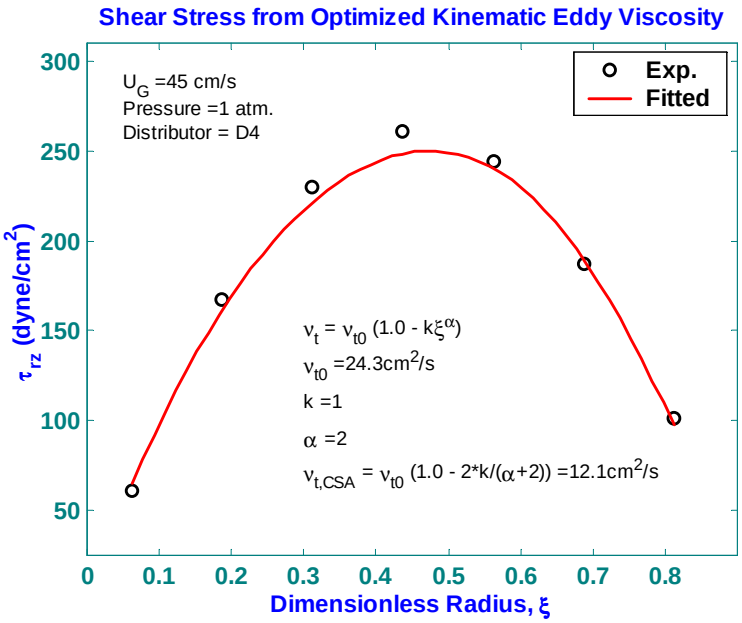

Figure B7. Comparison of experimental and optimized shear stress profile for uniform perforated plate distributor, D4 (0.15%, 0.5 mm) at a superficial gas velocity of 45 cm/s at atmospheric pressure.

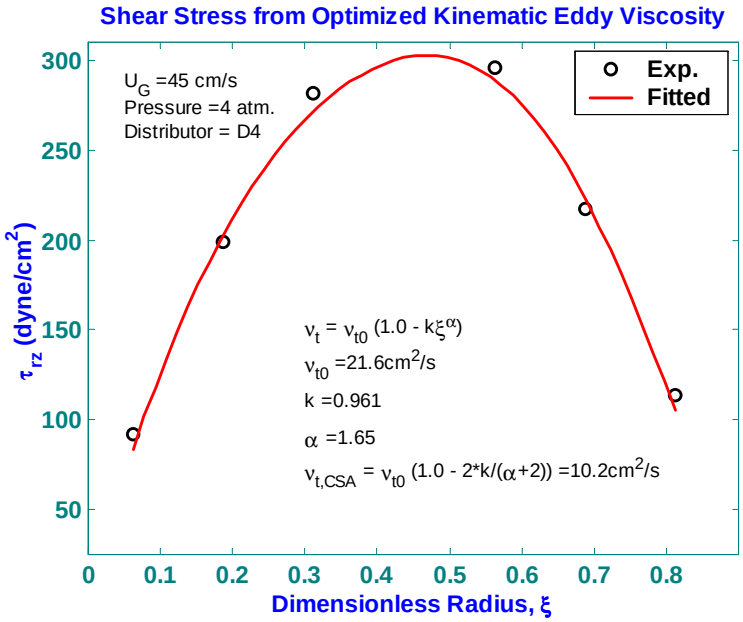

Figure B8. Comparison of experimental and optimized shear stress profile for uniform perforated plate distributor, D4 (0.15%, 0.5 mm) at a superficial gas velocity of 45 cm/s at P = 4 atm.

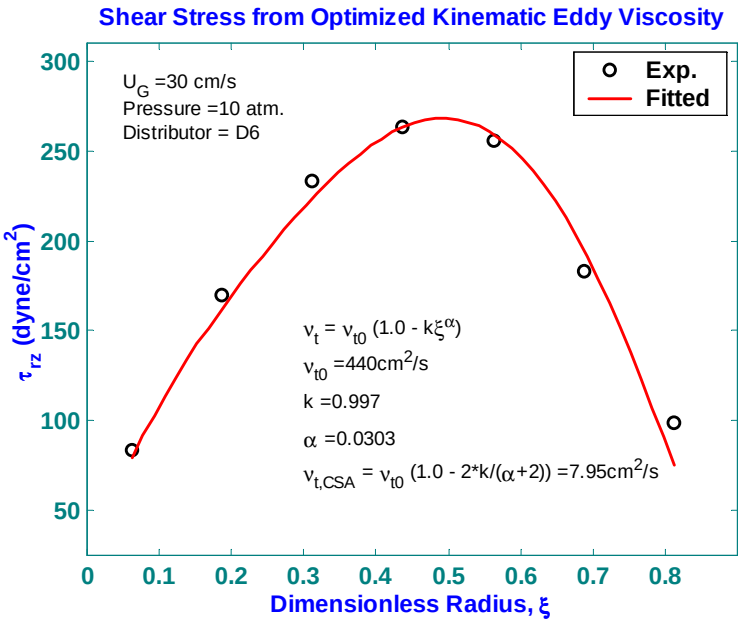

Figure B9. Comparison of experimental and optimized shear stress profile for uniform perforated plate distributor, D6 (1.0%, 1.25 mm) at a superficial gas velocity of 30 cm/s at P = 10 atm.

Appendix C. Axial Variation of the Eddy Diffusivity Tensor

Figure C1 shows the effect of axial averaging of the correlation coefficients discussed in Chapter 5 on the computed eddy diffusivity tensor. The operating condition for this data set was P = 1 atm and U_g = 30 cm/s using the perforated plate distributor D4. While Figures C1a to C1f shown in the left column were evaluated from axially averaged data, Figures C1g to C1l shown in the right column were evaluated at each of the z levels in the middle portion of the column and subsequently the means and standard deviations of all six components of the eddy diffusivity tensor were calculated along the axial direction. The bars shown in the figures in the right column thus represent ±1 standard deviation around mean. It is clear that the effect of axial averaging on D_{rr}, D_{zz}, $D_{\theta\theta}$ and D_{rz} is present but acceptable, while it is substantial for $D_{r\theta}$ and $D_{z\theta}$ with large standard deviations. Degaleesan (1997) reported that the off-diagonal components of the eddy diffusivity tensor are zero. While such is not the case at higher superficial gas velocities investigated in this study due to the large standard deviations on $D_{r\theta}$ and $D_{z\theta}$, these two components are not reported for other operating conditions. Additionally, because of no substantial effect of axial averaging, only the D_{rr}, D_{zz}, $D_{\theta\theta}$ and D_{rz} profiles obtained from averaged data are presented in Chapter 5.

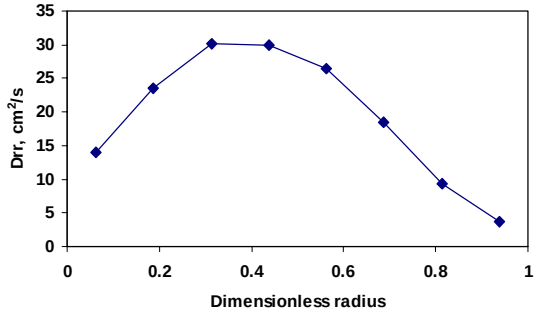
Drr, cm²/s
Dimensionless radius

(a)

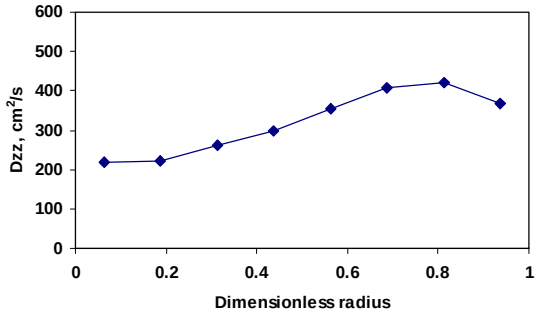
Dzz, cm²/s
Dimensionless radius

(b)

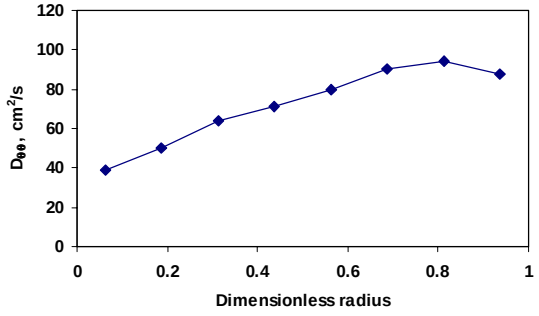
D₀₀, cm²/s
Dimensionless radius

(c)

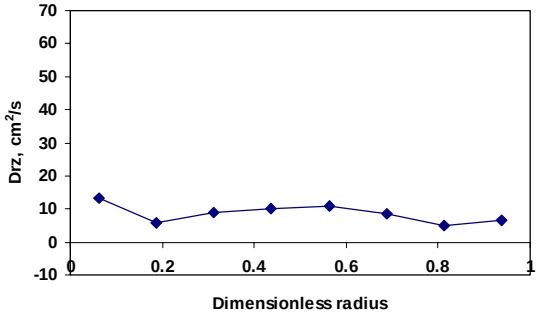
Drz, cm²/s
Dimensionless radius

(d)

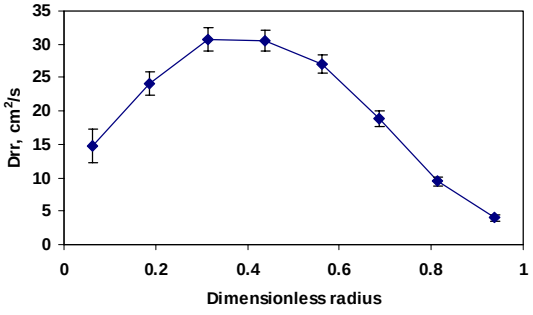
Drr, cm²/s
Dimensionless radius

(g)

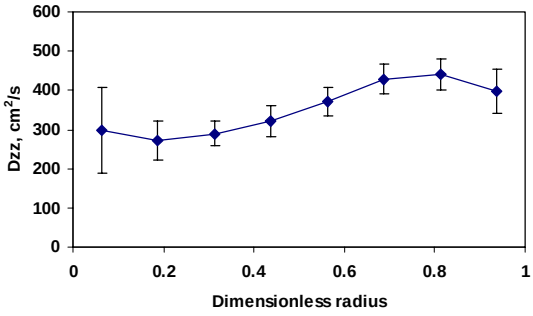
Dzz, cm²/s
Dimensionless radius

(h)

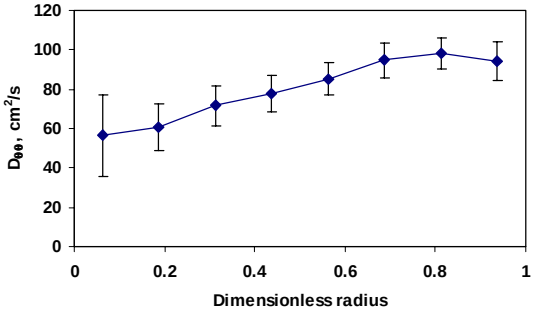
D₀₀, cm²/s
Dimensionless radius

(i)

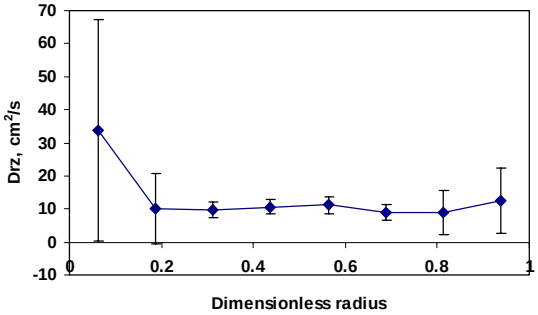
Drz, cm²/s
Dimensionless radius

(j)

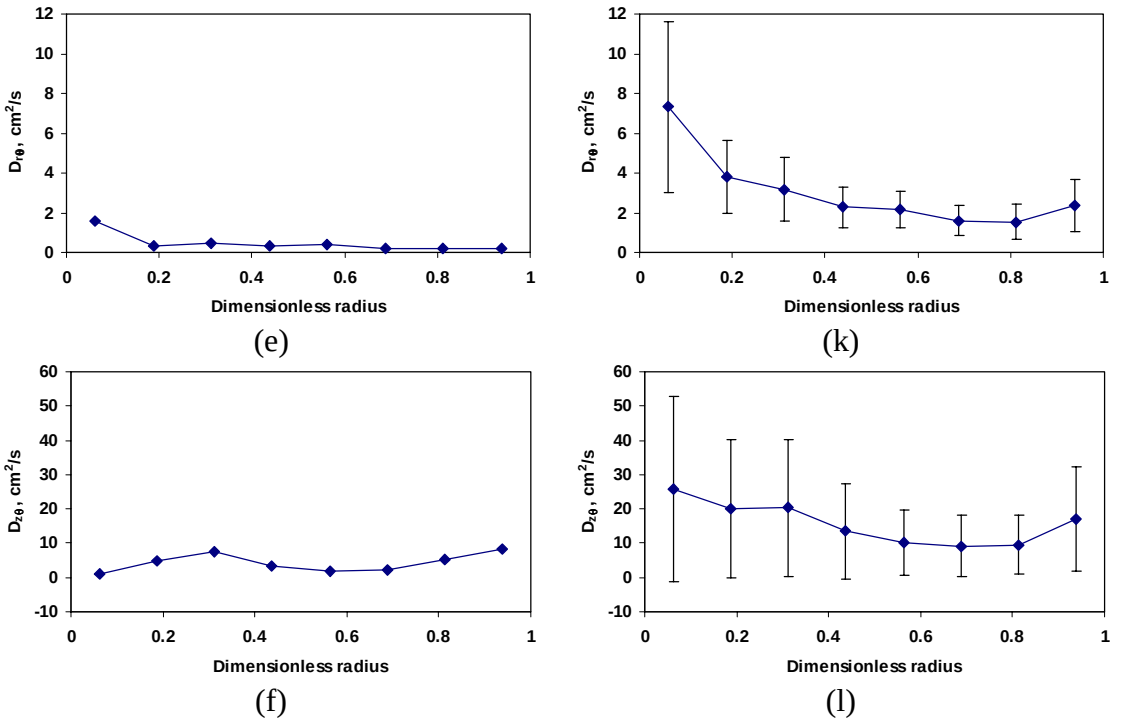

Figure C1. Radial profiles of eddy diffusivities (a)-(f) before and (g)-(l) after axially averaging of data obtained using distributor D4 at P = 1 atm; U_g = 30 cm/s.

Appendix D. Eddy Diffusivity

As mentioned earlier in Chapter 5, Degaleesan (1997) obtained the eddy diffusivity formulation, which is symmetric. However, the formulation of Durbin and Petterson Reif (2001) showed asymmetric eddy diffusivity tensor (refer to Equation (5-35).

$$D_{ij} = C_c \frac{k}{\varepsilon}\left(\overline{u_i' u_j'} - D_{kj}\frac{\partial U_i}{\partial x_k}\right) \tag{5-35}$$

where C_c is a constant and reported to vary in the range 0.11-0.20 and a commonly used value is 0.15. In this appendix, a comparison of the eddy diffusivities computed using Degaleesan (1997) and Durbin and Petterson Reif (2001) are made using the data obtained from uniform perforated plate, D4 (0.15% POA, d_o = 0.5 mm). For this case, to satisfy the overall liquid continuity as discussed in Section 5.11, a C_c value of 0.65 was needed and has been used to evaluate the diffusivities based on the formulation of Durbin and Petterson Reif (2001).

Figure D1 shows the comparison between the two methods of calculating eddy diffusivity tensor. As clearly seen from Figure D1, there exists a discrepancy in the values obtained using both methods. This discrepancy could partly arise because of the assumption that is made to calculate the dissipation rate, ε shown in Equation (5-35). In this study, the dissipation rate is taken to be the upper bound, i.e., gU_g. Also, the constant C_c value is obtained by adjusting the overall liquid continuity till it is satisfied within 1%. Thus, these two factors might contribute to the difference in the trends and values seen in Figure D1.

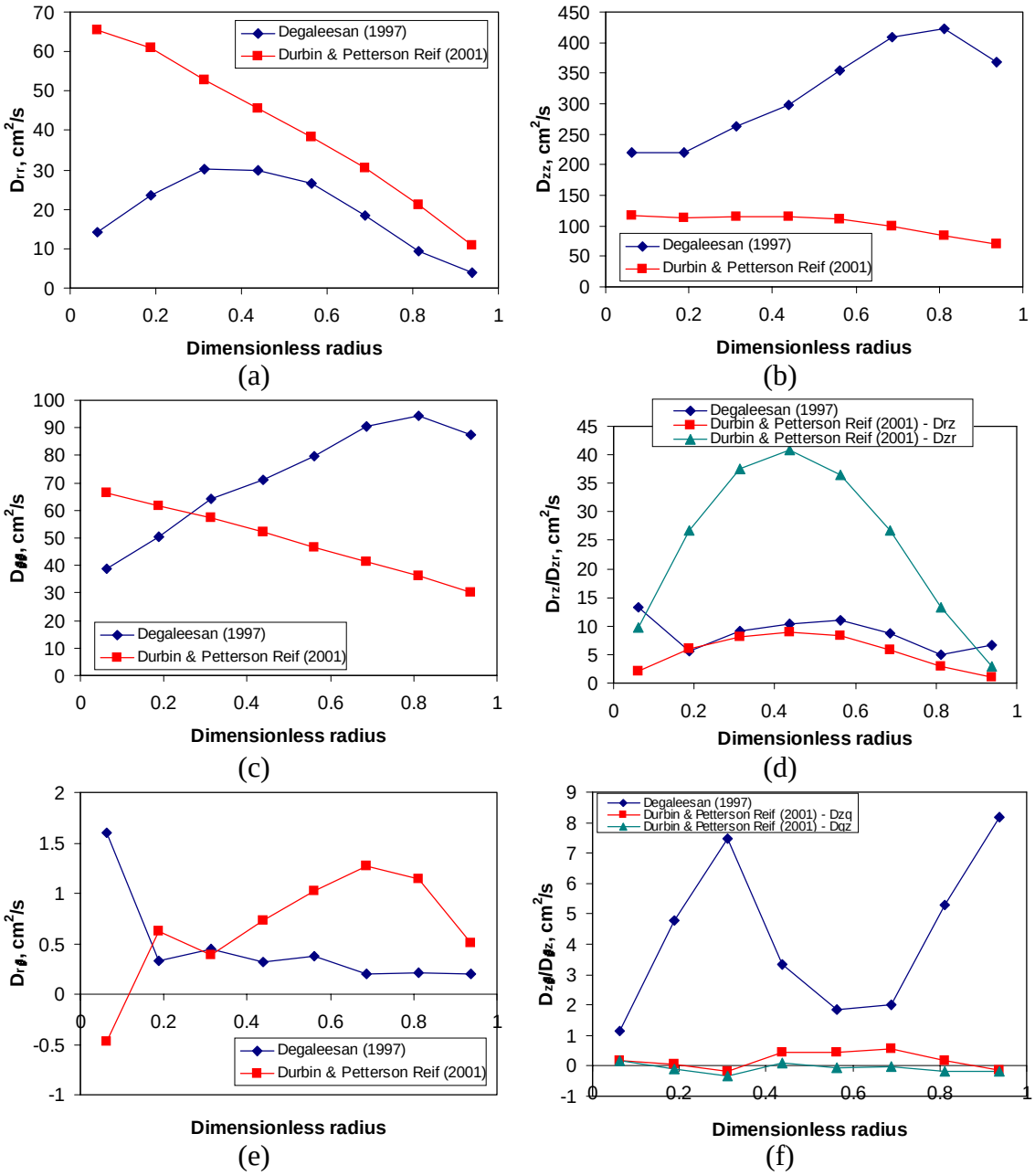

Figure D1. Comparison of radial profiles of eddy diffusivity obtained using distributor D4 at P = 1 atm; U_g = 30 cm/s: a) D_{rr}; b) D_{zz}; c) $D_{\theta\theta}$; d) D_{rz}; e) $D_{r\theta}$; f) $D_{z\theta}/D_{\theta z}$.

References

Adkins, D. R., Shollenberger, K. A., O'Hern, T. J., and Torczynski, J. R., 'Pressure Effects on Bubble Column Flow Characteristics', ANS Proceedings, 1996 National Heat Transfer Conference, **9**, 318-325 (1996).

Akita, K., and Yoshida, F., 'Gas Holdup and Volumetric Mass Transfer Coefficient in Bubble Columns', *Ind. Eng. Chem. Process Des. Dev*., **12**, 76-80 (1973).

Anderson, K. G., Rice, R. G., 'Local Turbulence Model for Predicting Circulation Rates in Bubble Column', *AIChE J*., **35** (3), 514-518 (1989).

Azbel, D., Two-Phase Flows in Chemical Engineering, Cambridge University Press, New York (1981).

Banks, R. B., and Chandrasekhara, D. V., 'Experimental Investigation of the Penetration of a High-Velocity Gas Jet Through a Liquid Surface', *J. Fluid Mechanics*, **15**, 13-34 (1963).

Barnea, D., 'A Unified Model for Predicting Flow-Pattern Transitions for the whole range of Pipe Inclinations', *Int. J. Multiphase Flow*, **13** (1), 1-12 (1987).

Beltran, F. J., Encinar, J. M., and Garcia-Araya, J. F., 'Modelling Industrial Wastewater Ozonation in Bubble Contactors. 2. Scale-up from Bench to Pilot Plant', *Ozone Science and Engineering*, **17**, 379-398 (1995).

Bendat, J. S. and Piersol, A. G., Random Data: Analysis and Measurement Procedures, John Wiley & Sons, New York (1986).

Bennett, M. A., West, R. M., Luke, S. P., Jia, X., and Williams, R. A., 'Measurement and Analysis of Flows in a Gas-Liquid Column Reactor', *Chem. Eng. Sci.*, **54**, 5003-5012 (1999).

Blenke, H., 'Loop Reactors', *Advances in Biochemical Engineering*, **13**, 121-214 (1979).

Botton, R., and Cosserat, D., 'Influence of Column Diameter and High Gas Throughputs on the Operation of a Bubble Column', *Chem. Eng. J*., **16**, 107-115 (1978).

Boussinesq, J., 'Theori de'l Ecoulement Tourbillant et Tumultueux des Liquides', *Acad. Sci. Paris*, **122**, 1298, (1896).

Boyles, A. P., Raymahasay, S., Sulidis, A. T., and Winterbottom, J. M., 'Oxidation of Aqueous Organic Pollutants in Industrial Waste Water by Heterogeneous Photocatalysis Using a Concurrent Downflow Bubble Column Contactor (CDC)', Water Pollution III: Modell., Meas. Predict., 3rd, 313-320, Eds. Wrobel, L. C., and Latinopoulos, P., Pub. Computational Mechanics Publications, Southhampton, UK (1995).

Braulick, W. J., Fair, J. R., and Lerner, B. J., 'Mass Transfer in a Sparged Contactor: Part I. Physical Mechanisms and Controlling Parameters', *AIChE J*., **11** (1), 73-79 (1965).

Broder, D. and Sommerfeld, M., 'Simultaneous Measurements of Continuous and Dispersed Phase in Bubble Columns by PDA', *Proceedings of the Ninth International Symposium on Applications of Laser Techniques to Fluid Mechanics*, Lisbon, Portugal, **2**, Paper 27.2 (1998).

Bukur, D. B., Daly, J. G., and Patel, S. A., 'Application of γ-ray Attenuation for Measurement of Gas Holdups and Flow Regime Transitions in Bubble Columns', *Ind. Eng. Chem. Res.*, **35**, 70-80 (1996).

Calderbank, P. H. and M. B., Moo-Young, 1961, 'The Continuous Phase Heat and Mass-Transfer Properties of Dispersion', *Chem. Eng. Sci.*, **16**, 39-54.

Camacho, F. G., Grima, E. M., Miron, S., Pascual, G., and Chisti, Y., 'Carboxymethyl Cellulose Protects Algal Cells Against Hydrodynamic Stress', *Enzyme and Microbial Tech.*, **29**, 602-618 (2001).

Camarasa, E., Vial, C., Poncin, S., Wild, G., Midoux, N., and Bouillard, J., 'Influence of Coalescence Behavior of the Liquid and of Gas Sparging on Hydrodynamics and Bubble Characteristics in a Bubble Column', *Chem. Eng. Process.*, **38** (4-6), 329-344, (1999).

Cartellier, A., 'Simultaneous Void Fraction Measurement, Bubble Velocity, and Size Estimate Using a Single Optical Probe in Gas-Liquid Two-Phase Flows', *Rev. Sci. Instrum.*, **63** (11), 5442-5453 (1992).

Cartellier, A., 'Optical Probes for Local Void Fraction Measurements: Characterization of Performance', *Rev. Sci. Instrum.*, **61** (2), 874-886 (1990).

Cassanello, M., Larachi, F., Kemoun, A., Al-Dahhan, M. H., and Dudukovic, M. P., 'Inferring Liquid Chaotic Dynamics in Bubble Columns', *Chem. Eng. Sci.*, **56**, 6125-6134 (2001).

Chabot, J. and De Lasa, H. I., 'Gas Holdup and Bubble Characteristics in a Bubble Column Operated at High Temperature', *Ind. Eng. Chem. Res.*, **32**, 2595-2601 (1993).

Chabot, J., Lee, S. L. P., Soria, A., and de Lasa, H. I., 'Interaction Between Bubbles and Fibre Optic Probes in a Bubble Column', *Can. J. Chem. Eng*., **70**, 61-68 (1992).

Chaouki, J., Larachi F., and Dudukovic, M. P., Non-Invasive Monitoring of Multiphase Flows, *Elsevier Science B. V.*, Amsterdam, Netherlands (1997).

Chen, J., Li, F., Degaleesan, S., Gupta, P., Al-Dahhan, M. H., Dudukovic, M. P. and Toseland, B. A., 'Fluid Dynamic Parameters in Bubble Columns with Internals', *Chem. Eng. Sci.*, **54** (13-14), 2187-2197 (1999).

Chen, J., Gupta, P., Degaleesan, S., Al-Dahhan, M. H., Dudukovic', M. P., and Toseland, B. A., 'Gas Holdup Distribution in Large Diameter Bubble Columns Measured by Computed Tomography', *Flow Measurement and Instrumentation*, **9**, 91-101 (1998).

Chen, W., Hasegawa, T., Tsutsumi, A., and Otawara, K., 'Scale-up effects on the time-averaged and dynamic behavior in bubble column reactors', *Chem. Eng. Sci*., **56**, 6149-6155 (2001).

Chisti, M. Y., Airlift Bioreactors, Elsevier Applied Science, London (1989).

Clark, N. N., Atkinson, C. M., and Flemmer, R. L. C., 'Turbulent Circulation in Bubble Columns', *AIChE J*., **33** (3), 515-518 (1987).

Craft, T. J., Launder, B. E., and Suga, K., 'Extending the Applicability of Eddy Viscosity Models through the Use of Deformation Invariants and Nonlinear Elements', Proc. of 5th LAHR Conference on Refined-Flow Modeling and Turbulence Measurement, Paris, 1993.

Darton, R. C., LaNauze, R. D., Davidson, J. F., Harrison, D., 'Bubble Growth due to Coalescence in Fluidised Beds', *Trans IChemE.*, **55**, 274-280 (1977).

Deckwer, W., Bubble Column Reactors, John Wiley & Sons (1991).

Deckwer, W. D. and Schumpe, A., 'Bubble Columns – the State of the Art and Current Trends', *Int. Chem. Eng.*, **27** (3), 405-422 (1987).

Deckwer, W. D., Louisi, Y., Zaidi, A., and Ralek, M., 'Hydrodynamic Properties of the Fischer-Tropsch Slurry Process', *Ind. Eng. Chem. Process Des. Dev.*, **19**, 699-708 (1980).

Deckwer, W. D., Adler, I., and Zaidi, A., 'A Comprehensive Study on CO2 - Interphase Mass Transfer in Vertical Cocurrent and Countercurrent Gas-Liquid Flow', *Can. J. Chem. Eng.*, **56**, 43-55 (1978).

Deckwer, W. D., Burckhart, R., and Zoll, G., 'Mixing and Mass Transfer in Tall Bubble Columns', *Chem. Eng. Sci.*, **29**, 2177-2188 (1974).

Deen, N. G., Solberg, T., and Hjertager, B. H., 'Large Eddy Simulation of the Gas-Liquid Flow in a Square Cross-Sectioned Bubble Column', *Chem. Eng. Sci.*, **56**, 6341-6349 (2001).

Deen, N. G., An Experimental and Computational Study of Fluid Dynamics in Gas-Liquid Chemical Reactors, Ph.D. Thesis, Aalborg University, Denmark (2001).

De Swart, J. W. A., Scale-up of a Fischer-Tropsch Slurry Reactor, Ph.D. Thesis, University of Amsterdam, The Netherlands (1996).

Degaleesan, S., Dudukovic', M. P., and Pan, Y., 'Application of Wavelet Filtering to the Radioactive Particle Tracking Technique', *Flow Measurement and Instrumentation*, **13** (1-2), 31-43 (2002).

Degaleesan, S., Turbulence and Liquid Mixing in Bubble Columns, Ph.D. Thesis, Washington University, Saint Louis, Missouri, USA (1997).

Delhaye, J. M., 'Hot-Film Anemometry in Two Phase Flow', Two Phase Flow Instrumentation, *Eleventh National ASME/AIChE Heat Transfer Conference*, Minneapolis, 58-69 (1969).

Deshpande, N. S., and Joshi, J. B., 'Simultaneous Measurements of Gas and Liquid Phase Velocities and Gas Holdup Using Laser-Doppler Velocimeter', *Chem. Eng. Comm.*, **162**, 151-168 (1997).

Devanathan, N., Investigation of Liquid Hydrodynamics in Bubble Columns via a Computer Automated Radioactive Particle Tracking (CARPT), Ph.D. Thesis, Washington University, Saint Louis, Missouri, USA (1991).

Devanathan, N., Moslemian, D., and Dudukovic', M. P., 'Flow Mapping in Bubble Columns Using CARPT', (1990).

Dicken, F. J., Williams, R. A., and Beck, M. S., 'Determination of Composition and Motion of Multicomponent Mixtures in Process Vessels Using Electrical Impedance Tomography - I. Principles and Process Engineering Applications', *Chem. Eng. Sci*., **48**, 1883-1897 (1993).

Drew, D. A. and Passman, S. L., Theory of Multicomponent Fluids, Springer, New York (1998).

Durbin, P. A. and Pettersson Reif, B. A., Statistical Theory and Modeling for Turbulent Flows, John Wiley & Sons (2001).

Ellenberger, J. and Krishna, R., 'A Unified Approach to the Scale-Up of Gas-Solid Fluidized Bed and Gas-Liquid Bubble Column Reactors', *Chem. Eng. Sci.*, **49**, 5391-5411 (1994).

Fan, L. S., Yang, G. Q., Lee, D. J., Tsuchiya, K., and Luo, X., 'Some Aspects of High Pressure Phenomena of Bubbles in Liquids and Liquid-Solid Suspensions', *Chem. Eng. Sci.*, **54** (21), 4681-4709 (1999).

Fan, L. S. and Tsuchiya, K., Bubble Wake Dynamics in Liquids and Liquid-Solid Suspensions, Butterworth-Heinemann, Boston (1990).

Fransolet, E., Crine, M., L'Homme, G., Toye, D., and Marchot, P., 'Analysis of Electrical Resistance Tomography Measurements Obtained on a Bubble Column', *Meas. Sci. Technol.*, **12**, 1055-1060, (2001).

Freedman, W., and Davidson, J. F., 'Hold-up and Liquid Circulation in Bubble Columns', *Trans. Instn. Chem. Engrs*., **47**, T251-T262 (1969).

Fregapane, G., Rubio-Fernández, H., Nieto, J., and Salvador, M. D., 'Wine Vinegar Production Using a Noncommercial 100-Litre Bubble Column Reactor Equipped with a Novel Type of Dynamic Sparger', *Biotechnology and Bioengineering*, **63** (2), 141-146 (1999).

Frijlink, J. J., Physical Aspects of Gassed Suspension Reactors, Ph.D. Thesis, Delft University of Technology, The Netherlands (1987).

Gaddis, E. S. and Vogelpohl, A., 'Bubble Formation in Quiescent Liquid Under Constant Flow Conditions', *Chem. Eng. Sci.*, **41**, 97-105 (1986).

Gavrilescu, M., and Roman, R. V., 'Flow Regimes in Bubble Column Reactors', *Revue Roumaine de Chimie*, **41** (9-10), 823-834 (1996).

Geary, N. W., and Rice, R. G., 'Circulation and Scale-up in Bubble Columns', *AIChE J*., **38** (1), 76-81 (1992).

George, D. L., Shollenberger, K. A., Torczynski, J. R., O'Hern, T. J., and Ceccio, S. L., 'Three-phase Material Distribution Measurements in a Vertical Flow Using Gamma-Densitometry Tomography and Electrical-Impedance Tomography', *Int. J. Multiphase Flow*, **27**, 1903-1930 (2001).

George, D. L., Torczynski, J. R., Shollenberger, K. A., O'Hern, T. J., and Ceccio, S. L., 'Validation of Electrical-Impedance Tomography for Measurements of Material Distribution in Two-Phase Flows', *Int. J. Multiphase Flow*, **26**, 549-581 (2000[a]).

George, D. L., Shollenberger, K. A., and Torczynski, J. R., 'Sparger Effects on Gas Volume Fraction Distributions in Vertical Bubble Column Flows as Measured by Gamma-Densitometry Tomography', Proceedings of FEDSM'00, 2000 ASME Fluids Engineering Division Summer Meeting, 1-8 (2000[b]).

Groen, J., S., Oldeman, R. G. C., Mudde, R. F., and van den Akker, H. E. A., 'Coherent Structures and Axial Dispersion in Bubble Column Reactors', *Chem. Eng. Sci*., **51** (10), Part A, 2511-2520 (1996).

Groen, J. S., Mudde, R. F., and van den Akker, H. E. A., 'Time Dependent Behavior of the Flow in a Bubble Column', *Trans. Inst. Chem. Engrs*., A9-A16 (1995).

Gross, R. W., and Kuhlman, J. M., 'Three-Component Velocity Measurements in a Laboratory Bubble Column', *Advances in Gas-Liquid Flows*, **99**, 157-165 (1990).

Gupta, P., Churn-Turbulent Bubble Columns – Experiments and Modeling, Ph.D. Thesis, Washington University, Saint Louis, Missouri, USA (2002).

Gupta, P., Ong, B., Al-Dahhan, M.H., Dudukovic, M. P., and Toseland, B. A., 'Hydrodynamics of Churn-Turbulent Bubble Columns: Gas-Liquid Recirculation and Mechanistic Modeling', *Catalysis Today*, **64** (3-4), 253-269 (2001).

Hammer, H., Schrag, H. J., Hektor, K., Schonau, H., Kusters, W., Soemarno, A., Sahabi, U., Napp, W., 'New Subfunctions on Hydrodynamics, Heat and Mass Transfer for Gas/Liquid and Gas/Liquid/Solid Chemical and Biochemical Reactors', Frontiers in Chemical Reaction Engineering, 464-474, John Wiley & Sons, New York (1984).

Hebrard, G., Bastoul, D., and Roustan, M., 'Influence of the Gas Sparger on the Hydrodynamic Behavior of Bubble Columns', *Trans IChemE*, **74**, Part A, 406-414 (1996).

Herringe, R. A. and Davis, M. R., 'Detection of Instantaneous Phase Changes in Gas-Liquid Mixtures', *J. Phys. E: Sci. Instr.*, **7**, 807-812 (1974).

Hikita, H., Asai, S., Tanigawa, K., Segawa, K., and Kitao, M., 'Gas Holdup in Bubble Columns', *Chem. Eng. J.*, 20, 59-67 (1980).

Hikita, H., and Kikukawa, H., 'Liquid-Phase Mixing in Bubble Columns: Effect of Liquid Properties', *Chem. Eng. J.*, **8**, 191-197 (1974).

Hills, J. H., 'The Operation of a Bubble Column at High Throughputs. I. Gas Holdup Measurements', *Chem. Eng. J.*, **12**, 89-99 (1976).

Hills, J. H., 'Radial Non-Uniformity of Velocity and Voidage in a Bubble Column', *Trans. Instn. Chem. Engrs.*, **52**, 1-9 (1974).

Hsu, S. H., Lee, W. H., Yang, Y. M., Chang, C. H., and Maa, J. R., 'Bubble Formation at an Orifice in Surfactant Solutions Under Constant-Flow Conditions', *Ind. Eng. Chem. Res*., **39**, 1473-1479 (2000).

Idogawa, K., Ikeda, K., Fukuda, T., and Morooka, S., 'Effect of Gas and Liquid Properties on the Behavior of Bubbles in a Column Under High Pressure', *Int. Chem. Eng*., **27** (1), 93-99 (1987[a]).

Idogawa, K., Ikeda, K., Fukuda, T., and Morooka, S., 'Formation and Flow of Gas Bubbles in a Pressurized Bubble Column with a Single Orifice or Nozzle Gas Distributor', *Chem. Eng. Comm.*, **59**, 201-212 (1987[b]).

Idogawa, K., Ikeda, K., Fukuda, T., and Morooka, S., 'Behavior of Bubbles of the Air-Water System in a Column Under High Pressure', *Int. Chem. Eng*., **26** (3), 468-474 (1986).

Idogawa, K., Ikeda, K., Fukuda, T., Morooka, S., 'Behavior of Bubbles of the Air-Water System in a Column Under High Pressure For Air-Water System', *Kagaku Kogaku Ronbunshu*, **11** (3), 253-258 (1985).

Ityokumbul, M. T., Kosari, N., and Bulani, W., 'Gas Holdup and Liquid Mixing at Low and Intermediate Gas Velocities I. Air-Water System', *Chem. Eng. J*., **53**, 167-172, 1994.

Jamialahmadi, M., Branch, C., and Müller-Steinhagen, H., 'Terminal Bubble Rise Velocity in Liquids', *Trans. IChemE.*, **72A**, 119-122 (1994).

Jamialahmadi, M., and Müller-Steinhagen, H., 'Effect of Superficial Gas Velocity on Bubble Size, Bubble Rise Velocity and Gas Holdup in Bubble Columns', *Developments in Chem. Eng. And Mineral Processing*, **1** (1), 16-31 (1993).

Jamialahmadi, M., and Müller-Steinhagen, H., 'Effect of Alcohol, Organic Acid and Potassium Chloride Concentration on Bubble Size, Bubble Rise Velocity and Gas Holdup in Bubble Columns', *Chem. Eng. J.*, **50**, 47-56 (1992).

Jiang, P, Lin, T. J., Luo, X., and Fan, L. S., 'Flow Visualization of High-Pressure (21 MPa) Bubble Column: Bubble Characteristics', *Trans IChemE*, **73**, Part A, 269-274 (1995).

Joshi, J. B., Parasu Veera, U., Prasad, Ch. V., Phanikumar, D. V., Deshphande, N. S., Thakre, S. S., and Thorat, B. N., 'Gas Holdup Structure in Bubble Column Reactors', *PINSA* **64 A** (14), 441-567 (1998).

Joshi, J. B. and Shah, Y. T., 'Hydrodynamic and Mixing Models in Bubble Column Reactors', *Chem. Eng. Commun.*, **11** (1-3), 165-199 (1981).

Joshi, J. B., 'Axial Mixing in Multiphase Contactors - A Unified Correlation', *Trans. Inst. Chem. Engrs*, **58** (3), 155-165 (1980).

Kang, Y., Cho, Y. J., Woo, Kim, K. I., and Kim, S. D., 'Bubble Properties and Pressure Fluctuations in Pressurized Bubble Columns', *Chem. Eng. Sci*., **55**, 411-419 (2000).

Kang, Y., and Shim, J. S., Cho, S. H., Choi, M. J., and Lee, K. W., 'Dehydration of Ortho-Boric Acid in a Three-Phase Bubble Column Reactor Operating at Low Pressure', *J. Chem. Tech. Biotechnology*, **63**, 313-320 (1995).

Kastanek, F., Zahradnik, J., Kratochvil, J., and Cermak, J., Chemical Reactions for Gas-Liquid Systems, Ellis Horwood, New York (1993).

Kawase, Y., and Tokunaga, M., 'Characteristic Mixing Length in Bubble Columns', *Can. J. Chem. Eng.*, **69**, 1228-1231 (1991).

Kawase, Y., and Moo-Young, M., 'Turbulence Intensity in Bubble Columns', *Chem. Eng. J*., **40** (1), 55-58 (1989).

Kemoun, A., Ong, B. C., Gupta, P., Al-Dahhan, M. H., and Dudukovic', M. P., 'Gas Holdup in Bubble Columns at Elevated Pressure via Computed Tomography', *International J. of Multiphase Flows*, 27 (5), 929-946 (2001).

Kling, G., 'Über die Dynamik der Blasenbildung Beim Begasen von Flüssigkeiten Unter Druck', *Int. J. Heat Mass Transfer*, **5**, 211-223 (1962).

Koide, J., Morooka, S., Ueyama, K., Matsura, A., Yamashita, F., Jwamoto, S., Kato, Y., Inoue, H., Shigeti, M., Suzuki, S., and Akehata, T., 'Behavior of Bubbles in Large Scale Bubble Columns', *J. Chem. Eng. of Japan*, **12**, 98-104 (1979).

Kojima, E., Unno, H., Sato, Y., Chida, T., Imai, H., Endo, K., Inoue, I., Kobayashi, J., Kaji, H., Nakanishi, H., and Yamamoto, K., 'Liquid Phase Velocity in a 5.5 cm Diameter Column', *J. Chem. Eng. Japan*, **13** (1), 16-21 (1980).

Kojima, H., Okumura, B., and Nakamura, A., 'Effect of Pressure on Volumetric Mass Transfer Coefficient and Gas Holdup in Bubble Column', *Chem. Eng. Sci.*, **52** (21/22), 4111-4116 (1997).

Kojima, H., Okumura, B., and Nakamura, A., 'Effect of Pressure on Gas Holdup in a Bubble Column and a Slurry Bubble Column', *J. Chem. Eng. Japan*, **24** (1), 115-117 (1991).

Kölbel, H., Borchers, E., and Langemann, H., 'GröBenverteilung der Gasblasen in Blasensäulen. Teil 1: EinflüBe von Flüssigkeitsviskosität und Säuleninnendruck', *Chem. Ing. Tech*., **33**, 668-675 (1961).

Krishna, R., J. M., van Baten, M. I. Urseanu and J., Ellenberger, 'Design and Scale Up of a Slurry Reactor for Fischer-Tropsch Synthesis', *Chem. Eng. Sci.*, **56**, 537-545 (2001).

Krishna, R., 'A Scale-up Strategy for a Commercial Scale Bubble Column Slurry Reactor for Fischer-Tropsch Synthesis', *Oil & Gas Science and Technology*, **55** (4), 359-393 (2000).

Krishna, R., M. I., Urseanu, J. M. van Baten and J., Ellenberger, 'Rise Velocity of a Swarm of Large Bubbles in Liquids', *Chem. Eng. Sci.*, **54**, 171-183 (1999).

Krishna, R., van Baten, J. M., and Ellenberger, J., 'Scale Effects in Fluidized Multiphase Reactors', *Powder Technology*, **100**, 137-146 (1998).

Krishna, R., and Ellenberger, J., 'Gas Holdup in Bubble Column Reactors Operating in the Churn-Turbulent Flow Regime', *AIChE J*., **42** (9), 2627-2634 (1996).

Krishna, R. and Ellenberger, J., 'A Unified Approach to the Scale-Up of Fluidized Multiphase Reactors', *Trans. I. Chem. E.*, **73(A)**, 217 (1995).

Krishna, R., de Swart, J. W. A., Hennephof, D. E., Ellenberger, J., and Hoefsloot, H. C., 'Influence of Increased Gas Density on Hydrodynamics of Bubble Column Reactors', *AIChE J.*, **40** (1), 112-119 (1994).

Kulkarni, A. A., Joshi, J. B., Ravi Kumar, V., and Kulkarni, B. D., 'Wavelet Transform of Velocity-Time Data for the Analysis of Turbulent Structures in a Bubble Column', *Chem. Eng. Sci.*, **56**, 5305-5315 (2001[a]).

Kulkarni, A. A., Joshi, J. B., Ravi Kumar, V., and Kulkarni, B. D., 'Application of Multiresolution Analysis for Simultaneous Measurement of Gas and Liquid Velocities and Fractional Gas Holdup in Bubble Column Using LDA', *Chem. Eng. Sci.*, **56**, 5037-5048 (2001[b]).

Kulkarni, A. A., Joshi, J. B., Ravi Kumar, V., and Kulkarni, B. D., 'Simultaneous Measurement of Holdup Profiles and Interfacial Area using LDA in Bubble Columns: Predictions by Multiresolution Analysis and Comparsion with Experiments', *Chem. Eng. Sci.*, **56**, 6437-6445 (2001[c]).

Kulkarni, A. A., Joshi, J. B., Ravi Kumar, V., and Kulkarni, B. D., 'Identification of the Principal Time Scales in Bubble Column by Wavelet Analysis', *Chem. Eng. Sci*., **56**, 5739-5747 (2001[d]).

Kumar, S. B., Moslemian, D., and Dudukovic', M. P., 'Gas Holdup Measurements in Bubble Columns Using Computed Tomography', *AIChE J*., **43** (6), 1414-1425 (1997).

Kumar, S. B., Moslemian, D., and Dudukovic', M. P., 'A γ-Ray Tomographic Scanner for Imaging Voidage Distribution in Two-Phase Flow Systems', *Flow Meas. Instrum*., **6** (1), 61-73 (1995).

Kumar, S. B., N. Devanathan, D. Moslemian and M. P. Dudukovic', 'Effect of Scale on Liquid Recirculation in Bubble Columns', *Chem. Engng., Sci*., **49** (24B), 5637-5652 (1994).

Kumar, S. B., Computed Tomographic Measurements of Void Fraction and Modeling of the Flow in Bubble Columns, Ph.D. Thesis, Washington University, Saint Louis, Missouri, USA (1994).

Kumar, A., Degaleesan, T. E., Laddha, G. S., and Hoelscher, H. E., 'Bubble Swarm Characteristics in Bubble Columns', *Can. J. Chem. Eng.*, **54**, 503 (1976).

Lain, S., Broder, D., Sommerfeld, M., 'Experimental and Numerical Studies of the Hydrodynamics in a Bubble Column', *Chem. Eng. Sci*., **54**, 4913-4920 (1999).

LaNauze, R. D., and Harris, I. J., 'Gas Bubble Formation at Elevated System Pressures', *Trans. Instn. Chem. Engrs*., **52** (4), 337-348 (1974).

Lapidus, L. and Elgin, J. C., 'Mechanics of Vertical-Moving Fluidized Systems', *AIChE J.*, **3**, 63-68 (1957).

Larachi, F., Kennedy, G., and Chaouki, J., 'A γ-ray Detection System for 3-D Particle Tracking in Multiphase Reactors', *Nuclear Instruments and Methods in Physics Research A*, **338**, 568-576 (1994).

Launder, B. E., Lecture Notes on "Turbulence Modeling in Industrial Flows", LesHouches Summer School on Computational Fluid Dynamics, 1993.

Lee, D. J., McLain, B. K., Cui, Z., and Fan, L. S., 'Pressure Effect on the Flow Fields and the Reynolds Stresses in a Bubble Column', *Ind. Eng. Chem. Res.*, **40**, 1442-1447 (2001).

Lee, J. C. and Meyrick, D. L., *Trans. Inst. Chem. Engrs.*, **48**, T37 (1970).

Leibson, I., Holcomb, E. G., Cacoso, A. G., and Jacmic, J. J., 'Rate of Flow and Mechanics of Bubble Formation from Single Submerged Orifices', *AIChE J.*, **2** (3), 296-306 (1956).

Letzel, H. M., Schouten, J. C., Krishna, R., and van den Bleek, C. M., 'Characterization of Regimes and Regime Transitions in Bubble Columns by Chaos Analysis of Pressure Signals,' *Chem. Eng. Sci.*, **52**, 4447 (1997[a]).

Letzel, H. M., Schouten, J. C., van den Bleek, C. M., and Krishna, R., 'Influence of Elevated Pressure on The Stability of Bubbly Flows,' *Chem. Eng. Sci.*, **52**, 3733 (1997[b]).

Letzel, H. M., Hydrodynamics and Mass Transfer in Bubble Columns at Elevated Pressures, Ph.D. Thesis, University of Amsterdam, The Netherlands (1997).

Levy, S., 'Prediction of Two-Phase Pressure Drop and Density Distributor From Mixing Length Theory', *J. Heat Transfer*, **85**, 137-152 (1963).

Lin, T. J., Juang, R. C., and Chen, C. C., 'Characterizations of Flow Regime Transitions in a High-Pressure Bubble Column by Chaotic Time Series Analysis of Pressure Fluctuation Signals', *Chem. Eng. Sci.*, **56**, 6241-6247 (2001).

Lin, T. J., Tsuchiya, K., and Fan, L. S., 'On the Measurements of Regime Transition in High-Pressure Bubble Columns', *Can. J. Chem. Eng*., **77**, 370-374 (1999).

Lin, T. J., Tsuchiya, K., and Fan, L. S., 'Bubble Flow Characteristics in Bubble Columns at Elevated Pressure and Temperature', *AIChE J*., **44** (3), 545-560 (1998).

Liu, W., Clark, N. N., and Karamavruc, A. I., 'Relationship Between Bubble Size Distributions and Chord-Length Distribution in Heterogeneously Bubbling Systems', *Chem. Eng. Sci*., **53** (6), 1267-1276 (1998).

Luo, X., Lee, D. J., Lau, R., Yang, G. Q., and Fan, L. S., 'Maximum Stable Bubble Size and Gas Holdup in High-Pressure Slurry Bubble Columns,' *AIChE J.*, **45** (4), 665-680 (1999).

Luo, H., Coalescence, Breakup and Liquid Circulation in Bubble Column Reactors, Ph.D. Thesis, Universitetet I Trondheim, Norges Tekniske Hϕgskole (1993).

Luo, H. and Svendsen, 'Turbulent Circulation in Bubble Columns from Eddy Viscosity Distributions of Single-Phase Pipe Flow', *Can. J. Chem. Eng.*, **69**, 1389-1394 (1991).

Massoudi, R. and King, A. D., 'Effect of Pressure on the Surface Tension of Water. Adsorption of Low Molecular Weight Gases on Water at 25°C', *J. Phys. Chem.*, **78**, 2262-2266 (1974).

Mei, R., Adrian, R. J., and Hanratty, T. J., 'Particle Dispersion in Isotropic Turbulence Under Stokes Drag and Basset Force with Gravitational Settling', *J. Fluid Mech.*, **225**, 481-495 (1991).

Mendelson, H. D., 'The Prediction of Bubble Terminal Velocities from Wave Theory', *AIChE.*, 13, 250-253 (1967).

Menzel, T., in der Weide, T., Staudacher, O., Wein, O., and Onken, U., 'Reynolds Shear Stress for Modeling of Bubble Column Reactors', *Ind. Eng. Chem. Res.*, **29**, 988-994 (1990).

Menzel, T., Onken, U., and Wein, O., 'Deterministic and Stochastic Components of the Liquid Velocity in Gas-Liquid Reactors', *Dechema-Monogr.*, **120** (Instationary Processes Dynamic Exp. Methods Catal., Electrochem. Corros.), 307-325 (1989).

Mikkilineni, S. and Knickle, H. N., 'The Effect of Gas Distributors on Holdup and Flow Pattern in Bubble Column', Part. Multiphase Processes (Proc. Int. Symp. Workshop), **3**, 127-145 (1987).

Mishima, K. and Ishii, M., 'Flow Regime Transition Criteria for Upward Two-Phase Flow in Vertical Tubes', *Int. J. Heat Mass Transfer*, **27** (5), 723-737 (1984).

Miyauchi, T., Furusaki, S., Morooka, S., and Ikeda, Y., 'Transport Phenomena and Reaction in Fluidized Catalysts Beds', in Advances in Chemical Engineering, **11**, 275-448 (1981).

Miyauchi, T., and Shyu, C. N., 'Flow of Fluid in Gas Bubble Columns', *Kagaku Kogaku*, **34**, 958-964 (1970).

Monin, A. S. and Yaglom, A. M., 'Statistical Fluid Mechanics: Mechanics of Turbulence (Volume 1)', The MIT Press, Cambridge (1971).

Mudde, R. F., Groen, J. S., van den Akker, H. E. A., 'Application of LDA to Bubbly Flows', *Nuclear Eng. Design*, **184**, 329-338 (1998).

Mudde, R. F., Groen, J. S., and Van Den Akker, H. E. A., 'Liquid Velocity Field in a Bubble Column: LDA Experiments', *Chem. Eng. Sci*., **52** (21/22), 4217-4224 (1997[a]).

Mudde, R. F., Lee, D. J., Reese, J., and Fan, L. S., 'Role of Coherent Structures on Reynolds Stresses in a 2-D Bubble Column', *AIChE J*., **43** (4), 913-926 (1997[b]).

Mudde, R. F., Bakker, R. A., van den Akker, H. E. A., 'Noise Analysis of Transmitted Light Beams for Determining Bubble Velocity and Gas Holdup Profiles in a Bubble Column', *Chem. Eng. Sci*., **47** (13/14), 3631-3638 (1992).

Nakanoh, M., and Yoshida, F., 'Gas Adsorption by Newtonian and Non-Newtonian Liquids in a Bubble Column', *Int. Eng. Chem. Process Des. Dev.*, **19**, 190-195 (1980).

Nottenkämper, R., Steiff, A., and Weinspach, P. M., 'Experimental Investigation of Hydrodynamics of Bubble Columns', *Ger. Chem. Engng*, **6**, 147-155 (1983).

O'Hern, T. J., Torcynski, J. R., Ceccio, S. L., Tassin, A. L., Chahine, G. L., Duraiswarmi, R., and Sarkar, K., 'Development of an Electrial Impedance Tomography System for Air-Water Vertical Bubble Column', Forum on Measurement Techniques in Multiphase Flows, ASME IMECEE (1995).

Ohnuki, A. and Akimoto, H., 'Model Development for Bubble Turbulent Diffusion and Bubble Diameter in Large Vertical Pipes', *J. Nuclear Science and Tech.*, **38** (12), 1074-1080 (2001).

Oyevaar, M. H., De la Rie, T., Van der Sluijs, C. L., and Westerterp, K. R., 'Interfacial Areas and Gas Holdups in Bubble Columns and Packed Bubble Columns at Elevated Pressures', *Chem. Eng. Process.*, **26**, 1-14 (1989).

Oyevaar, M. H., and Westerterp, K. R., 'Mass Transfer Phenomena and Hydrodynamics in Agitated Gas-Liquid Reactors and Bubble Columns at Elevated Pressures: State of the Art', *Chem. Eng. Process.*, **25**, 85-98 (1989).

Pannek, S., Pauli, J., and Onken, U., 'Determination of Local Hydrodynamic Parameters in Bubble Columns by the Electrodiffusion Method with Oxygen as Depolarizer', *J. Applied Electrochemistry*, **24**, 666-669 (1994).

Ramachandran, P. A., and Chaudhari, R. V., Three-Phase Catalytic Reactors, Gordon and Breach Science Publishers (1983).

Reese, J., and L. S. Fan, 'Transient Flow Structure in the Entrance Region of a Bubble Column Using Particle Image Velocimetry', *Chem. Eng. Sci.*, **49** (24B), 5623-5636 (1994).

Reichardt, H., 'Vollstandige Darstellung der Turbulenten Geschwindigkeitsverteilung in Glatten Rohren', *Z. Angew. Math. Mech.*, **31**, 208-219 (1951).

Reilly, I. G., Scott, D. S., De Bruijn, T. J. W., and MacIntyre, D., 'The Role of Gas Phase Momentum in Determining Gas Holdup and Hydrodynamic Flow Regimes in Bubble Column Operation', *Can. J. Chem. Eng.*, **72**, 3 (1994)

Reilly, I. G., Scott, D. S., De Bruijn, T., Jain, A., and Piskorz, J., 'A Correlation for Gas Holdup in Turbulent Coalescing Bubble Columns', *Can. J. Chem. Eng*., **64**, 705-717 (1986).

Rice, R. G., and Geary, N. W., 'Prediction of Liquid Circulation in Viscous Bubble Columns', *AIChE J*., **36** (9), 1339-1348 (1990).

Richardson, J. F. and Zaki, W. N., 'Sedimentation and Fluidization: Part I', *Trans. Inst. Chem. Engrs.*, **32**, 35-53 (1954).

Riquarts, H. P., 'Strömungsmechanische, Impulsaustausch und Durchmischung der Flüssigen Phase in Blasensäulen', *Chem. Ing. Tech.*, **53**, 60-61 (1981).

Rivas, O., Bresolin, G. A., Estevez, L. A., Santamaria, X., Cavicchioli, I., 'Effect of Gas Distribution on the Fluid Dynamics of Three-Phase Bubble Columns', *Rev. Tec. Inte*vep., **7** (2), 97-102 (1987).

Rubio, F. C., Garcia, J. L., Molina, E., and Chisti, Y., 'Steady-state Axial Profiles of Dissolved Oxygen in Tall Bubble Column Bioreactors', *Chem. Eng. Sci.*, **54**, 1711-1723 (1999).

Ruzicka, M., Zahradnik, J., Drahos, J., and Thomas, N. H., 'Homogeneous-Heterogeneous Regime Transition in Bubble Columns', *Chem. Eng. Sci.*, **56**, 4609-4626 (2001).

Sannaes, B. H., Solids Movement and Concentration Profiles in Slurry Column Reactors, Dr. Ing. Thesis, Norwegian University of Science and Technology, Norway (1997).

Sarrafi, A., Jamialahmadi, M., Müller-Steinhagen, H., and Smith, J. M., 'Gas Holdup in Homogeneous and Heterogeneous Gas-Liquid Bubble Column Reactors', *Canadian J. Chem. Eng.*, **77**, 11-21 (1999).

Sato, Y. and Sekoguchi, K., 'Liquid Velocity Distribution in Two-Phase Bubble Flow', *Int. J. Multiphase Flow*, **2**, 79 (1975).

Schlichting, H., Boundary Layer Theory, McGraw Hill, New York, 602-609 (**1979**).

Schmitz, D. and Mewes, D., 'Tomographic Imaging of Transient Multiphase Flow in Bubble Columns', *Chem. Eng. J.*, **77**, 99-104 (2000).

Schügerl, K., Lubbert, A., Korte, T., and Diekmann, J., 'Measuring Techniques for Characterizing Gas/Liquid Reactors', International Chem. Eng., 27 (4), 583-596 (1977).

Seeger, A., Affeld, K., Kertzscher, U., Goubergrits, L., and Wellnhofer, E., 'Assessment of Flow Structures in Bubble Columns by X-ray Based Particle Tracking Velocimetry', 4th International Symposium on Particle Image Velocimetry (2001).

Sekizawa, T., Kubota, H., and Chung, W. C., 'Apparent Slip Velocity with Recirculating Turbulent Flow in Bubble Columns', *J. Chem. Eng. Japan*, **16** (4), 327-330 (1983).

Serizawa, A., Kataoka, I., and Michiyoshi, I., 'Turbulence Structure of Air-Water Bubbly Flow – I. Measuring Techniques', *Int. J. Multiphase Flow*, **2**, 221-233 (1975).

Sheng, Y. Y., and Irons, G. A., 'A Combined Laser Doppler Anemometry and Electrical Probe Diagnostic for Bubbly Two-Phase Flow', *Int. J. Multiphase Flow*, **17** (5), 585-598 (1991).

Shollenberger, K. A., George, D. L., and Torczynski, J. R., 'Effect of Liquid Viscosity on the Development of Gas Volume Fraction Profiles in Vertical Bubble Column Flows', 4th International Conference on Multiphase Flow, 1-12 (2001).

Shollenberger, K. A., George, D. L., and Torczynski, J. R., 'Effect of Sparger Geometry on Gas-Volume Fraction in Bubble Column Flows Measured by Gamma-Densitometry Tomography (GDT)', *AIChE* 2000 Annual Meeting, Paper No. 344c (2000).

Shollenberger, K. A., Torczynski, J. R., Adkins, D. R., O'Hern, T. J., and Jackson, N. B., 'Gamma-Densitometry Tomography of Gas Holdup Spatial Distribution in Industrial-Scale Bubble Columns', *Chem. Eng. Sci*., **52** (13), 2037-2048 (1997).

Shollenberger, K. A., Torczynski, J. R., Adkins, D. R., and O'Hern, T. J., 'Bubble Column Measurements Using Gamma Tomography', *Fluid Measurement and Instrumentation*, **FED 211**, 25-30 (1995).

Snyder, W. H. and Lumley, J. L., 'Some Measurements of Particle Velocity Autocorrelation Functions in a Turbulent Flow', *J. Fluid Mech.*, **48**, 41-71 (1971).

Snabre, P. and Magnifotcham, F., 'I. Formation and Rise of a Bubble Stream in a Viscous Liquid', *Eur. Phys. J. B*, **4**, 369-377 (1998).

Sotelo, J. L., Benitez, F. J., Beltran-Heredia, J., and Rodriguez, C., 'Gas Holdup and Mass Transfer Coefficients in Bubble Columns. I. Porous Glass-Plate Diffusers', *Int. Chem. Eng*., **34** (1), 82-90 (1994).

Speziale, C. G., 'On Nonlinear *k-l* and *k-ε* models of turbulence', *J. of Fluid Mechanics*, **178**, 459-475 (1987).

Sriram, K. and Mann, R., 'Dynamic Gas Disengagement: A New Technique for Assessing the Behavior of Bubble Columns', *Chem. Eng. Sci.*, **32**, 571-580 (1976).

Stegeman, D. Hydrodynamic Studies of Two and Three Phase Systems: Pressure Influence, PhD. Thesis, Universiteit Twente, The Netherlands (1994).

Steinemann, J. and Buchholz, R., 'Application of an Electrical Conductivity Microprobe for the Characterization of Bubble Behavior in Gas-Liquid Bubble Flow', *Particle Characterization*, **1** (3), 102-107 (1984).

Tadaki, T., and Maeda, S., *Kagaku Kogaku*, **27**, 147 (1963).

Tassin, A. L., and Nikitopoulos, D. E., 'Non-intrusive Measurements of Bubble Size and Velocity', *Experiments in Fluids*, **19**, 121-132 (1995).

Tennekes, H. and Lumley, J. L. A First Course in Turbulence, MIT Press, Cambridge (1972).

Terasaka, K, Hieda, Y., and Tsuge, H., 'SO_2 Bubble Formation from an Orifice Submerged in Water', *J. Chem. Eng. Japan*, **32** (4), 472-479 (1999).

Tomiyama, A., Kataoka, I., and Sakaguchi, T., 'Drag Coefficient of Bubbles (1st report, Drag Coefficients of a Single Bubble in a Stagnant Liquid)', *Trans. JSME Part B*, **61** (587), 2357-2364 (1995)

Tsuchiya, K. and Nakanishi, O., 'Gas Holdup Behavior in a Tall Bubble Column with Perforated Plate Distributors', *Chem. Eng. Sci*., **47**, 13/14 (1992).

Tsuge, H., Nakajima, Y., and Terasaka, K., 'Behavior of Bubbles Formed from a Submerged Orifice Under High System Pressure', *Chem. Eng. Sci*., **47** (13/14), 3273-3280 (1992).

Tsuge, H., 'Hydrodynamics of Bubble Formation From Submerged Orifices', Encyclopedia of Fluid Mechanics, **3**, Chapter 9, 192-232 (1985).

Tsuge, H., and Hibino, S., 'Bubble Formation From An Orifice Submerged In Liquids', *Chem. Eng. Comm*., **22**, 63-79 (1983).

Ueyama, K., Morooka, S., Koide, K., Kaji, H., Miyauchi, T., 'Behavior of Gas Bubbles in Bubble Columns', *Ind. Eng. Chem. Process Des. Dev*., **19**, 4, 592-599 (1980).

Ueyama, K., and Miyauchi, T., 'Properties of Recirculating Turbulent Two-Phase Flow in Gas Bubble Columns', *AIChE J*., **25** (2), 258-266 (1979).

Vemeer, D. J. and Krishna, R., 'Hydrodynamics and Mass Transfer in Bubble Columns Operating in the Churn-Turbulent Regime', *Ind. Engng. Chem. Process Design & Dev.*, **20** (3), 475-482 (1981).

Vial, C., Laine, R., Poncin, S., Midoux, N., and Wild, G., 'Influence of Gas Distribution and Regime Transitions on Liquid Velocity and Turbulence in a 3-D Bubble Column', *Chem. Eng. Sci.*, **56**, 1085-1093 (2001[a]).

Vial, C., Poncin, S., Wild, G., and Midoux, N., 'A Simple Method for Regime Identification and Flow Characterisation in Bubble Columns and Airlift Reactors', *Chem. Eng. Processing*, **40**, 135-151 (2001[b]).

Vial, C., Camarasa, E., Poncin, S., Wild, G., Midoux, N., and Bouillard, J., 'Study of Hydrodynamic Behavior in Bubble Columns and External Loop Airlift Reactors through Analysis of Pressure Fluctuations', *Chem. Eng. Sci.*, **55**, 2957-2973 (2000).

Wallis, G. B., One-Dimensional Two-Phase Flow, McGraw Hill, New York (1969).

Walter, J. F., and Blanch, H. W., 'Bubble Breakup in Gas-Liquid Bioreactors: Break-up in Turbulent Flows', *Chem. Eng. J.*, **32**, B7-B17 (1986).

Warsito, W., and Fan, L. S., 'Measurement of Real-Time Flow Structures in Gas-Liquid and Gas-Liquid-Solid Flow Systems Using Electrical Capacitance Tomography (ECT)', *Chem. Eng. Sci.*, **56**, 6455-6462 (2001).

Wender, I., 'Reactions of Synthesis Gas', *Fuel Processing Technology*, **48**, 189-297 (1996).

Wilcox, D. C., Turbulence Modeling for CFD, DCW Industries, La Canada, California (1994).

Wilkinson, P. M., Spek, A. P., and Van Dierendonck, L. L., 'Design Parameters Estimation for Scale-Up of High-Pressure Bubble Columns', *AIChE J.*, **38** (4), 544-554 (1992).

Wilkinson, P. M. and Direndonck, L. L. van, 'Pressure and Gas Density Effects on Bubble Breakup and Gas Holdup in Bubble Columns', *Chem. Eng. Sci.*, **45**, 2309-2315 (1990).

Wilkinson, P. M., Physical Aspects and Scale-up of High Pressure Bubble Columns, Ph.D. Thesis, University of Groningen, The Netherlands (1991).

Wu, Y., Ong, B., and Al-Dahhan, M. H., 'Predictions of Radial Gas Holdup Profiles in Bubble Column Reactors', *Chemical Engineering Science*, **56**, 1207-1210 (2001).

Wu, Y., and Al-Dahhan, M. H., 'Prediction of Axial Liquid Velocity Profile in Bubble Columns', *Chem. Eng. Sci.*, **56**, 1127-1130 (2001).

Yang, Z., Rustemeyer, U., Buchholz, R., and Onken, U., 'Profile of Liquid Flow in Bubble Columns', *Chem. Eng. Comm.*, **49**, 51-67 (1986).

Yao, B. P., Zheng, C., Gasche, H. E., and Hofmann, H., 'Bubble Behavior and Flow Structure of Bubble Columns', *Chem. Eng. Process*., **29**, 65-75 (1991).

Yoo, D. H., Terasaka, K., and Tsuge, H., 'Behavior of Bubble Formation at Elevated Pressure', *J. Chem. Eng. Japan*, **31** (1), 76-82 (1998).

Yoshida, F., and Akita, K., 'Performance of Gas Bubble Columns: Volumetric Liquid-Phase Mass Transfer Coefficient and Gas Holdup', *AIChE J*., **11** (1), 9-13 (1965).

Yu, Y. H., and Kim, S. D., 'Bubble Properties and Local Liquid Velocity in the Radial Direction of Cocurrent Gas-Liquid Flow', *Chem. Eng. Sci*., **46** (1), 313-320 (1991).

Zahradnik, J., Rudolf, P., and Kastanek, F., 'The Effect of Liquid Phase Properties on Gas Holdup in Bubble Column Reactors', *Collection Czechoslovak Chem. Commun.*, **52**, 335-347 (1987).

Zhang, M., Fan, M., and Yu, G., Wang, S., 'Turbulent Liquid Flow in Gas-Liquid Bubble Column', *Chinese J. Chem. Eng*., **7** (3) 189-195 (1999).

Zehner, P., ‘Momentum, Mass and Heat Transfer in Bubble Columns. Flow Model of the Bubble Column and Liquid Velocities’, *Institution of Chemical Engineers*, **26**, 22-35 (1986).

Zuber, N. and Findlay, J. A., ‘Average Volumetric Concentration in Two-Phase Flow Systems’, *J. Heat Transfer*, **87c**, 453-468 (1965).